Small-molecule modulators targeting IRE1α for RNA splicing regulation and METTL16 for RNA methylation inhibition

Dissertation

For the achievement of the academic degree of the

Doctor of Natural Sciences

(Dr. rer. nat.)

Submitted to
The Department of Chemistry and Chemical Biology
Technical University of Dortmund

Yang Liu

Chongqing, China

Dortmund, 2025

The work presented in this thesis was executed from September 2021 to August 2025 under the supervision of V-Prof. Dr. Peng Wu at the Max Planck Institute for Molecular Physiology and the Department of Chemistry and Chemical Biology of TU Dortmund University.

1st Examiner: Prof. Dr. Dr. h.c. Herbert Waldmann

2nd Examiner: V-Prof. Dr. Peng Wu

Dean: Prof. Dr. Stefan M. Kast

Results presented in this thesis contributed to the following publications:

- **Liu, Y**.[#]; Avathan Veettil, A. K. [#]; Gasper, R.; Jiang, M.; Wagner, L.; Hastürk, O.; Wu, P. *, Harnessing Indole Scaffolds to Identify Small-molecule IRE1α Inhibitors Modulating XBP1 mRNA Splicing. *Nature Communications*, accepted in principle.

- **Liu, Y**.[#]; Goebel, G. L. [#]; Kanis, L.; Hastürk, O.; Kemker, C.; Wu, P., Aminothiazolone Inhibitors Disrupt the Protein–RNA Interaction of METTL16 and Modulate the m6A RNA Modification. *JACS Au*, 2024, 4, 4, 1436–1449.

The work of the author also contributed to the following publications during the PhD studies:

- Avathan Veettil, A. K. [#]; **Liu, Y.**[#]; Wagner, L.; Hastürk, O.; Nguyen, S. T.; Wu, P., Pyrazolylpyrimidinamines decorated via Petasis reaction as small-molecule activators of the RNA-degrading ribonuclease IRE1α. Manuscript submitted.

- Roy, S.; **Liu, Y**.; Wu, P., Molecular Dynamics Simulation-Based Analysis of Advanced Small-Molecule Kinase Inhibitors Identified pre-let-7 miRNA Binders. *ChemBioChem*, 2025, doi:10.1002/cbic.202500421.

- Azam, U.; Humayun, W. A.; Veettil, A. K. A.; **Liu, Y**.; Hastuerk, O.; Jiang, M.; Sievers, S.; Wu, P.; Naseer, M. M., Identification of 5-amino-1,3,4-thiadiazole appended isatins as bioactive small molecules with polypharmacological activities. *RSC Medicinal Chemistry*, 2025, 16, 2004-2018.

- Borgelt, L. [#]; Hohnen, L. [#]; Pallesen, J.S. [#]; Hommen, P. [#]; Goebel, G. L. [#]; Bosica, F.; **Liu, Y**.; O’Mahony, G.; Wu, P., N-Biphenyl Pyrrolinones and Dibenzofurans as RNA-Binding Protein LIN28 Inhibitors Disrupting the LIN28–Let-7 Interaction. *ACS Medicinal Chemistry Letters*, 2023, 14, 12, 1707–1715.

- Hui, C. G.; **Liu, Y**.; Jiang, M.; Wu, P., Cyclobutane-containing scaffolds in bioactive small molecules. *Trends in Chemistry***,** 2022, 4 (8), 677-681.

[#] Authors contributed equally

Methods displayed in this dissertation can also be found in the following master's thesis:

- O. Hastürk, “Evaluation of small-molecule modulators targeting the RNA-cleaving protein IRE1α”, Master Thesis, 2023

- L. Wagner, “Evaluation of small molecule inhibitors for the RNA methyltransferase METTL16”, Master Thesis, 2024

The compounds synthesized in this thesis were from collaborations with Amrutha Krishnan Avathan Veettil and Dr. Georg Goebel. Compound synthesis methods and compound characterizations might be published and discussed in their doctoral theses with more details.

Acknowledgments

I am deeply grateful to have reached this stage in my life, which was a memorable journey. I am very thankful to everyone who contributed to the success of the research and made this journey memorable. Thank you all for your support and encouragement.

First and foremost, I would like to thank my supervisor, V-Prof. Dr. Peng Wu, for his constructive guidance and generous support over the years. The academic freedom and environment he provided allowed me to become a researcher to think independently. I am very grateful to have worked in such a warm group.

I would like to thank Prof. Dr. Dr. h.c. Herbert Waldmann, for kindly taking on the role of my first examiner and founding the Chemical Genomics Centre.

I would like to express my gratitude to my TAC members, Prof. Dr. Rasmus Linser and Prof. Dr. Barbara Saccà, for their valuable suggestions and feedback on my projects throughout my PhD.

Thanks to Prof. Jessica A. Brown (University of Notre Dame) for providing the METTL16 plasmid.

I am very thankful to the Crystallography and Biophysics facility for their resources, support, and guidance. I am especially grateful to Dr. Raphael Gasper-Schönenbrücher for his generous support and professional guidance in crystallography and biophysical fundamentals, as well as the experimental work.

I would like to thank Dr. Sonja Sievers, Dr. Philipp Lampe, and the COMAS team for providing valuable compound libraries and their constant assistance with compound ordering.

Thanks to my excellent co-workers: the talented Chemists Amrutha Krishnan, Dr. Georg Goebel, Dr. Fubao Huang, Mao Jiang, and their students, for synthesizing active compounds, which made this work possible. Special thanks go to my Master's students and intern, Oguz Hastürk, Leon Wagner, and Huzhuyue Xie. For their assistance and contributions to my project. Thanks also to Xiaqiu Qiu and Dr. Lydia Borgelt for their help during my PhD.

Thanks to Amrutha Krishnan Avathan, Dr. Zhou Zhao, Dr. Xiu-Fen Cheng, and Leon Wagner for proofreading my dissertation and giving helpful comments and corrections.

I am very thankful to Dr. Lucia Sironi and Christa Hornemann for their constant support and encouragement during the entirety of my PhD. I am very grateful to be a member of IMPRS.

I would like to thank all the people of the Peng Wu group, CGC, and Department 4, for providing a wonderful work environment and many enjoyable social events.

I am thankful to all my friends and peers, especially Dr. Xiu-Fen Cheng, for the time we spent together and for the encouragement during my tough days

Last but not least, I would like to deeply thank my family and Dr. Zhou Zhao for their unwavering support.

Table of Contents

Abstract

RNA modifications play crucial roles in regulating the biological activities of RNAs. Thus RNA-modifying proteins that carry these functions are promising targets for small-molecule modulators. Such modulators can serve as essential tool compounds for furthering understanding of RNA biology, offer new therapeutic entities for the treatment of diseases involving RNA dysregulation, and drive drug discovery and chemical biology research. The Thesis describes the identification of new chemotypes and the development of novel small-molecule inhibitors targeting two such RNA-modifying proteins, the ribonuclease IRE1α and the RNA m^6A methyltransferase METTL16. Such molecules were characterized as feasible starting points for the discovery of new small-molecule drug candidates for the associated diseases.

IRE1α functions as a crucial effector in the unfolded protein response (UPR) under the endoplasmic reticulum stress (ER stress). It catalyzes the splicing of X-box binding protein mRNA (*XBP1*), producing spliced *XBP1* mRNA and generating XBP1s protein. XBP1s is a transcription factor that further upregulates UPR genes to restore ER harmony. Additionally, IRE1α relieves the ER stress by degrading select mRNAs through the regulated IRE1-dependent decay (RIDD) pathway. Dysregulation of IRE1α signaling has been associated with a wide range of diseases, making IRE1α inhibition via small molecules a promising strategy to address these diseases. In one part of the Thesis, an IRE1α RNase inhibitor compound IA01 bearing an indole scaffold was identified through in-house compound library screening. After resynthesizing and validating the hit compound IA01, a comprehensive structure-activity relationship study was carried out to yield compounds with improved potency. Among the structurally modified derivatives and analogues, IA107 exhibited the best activity in inhibiting both dephosphorylated IRE1α and phosphorylated IRE1α, with IC_{50} values of 16 nM and 9 nM, respectively. A resolved co-crystal complex structure of IRE1α with IA107 revealed the allosteric RNase inhibition mechanism, in which IA107 binds to the kinase domain of IRE1α to exert its RNase-inhibiting activity. Unlike other reported allosteric inhibitors that bind to the kinase domain and inhibit the RNase activity by disrupting IRE1α dimerization. IA107 did not impact IRE1α dimer assembly. Subsequent cellular evaluations showed that IA107 inhibited the *XBP1* mRNA splicing induced by ER stress. However, limited cellular activity was observed for IA107, which could be explained by the potentially low cellular permeability associated with the presence of a carboxyl group. The following ester-prodrug approach was

successfully demonstrated to be an efficient strategy to yield an analogue with significantly improved cellular activity in inhibiting *XBP1* splicing by around 50-fold.

In another part of the Thesis, medicinal chemistry efforts were carried out to discover small-molecule-based regulation of the RNA N^6-methyladenosine (m^6A) methylation, which is the most abundant mRNA modification in eukaryotic RNAs. The m^6A RNA modification regulates RNA stability and associates with physiological and pathological functions. Methyltransferase METTL16 catalyzes the transfer of a methyl group from S-adenosylmethionine (SAM) to the N^6 position of adenosine in specific RNA substrates. Besides the methyltransferase activity, METTL16 functions as an RNA-binding protein to impact the metabolism of RNA substrates. Although the dysregulation of METTL16 has been associated with numerous human diseases and small molecules regulating METTL16 activity could be of great value, no such small-molecule inhibitors have been sufficiently characterized yet. In this part of the Thesis, a novel class of aminothiazolone-based METTL16 inhibitors was initially identified in a fluorescence polarization-based hit evaluation campaign. Structural modifications performed based on the initial hit yielded more potent analogues, such as compound **45**, which showed a strong inhibitory activity with a single-digit micromolar IC_{50} value against the METTL16–RNA interaction. This new class of aminothiazolone inhibitors was comprehensively characterized in this study and can be used as a promising chemical tool to probe the unknown function of METTL16 involved in cellular pathways. Furthermore, both the discovery pipeline and the identified aminothiazolones laid a solid foundation for the further development of METTL16 targeting small molecules for therapeutic applications.

IRE1α and METTL16 are RNA-modifying proteins that play a critical role in RNA regulation, including splicing, translation, and degradation. These two proteins are involved in various human diseases, such as cancers, metabolic disorders, and neurodegenerative diseases. While targeting RNA directly with small molecules is challenging, modulating RNA function through targeting the related RNA-binding and -modifying proteins, such as IRE1α and METTL16, offers an alternative strategy. This Thesis reported a series of indole-based IRE1α inhibitors with a distinct mode of action, and a series of first-in-class aminothiazolone-based METTL16 inhibitors. These inhibitors advanced the drug discovery targeting IRE1α and METTL16, and laid the foundation for the development of RNA-targeted therapies. Further efforts in optimizing inhibitors to enhance the inhibitors' potency and selectivity, as well as designing bifunctional molecules, are expected to provide new insight into the biological functions of these molecules.

Kurzzusammenfassung

RNA-Modifikationen spielen eine zentrale Rolle in der Regulation Biologischer RNA-Aktivitäten. RNA-modifizierende Proteine gelten daher als vielversprechenden Ziele für *small-molecule* Modulatoren. Diese Modulatoren dienen als Werkzeuge sowohl zur Erforschung der RNA-biologie, als auch für neue therapeutische Ansätze für RNA-assoziierte Erkrankungen und fördern die Wirkstoffentwicklung in der chemischen Biologie. Diese Dissertation beschreibt die Identifizierung neuer Chemotypen und die Entwicklung neuartiger Inhibitoren für zwei solcher RNA-modifizierende Proteine, die Ribonuklease IRE1α und die RNA-m^6A-Methyltransferase METTL16. Diese Moleküle bilden vielversprechende Ausgangspunkte für die Entdeckung künftiger Arzneimittelkandidaten.

IRE1α ist ein zentraler Effektor der Unfolded Protein Response (UPR) unter Stress des Endoplasmatischem Retikulums (ER-Stress). Es katalysiert das Spleißen der X-Box-bindenden Protein mRNA (*XBP1*), wodurch das Transkriptionsfaktorprotein XBP1s entsteht, das UPR-Gene aktiviert, um die Harmonie im ER wiederherzustellen. Darüber hinaus lindert IRE1α den ER-Stress, indem es ausgewählte mRNAs über den regulierten IRE1-abhängigen Abbauweg (RIDD) abbaut. Eine Fehlregulation der IRE1α-Signalübertragung wurde mit einer Vielzahl von Erkrankungen in Verbindung gebracht, sodass die Inhibierung von IRE1α durch *small molecules* eine vielversprechende Strategie für die Behandlung dieser Erkrankungen darstellt. In Rahmen dieser Arbeit wurde durch ein betriebsinternes Screening ein IRE1α-RNase-Inhibitor namens IA01 identifiziert, der ein Indolgerüst aufweist. Es wurde eine umfassende Struktur-Wirkungs-Beziehungsstudie auf Basis von IA01 durchgeführt, um Verbindungen mit verbesserter Wirksamkeit zu erhalten. IA107 war das optimierteste Derivat, welches mit einem IC_{50} von 16 nM für dephosphoryliertes IRE1α und 9 nM für phosphoryliertes IRE1α, beide Formen von IRE1α mit hoher Wirksamkeit inhibieren konnte. Die Kristallstrukturanalyse zeigte, dass IA107 allosterisch über Bindung an die Kinasedomäne wirkt, jedoch die Dimerisierung von IRE1α nicht beeinträchtigt. In Zellmodellen zeigte IA107 eine begrenzte Aktivität gegen ER-Stress-induziertes XBP1-Spleißen, was durch eine geringe Zellpermeabilität aufgrund der Carboxylgruppe erklärt werden könnte. Ein Ester-Prodrug-Ansatz konnte die zelluläre Wirksamkeit um das 50-fache verbessern.

Ein weiterer Teil der Arbeit widmete sich der Regulierung der m6A-Methylierung, der häufigsten reversiblen Modifikation in eukaryotischer mRNA, mit *small molecules*. Die m6A-RNA-Modifikation reguliert die Stabilität von RNA und steht im Zusammenhang mit

physiologischen und pathologischen Funktionen. Die Methyltransferase METTL16 katalysiert die Übertragung einer Methylgruppe von S-Adenosylmethionin (SAM) auf die N6-Position von Adenosin in spezifischen RNA-Substraten. Neben der Methyltransferase Funktion beeinflusst METTL16 außerdem den Metabolismus von RNA Substraten als RNA-bindendes Protein. Obwohl die Dysregulation von METTL16 mit zahlreichen menschlichen Krankheiten in Verbindung gebracht wurde und Inhibitoren, die die METTL16-Aktivität regulieren, von großem Wert sein könnten, sind bisher noch keine solchen Inhibitoren ausreichend charakterisiert worden. In diesem Teil der Arbeit haben wir eine neue Klasse von Aminothiazolon-basierten METTL16-Inhibitoren identifiziert, die ursprünglich in einer Fluoreszenzpolarisations-basierten Hit-Evaluierungs-Kampagne identifiziert wurden. Strukturelle Modifikationen auf Basis der ersten Hit-Struktur führten zur Identifizierung wirksamerer Analoga, wie beispielsweise Verbindung **45**, die eine starke inhibitorische Aktivität mit einem IC_{50}-Wert im einstelligen Mikromolarbereich gegenüber der METTL16-RNA Interaktion zeigte. Diese neue Klasse von Aminothiazolon-Inhibitoren wurde in dieser Studie umfassend charakterisiert und kann als vielversprechendes chemisches Werkzeug zur Untersuchung der unbekannten Funktion von METTL16 in zellulären Signalwegen eingesetzt werden. Darüber hinaus legten sowohl die Entdeckungspipeline als auch die identifizierten Aminothiazolone eine solide Grundlage für die weitere Entwicklung von METTL16-gerichteten Inhibitoren für therapeutische Anwendungen.

IRE1α und METTL16 sind RNA-modifizierende Proteine, die eine entscheidende Rolle bei der RNA-Regulation spielend, einschließlich Spleißen, Translation und Abbau von RNA. Diese beiden Proteine sind an verschiedenen menschlichen Krankheiten, wie Krebs, Stoffwechselstörungen und neurodegenerativen Erkrankungen, beteiligt. Während das direkte Binden und Modulieren von RNA mit *small molecules* eine Herausforderung darstellt, bietet die gezielte Beeinflussung von RNA-bindenden und -modifizierenden Proteinen wie IRE1α und METTL16, die mit der RNA-Funktion assoziiert sind, eine vielversprechende alternative Strategie. Diese Arbeit berichtet über eine Reihe von Indol-basierten IRE1α-Inhibitoren mit einem einzigartig Wirkmechanismus und eine Reihe von ersten Aminothiazolon-basierten METTL16-Inhibitoren. Diese Inhibitoren haben die Wirkstoffforschung gegen IRE1α und METTL16 vorangetrieben und den Grundstein für die Entwicklung von RNA-gerichteten Therapien gelegt. Weitere Anstrengungen zur Optimierung der Inhibitoren hinsichtlich ihrer Wirksamkeit und Selektivität sowie zur Entwicklung bifunktioneller Moleküle dürften neue Einblicke in die biologischen Funktionen dieser Moleküle liefern.

1. Introduction

1.1 RNA biogenesis

1.1.1 Central Dogma

The central dogma in biology is a framework that indicates the genetic information transfer through the biomacromolecules DNA, RNA, and protein. Since its introduction by Francis Crick in 1958 and further elaboration in 1970[1, 2], the concept has been debated and developed over the last decades. The traditional concept of the central dogma is that DNA encodes genetic information and can be transcribed into RNA, which is further translated into proteins. Genetic information transfer includes three general processes that occur in all cells: DNA self-replication, DNA to RNA transcription, and RNA to protein translation. In parallel, three exceptions may occur in special circumstances: RNA self-replication, RNA to DNA reverse transcription, and DNA to protein translation. In comparison to the previous two sets of scenarios, three unknown transfers that postulate never happened: protein to DNA, protein to RNA, and protein to protein[1] (Figure 1). The central dogma draws a gene expression conceptual framework and provides a foundation for the understanding of molecular biology and cellular function.

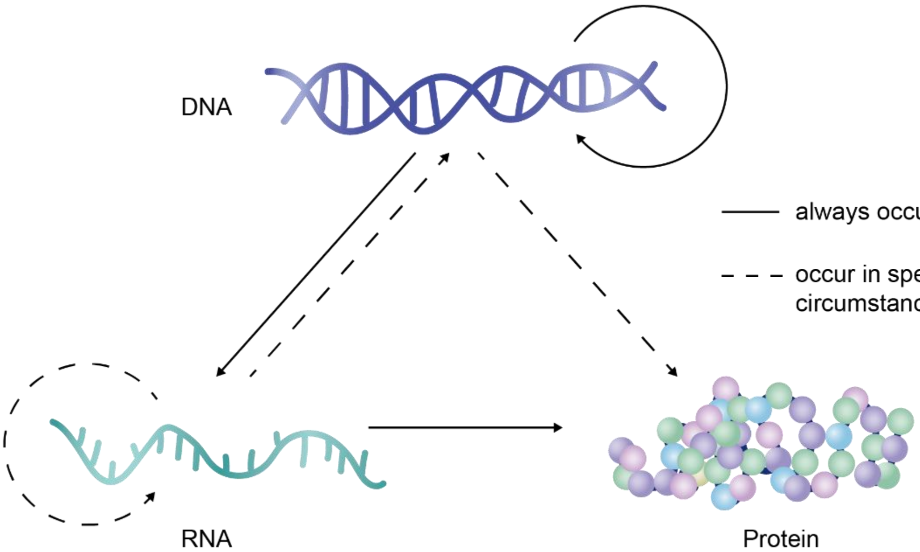

Figure 1. General depiction of the central dogma, which involves the transfer of genetic information through DNA, RNA, and protein.

1.1.2 RNA transcription and transcriptome

RNA transcription is the process of transferring genetic coding information from DNA to RNA (Figure 2A). The transcription initiates upon RNA polymerase binding to the promoter region of DNA[3]. Once bound, the double-stranded DNA unwinds to expose the template strand, then the RNA strand is elongated by RNA polymerase using the nucleoside triphosphate (NTP) as substrates and unwound DNA as a template. The polymerase further transfers the nucleotide moiety from the NTP to the 3'terminal hydroxyl group of the nascent transcript and releases the diphosphate[4] (Figure 2B). When reaching the terminator, the RNA polymerase dissociates from the template DNA, the newly transcribed RNA is released from the complementary DNA strand, and the transcription is terminated[5].

The transcriptome means the set of all RNA transcripts from DNA, which includes mRNA and noncoding RNAs. Only around 1.5% of the human genome is transcribed to mRNA that encodes protein, while ~70% of the genome is transcribed to noncoding RNAs, such as long noncoding RNA (lncRNA), microRNA (miRNA), small interfering RNA (siRNA), ribosomal RNA (rRNA), transfer RNA (tRNA), and small nuclear RNA (snRNA) etc.[6].

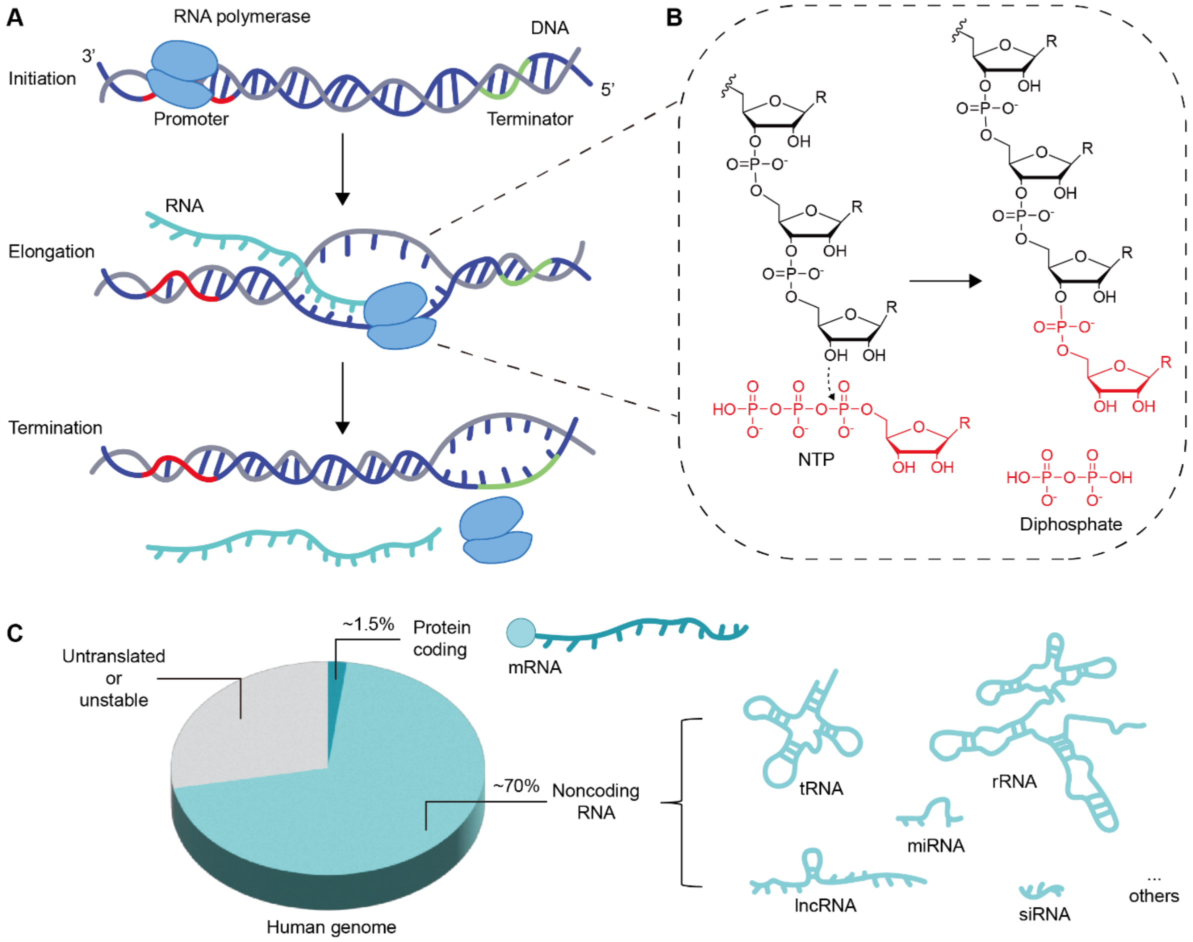

Figure 2. RNA transcription and genome organization. (A). Illustration of RNA transcription processes. (B). RNA elongation reaction. R, base. (C). Human genome organization.

1.2 RNA post-transcriptional modification

RNA post-transcriptional modification refers to the biological processes that occur in eukaryotic cells after RNA transcription. These modifications structurally or chemically alter RNA and play an essential role in regulating RNA stability and metabolism[7]. Over the past decades, more than 170 types of chemical modifications have been identified in different types of RNAs[8, 9]. Canonical RNA post-transcriptional modifications include capping, polyadenylation, splicing, and chemical modifications on the nucleobases[10, 11].

1.2.1 RNA 5’ end capping

The 5’ capping modification adds a methylated guanine nucleotide (7-methylguanosine (m^7G)) structure to the 5’ end of the eukaryotic precursor mRNA (pre-mRNA) via a triphosphate linkage. This capping process includes three reactions that are catalyzed by RNA triphosphatase, RNA guanylyltransferase, and RNA guanine-N^7 methyltransferase, respectively (Figure 3). The cap structure is also found in other noncoding RNAs, for example, the snRNA[12]. Recently, it has been found in bacteria that some RNA species carry 5’ end structures that are similar to the eukaryotic cap structure[13, 14]. The 5’cap plays an important role in regulating various RNA processes such as export, degradation, splicing, and translation.

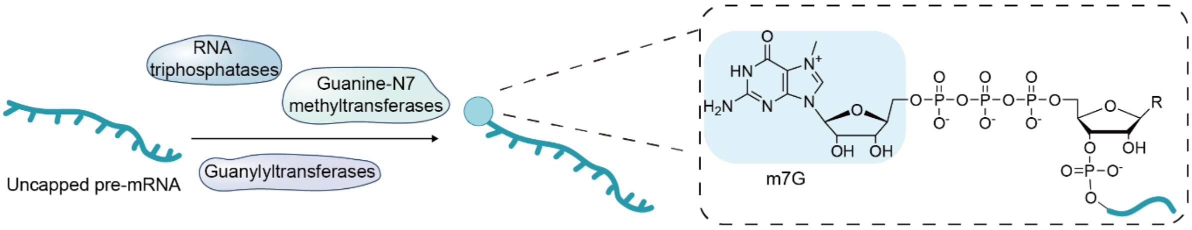

Figure 3. Illustration of RNA 5’ end capping and the structure of m^7G cap.

1.2.2 RNA splicing

RNA splicing is the process of removing the noncoding introns and joining the protein-coding exons in pre-mRNA, which is critical for eukaryotic genes to be translated into proteins. Several splicing methods were identified in nature, and the most common splicing method in eukaryotic cells is the spliceosome splicing[15-17]. The spliceosome is a large protein-RNA complex composed of small nuclear RNAs (snRNAs) and RNA-binding proteins. Initially, snRNA associates with specific proteins to form small nuclear ribonucleoproteins (snRNPs) complexes, which then interact with other snRNPs and to assemble the spliceosome and catalyze RNA cleavage and exon ligation (Figure 4A)[17-19]. Apart from the spliceosome splicing, other splicing methods, including self-splicing, endoribonuclease-mediated splicing (e.g., tRNA splicing, IRE1α-mediated splicing) have also been found[17, 20, 21].

The IRE1α-mediated splicing is an unconventional and highly specific splicing process in response to endoplasmic reticulum (ER) stress[22]. The splicing substrates are very specific: *HAC1* mRNA in yeast[23], *bZIP60* mRNA in plants[24], and *XBP1* mRNA in mammals[22]. Though other IRE1α-cleaving RNA substrates have been identified, no further ligation of exons was observed for those RNAs. They are degraded by IRE1α instead of splicing[25, 26]. In mammals, IRE1α catalyzes the splicing of a 26 nt intron of *XBP1* mRNA (*XBP1u*) under ER stress. The RNase activity of IRE1α is activated by ER stress, which recognizes two cleavage sites with the CNGCAG sequence on the *XBP1* mRNA. IRE1α cleaves the RNA at these C|G sites, then the exons are ligated by RtcB ligase to produce the spliced *XBP1* (*XBP1s*) mRNA[27, 28]. The *XBP1s* mRNA is translated to the spliced XBP1 protein (XBP1s), which is a transcription factor that regulates the expression of protein-folding related genes to alleviate ER stress[29-31]. The unspliced *XBP1u* mRNA can be translated into a shorter 29 kDa XBP1u protein. However, the XBP1u is unstable (Figure 4B)[31].

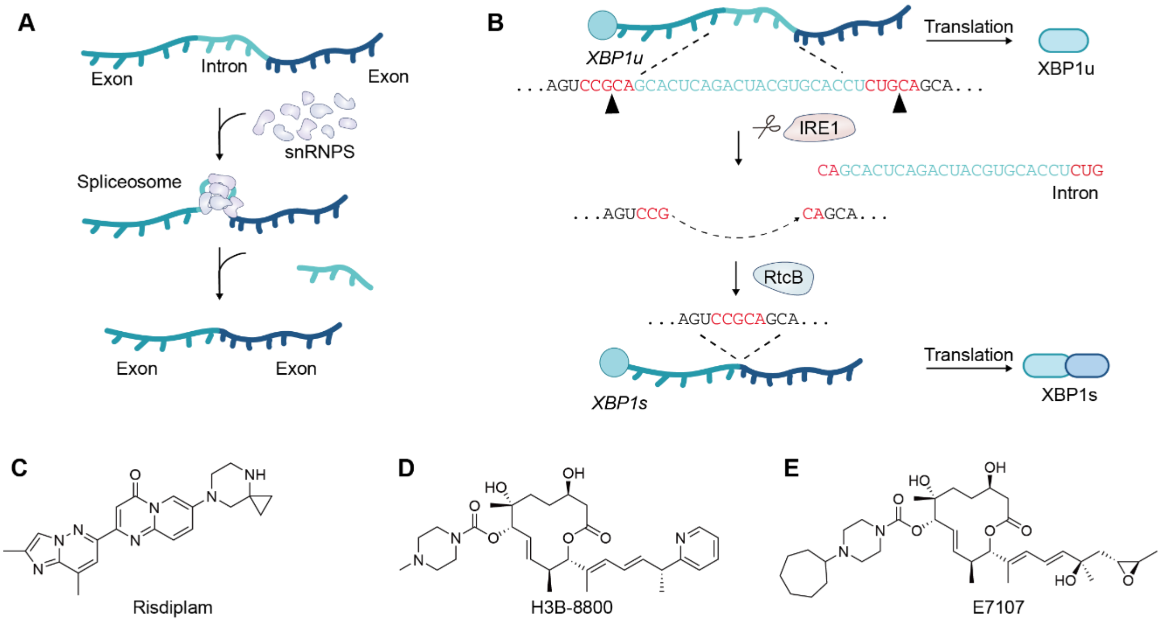

Figure 4. RNA splicing and targeting molecules. (A). Illustration of RNA splicing by the spliceosome. (B). IRE1α-mediated *XBP1* RNA splicing, the cleaving site, and the intron sequence. (C). Chemical structure of risdiplam. (D). Chemical structure of H3B-8800. (E). Chemical structure of E7107.

RNA splicing is an important biological process, produces active transcripts and plays a critical role in cellular processes. Modulators targeting RNA splicing have emerged as promising drug candidates. Several drugs that target RNA splicing have been approved to treat the relevant diseases, for example, the small-molecule drug risdiplam (Figure 4C)[32] and the antisense oligonucleotide nusinersen[33], both targeting *SMN2* splicing for the treatment of spinal muscular atrophy. Small-molecule spliceosome modulators are an alternative strategy for modulating RNA splicing. For example, compounds H3B-8800 (Figure 4D) and E7107 (Figure 4E) inhibit the spliceosome complex to suppress the splicing[34, 35]. The identification of an increasing number of RNA splicing modulators paves the way for ongoing drug discovery efforts that aim to develop RNA splicing-targeting therapies for a broader range of diseases.

1.2.3 Epitranscriptomic modification

Epitranscriptomic modifications are chemical modifications to the RNA bases. A variety of these modifications have been identified in all four RNA bases, among which N^6-methyladenosine (m^6A) is a widely distributed adenosine methylation modification and the most abundant mRNA modification in eukaryotes (Figure 5A)[36]. While N^7-methylguanosine (m^7G) is well-known as cap modification of mRNA, it is commonly found in tRNA, rRNA and mRNA internal regions[37-40] (Figure 5B); 5-methylcytidine (m^5C) modification is the prevalent modifications in cytidine which is found in rRNA, tRNA and mRNA regulating the RNA stablility[41] (Figure 5C); Pseudouridine (Ψ) is an isomer of the uridine, and it is the most prevalent RNA modification across all RNAs, though it is less abundant than m^6A in mRNA. Pseudouridine stabilizes RNA and promotes RNA functions (Figure 5D)[42]. These modifications are typically performed by "writer" proteins and removed by "eraser" proteins. In addition to catalytic proteins, the modified RNA is recognized by "reader" proteins, which further activate downstream processes. For example, in the case of the m^6A modification, the methyl group at the N^6 position of the adenosine is added by the methyltransferases (e.g., METTL3/METTL14 protein complex or METTL16), and removed by the demethylase (e.g., FTO or ALKBH5)[43-46], and recognized by the reader proteins (e.g., YTHDF1-3, or YTHDC1/2) to regulate RNA splicing, exportation, translation, and decay[47-49].

RNA modifications play an essential role in various biological processes, regulating gene expression, RNA processing, RNA stability, and RNA localization[50-52]. RNA modifications show great potential for disease prevention, diagnosis, and treatment. N^1-methylpseudouridine was used in mRNA vaccines to stabilize RNA and promote its translation[53, 54]. Due to the increased urinary excretion of pseudouridine (Ψ) seen in cancer patients, it has emerged as a potential biomarker for cancer diagnosis[55, 56]. The mutations and variations of RNA regulator genes are linked to various human diseases. The inhibitors targeting m^6A writer METTL3/METTL14 are reported to be active in acute myelogenous leukemia (AML)[57].

Additionally, eraser protein FTO has been associated with melanoma[58]. m^{1}A level is upregulated in bladder urothelial carcinoma due to the high expression of the regulatory methyltransferase hTrm6p/hTrm61p[59]. Treating relevant diseases with drugs that target epitranscriptomic RNA modifications is an emerging area of drug discovery.

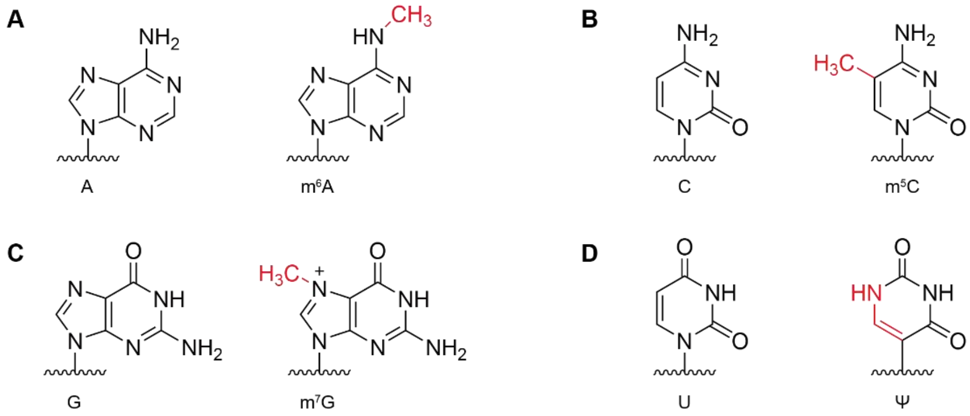

Figure 5. Structures of RNA bases and their selected internal chemical modifications.

1.2.4 RNA polyadenylation

Polyadenylation is a vital post-transcriptional modification involving the covalent attachment of a stretch of adenosine monophosphates to the 3′ end of RNA molecules[60]. In mammals, the average length of poly(A) tails is around 200 nucleotides[61]. Polyadenylation is typically attached to mRNA, thereby affecting the downstream translation process[62]. However, polyadenylated modifications are also observed in many non-coding RNAs after transcription[63]. Polyadenylation contributes to the localization and stability of mRNA, functioning as a key regulator of gene expression[60]. In the nucleus, mRNA is cleaved at the 3′ end by the cleavage and polyadenylation specificity factor (CPSF) complex, then a poly(A) tail is added by the poly(A) polymerase (PAP) with the nuclear poly(A)-binding protein (PABPN) binds to the tail and regulates its length[64]. Afterwards, the mature mRNA with poly(A) tail is exported from the nucleus to the cytoplasm, and the polyadenylation site will be recognized and bound by the cytoplasmic poly(A)-binding protein (PABPC) to facilitate translation by ribosomes[65]. The studies show that the length of polyadenylation affects the RNA translation efficiency, with a longer poly(A) tail on mRNA being translated more efficiently as it is bound by PABPC[66]. The control of poly(A) tails determines mRNA decay, the deadenylation shortening the poly(A) tail will facilitate the mRNA decay[67]. The deadenylation rates align with the half-lives of transcripts, which can vary by more than 1,000-fold[68] (Figure 6).

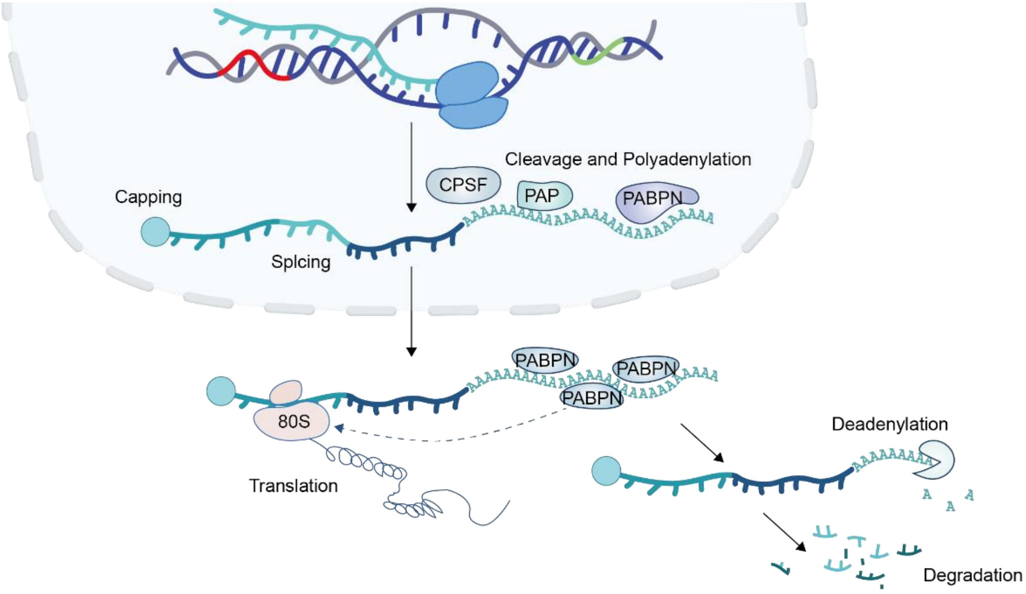

Figure 6. Overview of the mRNA polyadenylation and its function.

1.2.5 RNA decay

RNA decay is a fundamental process in cells that regulates gene expression. The eukaryotic mRNA decay is mostly mediated by the deadenylation-dependent decay, which is initiated by the poly(A) tail deadenylation[69]. Exonucleases, such as PAN2-PAN3 and CCR4-NOT (carbon catabolite repression 4-negative on TATA) complexes, are dedicatedly to shortening the poly(A) tails. Deadenylation typically leads to the 5’ end decapping catalyzed by the mRNA decapping enzyme DCP1/DCP2 complex, and followed by 5’ to 3’ RNA decay mediated by the exoribonuclease XRN1 (5’-3’ exoribonuclease 1) [70, 71]. Alternatively, deadenylation can lead to the exosome-mediated 3’ to 5’ RNA degradation[72, 73] (Figure 7A). Other deadenylation-independent RNA decay pathways have also been identified. For example, the 5’ to 3’ RNA decay is initiated by decapping, followed by XRN1 degradation[74] (Figure 7B).

Strategies that enhance RNA degradation or inhibit RNA decay can be alternative ways for targeting undruggable or difficult-to-target proteins. For example, the molecule targeting the CCR4-NOT complex inhibits poly(A) tail-containing RNA digestion, which could be a potential treatment strategy for breast cancer[75, 76]. Recently, novel approaches such as ribonuclease-targeting chimeras that link the RNA binder with ribonuclease L ligand have been reported to induce disease-associated RNA degradation[77, 78].

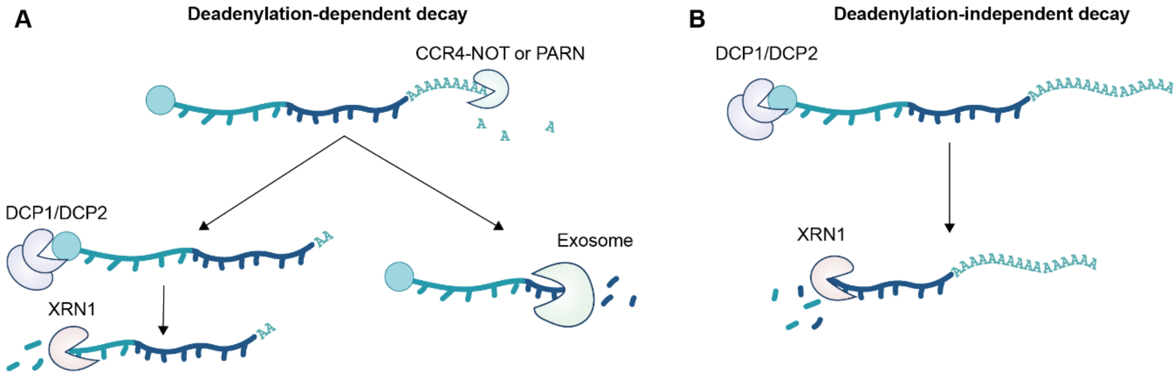

Figure 7. Illustration overview of the RNA decay process. (A). Deadenylation-dependent RNA decay. (B). Deadenylation-independent RNA decay.

1.3 Ribonuclease IRE1α

1.3.1 Unfolded protein response

The endoplasmic reticulum (ER) is an important organelle for protein synthesis, protein folding, and transportation in eukaryotic cells, responsible for protein quality control and protein homeostasis[79]. The functionality of the ER can be perturbed by various factors, including diseases, environmental changes (e.g., temperature), and exposure to certain chemical compounds, which lead to the accumulation of unfolded and misfolded proteins inside the ER lumen, thereby inducing the ER stress[80]. The conserved unfolded protein response (UPR) pathway is activated in response to the ER stress, with the aim of alleviating the stress and maintaining ER homeostasis. However, if the homeostasis is not reestablished within a certain time, UPR will induce apoptosis. This might be a way to eliminate cells that are still in a stress condition that cannot be alleviated by UPR[81].

UPR is regulated by three ER transmembrane sensors: inositol-requiring enzyme 1α (IRE1α), activating transcription factor 6 (ATF6), and double-stranded RNA-activated protein kinase (PKR)-like ER kinase (PERK)[82](Figure 8).

The most conserved UPR sensor, IRE1α, is a bifunctional kinase and endoribonuclease protein. Under the unstressed condition, IRE1α luminal domain binds to the chaperone BiP and maintains the inactive state. Upon ER stress, the chaperone Bip binds to the misfolded protein and dissociates from IRE1α's luminal domain and triggering the cytosolic domains' dimerization and autophosphorylation, thereby activating IRE1α[83, 84]. As aforementioned in section 1.2, the activated IRE1α catalyzes the nonconventional *XBP1* mRNA splicing, yielding the transcription factor XBP1s protein, which further promotes the expression of protein-folding related genes to regulate ER stress[29-31]. In addition to the *XBP1* mRNA splicing, IRE1α activation induces the regulated IRE1α-dependent decay (RIDD), which degrades a set of mRNAs with a loop sequence CNGCAGN[85], thereby reducing the protein folding load in the ER[86, 87]. Under acute stress, IRE1α activation leads to apoptosis and programmed cell death through the activation of c-Jun N-terminal kinase (JNK) pathways[88, 89].

The second sensor ATF6 is a transcription factor with a large ER-luminal domain. Once activated by ER stress, ATF6 translocates from the ER to the Golgi complex via transport vesicles and is processed by proteases S1P and S2P (site-1 and site-2 proteases) to release the N-terminal cytosolic activating domain (ATF6N)[90, 91]. ATF6N subsequently transports to the nucleus to activate UPR target genes that encode chaperones and enzymes, which promote protein folding as well as misfolded protein degradation. ATF6(N) acts in parallel with XBP1s with some shared pathways [90, 92].

Last but not least, PERK is a transmembrane kinase that is activated by ER stress through oligomerization and autophosphorylation. The activated PERK further phosphorylates the eukaryotic translation initiation factor eIF2α, which inactivates eIF2α and reduces mRNA translation and protein synthesis[82]. Consequently, PERK activation decreases the newly synthesized proteins in the ER and restores the ER stress. However, some mRNAs with short open reading frames, such as the transcription factor ATF4, are selectively translated under limited eIF2 activity[93]. ATF4 activates various response genes involved in protein synthesis, amino acid metabolism, autophagy, and apoptosis[94, 95]. Among the target genes of ATF4, transcription factor C/EBP homologous protein (CHOP) and growth arrest and DNA damage–inducible 34 (GADD34) play an important role in UPR. CHOP regulates genes encoding apoptosis-related components, and GADD34 functions in a feedback loop to dephosphorylate eIF2α and restore protein synthesis[96, 97].

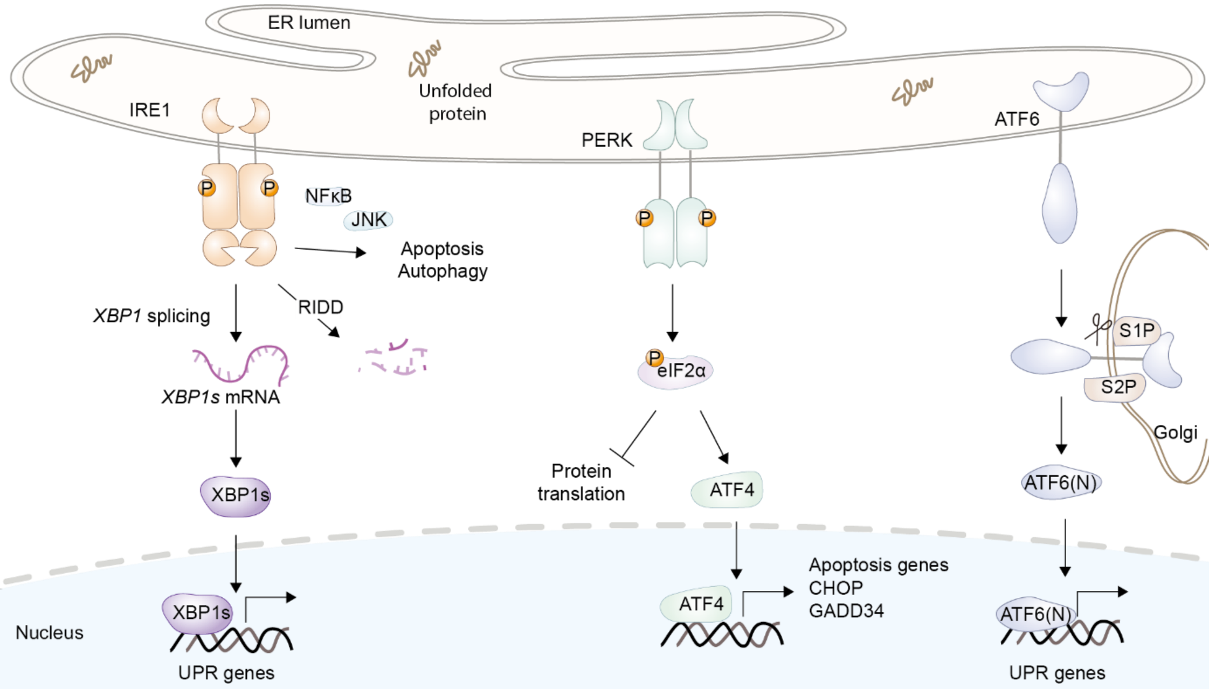

Figure 8. Unfolded protein response signaling pathways. Accumulation of unfolded protein in the ER lumen triggers the UPR pathways to restore ER homeostasis.

UPR is a critical cellular stress pathway in response to ER stress to restore ER homeostasis through the three aforementioned main sensors. The UPR is essential for cell survival under stress conditions, and the dysregulation of the UPR pathway is associated with various diseases, such as cancer, diabetes, and metabolic disorders[98]. Thereby, small molecules targeting UPR sensors that regulate the UPR pathway create new opportunities to investigate the underlying mechanisms and develop bioactive compounds.

1.3.2 IRE1α in human diseases

IRE1α is the most conserved UPR sensor and has been associated with a wide range of diseases, for example, various cancers[99-101], neurodegenerative diseases[102], metabolic disorders[103, 104], and inflammatory diseases[105]. Cancer cells are often exposed to ER stress and benefit from the deregulated UPR to adapt to the hostile tumor microenvironment, support growth, and evade cell death[106]. IRE1α activity contributes to the basal expression of oncogenic factors IL-6, IL-8, CXCL1, GM-CSF, and TGFβ2 in triple-negative breast cancer (TNBC) cells, and the IRE1α RNase inhibitor improves the current chemotherapeutic effects[99, 107]. IRE1α-XBP1 arm enables TNBC cells to adapt to hypoxic conditions by XBP1 interacting with hypoxia-inducing factor 1α (HIF1α)[100]. Inhibiting the IRE1α-XBP1 pathway reduces leukemia cell survival[108]. Overexpression of XBP1 drives multiple myeloma pathogenesis in mice[109]. IRE1α promotes the survival of prostate cancer cells, and the deletion of IRE1α or XBP1 inhibits cell growth *in vivo*[110]. IRE1α signaling has also been associated with glioblastoma, liver cancer, and pancreatic cancer, etc.[111-113], making it a promising target for developing anticancer drugs.

Accumulation of misfolded proteins serves as a hallmark for neurodegenerative diseases. Hence, protein quality control plays a crucial role in pathological processes[114]. IRE1α signaling has been identified as the causative factor to accelerate the progression of Alzheimer’s disease (AD). Phosphorylation activation of IRE1α in the human brain is positively correlated with the AD histopathology. The IRE1α RNase knockout mouse model showed alleviation of AD progression, characterized by the reduced amyloid β load, improved cognitive and synaptic function, and attenuated astrogliosis[115]. IRE1α activation drives Parkinson’s disease (PD) progression by inducing neuron death through autophagy, and inhibiting IRE1α reduces the progression of α-synuclein-caused PD[116]. In addition to AD and PD, IRE1α plays an important role in Huntington's disease (HD). The upregulation of IRE1α promotes HD and increases mutant huntingtin protein (mtHTT) aggregation[117]. Overall, inhibition of IRE1α activity is a potential therapeutic approach for these neurodegenerative diseases.

IRE1α stands as an important sensor of UPR, plays a crucial role in sensing and regulating stress, and controls the initiation and progression of various diseases. Small molecules targeting IRE1α show promise as therapeutics for relevant diseases. Over the last few decades, many molecules have been reported[118], and some are already in preclinical and early clinical development. For example, compound ORIN1001, which was developed to treat advanced solid tumors, has finished the phase 1 trials[119]. While targeting IRE1α implied great therapeutic potential, developing safe and potent drugs remains challenging.

1.3.3 IRE1α structure and activation mechanism

Two ERN genes (ERN1 and ERN2) have been identified in the human genome to encode IRE1α and IRE1β isoform proteins. IRE1α is ubiquitously expressed in most tissues and plays a crucial role in the UPR pathway. IRE1β is expressed in response to tissue restriction and is primarily found in intestinal epithelial cells of the mucosal surface, such as bronchial epithelial cells[120] and the intestinal epithelial barrier cells of the gastrointestinal[121]. IRE1α and IRE1β have highly similar sequences and overall structures[122] (Figure 9A, 9B). However, the exact function and the molecular function of IRE1β remain unknown[123].

IRE1α protein consists of a N-terminal luminal domain (residue 19-443) located inside the ER lumen and a cytosolic domain, connected by a transmembrane region (Figure 9B). The luminal domain (LD) functions as a stress sensor to detect unfolded proteins through the competitive dissociation of chaperone BiP[84] (Figure 9C). The dissociation of BiP from the LD released LD to form homodimers and further led to the cytosolic domain activation through dimerization and autophosphorylation[124]. The cytosolic domain of IRE1α contains a protein kinase domain (residue 571-832) and a kinase extension nuclease (KEN) domain (residue 835-963), also known as the RNase domain (Figure 9D). The kinase domain with the function of serine/threonine-protein kinase undergoes autophosphorylation upon dimerization, the phosphorylation induces conformation changes that lead to the RNase domain activation and activate IRE1α[125]. The kinase domain plays a crucial role in the RNase domain activity, and mutations in the kinase domain reduce the RNase activity[126, 127]. The autophosphorylation of the kinase domain promotes the dimerization, phosphorylated IRE1α cytoplasmic region forms a symmetric dimer, which was reported to be critical for the ribonuclease function (Figure 9D)[128]. Studies suggest that the dimerization composes a catalytic surface on the RNase domain for the ribonuclease function, and the mutations of the dimer interface residues disrupt the ribonuclease activity[129]. Small molecule IRE1α modulators that bind to the kinase domain can allosterically block or promote RNase activity: inhibitors that bind to the kinase domain disrupt the dimer formation and inhibit the RNase activity, and kinase domain binding activators activate RNase activity by promoting the dimer formation[130].

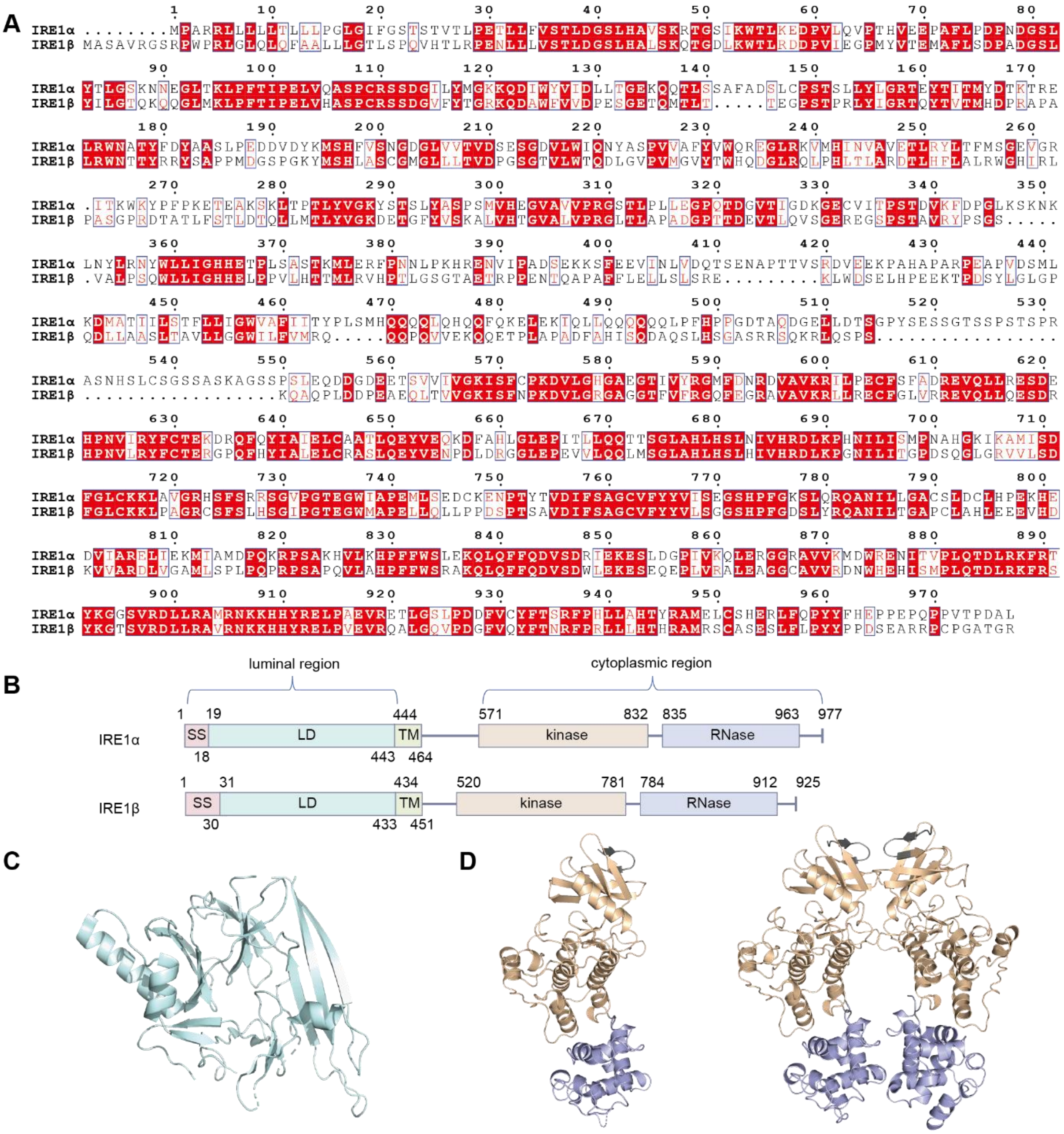

Figure 9. IRE1α and IRE1β sequence and domains. (A). Sequence alignment of IRE1α and IRE1β. (B). Schematic illustration overview of IRE1α and IRE1β domains. SS: signal sequence. LD: luminal domain. TM: transmembrane region. (C). Crystal structure of human IRE1α luminal domain. PDB 2hz6. (D). Crystal structure of human IRE1α cytoplasmic domain, monomeric dephosphorylated IRE1α (PDB 6w3b), and the back-to-back dimeric phosphorylated IRE1α (PDB 6w3c). The kinase domain was shown in wheat, and the RNase domain was shown in purple.

1.3.5 Small molecules targeting IRE1α RNase

1.3.5.1 RNase activators

Some small molecules bind to the kinase domain and activate the RNase activity of IRE1α. Compound APY29 was the first reported activator to bind the yeast IRE1α (yIRE1α) kinase domain, revealing a novel oligomerizing structure of yIRE1α[131] (Figure 10A). The APY29-bound yIRE1α exhibits a back-to-back oligomeric state that positions the kinase domain for trans-autophosphorylation and organizes the RNase domain to form an interaction surface and a catalysis pocket for catalyzing RNA cleavage[131, 132]. Later, structure-activity relationship studies based on APY29 were performed to yield more potent activators. For example, the cmp6 (also known as IPA, IRE1α/PERK activator) with the methyl thioether group showed the best potency (Figure 10B), activating IRE1α RNase activity 900-fold at the test concentration of 1 μM. Like APY29, cmp6 promotes IRE1α oligomerization and activation[133].

Compound **3** with an imidazo[1,2-*b*]pyridazine scaffold was identified as a human IRE1α (hIRE1α) kinase inhibitor with an IC_{50} value of 218 nM against the autophosphorylation activity[134], it was subsequently found to enhance the RNase activity of unphosphorylated hIRE1α with an EC_{50} value of 143 nM (Figure 10C)[135]. The co-crystal structure showed that upon compound 3 binding, IRE1α formed back-to-back dimers to adopt a kinase-active conformation and drive RNase activity[135]. Both APY29 and compound 3 are classified as type I kinase inhibitors, which bind to the active conformation of the protein kinase ATP pocket (DFG-in)[131]. Subsequent study shows that many type I kinase inhibitors can promote IRE1α dimerization and activate IRE1α activity. Comparison of the structure of kinase binding activators and inhibitors suggests that the type 1 kinase inhibitors activate IRE1α by stabilizing the active conformation of the kinase pocket (Figure 10D)[136].

Several potent activators were reported by Genentech, among which a unique activator, G1749 (Figure 10E), with a similar structure to the inhibitor KIRA8, showed an activation activity against unphosphorylated IRE1α RNase but an inhibitory activity against the phosphorylated IRE1α RNase. The co-crystal structure of G1749 in complex with unphosphorylated IRE1α displayed that G1749 occupies a front pocket near the DFG motif. The binding of G1749 appears to push the activation loop upwards. However, G1749 seems not to stabilize or promote the unphosphorylated IRE1α dimerization like the reported kinase-binding RNase activators. Besides G1749, more traditional IRE1α activators such as G9807 were also reported (Figure 10F), which preserve a similar mode of action to the previously published activators that activate IRE1α through stabilizing and inducing dimerization[126].

Pharmacologic IRE1α/XBP1 activators IXAs have been identified through a high-throughput screening (HTS) and characterized (Figure 10G). These compounds were suggested not to bind to the kinase active site. However, the exact mechanism of these activators requires further investigation[137, 138].

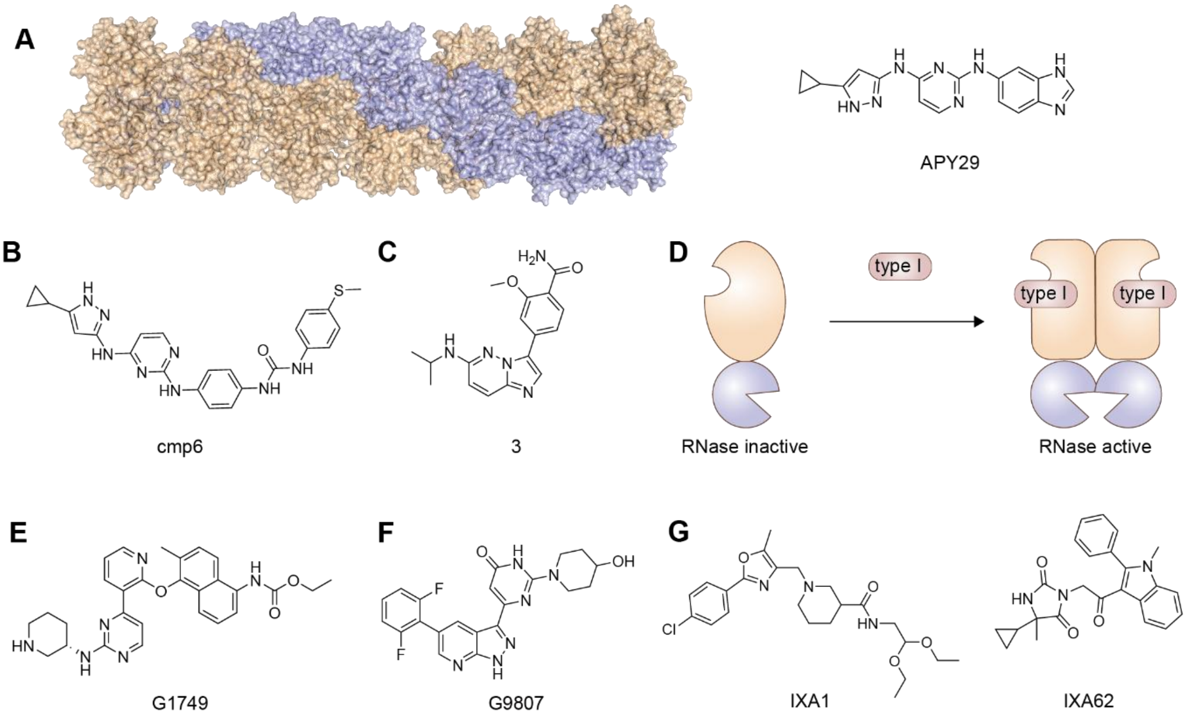

Figure 10. IRE1α RNase activators. (A). Oligomeric structure of phosphorylated yIRE1α in complex with APY29 (PDB 3fbv), and the chemical structure of APY29. Kinase domains were shown in wheat color, and RNase domains were shown in purple. (B). Chemical structure of cmp6 (IPA). (C). Chemical structure of compound 3. (D). Schematic illustration of type I kinase inhibitor allosterically activating IRE1α RNase activity. (E). Chemical structure of G1749. (F). Chemical structure of G9807. (G). Selected structures of IXA activators.

1.3.5.2 RNase inhibitors

Depending on the binding site, the reported IRE1α RNase inhibitors can be classified into two broad classes: the aforementioned kinase domain binder RNase allosteric inhibitors and RNase domain binders, which target the RNase catalytic site.

Type II kinase inhibitors, which bind to the inactive conformation of kinase (DFG-out), are found to inhibit the IRE1α RNase activity by displacing αC-helix and disrupting the back-to-back dimer formation[136]. Compound **3** (KIRA3), KIRA7, and AMG-18(KIRA8) are selected examples of such type II kinase inhibitors (Figure 11A)[139-141]. Compound **3**, with an IC_{50} of 3.12 μM against IRE1α autophosphorylation and an IC_{50} of 0.82 μM against phosphorated IRE1α RNase activity, was obtained through the structural modification of a type II kinase inhibitor[139]. Further structural modifications based on compound 3 resulted in the development of more potent compounds in later studies. Compound **3** was referred to as KIRA3, which means the kinase inhibiting RNase attenuator (KIRA)[136]. Among these obtained analogues, compound **13** (KIRA7) with a kinase IC_{50} value of 0.11μM and a RNase IC_{50} value of 0.22 μM, showed anti-fibrotic activity in bleomycin-induced pulmonary fibrosis mouse models[140].

Compound **18** was developed based on SAR studies of a hit from Amgen's small-molecule library screening. Compound **18** showed potent activity in the IRE1α enzymatic assay and the cellular XBP1 luciferase assay without impairing tumor cell viability[141]. In later studies, it was renamed as AMG-18 or KIRA8[126, 140]. Apart from the type II kinase inhibitors, GSK2850163 was revealed as a type III kinase inhibitor that binds to an allosteric site (Figure 11B). GSK2850163-bound phosphorated IRE1α showed a back-to-back dimeric state with the αC-helix pushed and DFG motif shifted conformation (PDB: 4yz9), inhibiting both kinase activity and RNase activity of IRE1α[142]. Later, the imidazole[1,2-b]pyridazin-8-amine kinase inhibitors were discovered through screening of the analogues of a type I kinase inhibitor that activates IRE1α RNase activity. The crystal structure of hit compound **2** in complex with IRE1α showed an unusual conformation change in the kinase domain (PDB: 6hx1), with the disordered αC-helix and a “DFG up” conformation[143]. SAR studies based on compound **2** yielded compound **31** (Figure 11C), which is more potent and selective, with the IC_{50} values of 160 nM and 80 nM against the kinase and the RNase activity, respectively. Further cellular evaluations showed that compound 31 inhibits IRE1α oligomerization, confirming that the inhibitors inhibit the RNase function by disrupting IRE1α assembly[143].

A series of hydroxy-aryl-aldehyde (HAA) compounds were reported as IRE1α RNase inhibitors that bind directly to the RNase domain[144-146](Figure 11D). The hydroxy aryl aldehyde moiety covalently binds to the IRE1α RNase domain residue lysine 907 (K907) and forms a stable imine bond, inhibiting the RNase activity of IRE1α and downstream *XBP1* mRNA splicing[146]. Among the HAA compounds, ORIN1001(MKC8866) discovery showed promising progress and finished the phase one clinical trial for the treatment of advanced solid tumors[119].

Additionally, IRE1α inhibitors with an unconfirmed binding site were identified, such as toyocamycin and doxorubicin (Figure 11E), which were identified to inhibit the IRE1α-XBP1 activity in cancer cells, however, the mode of action remains unclear[147, 148].

Despite the discovery of many IRE1α inhibitors with promising progress, there remains a significant need for novel inhibitor chemotypes with a distinct mode of action. Such compounds could provide an alternative therapeutic option. For example, selectively targeting one pathway of IRE1α over another could offer a more precise solution for each pathway-related disease.

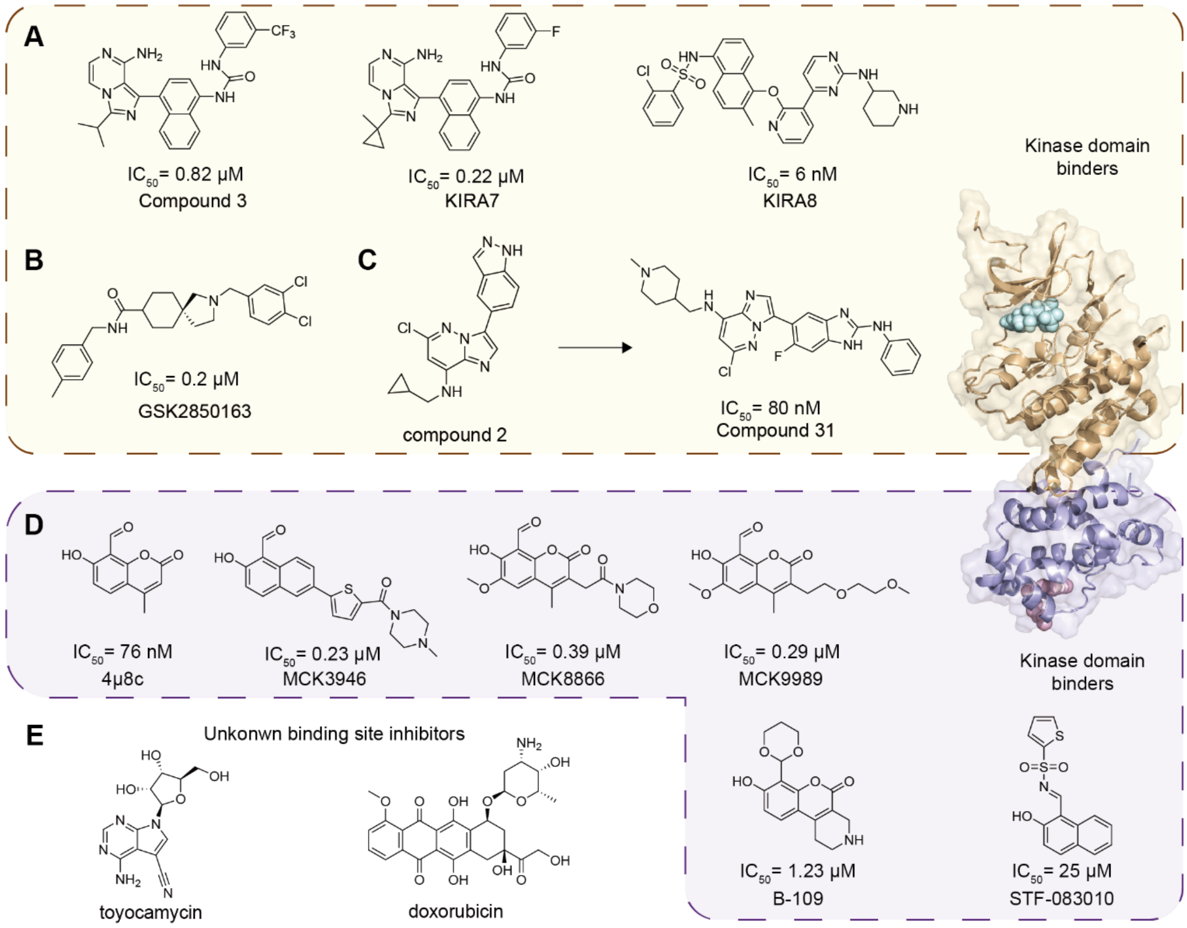

Figure 11. IRE1α RNase inhibitors. (A). Type II kinase inhibitors inhibit IRE1α RNase activity. (B). GSK2850163, as a type III kinase inhibitor, inhibits IRE1α RNase activity. (C). SAR study based on compound 2 yielded the more potent compound 31. (D). Hydroxy aryl aldehyde covalent inhibitors directly bind to the RNase domain. (E). IRE1α RNase inhibitors with an unknown binding site.

1.4 RNA m^6A methyltransferase METTL16

1.4.1 m^6A-modifying enzymes and targeting molecules

m^6A modification is widely found in both eukaryotic and prokaryotic RNA and occurs in various RNA species. It is the most abundant internal mRNA modification in eukaryotic mRNA and plays an important role in RNA biology[36]. The addition of a methyl group to the N^6 adenosine is catalyzed by methyltransferase enzymes, also known as the "m^6A writers", for example, methyltransferase-like proteins 3 and 14 complex (METTL3/METTL14)[45], METTL5–tRNA methyltransferase 112 complex (TRMT112)[149], METTL16[43], and zinc-finger CCHC domain-containing protein 4 (ZCCHC4)[150]. The primary m^6A methyltransferase is a protein complex composed of METTL3 (methyltransferase-like protein 3), METTL14 (methyltransferase-like protein 14), and other subunit proteins. Within this METTL3/14 complex, METTL3 functions as the catalytic enzyme while METTL14 functions as the RNA-binding protein. Other protein components, such as WTAP (Wilms' tumor 1-associated protein), ZC3H13 (zinc finger CCCH domain-containing protein 13), RBM15 (RNA-binding motif protein 15), and VIRMA (Vir-like m^6A methyltransferase associated), function as regulatory subunits[151, 152]. The METTL3/14 complex catalyzes the majority of the RNA m^6A modification with the RR$\underline{\text{A}}$CH (R: A or G; H: A, C, or U) sequence[45]. By contrast, METTL16 was identified as a methyltransferase that only targets specific RNAs, including U6 small nuclear RNA (snRNA) and methionine adenosyltransferase 2A mRNA (*MAT2A*), which not only contain the consensus UAC$\underline{\text{A}}$GAGAA motif but also a defined secondary structure for METTL16 recognition[43, 153, 154]. For a long time, the m^6A modification was considered irreversible until the identification of the first m6A "eraser" enzyme, the fat mass and obesity-associated protein (FTO) in 2011[44], followed by the identification of another m^6A eraser protein, the AlkB homolog 5 (ALKBH5) in 2013[46], uncovering the reversible regulation of the m^6A modification (Figure 12A).

In recent years, researchers have studied the associations of m^6A and related proteins with human diseases, particularly cancers[155]. These proteins are emerging as promising targets for drug discovery. Many small molecules have been identified as modulators that target m^6A-modifying and m^6A-binding proteins[156, 157]. Inhibitors targeting the m^6A writer METTL3 have been most widely studied, many inhibitors have been reported, such as UZH2[158], STM2457[57], EP652[159] and SCT-15 (NCT05584111) (Figure 12B). Among these inhibitors, STC-15 is the first METTL3 inhibitor entering clinical trials for advanced malignancies. The phase 1 clinical study on SCT-15 has been completed in December 2024 (NCT05584111). In addition to inhibitors, PROTAC strategies targeting METTL13 degradation have also been reported as promising anti-cancer approaches by linking the METTL3 inhibitor UZH2 to E3 ligase ligands (Figure 12C)[160-162]. In parallel, small molecules that target the m^6A erasers (e.g., FTO and ALKBH5) and the m^6A readers (e.g., YTHDF1 and YTHDC1) have been reported, with the potential to target a wide range of diseases such as breast cancer and leukemia[163-166].

Despite the significant progress in discovering METTL3-targeting drugs, few molecules have been identified for the recently discovered m^6A writer METTL16. Before our work, only two drugs: lumacaftor (VX-809) and nilotinib (Figure 12D), have been identified as potential METTL16 inhibitors through virtual screening[167]. Although the *in silico* data looks promising, the activity of these two compounds cannot be confirmed without experimental validation. There is an urgent need to identify and validate METTL16-targeting molecules, to confirm METTL16's biological function as a drug target, and to develop drug-like compounds with therapeutic potential.

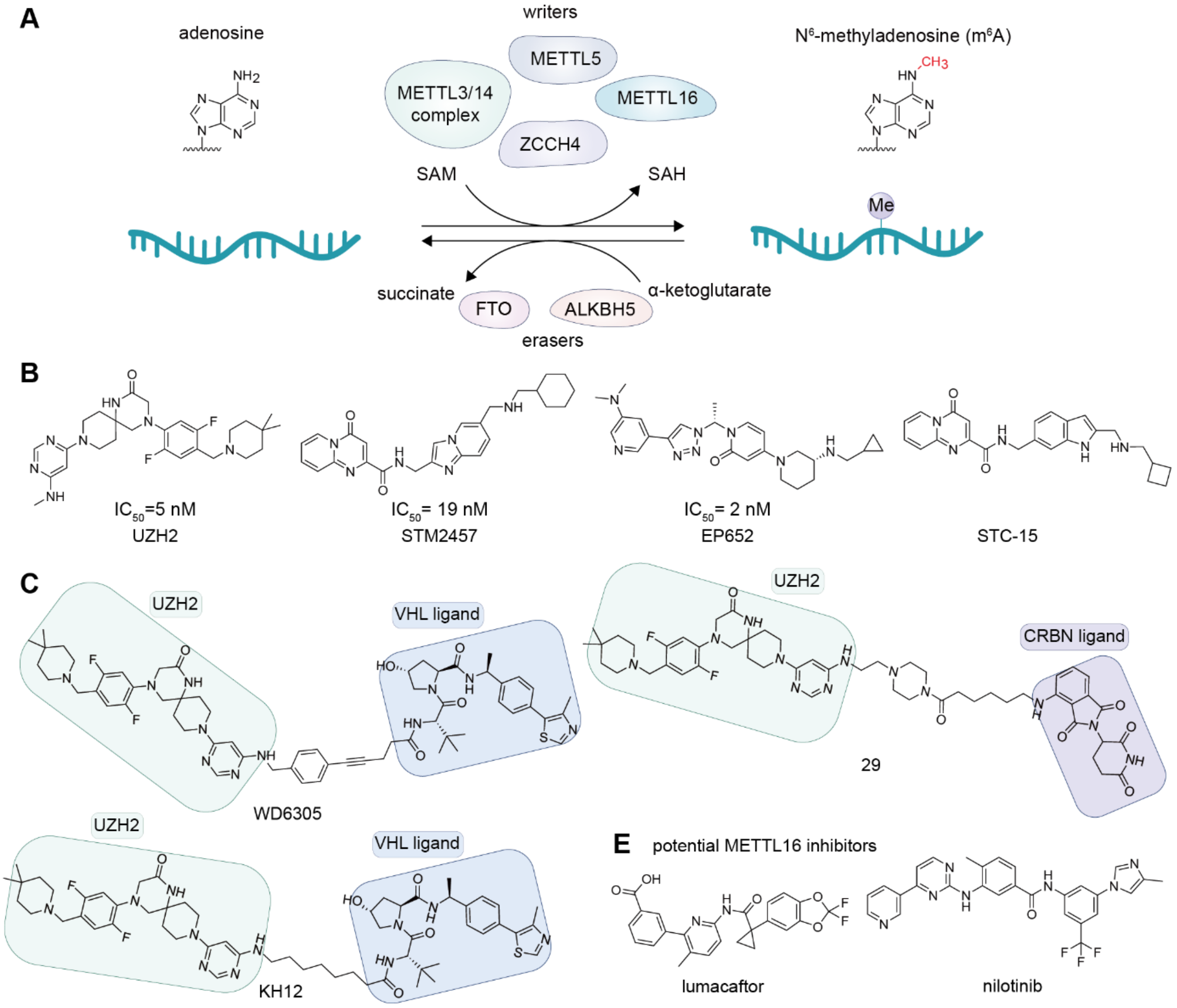

Figure 12. m^6A modifying enzymes and selected molecules. (A). Reversible regulation of m^6A modification. (B). Reported METTL3 inhibitors. (C). Reported METTL3 targeting PROTACs. (D). Potential METTL16 inhibitors through virtual screening.

1.4.2 METTL16 structure

Human METTL16 protein with a total of 562 amino acids contains a N-terminal methyltransferase domain (MTD, residues 1-288) followed by two vertebrate conserved regions (VCR), VCR1 (residues 289-400) and VCR2(514-562) which are connected by a disordered linker[168] (Figure 13A).

METTL16 MTD is responsible for methyltransferase catalysis, which interacts with the substrate RNA and the cofactor SAM, subsequently transferring the methyl group from SAM to the N^6 position of adenosine. The N-terminal residues 1-78 region (residue 1-78) was reported to be critical for specific RNA interaction, and the truncated protein (residue 40-291) loses the binding and methylation activity towards its substrate *MAT2A* hairpin 1[168]. METTL16 has a Rossmann fold (residues 79-288), which is conserved in class 1 methyltransferase, such as METTL3. Although the sequence and the β-sheets organization are distinct in both proteins, the 3D architectures of the Rossmann folds of METTL3 and METTL16 are similar[169]. The crystal structure of the METTL16 MTD in complex with S-adenosylhomocysteine (SAH) indicated that the SAH was bound within the deep pocket of the Rossmann fold, which is also most likely bound by SAM (PDB: 6B92) through the interaction between its adenine group and threonine 164 (T164) [169] (Figure 13B). Like the general mechanism of m^6A methyltransferase, which requires a conserved [DNSH]PP[YFW] motif for catalysis[170], METTL16 contains the catalytic NPPF (Asn-Pro-Pro-Phe, residues 184-187) motif in a loop close to the SAH molecule, which undergoes conformational changes upon SAH binding (Figure 13C)[153, 168, 169]. The methylation target adenine base of substrate *MAT2A* hp1 RNA was also captured in a pocket near the catalytic NPPF motif, with an induced fit mechanism (Figure 13D).

To date, no crystal structure of the whole C-terminal VCR domains of METTL16 has been resolved due to the challenges of crystallizing the long-disordered region (residue 402-498). The structures of the two VCRs were reported in 2020, by crystallization of the deletion protein that lacks the linker between VCR1 and VCR2 (Figure 13E, PDB 6m1u). The subsequent studies indicated that these VCRs enhance the binding and methylation activity towards structured METTL16 RNA substrates, including U6 snRNA and *MAT2A* hp1[171].

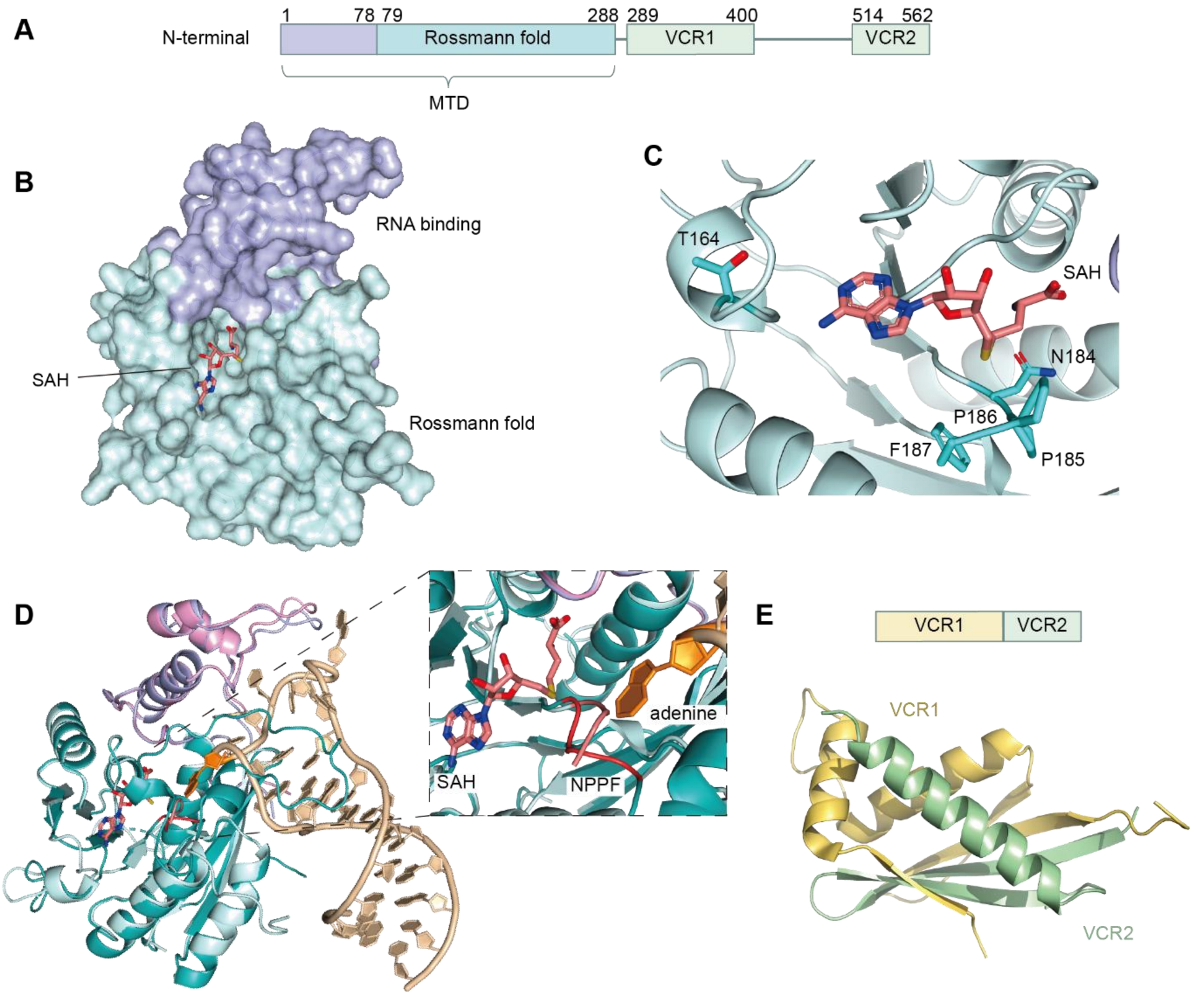

Figure 13. METTL16 structure. (A). Overview of METTL16 domains. MTD: methyltransferase domain. VCR: vertebrate conserved region. (B). SAH binds to a deep pocket in the Rossmann fold region. PDB: 6b92.RNA binding region was shown in purple and the Rossmann fold was shown in palecyan. (C). SAH binding pocket is close to the NPPF catalytic motif. (D). Superimposition of SAH-bound METTL16 (PDB: 6b92, RNA binding region was shown in purple and the Rossmann fold was shown in palecyan) with the MAT2A-hp1-bound METTL16 (PBD: 6du4, RNA binding region was shown in pink and the Rossmann fold was shown in teal, MAT2A-hp1 RNA was shown in wheat). SAH-bound METTL16: RNA binding region was shown in purple, the Rossmann fold was shown in pale cyan, NPPF motif was shown in deep salmon. MAT2A-hp1-bound METTL16: RNA binding region was shown in pink, the Rossmann fold was shown in teal, MAT2A-hp1 RNA was shown in wheat, NPPF motifs were shown in red, and targeted adenine was shown in orange. (E). Structure of the VCR domains.PDB: 6m1u

1.4.3 METTL16 targets and function

Unlike the canonical methyltransferase METLL3/ METTL14 complex, METTL16 functions independently and targets specific RNAs that not only contain the consensus sequence (UACAGAGAA) but also have a defined secondary structure[43, 153, 154]. The identified methylation substrates so far only include *MAT2A* mRNA and the U6 snRNA. Other RNAs, like the *MALAT1* (metastasis-associated lung adenocarcinoma transcript 1) long noncoding RNA, have been shown to bind METTL16, but do not undergo further methylation[154].

MAT2A mRNA encodes the methionine adenosyltransferase 2A protein (MAT2A), which serves as the catalytic subunit of the methionine adenosyltransferase 2 (MAT2) complex. MAT2 complex is responsible for the synthesis of SAM from methionine[172]. SAM, as the main methyl donor in eukaryotic cells, plays a crucial role in many biological processes. The SAM level is kinetically regulated by METTL6, since the MAT2A protein expression is regulated by the post-translational modifications of its precursor mRNA. Under high SAM conditions, METT16 binds and methylates the hairpins with the UACAGARAA in the 3'-UTR region of *MAT2A* mRNA (Figure 14A), promotes RNA degradation, and prevents further splicing and translation. On the contrary, under SAM limiting conditions, METTL16 binds to the 3'-UTR region without further methylation. This increases the mRNA splicing and protein expression, thereby further increasing the SAM level (Figure 14B)[43, 173].

U6 snRNA is an essential component of the spliceosome and is responsible for mRNA splicing[174]. METTL16 catalyzes the methylation of U6 snRNA at the adenosine 43 (A43) position with the conserved sequence. However, the precise role and regulatory mechanisms of METTL16 in the splicing machinery remain unknown[154].

METTL16 was reported to interact with *MALAT1* lncRNA triple helix, however, the specific methylation activity on this RNA substrate was not detected *in vitro*[175, 176]. In addition to *MALAT1* RNA, METTL16 was proposed to bind a variety of mRNA and ncRNA substrates[177, 178]. The biological function of METTL16 as such an RNA-binding protein is yet to be discovered.

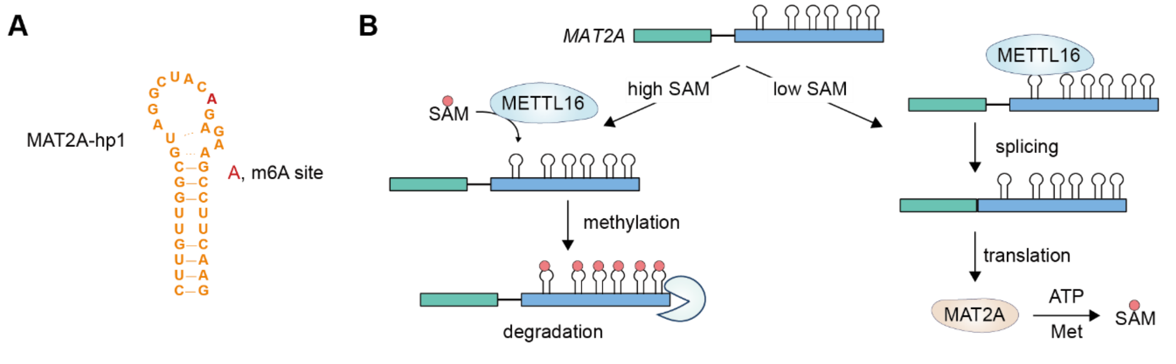

Figure 14. METTL16 substrate *MAT2A* RNA and the downstream pathway. (A). Sequence and secondary structure of MAT2A-hp1. (B). Graphic overview of the dynamical regulation network of SAM level by METTL16.

1.4.4 METTL16 in human disease

METTL16 is essential for the survival of mammals. Knock-out of METTL16 in cells was unsuccessful[43], and the mouse embryos lacking *Mettl16* are unable to undergo further development[168]. The dysregulation of METTL16 has been reported to be associated with various diseases, especially cancers[179]. In addition to its methyltransferase function, METTL16 has been shown to promote translation in the cytoplasm through interacting with the eukaryotic initiation factors to promote tumorigenesis (Figure 15)[180, 181]. METTL16 was found to be overexpressed in hepatocellular carcinoma (HCC), and the increased expression was correlated with poor prognosis in patients[180, 182]. METTL16 recruits the (eIF3) subunits eIF3a/b and ribosomal RNAs to facilitate the ribosome formation, thereby stimulating translation initiation and promoting oncogenic protein synthesis, further facilitating tumorigenesis. The depletion of METTL16 inhibited proliferation, migration, and invasion in HCC cells, and strongly reduced tumor growth *in vivo*[180]. METTL16 has been implicated to play an important role in lung tumorigenesis as well, by interacting with eIFs to promote translation. METTL16 interacts with eIF4E2, promotes eIF4E2 dissociation from the mRNA 5’ cap structure, and increases selective oncogenic protein translation. The suppression of METTL16 downregulates the translation of key oncogenes and inhibits lung tumorigenesis[181]. METTL16 was reported to promote colorectal cancer (CRC) progression through regulating glycolytic metabolism[183]. In CRC, METTL16 increases the expression of SOGA1 (suppressor of glucose autophagy associated 1) by binding to the IGF2BP1(insulin-like growth factor 2 mRNA binding protein 1), subsequently SOGA1 upregulates PDK4 (pyruvate dehydrogenase kinase 4), which was associated with drug resistance and poor prognosis in CRC patients[183].

Although METTL16 has mostly been studied in cancer, recent research displayed its role in other diseases such as nonalcoholic fatty liver disease (NAFLD)[184], diabetic nephropathy[185], and coronary heart disease (CHD)[186]. The expression of METTL16 was found to be upregulated in both *in vivo* and *in vitro* NAFLD models[184]. METTL16 was found to be overexpressed in diabetic nephropathy disease models as well, with an increased overall m^6A modification level, and the deletion of METTL16 alleviated kidney injury[185]. The knockdown of METTL16 in the CHD mouse model largely restores the cardiac function, and decreases cardiac fibrosis and lipid levels[186].

METTL16 functions as an RNA m^6A methyltransferase as well as an RNA-binding protein, implying crucial biological functions. While METTL3/METTL14 has been the focus of numerous research in recent decades, METTL16 has recently received increased attention. The overexpression of METTL16 in various cancers and diseases highlights its potential as a therapeutic target for drug discovery.

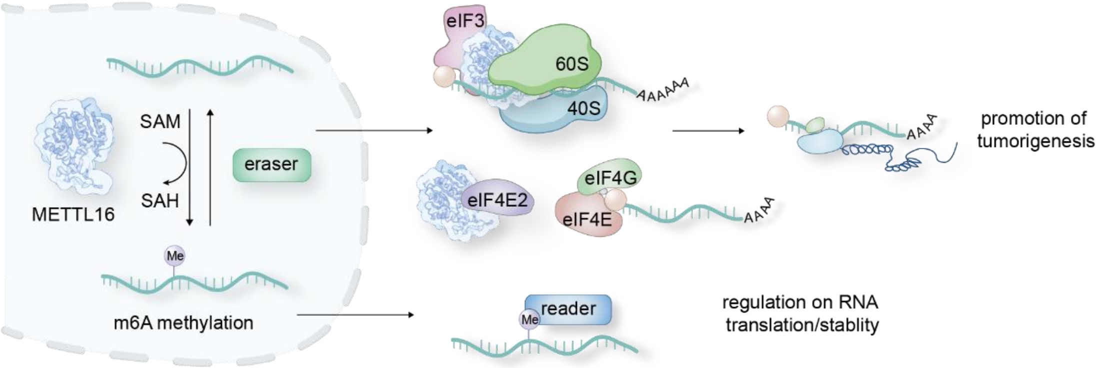

Figure 15. METTL16 promotes tumorigenesis through interacting with eIFs in the cytosol.

1.5 Aims

Small-molecule modulators targeting RNA-binding and modifying proteins are essential tools for understanding RNA biology, offering new therapeutic strategies for diseases involving RNA dysregulation, and driving drug discovery and chemical biology research. This thesis focuses on the development of modulators targeting specific RNA-modifying proteins, particularly the RNA m^6A methyltransferase METTL16 and the ribonuclease IRE1α. The aim of this thesis is to discover novel inhibitors targeting these two RNA-modifying proteins, further regulating related RNA splicing, degradation, and methylation (Figure 16).

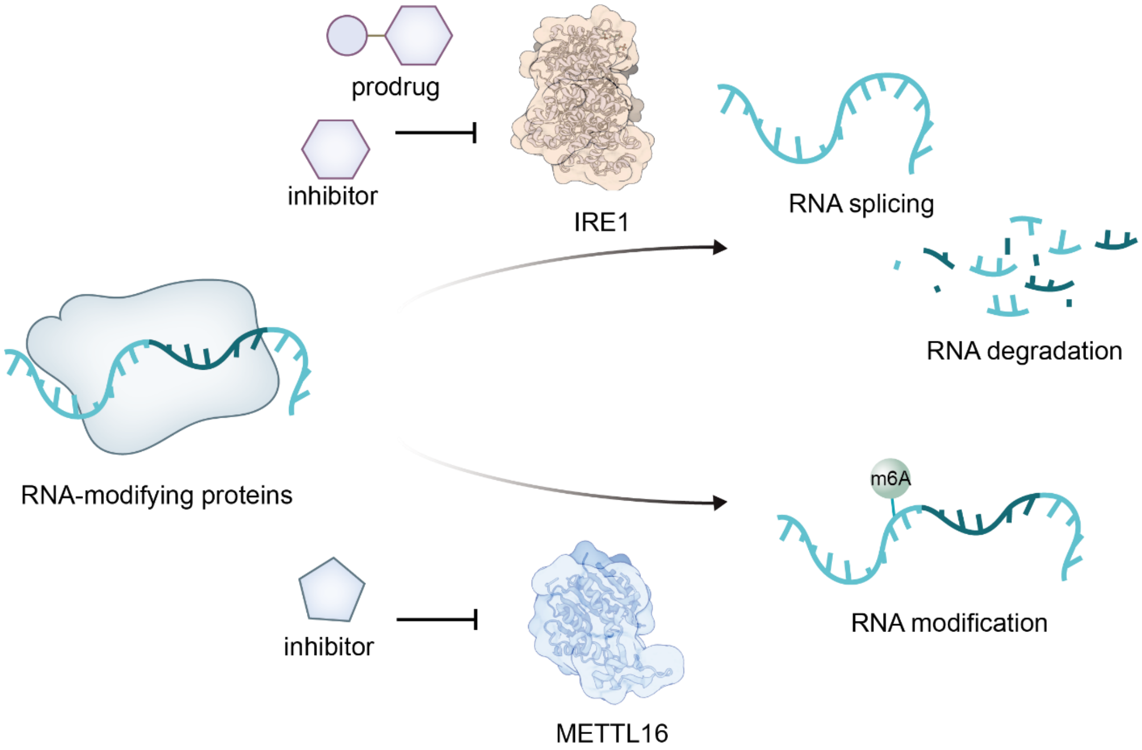

Figure 16. Aim of this Thesis. Discovery of small-molecule inhibitors of two RNA-modifying proteins to regulate RNA metabolism and related pathways.

IRE1α is a crucial effector in the UPR pathway under ER stress. IRE1α splices the mRNA of X-box binding protein, promotes XBP1s protein translation, and further upregulates UPR genes. IRE1α also restores ER harmony by promoting RNA degradation through the regulated IRE1α-dependent decay (RIDD) pathway. Dysregulation of IRE1α signaling has been implicated in various diseases, and only one IRE1α inhibitor is under clinical trial for tumor therapy to date. IRE1α modulators are crucial for understanding the UPR and expanding chemical diversity for drug discovery. Identification of novel IRE1α inhibitory chemotypes would expand the chemical variety of IRE1α inhibitors.

The RNA N^6-methyladenosine (m^6A) methylation is one of the most abundant RNA modifications in eukaryotic RNAs, affecting RNA stability and function, implying important roles in physiological and pathological processes. Methyltransferase METTL16 installs the methyl group from S-adenosylmethionine (SAM) to the adenosine N^6 position of specific RNA substrates. No METTL16 inhibitors have been reported and validated before. Therefore, the second aim is to identify and characterize the first-in-class METTL16 inhibitor to fill the unmet need.

The identified IRE1α and METTL16 modulators will have implications for investigating RNA splicing and methylation pathways, respectively, and offering novel insight to develop translational reagents in UPR and m^6A-relevant diseases, such as cancers and neurodegenerative diseases.

2. Results and Discussion

2.1 Discovery of small-molecule modulators targeting IRE1α for regulating *XBP1* mRNA splicing

*Parts of the result described in this section will be published in Liu, Y.[#]; Avathan Veettil, A. K. [#]; Gasper, R.; Jiang, M.; Wagner, L.; Hastürk, O.; Wu, P. *, Harnessing Indole Scaffolds to Identify Small-molecule IRE1α Inhibitors Modulating XBP1 mRNA Splicing. Accepted in principle*

2.1.1 FRET assay establishment for IRE1α

To establish IRE1α-related assays, the truncated IRE1α protein containing the kinase and the kinase extension nuclease domain (F571-H963, Figure 17A) was expressed and purified using a Bac-to-Bac baculovirus expression system. Due to the phosphorylation of IRE1α playing a crucial role in the RNase activity of IRE1α[187], both phosphorylated and unphosphorylated IRE1α protein states were purified, respectively (Figure 17B), and the phosphorylation states of the proteins were confirmed by LC-MS analysis (Figure 17C, 17D).

A dual-labelled FAM-XBP1-BHQ RNA hairpin was used to establish the fluorescence resonance energy transfer (FRET) cleavage assay for compound screening. When IRE1α cleaves the RNA, the FAM fluorophore will be separated from the BHQ and will no longer be quenched, then the fluorescence signal of FAM can be detected by a plate reader (Figure 17E). To establish the assay, IRE1α and p-IRE1α protein concentration titration was performed (Figure 17F, 16G). The final concentration of 37 nM IRE1α with 100 nM FAM-XBP1-BHQ RNA gives an excellent signal curve that can be used for identifying inhibitors as well as activators. The concentration of IRE1α was further adapted to 40 nM for the FRET assay. For the p-IRE1α FRET assay, 4 nM of p-IRE1α and 200 nM of FAM-XBP1-BHQ were used. The catalytic efficiencies of p-IRE1α and IRE1α were evaluated through the Michaelis-Menten kinetics study using the FRET-based cleavage assay with different concentrations of RNA substrate (Figure 17H). As expected, the result showed that the RNase activity of p-IRE1α is more efficient than that of IRE1α.

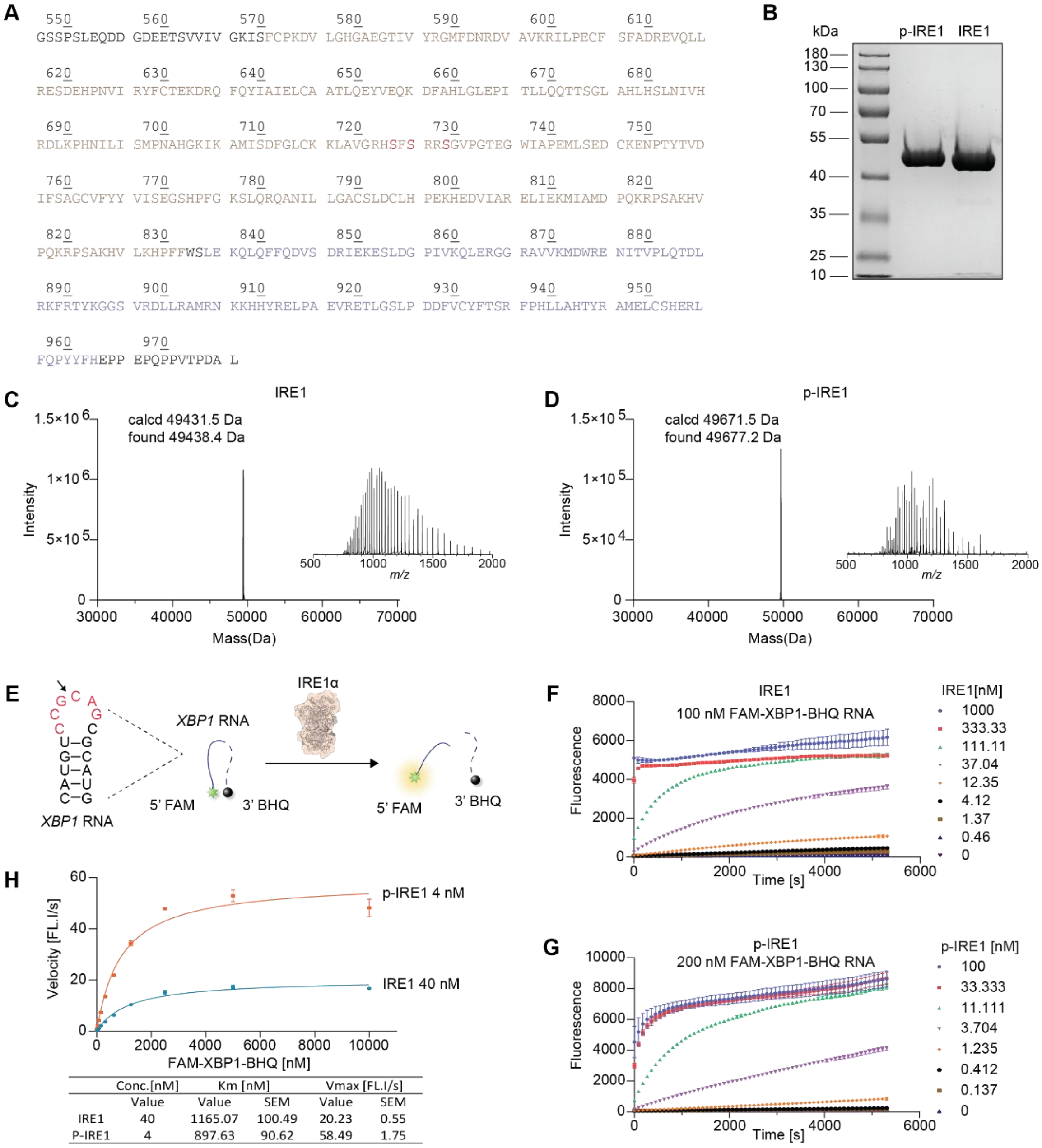

	Conc.[nM]	Km [nM]		Vmax [FL.I/s]	
	Value	Value	SEM	Value	SEM
IRE1	40	1165.07	100.49	20.23	0.55
P-IRE1	4	897.63	90.62	58.49	1.75

Figure 17. IRE1α protein purification and FRET assay establishment. (A). The sequence of truncated IRE1α (547-977). Kinase domain F571-F832 (according to UniProt) is shown in brown, the kinase-extension nuclease (KEN) domain L835-H963 is shown in purple, and three phosphorylation sites are shown in red. (B). Purified phosphorylated IRE1α (p-IRE1α) and unphosphorylated IRE1α (IRE1α). (C). Deconvoluted mass spectra of purified IRE1α protein. (D). Deconvoluted mass spectra of purified p-IRE1α protein. (E). Graphic illustration of the FRET cleavage assay. (F). FRET signals of IRE1α titration with a fixed FAM-XBP1-BHQ concentration at 100 nM. (G). FRET signals of p-IRE1α titration with a fixed FAM-XBP1-BHQ concentration at 100 nM. (H). Michaelis-Menten kinetics of p-IRE1α and IRE1α to evaluate the catalytic efficiency.

2.1.2 Identification of IA01 as IRE1α hit

To identify small-molecule IRE1α modulators, a compound library screening was performed against an in-house chemical library containing 11393 compounds obtained from the

Compound Management and Screening Center Dortmund (COMAS) using a FRET-based cleavage assay with final concentrations of 40 nM IRE1α protein, 5 μM compound, and 100 nM FAM-XBP1-BHQ (Figure 18A). Compound IA01 bearing an indole scaffold was identified as an IRE1α inhibitor hit with IC_{50} values of 0.3 μM and 0.32 μM against IREα and p-IRE1α, respectively (Figure 18B, 18C). An orthogonal gel-based cleavage assay was performed to validate the inhibitory activity, in which IA01 inhibited p-IRE1α RNase activity dose-dependently (Figure 18D). IRE1α and p-IRE1α DSF assays were performed to validate the direct interaction between compound IA01 and the two proteins (Figure 18E, 18F). These results indicated that IA01 can stabilize both IRE1α and p-IRE1α protein in a dose-dependent manner, which confirms the binding of IA01 to both proteins. An isothermal titration calorimetry experiment was carried out to evaluate the binding affinity of IA01 to IRE1α by titrating IA01 into IRE1α protein (Figure 18G), resulting in a K_D value of 12 μM.

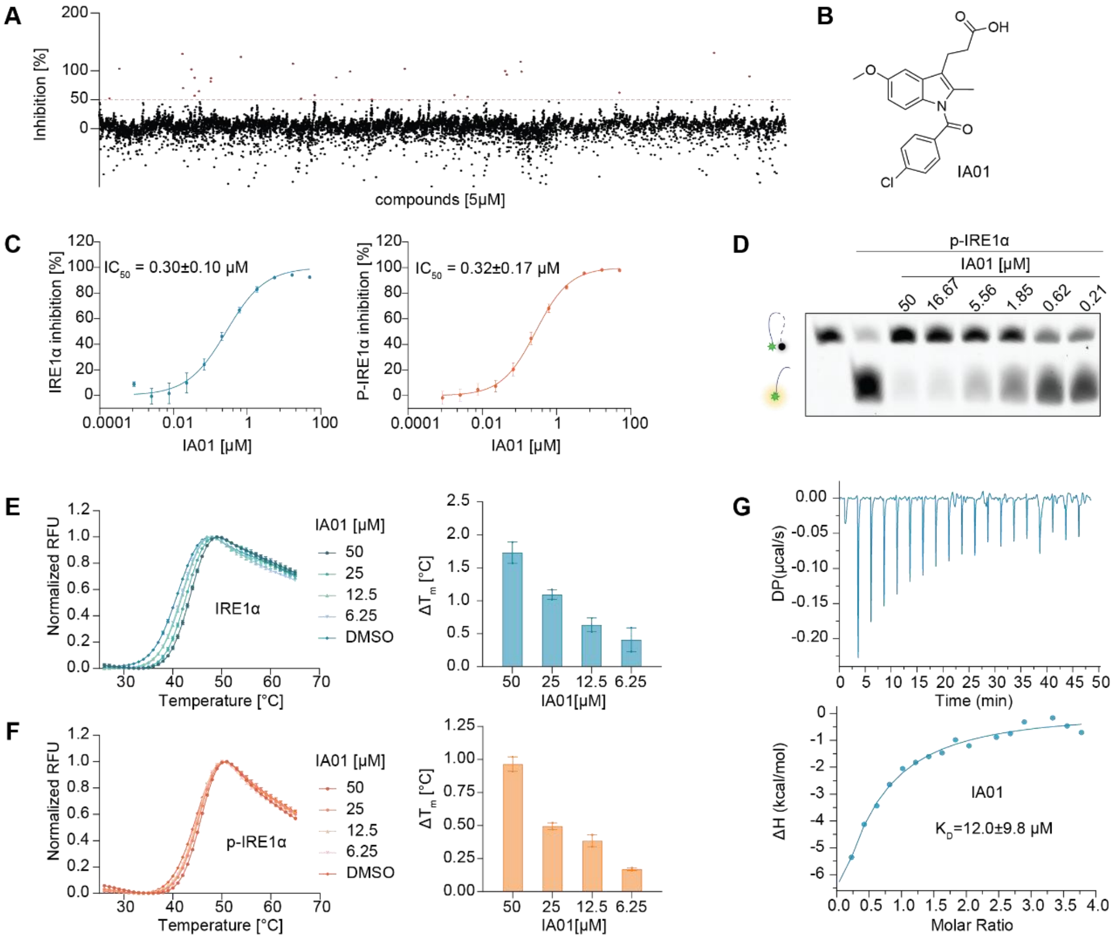

Figure 18. Identification and characterization of the IRE1α hit compound IA01. (A). In-house compound library screening identified hit compound IA01. Primary hits: >50%. (B). Structure of the indole hit IA01. (C). IA01 inhibitory potency against IRE1α and p-IRE1α RNase activity measured by FRET-based assay. (D). IA01 inhibited p-IRE1α RNase activity measured by gel-based cleavage assay. (E). IRE1α melting curves and ΔT_m values under different concentrations of IA01 treatment. (F). P-IRE1α melting curve and ΔT_m values under

different concentrations of IA01 treatment. (G). ITC assay showed a K_D of 12.0±9.81 μM by titrating 200 μM IA01 into 10 μM IRE1α protein.

2.1.3 SAR studies derived from IA01

The activities of indomethacin and auxin analogs from our in-house compound library were evaluated due to the structural similarity between IA01, indomethacin, and auxin (Figure 19). However, under 50 μM tested concentration, neither indomethacin, auxin, nor their analogs showed an inhibitory activity higher than 50% against IRE1α.

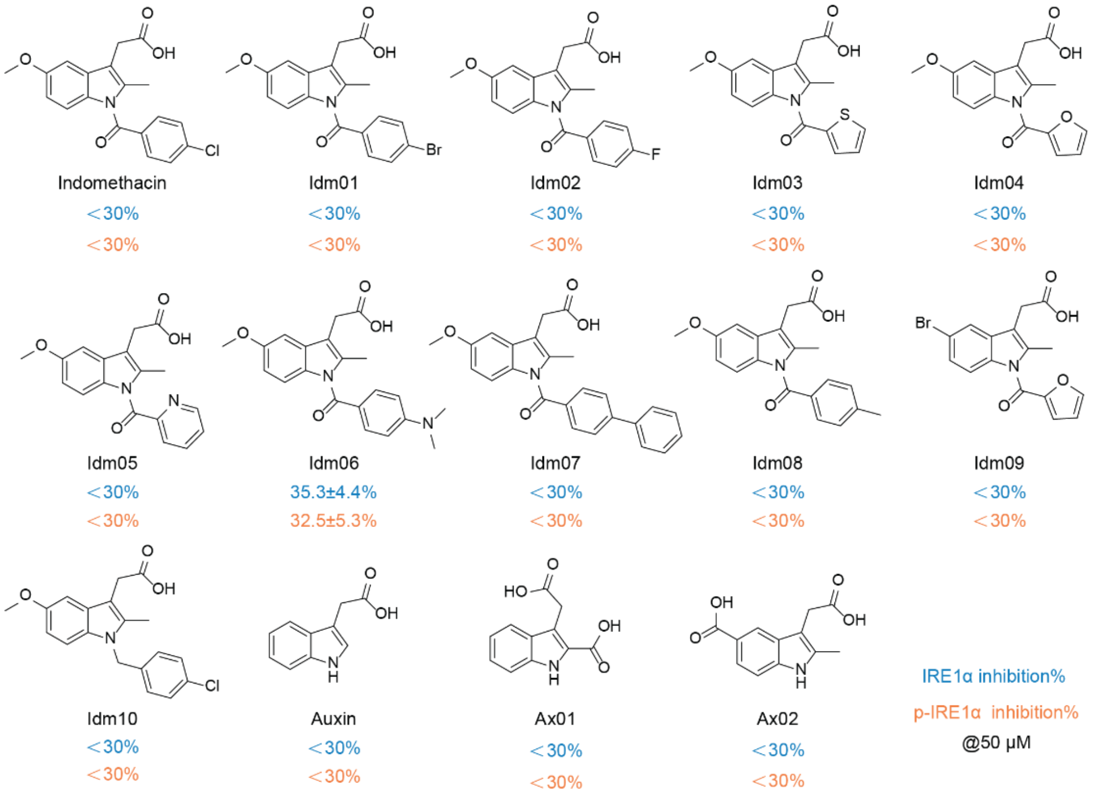

Figure 19. IRE1α and p-IRE1α inhibition activity of indomethacin, auxin, and their analogs.

To improve the potency of IA01, a structure-activity relationship study was conducted based on the indole scaffold of IA01 (Figure 20). Subgroup modifications at the R^1, R^2, and R^3 substituents were performed to improve the activity and to study the chemical structure features of IRE1α inhibition. First, analogs of IA01 with different subgroups at R^1 position were evaluated (Figure 20A). However, all substitutions of this propionic acid group led to the decreased activities. Only the butyric acid group has an inhibitory activity of around 40% at 50 μM tested concentration. While other substitutes like esters, ketone, alkyl groups, aromatic rings, and the aliphatic heterocyclic ring decrease the activity to less than 30% at 50μM. The modifications at the R^2 position were more tolerated, as a variety of acyl groups can be altered

(Figure 20B). Among them, the *N*-benzoyl compound IA64 was the most potent one, with an IC_{50} value of 0.03 μM against both IRE1α and p-IRE1α states. Based on the observed structure-activity relationship of IA01 and IA64, the modifications at the R^3 position were performed by fixing the R^1 as the propionic acid group and the R^2 as the benzoyl group (Figure 20C). Replacing the methoxy group with a bromide group yielded the most potent compound, IA107, with a 20-fold increase in potency compared to the initial hit compound IA01, which showed IC_{50} values of 0.016 μM and 0.009 μM against IRE1α and p-IRE1α, respectively.

Due to the potent inhibition of the thiophene-2-carbonyl compound IA03 and the 3-cyanobenzoyl compound IA30, two mini-collections were synthesized based on these two compounds, using different halogenated groups to replace the 5-methoxy group. The activity results showed that most of the analogs in these collections retained the inhibitory potency. However, no significant improvements on the activity were observed (Figure 20D, 20E).

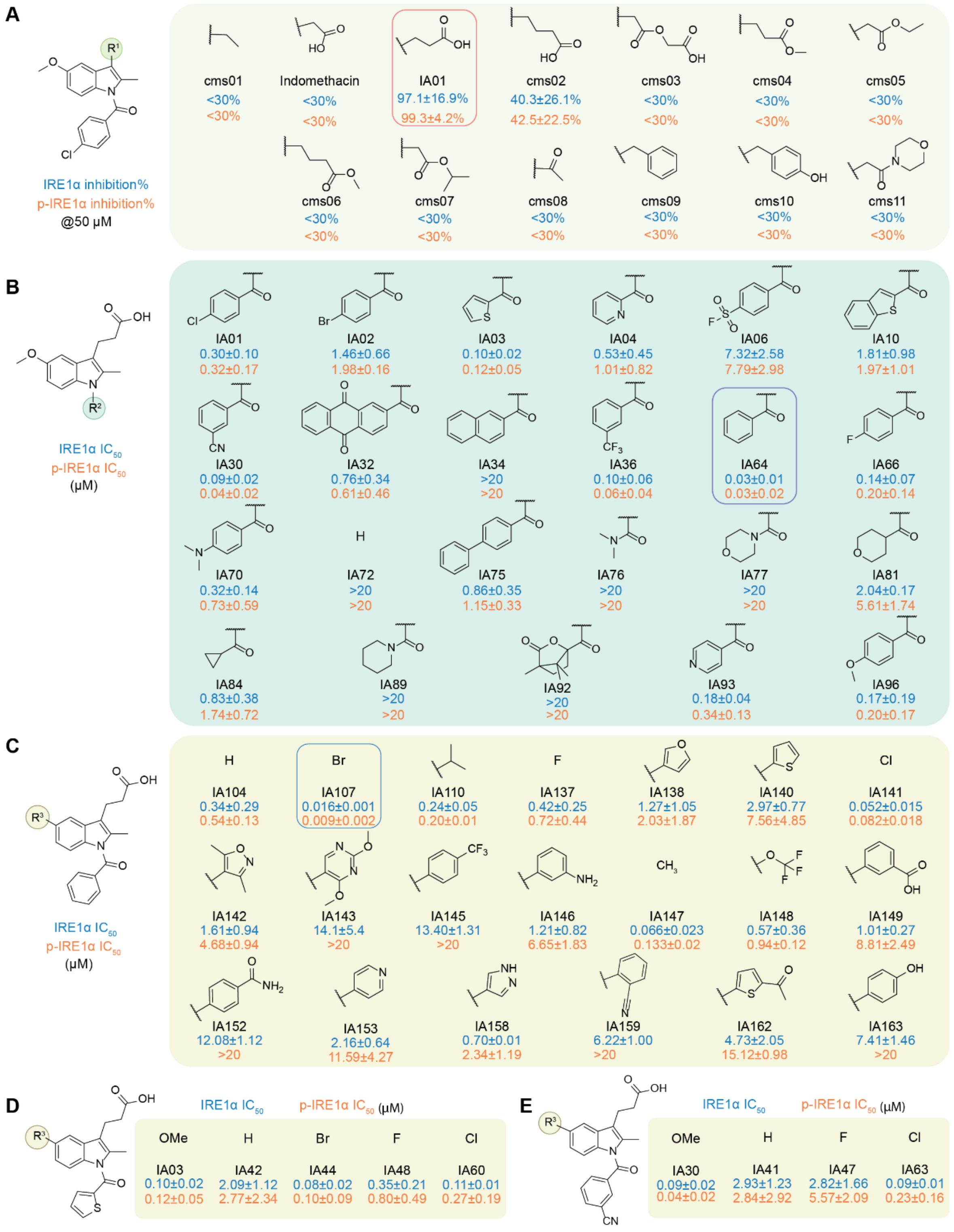

Figure 20. Overview of the evaluated indole analogs as IRE1α inhibitors. (A). Indole analogs with different substituents at the C-3position (R^1). (B). Indole analogs with different substituents at the N-position (R^2). (C). Indole analogs with different substituents at the C-5 position (R^3). (D). A small collection of analogs based on IA03. (E). A small collection of analogs based on IA30.

2.1.4 Evaluation of the indole-containing IRE1α inhibitors

More potent compounds were obtained from the structural modification of the indole scaffold of IA01. To validate the inhibitory activity, an orthogonal gel-based cleavage assay was performed. The best-performing compound from modifying the R^2 position, IA64 (Figure 21A), and the most potent compound IA107 (Figure 21B) were evaluated through the gel-based assay. Both IA64 and IA107 inhibited the cleavage of FAM-XBP1-BHQ RNA hairpin by p-IRE1α does-dependently. The activity of IA64 improved 10-fold compared to IA01 (Figure 21D), and among all obtained indole-bearing inhibitors, compound IA107 showed the best potency (Figure 21C, 21D).

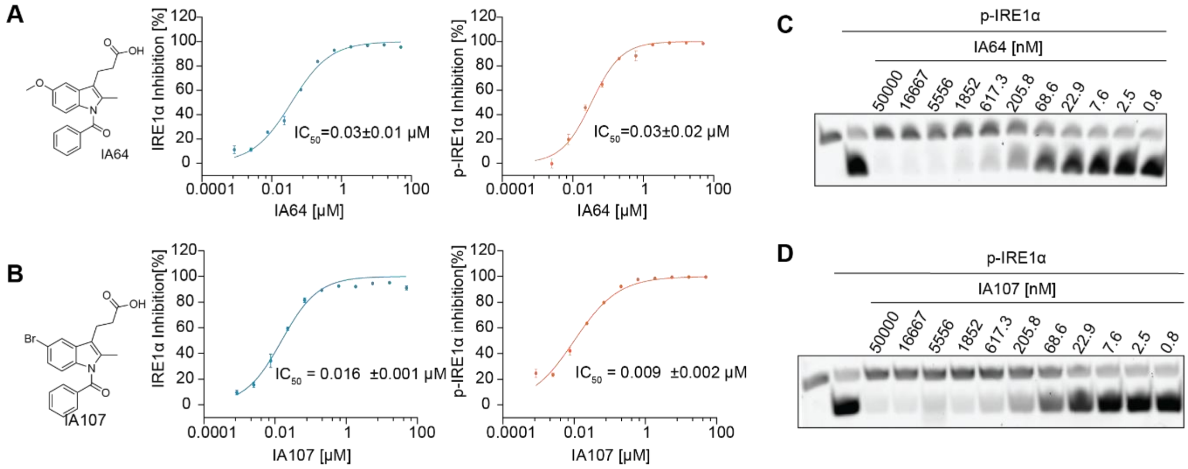

Figure 21. Compounds validation through orthogonal gel-based cleavage assay. (A). Structure and the activity of IA64, the best-performing compound from modifying the R^2 position. (B). Structure and the activity of the most potent compound IA107. (C). IA64 dose-dependently inhibited phosphorylated IRE1α RNase activity in a gel-based RNA-cleavage assay. (D). IA107 dose-dependently inhibited phosphorylated IRE1α RNase activity in a gel-based RNA-cleavage assay.

To validate the binding interaction of the indole-containing inhibitors to IRE1α, a differential scanning fluorimetry (DSF) assay was performed. Compound IA34, which bears a naphthoyl group, showed IC_{50} > 20 μM against both IRE1α proteins, was used as a negative control (Figure 20B). The DSF results showed that IA30, IA64, IA107, IA141, and IA147 dose-dependently stabilized IRE1α protein (Figure 22A-D), and the changes in melting temperature (ΔT_m) are correlated with the inhibitory activities tested in biochemical assays. The negative compound IA34 did not show any detectable impact on the thermal stability of IRE1α and p-IRE1α protein (Figure 22A). The compounds were evaluated against p-IRE1α in the DSF assay, which showed consistent results (Figure 22E-H). The DSF assay results indicated the binding interaction of the indole compounds to IRE1α and p-IRE1α proteins.

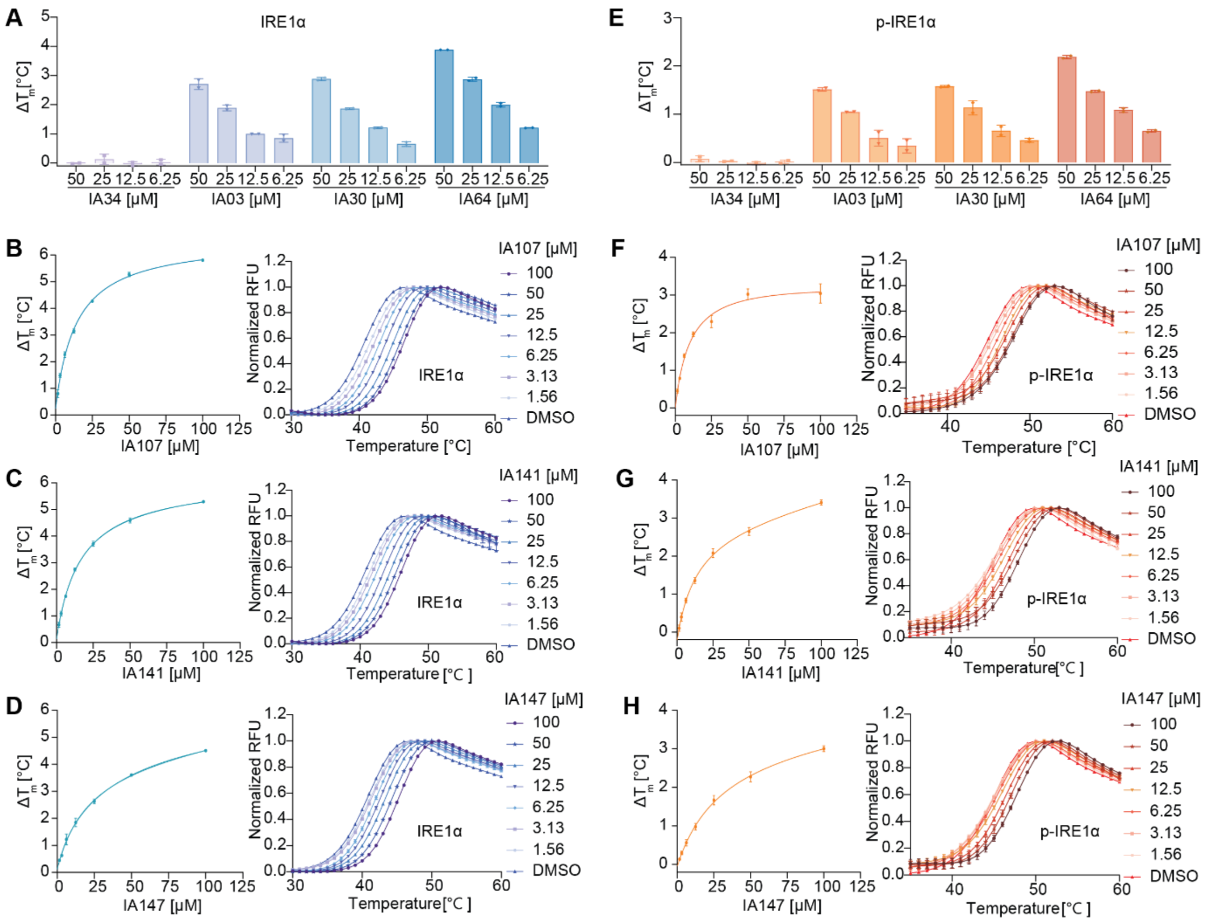

Figure 22. Binding confirmation through DSF assay. (A). The ΔT_m of IRE1α under compound IA34, IA03, IA30, and IA64 treatments. (B). The ΔT_m values and the melting curves of IRE1α under different concentrations of compound IA107 treatments. (C). The ΔT_m values and the melting curves of IRE1α under different concentrations of compound IA141 treatments. (D). The ΔT_m values and the melting curves of IRE1α under different concentrations of compound IA147 treatments. (E). The ΔTm of p-IRE1α under compound IA34, IA03, IA30, and IA64 treatments. (F). The ΔT_m values and the melting curves of p-IRE1α under different concentrations of compound IA107 treatments. (G). The ΔT_m values and the melting curves of p-IRE1α under different concentrations of compound IA141 treatments. (H). The ΔT_m values and the melting curves of p-IRE1α under different concentrations of compound IA147 treatments.

To measure the binding affinity of the indole inhibitors, ITC experiments were performed by titrating 200 μM compounds to 10 μM IRE1α protein. The ITC titration results showed that IA64, IA107, IA141, and IA147 had the K_D values of 2.96 μM, 0.94 μM, 1.82 μM, 2.99 μM against IRE1α, respectively (Figure 23A, 23B). And the negative compound IA34 did not show any binding signal from the ITC experiment (Figure 23C). The binding affinity of the most potent compound IA107 was further validated by a microscale thermophoresis (MST) experiment. A K_D value of 1.3 μM against dephosphorylated IRE1α was obtained from the MST measurement (Figure 23D), which was consistent with the ITC result and confirmed the binding affinity between IA107 and IRE1α. The affinity of IA107 against phosphorylated IREα was further measured through MST assay. The MST result showed that IA107 had a higher binding affinity (~10-fold) towards p-IRE1α compared to IRE1α, with a binding affinity K_D of 152 nM. We assume that IA107 may prefer to bind the dimeric protein state of IRE1α, since p-IRE1α has a significantly higher dimeric protein population compared to IRE1α, causing the affinity difference between IRE1α and p-IRE1α[126]. This may further explain the discrepancy between the binding affinity K_D with the IC_{50} value against IRE1α. Only the dimeric IRE1α protein can form a proper RNase catalytic pocket, and the monomeric proteins were considered inactive[128, 188]. Once the dimeric IRE1α protein was bound and inhibited, the RNase activity will subsequently be inhibited.

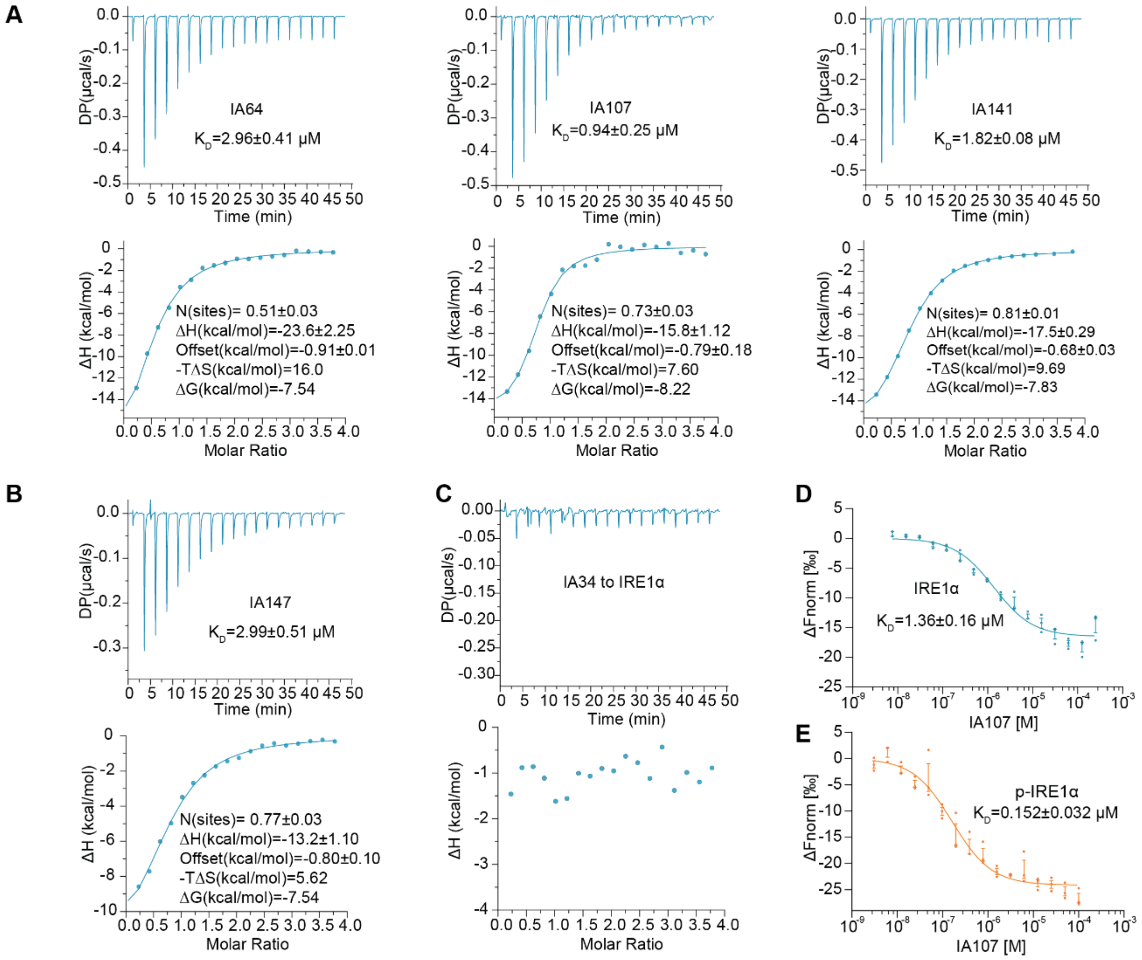

Figure 23. Binding affinities of the indole-containing inhibitors measured by ITC and MST confirmation through DSF assay. (A). (B). The binding affinities of compound IA64, IA107, IA141, and IA147 by ITC titration. (C). The ITC titration of negative compound IA34. (D). The MST measurement of IA107 binding affinity to IRE1α. (E). The MST measurement of IA107 binding affinity to p-IRE1α.

2.1.5 IA107 binding pocket study

IRE1α has two potential binding sites at the kinase and RNase domains, respectively, that can be targeted by small molecules to modulate the RNase activity[130]. To investigate the binding pocket of IA107, a Michaelis–Menten kinetic analysis of IA107 was performed to determine whether IA107 competes with the *XBP1* RNA substrate (Figure 24A). The result demonstrated that the Michaelis constant K_m value for IRE1α incubated with DMSO was 876.5 nM, and the K_m values for IRE1α that were incubated with 0.01 μM, 0.1 μM, and 1 μM IA107 were 915.5 nM, 819.2 nM, and 1210 nM, respectively. Only minor changes in the K_m values were observed under the treatment of different concentrations of IA107. However, the calculated V_{max} decreased dose-dependently upon IA107 treatment, as the V_{max} for the DMSO control, 0.01 μM, 0.1 μM, and 1 μM IA107 were 10.98 FL. I/s (fluorescence intensity/second), 7.98 FL. I/s, 2.33 FL. I/s and 0.9 FL. I/s, respectively. The changes in K_m and V_{max} indicate IA107 is a non-competitive inhibitor of the *XBP1* RNA substrate, and suggest that IA107 does not bind to the RNase pocket.

To evaluate the kinase ATP-binding pocket binding interaction, a LanthaScreen^{TM} Eu kinase binding assay was performed using Alexa fluor-labeled kinase tracer 236 (with a K_D value of 160 nM to IRE1α), GST-tagged-IRE1α protein and Eu-anti-GST antibody (Figure 24B). A high FRET signal is observed when the kinase tracer binds to the kinase ATP-binding pocket of the GST-tagged-IRE1α with the Eu-labelled anti-tag antibody. If the compound binds to the ATP-binding pocket and displaces the tracer, the FRET signal will decrease. The kinase binding assay demonstrated that IA107 indeed inhibited the kinase tracer binding, with an IC_{50} value of 768 nM, which indicates IA107 bound to the ATP-binding pocket of IRE1α. To further confirm the binding pocket, competitive ITC experiments were performed. Compound G1749, a previously reported IRE1α RNase activator that binds to the IRE1α kinase domain, was used as a reference compound (Figure 24C). Competitive titrations were performed by pre-incubating IRE1α with different concentrations of IA107 and then titrating G1749 to the IRE1α protein. The results showed that the binding affinity of G1749 decreased in the presence of IA107 in a dose-dependent manner: titration of G1749 into IRE1α without IA107 gave a K_D value of 11.9 nM (Figure 24C); when IRE1α was pre-incubated with 50 μM IA107, a K_D value of 221 nM was obtained; when pre-incubated with 200 μM IA107, the K_D value increased to 2120 nM; G1749 did not show any binding signal when IRE1α was pre-incubated with 1 mM IA107 (Figure 24D). Additionally, pre-incubating IRE1α with different concentrations of negative compound IA34 did not impact the binding of G1749 to IREα (Figure 24E). IA107 affected the binding between G1749 and IRE1α, and the binding of IA107 to IRE1α can displace G1749 binding, which suggests IA107 and G1749 share the same binding pocket. In addition, competitive titrations were performed by titrating IA107 to IRE1α which were pre-incubated with different concentrations of G1749 as well, the presence of G1749 impacts IA107 binding affinity: without the addition of G1749, IA107 showed a K_D value of 0.94 μM towards IRE1α (Figure 23A); pre-incubating IRE1α with G1749 at 5 μM decreased the binding affinity to a K_D value of 2.25 μM; when the concentration of G1749 increased to 50 μM, the binding signal of IA107 to IRE1α was not detectable, the presence of G1749 displaces the binding of IA107 towards IRE1α (Figure 24F). In summary, the competitive ITC titrations further confirm that IA107 binds to the kinase domain of IRE1α.

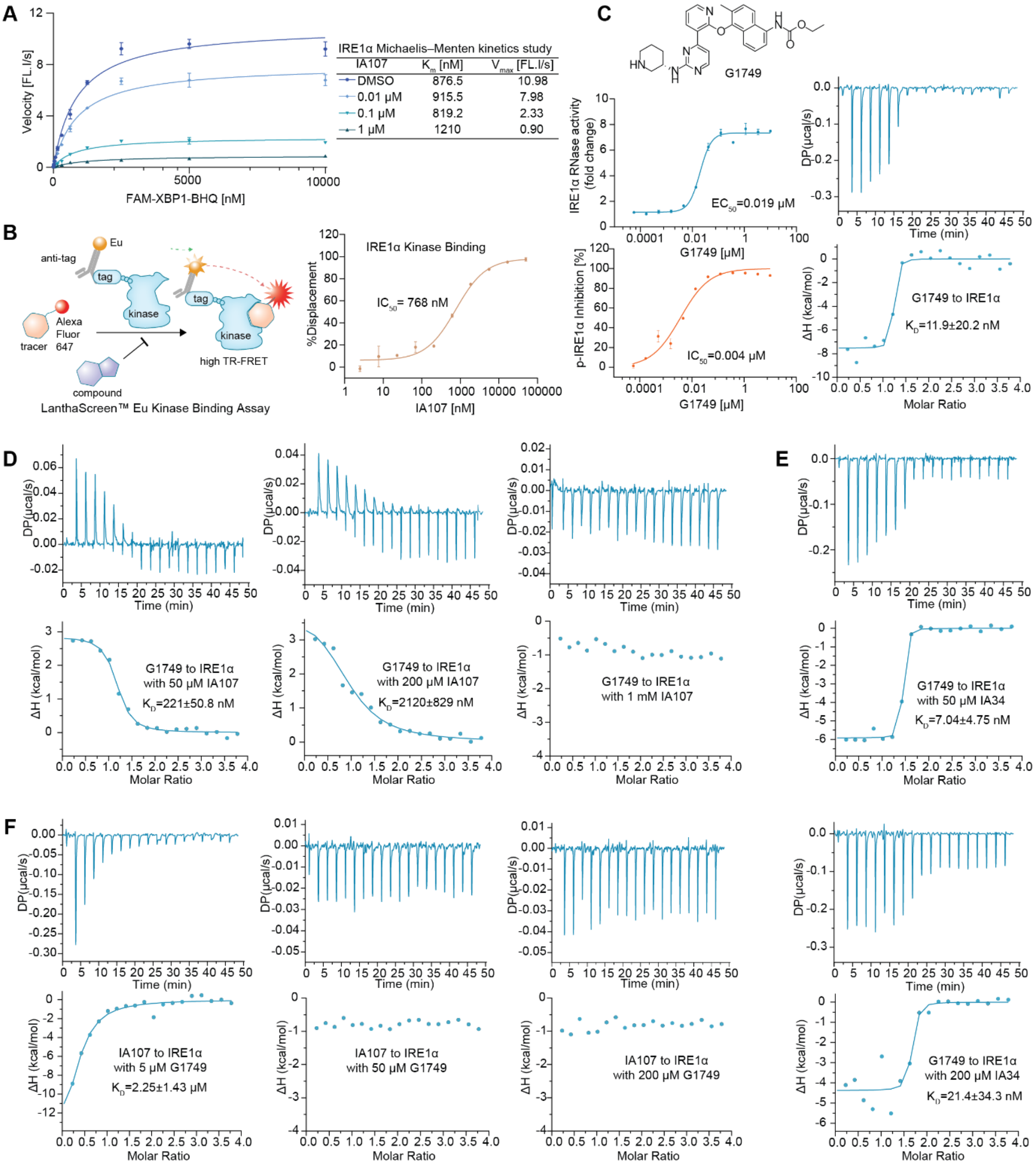

Figure 24. IA107 binding pocket identification. (A). Michaelis–Menten kinetic analysis of IRE1α under different IA107 concentrations. (B). The LanthaScreen^{TM} Eu kinase binding assay and the activity of IA107 bind to IRE1α kinase domain. (C). Reference compound G1749, the structure of G1749, the activities of G1749 in FRET-base assays and the affinity of G1749 against IRE1α measured by ITC titration. (D). Competitive ITC titration experiments by titrating 200 μM G1749 into 10 μM IRE1α pre-incubated with different concentrations of IA107 (50 μM, 200 μM, 1mM) respectively. (E). Competitive ITC titration experiments by titrating 200 μM G1749 into 10 μM IRE1α pre-incubated with different concentrations of negative compound IA34 (50 μM, 200 μM) respectively. (F). Competitive ITC titrations by titrating 200 μM IA107 into 10 μM IRE1α pre-incubated with different concentrations of G1749 (5 μM, 50 μM, 200 μM), respectively.

2.1.6 Crystal structure of IA107 and the inhibitory mechanism studies

To better understand the binding mode and the inhibitory mechanism, the crystal structure of p-IRE1α in complex with IA107 was resolved (PDB 9gow). The overall resolution of this co-structure is 3-Å, and the resolved structure contains four copies within one asymmetric unit. Compound IA107 binds to the kinase ATP-binding pocket of IRE1α as expected. IA107 densities were well resolved in all four copies in the asymmetric unit, with the only fitted orientation, indicating the full occupancy of IA107 in all chains with the only possible conformation (Figure 25A). Among the 4 copies, chain A and chain B formed a back-to-back dimer, and chain C formed the dimer with chain D from the symmetry mate (Figure 25B). In the structure, chains A, B, and C were well resolved and showed good density, while the residues K851 to M948 of chain D were deleted due to the poor electron density data.

Three crucial hydrogen bonds were found between IA107 and p-IRE1α: two hydrogen bonds formed between the propionic acid group of IA107 with the DFG-motif (Asp-Phe-Gly, residue 711-713) backbone aspartic acid D711 residue and the kinase catalytic lysine K599; the third bond was found between the carbonyl amide group of IA107 and the hinge region backbone cysteine C645 (Figure 25C, 24D). The hydrogen bond formations between the propionic acid group and IRE1α explained the chemical modifications at this position of IA01, resulting in the loss of inhibitory activity (Figure 20A). To further confirm the hydrogen bond formed with the carbonyl amide group, compound IA164 was synthesized without the carbonyl group (Figure 25E). The inhibitory activity of IA164 against both IRE1α and p-IRE1α was completely lost, validating the importance of the hydrogen bond interaction between the carbonyl group and IRE1α protein. Furthermore, the *N*-benzoyl motif of IA107 faced toward the adenine pocket and formed hydrophobic interactions with the kinase hinge region (Figure 25C). A cyclohexane-substituted analog IA165 was synthesized to evaluate the binding interaction at the hydrophobic channel (Figure 25F). The FRET-based cleavage assays showed that the activity of IA165 against both IRE1α and p-IRE1α decreased compared to IA107, with IC_{50} values of 1.15 µM and 3.62 µM, respectively, indicating that the aromatic group at the *N*-substituent position is preferred. Both cyclohexane and phenyl groups are hydrophobic groups that can interact with the hinge region through hydrophobic interactions. However, the cyclohexane group with electron-donating property may weaken the hydrogen bond formation between protein C645 and the amide carbonyl group of the compound, decreasing the activity.

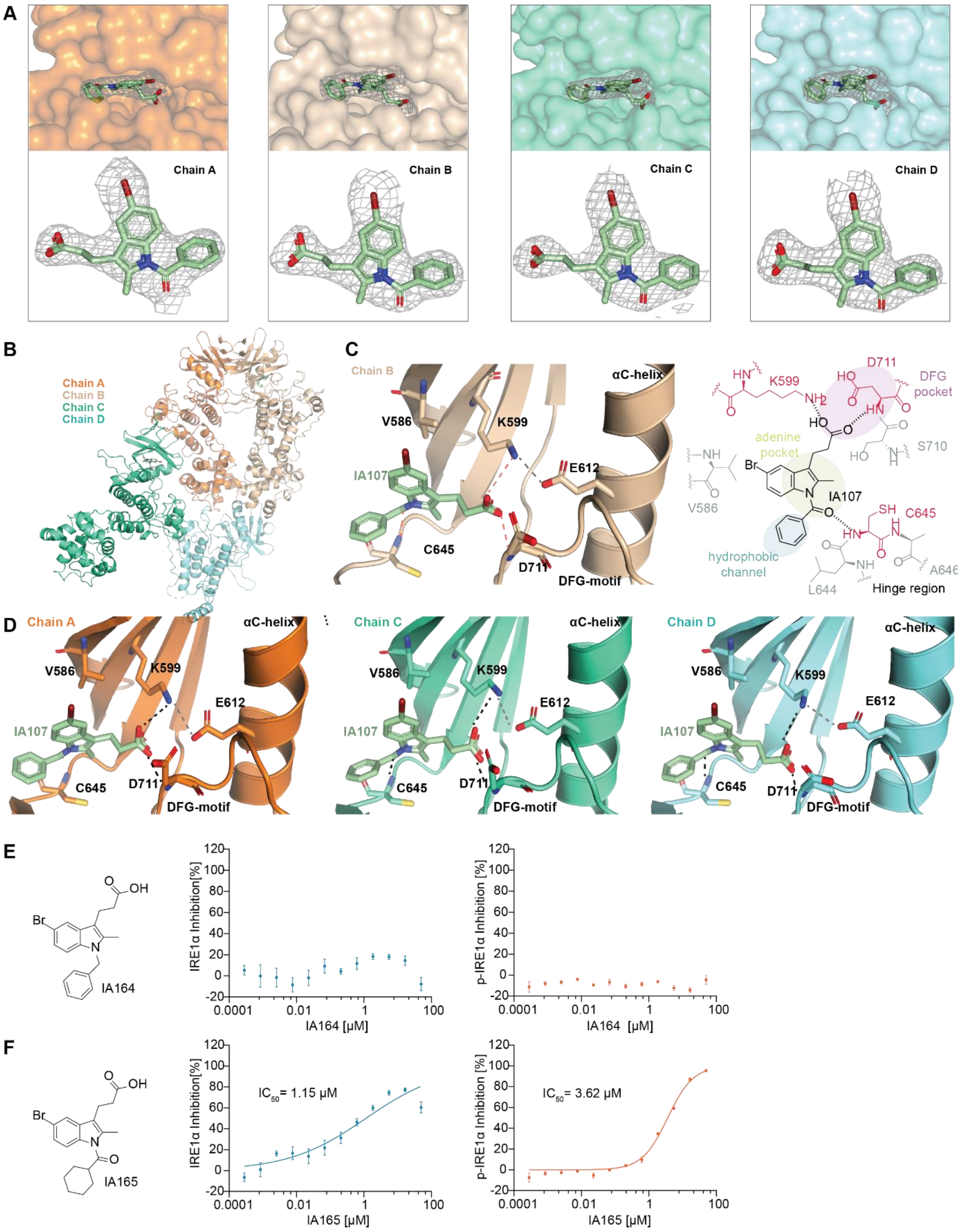

Figure 25. Binding interaction of IA107 to p-IRE1α. (A). The 2Fo-Fc electron density maps of IA107 in different chains. Shown in σ 1.0. (B). The cartoon view of four copies in one asymmetric unit. Chain A and chain B formed a back-to-back dimer. (C). IA107 binding interactions and the hydrogen bond formed between IA107 and chain B. (D). IA107 binding interactions and the hydrogen bond formed between IA107 and chain A, C, and D, respectively. (E). The activities of compound IA164 without the carbonyl group against IREα and p-IRE1α in the FRET assay. (F). The activities of compound IA165 with a cyclohexane group at the *N*-position against IREα and p-IRE1α in the FRET assay.

The conformational changes of IA107-bound p-IRE1α in key structural elements of the kinase domain, including the DFG motif, the K599-E612 salt bridge, and the αC-helix, were analyzed for their crucial role in the regulation of RNase domain activity[130]. IA107 interacted with lysine K599 with the observed *N*-terminal αC-helix shift outwards, and the salt bridge between K599 and glutamic acid E612 of the αC-helix remained intact (Figure 25C, Figure 26A). In contrast, the p-IRE1α structures in complex with two reported inhibitors, KIRA8 and G0701(a G1749 analog)[126, 189], showed that the bindings of KIRA8 and G0701 push the αC-helix out and break the K599-E612 salt bridge (Figure 26A). Compared to the apo from p-IRE1α structure, upon IA107-binding, the conformation of K599 and E612 residues only had a minor shift (Figure 26A). The DFG motif did not show any significant changes as well, which adopts a DFG-in conformation in both apo form and IA107-bound structures (Figure 26B). A slightly shifted conformation was observed at the activation loop (residues 711-741) of IA107-bound p-IRE1α, but the overall structure of the activation loop is similar to that of the apo-form (Figure 26C). By aligning the structure with the apo form p-IRE1, the αC-helix was found to push more outward upon IA107 binding (Figure 26D). The other chains A, C, and D also showed an intact salt bridge of K599-E612, a DFG-in conformation, and an outward αC-helix shift (Figure 26E-G). This confirmed the structural elements shift observed.

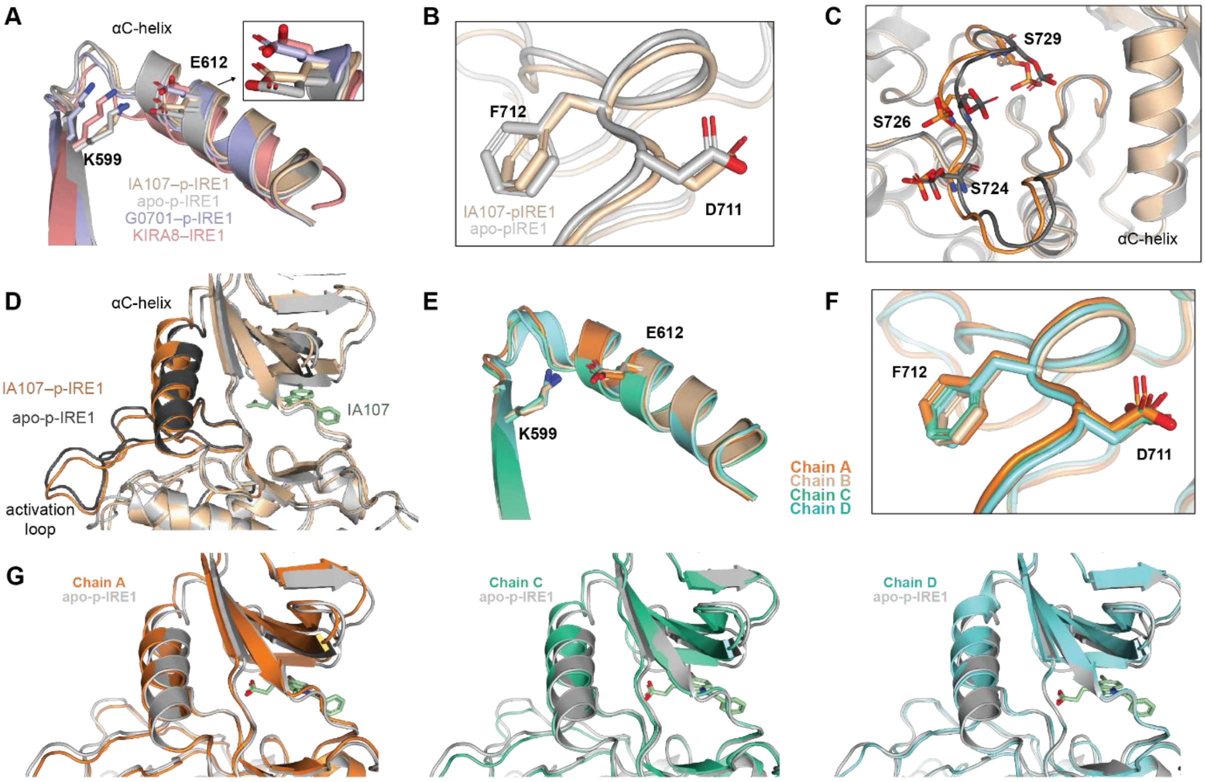

Figure 26. Structural elements analysis of IA107 bound p-IRE1α. (A). Superimposition view of the αC-helix and the K599-E612 salt bridge and of the IA107-bound p-IRE1α (chain B, wheat, PDB 9gow), apo-pIRE1α (grey,

PDB 6w3c), G0701-pIRE1α (purple, PDB 6w3e) and KIRA8-IRE1α (pink, 6urc). (B). The superimposition view of the DFG motif of the IA107-bound p-IRE1α (chain B, wheat, PDB 9gow) and apo-pIRE1α (grey, PDB 6w3c). (C). Superimposition view of the phosphorylation sites and the activation loop from IA107-bound p-IRE1α (chain B, wheat, PDB 9gow) and apo form p-IRE1α (grey, PDB 6w3c), the activation loops with phosphate groups are shown in highlight color. (D). The confirmation of the αC-helix upon IA107 binding compared to the apo form. (E). Superimposition view of the αC-helix in each chain of IA107-bound p-IRE1α (F). Superimposition view of the DFG motif of each chain in the asymmetric unit. (G). Superimposition view of chains A, C, and D with the apo form p-IRE1α in the asymmetric unit.

IRE1α assembles through dimerization and oligomerization to promote the RNase activity[125, 190, 191]. The kinase domain-binding modulators have been reported to activate RNase activity by promoting IRE1α dimerization and to inhibit the RNase activity by inhibiting dimerization[136, 191, 192]. The dimer interface of IA107-bound p-IRE1α was analyzed to understand the inhibitory mechanism of IA107. The dimer structure of chain A and chain B has a lower B-factor compared to the dimer formed by chain C and the symmetry mate chain D (Figure 27A), making the dimer structure of AB more reliable than the dimer of CD. Hence, the AB dimer was mainly analyzed in this study. The overall interactions of the two protomers from the kinase domain were not significantly affected upon IA107 binding, it remains a similar structure with the apo form (Figure 27B, 27C). On the other hand, the RNase domain dimer of the IA107-p-IRE1α complex is more separated in comparison with the apo p-IRE1α (Figure 27B). When having a closer look at the kinase domain interface, most of the hydrogen bonds between two protomers remained intact (Figure 27C), for example, the interactions between threonine T631 (protomer 1) with lysine K568 (protomer 2), arginine R617 (protomer 1) with aspartic acid D592 (protomer 2), aspartic acid D620 (protomer 1) with arginine R627 (protomer 2), aspartic acid D621 (protomer 1) with lysine K706 (protomer 2), etc. Slight shifts of the individual residues located at the dimer interface of the kinase domain were observed (Figure 27D), which we expected to have little effect on dimer interactions. In contrast, the residues located at the dimer interface of the IA107-bound p-IRE1α RNase domain are significantly shifted compared with the apo form structure (Figure 27E). Upon IA107 binding, the hydrogen bonds formed between histidine H909 and aspartic acid D847 of each protomer were disrupted (Figure 27F), further displacing the key catalytic residue H910 and the ribonuclease active site[188], and such displacement is presumed to be the main reason for the inhibition of the RNase activity by IA107.

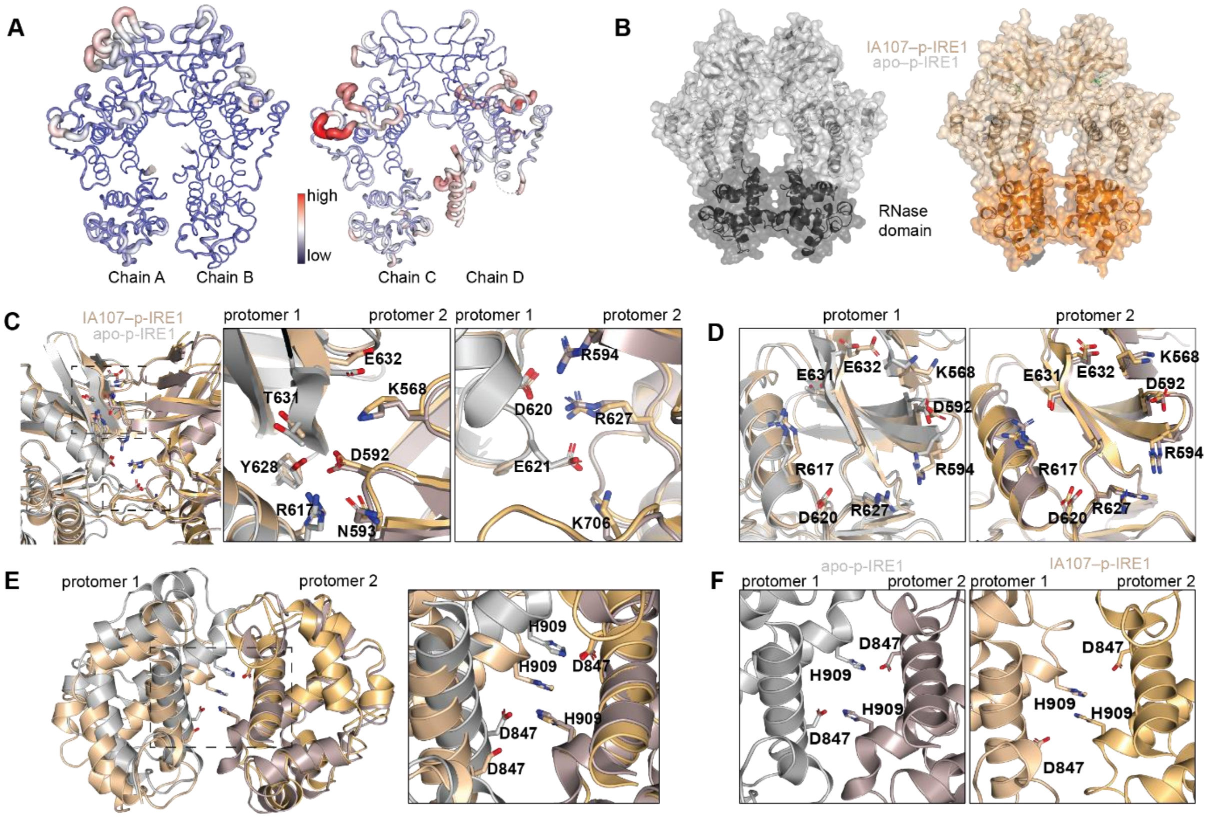

Figure 27. IA107-bound p-IRE1α dimer interfaces. (A). The B factors of the dimers formed by chain A and chain B and chain C with symmetry mate chain D. (B). Surface views of the back-to-back dimers of the apo-form p-IRE1α (grey) and the IA107–p-IRE1α (wheat). (C). Superimposition views of the key interactions at the kinase domain dimer interface. (D). Conformation of interacting residues of each protomer. (E). Bottom-up views of RNase domain overlay and an enlarged view showing the key interaction residues D847 and H909. (F). RNase domain interacting residues of apo-form p-IRE1α (grey) and the IA107–p-IRE1α (wheat).

It is assumed that the key interactions between two kinase domain protomers of IA107-bound p-IRE1α would be sufficient to sustain the formation of the back-to-back dimers. To validate our hypothesis, the dimerization and oligomerization of p-IRE1α were evaluated through DSS cross-linking assays. The reported p-IRE1α inhibitors compound G1749 and KIRA8[126], which inhibit p-IRE1α dimerization, were used as reference compounds (Figure 24C, 27A). First, the DSS cross-linking was coupled with mass photometry measurements to evaluate the assemblies of p-IRE1α. The result showed that different from KIRA8 and G1749, which disrupted the dimerization and oligomerization of p-IRE1α, compound IA107 did not inhibit the assembly of p-IRE1α (Figure 28B, 28C). P-IRE1α retained its ability to dimerize and oligomerize under 100 μM IA107 treatment, and the percentages of dimerized and oligomerized protein population are comparable to those of the DMSO control. The DSS cross-linking assay was performed with SDS-PAGE gel analysis to validate the observation, which gave a consistent result that KIRA8 inhibited the p-IRE1α assembly, whereas IA107 did not (Figure 28D).

In conclusion, the indole-containing compound IA107 binds to the kinase ATP-binding pocket of p-IRE1α, pushing the αC-helix out while the K599-E612 salt bridge is intact. The kinase domain of the two protomers interacted with each other and maintained the back-to-back dimeric conformation upon IA107 binding. Although the dimeric and oligomeric assemblies of p-IRE1α were not disrupted, the protomers were more separated at the RNase domains, which led to the displacement of key catalytic residues and resulted in the inhibition of the RNase activity (Figure 28E).

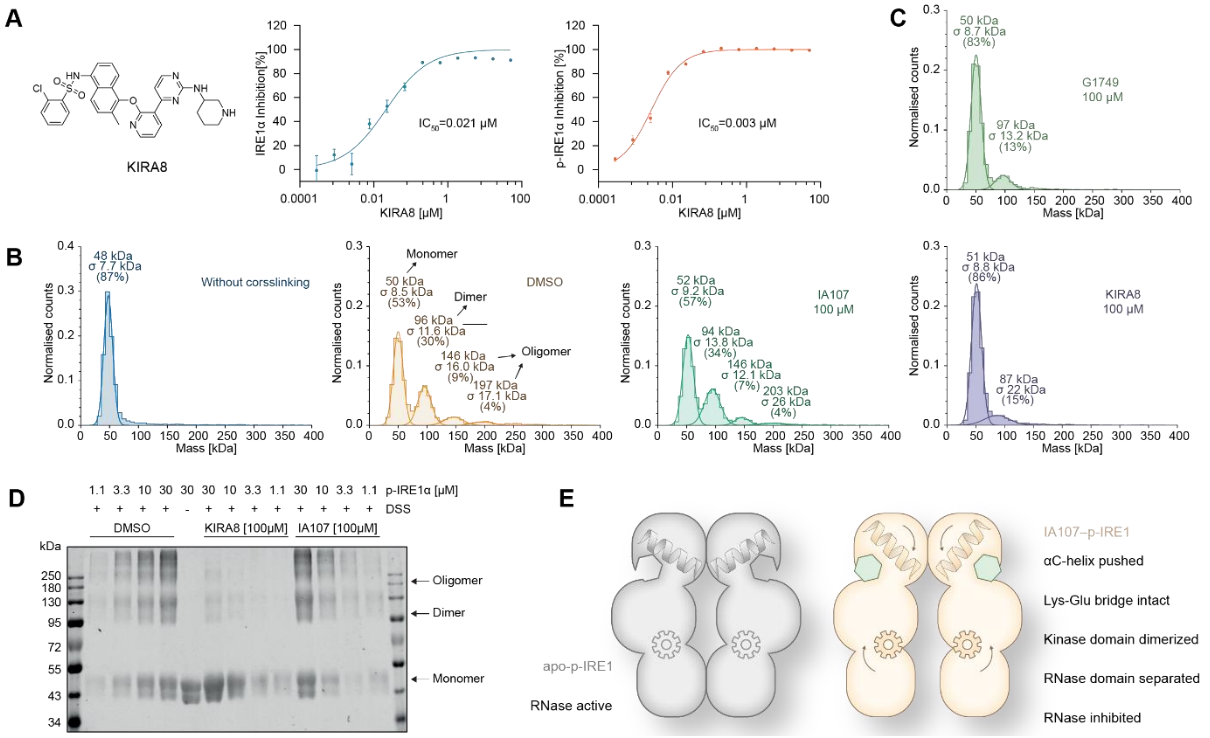

Figure 28. IA107 does not impact the assembly of p-IRE1α. (A). Structure and in-house tested activity of KIRA8 in FRET cleavage assay. (B), (C). Mass photometry measurement of p-IRE1α dimerization and oligomerization. (D). Measurement of p-IRE1α dimerization and oligomerization by SDS-PAGE. (E). Summary of the IA107 inhibition mechanism in comparison with that of apo-p-IRE1α.

The activity of IA107 against IRE1α was evaluated and compared using different RNA substrates. In addition to *XBP1*, a dual-labeled *BLOC1S1* RNA hairpin (FAM-BLOC1S1-BHQ) was evaluated in the FRET-based cleavage as the RIDD substrate. The FRET-based cleavage assays using two different RNA substrates demonstrated that p-IRE1α was highly effective in the *BLOC1S1* RNA splicing (RIDD target), exhibiting a comparable activity with the XBP1-hp1 sequence (Figure 29A, 29B). IA107 and the reported inhibitors KIRA8 and G1749 exhibited inhibitory activity against the IRE1α-mediated cleavage of RIDD substrate *BLOC1S1* in both the FRET-based and gel-based cleavage assays (Figure 29C, 29D). IA107 showed an

IC_{50} of 63 nM against *BLOC1S1* cleavage in the FRET assay. Though the activity is slightly decreased compared to the substrate with the *XBP1* sequence, it was still in a reasonable range.

The activity of the inhibitors against the microRNA 17 precursor hairpin RNA substrate was also evaluated[193]. However, the results showed that IA107 lost its inhibitory activity when using the microRNA 17 precursor hairpin RNA as p-IRE1α substrate (Figure 29E). In contrast, compound KIRA8 inhibited the cleavage activity, and compound G1749 exhibited partial inhibition of cleavage activity. We assumed that microRNA17 could be classified as the "RIDDLE" (regulated IRE1-dependent decay lacking endomotif)[25] targets of IRE1α. For the RIDDLE activity of IRE1α, the cleaving RNA substrates are less restricted but in favor of GC, and the activity strictly requires the phospho-oligomerization of IRE1α[25]. Since IA107 did not inhibit the oligomerization of p-IRE1α, it is predictable that it would not block this "RIDDLE" activity. Conversely, KIRA8 inhibited the dimerization and oligomerization of IRE1α, and will therefore inhibit the activity. G1749 is a unique compound that activates dephosphorylated IRE1α but inhibits phosphorylated IRE1, and such unique activity and mechanism of G1749 may contribute to the partial inhibition. It might also be due to that p-IRE1α protein has some dephosphorylated protein leftover from purification and causes this partial inhibition by G1749. It is assumed that the appropriate dimerization of the RNase domain is crucial for forming the pocket that can effectively recognize and cleave specific sequences like *XBP1* RNA and the RIDD RNA targets. IA107 inhibited the proper formation of this cleaving pocket, leading to the inhibition of cleaving those targets. Moreover, the "RIDDLE" effect of p-IRE1α, which requires the oligomerization of IRE1α, cannot be inhibited by IA107, suggesting that such low-specific and inefficient activity doesn't need a specific cleaving pocket to be formed.

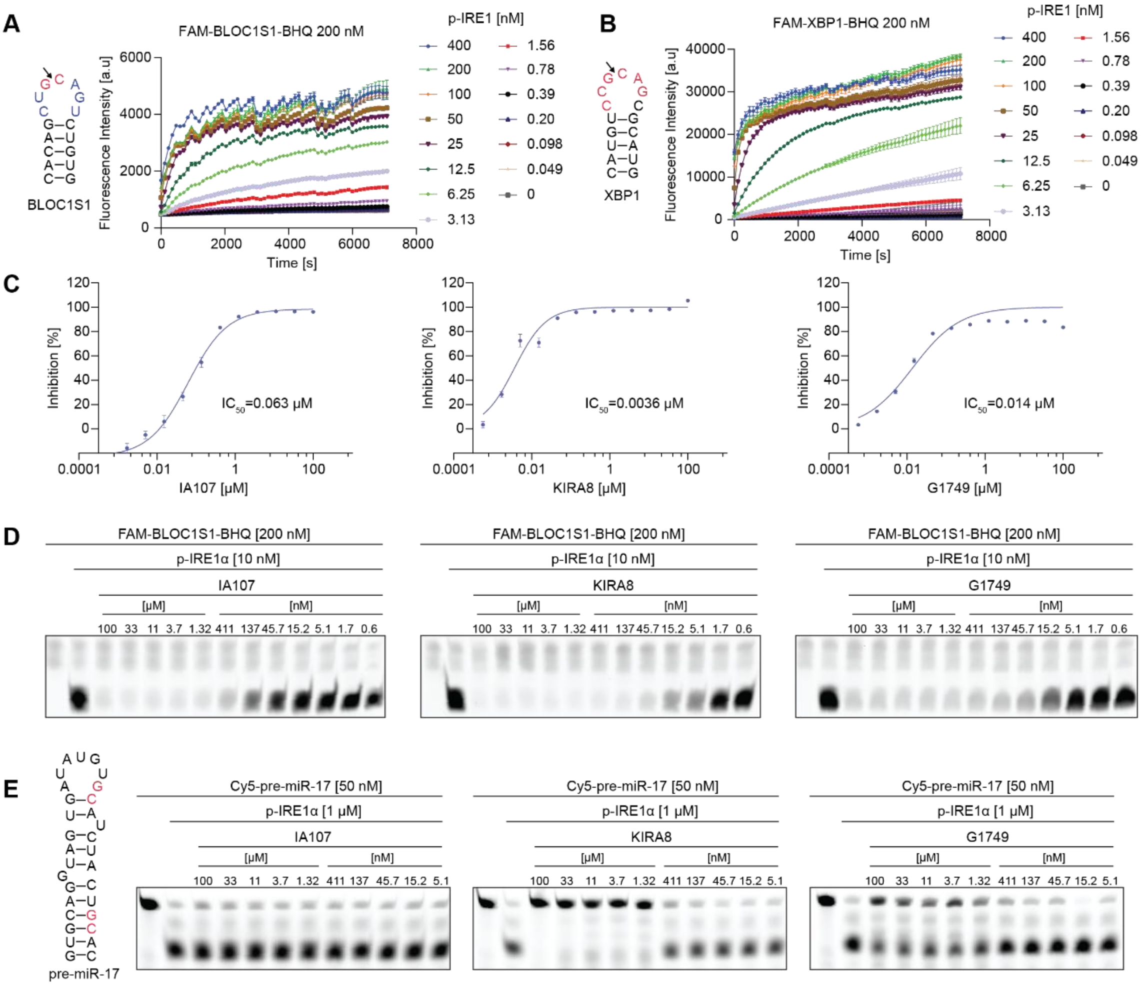

Figure 29. IA107 activity against different IRE1α substrates. (A). FRET-based assay titration of p-IRE1α using 200 nM FAM-BLOC1S1-BHQ RNA. (B). FRET-based assay titration of p-IRE1α using 200 nM FAM-XBP1-BHQ RNA. (C). FRET-based cleavage assay using 200 nM FAM-BLOC1S1-BHQ and 10 nM p-IRE1α protein. (D). Gel-based *BLOC1S1* cleavage assay, performed by loading the samples after the 30 min FRET measurement onto a 15% urea-PAGE gel. (E). Gel-based pre-miR 17 cleavage assays, the compounds were incubated with p-IRE1α protein for 30 min, then the Cy5 labeled pre-miR-17 RNA was added and incubated for 20 h at room temperature, then analyzed by a 15% urea-PAGE.

2.1.7 Kinase profiling of IA107

The kinase ATP-binding pocket of human kinases is highly conserved due to its role in ATP binding, making it challenging to develop selective kinase inhibitors[194]. To evaluate the selectivity of IA107, a kinase profiling against 90 selected human kinases was performed. As shown in the kinome phylogenetic tree (Figure 30A), IA107 presented a minimal to low effect (< 30% inhibition) against the tested kinases at 5 µM. In addition to IRE1α, IA107 showed an inhibitory effect against IRE1β with an IC_{50} of 144 nM in the LanthaScreenTM Eu kinase binding assay (Figure 30B). The 2-fold selectivity over IREβ is not surprising, since the kinase domain of IREβ and IRE1α shares 80% sequence similarity. Besides IRE1α and IRE1β, only TGFBR1 was inhibited by IA107 with a higher than 50% inhibition (54%) (Figure 30A).

To gain insights into the chemical features of IA107 that are relevant to its selectivity, sequence alignments and structure alignments of IRE1α, IREβ, TGFBR1, and EGFR (on which IA107 is not active, < 30% inhibition at 5 µM) kinase domains were performed. The sequence and structure of the IREβ kinase domain (the structure was predicted by Alphafold) are highly identical to those of IRE1α (Figure 30C, 30D). Notably, the key residues that form hydrogen bonds with IA107 are conserved and positioned similarly (Figure 30C), allowing IA107 to bind to the ATP-binding pocket of IRE1β and further inhibit its activity. For TGFBR1, the kinase domain structure is slightly different compared to IRE1α (Figure 30D). Though the interacting residue cystine (C645 of IER1α) is replaced by a glutamic acid in TGFBR1, the interacting lysine and aspartic acid residues are in place to interact with IA107 (Figure 30C), which might explain the decreased binding affinity of IA107 towards TGFBR1. EGFR with an extended αC-helix formed a kinase ATP-binding pocket that differs from IRE1α (Figure 30F). Although the conserved aspartic acid (D711 in IRE1α) remains, the lack of interacting lysine and cystine residues in EGFR prevented IA107 from binding (Figure 30C).

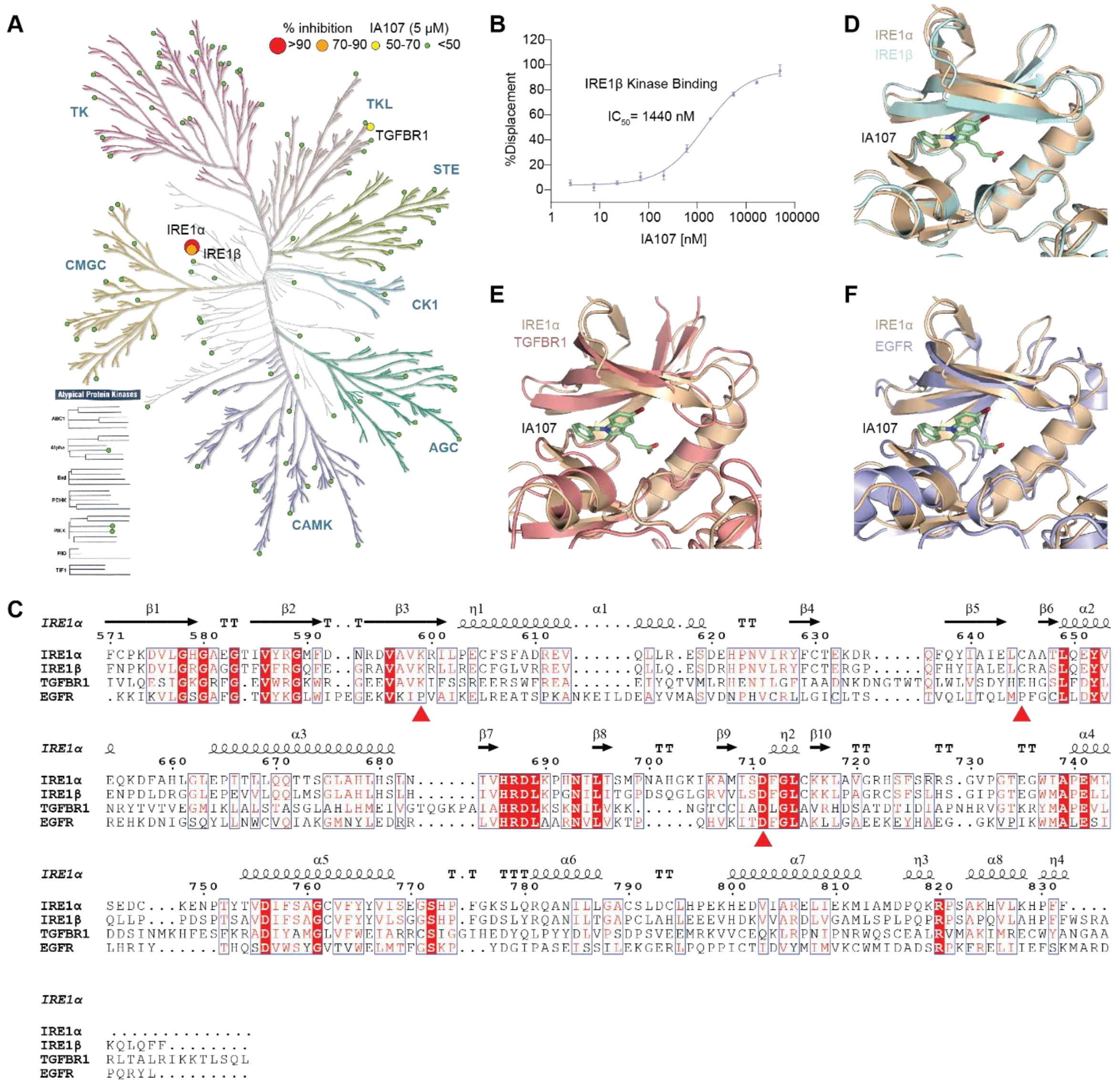

Figure 30. IA107 selectivity over other human kinases. (A). Kinome phylogenetic tree of IA107 kinase profiling at a concentration of 5 μM. (B). IA107 bound to the IRE1β kinase domain with an IC_{50} of 1440 nM in the LanthaScreenTM Eu kinase binding assay (Thermo Fisher SelectScreen). (C). sequence alignment of IRE1α, IRE1β, TGFBR1 and EGFR. (D). Structure alignment of the kinase domains of IRE1α (wheat, PDB 9gow) and IRE1β (cyan, AF-Q76MJ5-F1). (E). Structure alignment of the kinase domains of IRE1α (wheat, PDB 9gow) and TGFBR1 (pink, PDB 5e8s). (F). Structure alignment of the kinase domains of IRE1α (wheat, PDB 9gow) and EGFR (light blue, PDB 8a27).

2.1.8 Cellular activity of IA107 and a prodrug strategy

ER stress activates IRE1α and further induces *XBP1* mRNA splicing[22]. To evaluate the downstream effects of IA107 treatment, ER stress-induced *XBP1* splicing was evaluated via qPCR. The A549 cells were pre-treated with IA107 for 2h, then the ER stress was induced by tunicamycin treatment for 2h. Then an RT-qPCR experiment was performed to evaluate the spliced *XBP1* mRNA level (Figure 31A). The data showed that tunicamycin induces XPB1 mRNA splicing, and the pretreatment of IA107 inhibits the splicing in a dose-dependent manner. A protein thermal stability assay was performed to see the binding interaction between IA107 and wild-type protein using A549 cell lysate (Figure 31B). The result indicated that compound IA107 can concentration-dependently stabilize IRE1α wild-type protein in cell lysate, indicating the binding ability of IA107 to the full-length IRE1α protein. A decreased activity was observed in the *XBP1* mRNA splicing qPCR assay compared with the data from *in vitro* assays.The possible reason could be that the propanoic acid of IA107 limited its cell membrane permeability [195]. However, the structural modification data and the binding interaction indicate that this propanoic acid is crucial for the activity. To overcome the poor permeability and keep the crucial function of the carboxylic acid, an ester-based prodrug IAPD1 was designed and synthesized to improve the cellular uptake (Figure 31C).

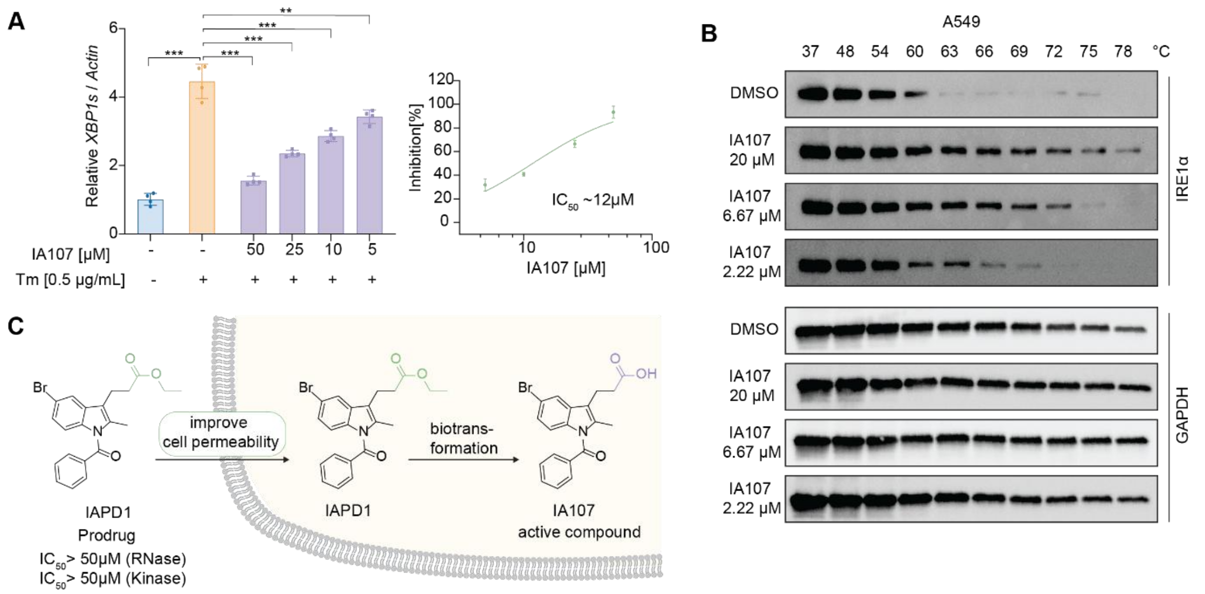

Figure 31. IA107 inhibits ER stress-induced *XBP1* mRNA splicing and target engagement. (A). IA107 inhibited ER stress-induced *XBP1* splicing in a dose-dependent manner in A549 cells. The cells were pre-treated with IA107 for 2 h and co-treated with tunicamycin (Tm) for 2 h to induce ER stress. The results were analyzed using one-tailed independent Student's t-test, ** $p < 0.01$, *** $p < 0.001$. (B). IA107 stabilized the wild-type IRE1α dose-dependently in A549 cell lysate. (C). Illustration of the ester pro-drug strategy to improve cell permeability.

IAPD1 was synthesized and evaluated using *in vitro* assays. As expected, IAPD1 with an ester substitute did not show any activity against IRE1α or p-IRE1α in the FRET-based *XBP1* cleavage assay (Figure 32A). IAPD1 did not show kinase binding activity against IRE1α in the LanthaScreen kinase binding assay (Figure 32B). The activity loss of IAPD1 is due to the substitution of the critical propanoic acid group of IA107. However, upon the treatment of

IAPD1 in cells, the inactive prodrug can be transformed into an active form. The qPCR result demonstrated that the treatment of IAPD1 in A549 cells inhibited the ER stress-induced *XBP1* mRNA splicing in a dose-dependent manner (Figure 32C), with an IC_{50} value of 180 nM. At the same time, the IRE1α transcription was not affected (Figure 32D). The consistent results were also observed in HCT116 and HT29 cell lines (Figure 32E-H), IAPD1 inhibited ER stress-induced *XBP1* mRNA splicing with IC_{50} values of 0.22 μM and 0.16 μM in HCT116 and HT29 cells, respectively.

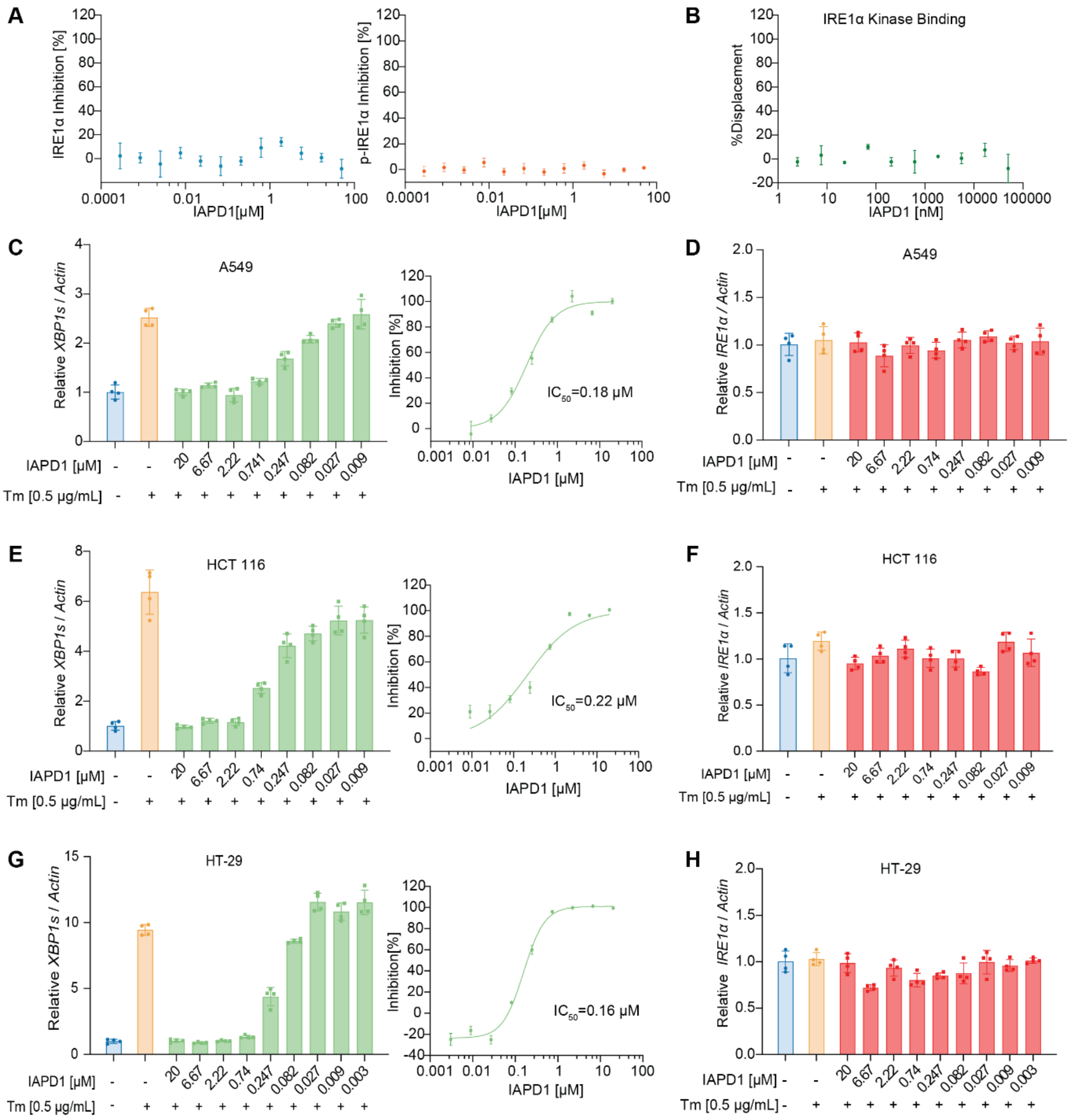

Figure 32. Prodrug IAPD1 inhibits *XBP1* mRNA splicing with improved activity. (A). The activities of IAPD1 against IRE1α and p-IRE1α, measured by FRET-based cleavage assay. (B). The activity of IAPD1 against IRE1α kinase binding. measured by LanthaScreen kinase binding assay. (C). IAPD1 showed potent inhibition of ER stress-induced *XBP1* splicing in A549 cells, with an IC_{50} of 0.18 μM. (D). IRE1α transcription level was not significantly impacted by the treatment of IAPD1 in A549 cells. (E). IAPD1 inhibited ER stress-induced *XBP1*

splicing in HCT116 cells with an IC_{50} of 0.22 μM. (F). IRE1α transcription level was not significantly impacted by the IAPD1 treatment in HCT116 cells. (G). IAPD1 inhibited ER stress-induced *XBP1* splicing in HT29 cells, with an IC_{50} of 0.16 μM. (H). IRE1α transcription level was not significantly impacted by the IAPD1 treatment in HT29 cells.

In addition to assessing the transcription level of *XBP1s* mRNA, the expression level of XBP1s protein was also evaluated in A549 cells and MDA-MB-231 cells using western blot analysis to gain a more comprehensive understanding of the downstream effects of IAPD1(Figure 33A, 33B). The western blot analysis revealed that IAPD1 treatment dose-dependently inhibited XBP1s protein expression induced by ER stress, which validated the activity of IAPD1 in IRE1α downstream pathways.

To evaluate the target engagement of IAPD1 in A549 cells, a cellular thermal shift assay was performed (Figure 33C). The result indicated that compared to the DMSO control, the treatment of IAPD1 under different concentrations stabilized IRE1α protein in cells dose-dependently, whereas it did not impact the thermal stability of the housekeeping protein GAPDH, validating the target engagement of IAPD1 in cells. Additionally, the cytotoxicity of the most potent compound IA107 and the prodrug IAPD1 was evaluated in A549, HCT116, MDA-MB-468, and HT29 cells through an antiproliferation assay (Figure 33D). IA107 and IAPD1 show very minimal antiproliferation ability against all four tested cell lines, with the inhibition percentage less than 30% under the highest concentration of 50 μM, which suggests that compounds IA107 and IAPD1 are not cytotoxic.

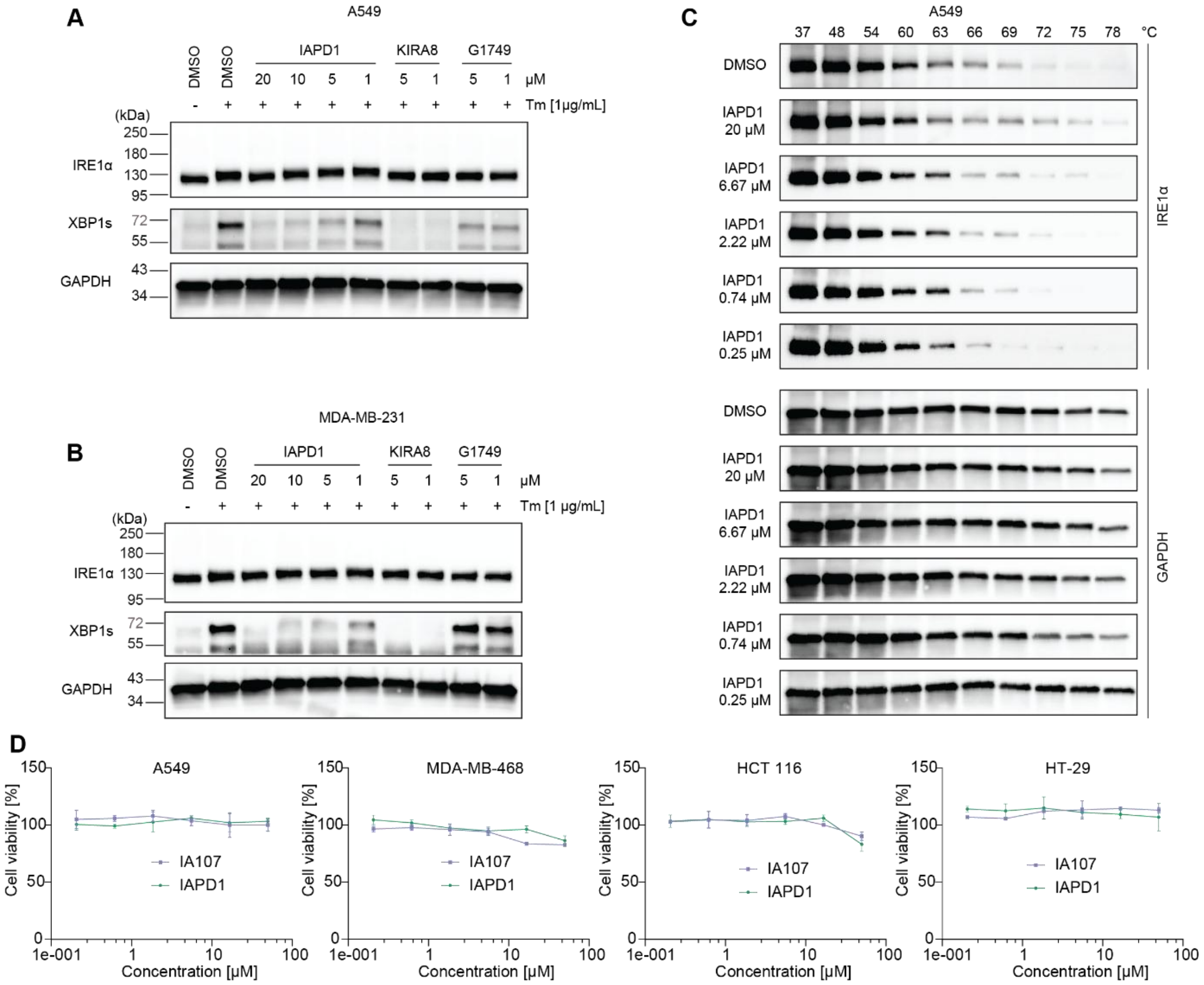

Figure 33. IAPD1 inhibits ER stress-induced XBP1 protein expression without cytotoxicity. (A)., (B). IAPD1 dose-dependently inhibited ER stress-induced XBP1 protein expression in A549 cells and MDA-MB-231 cells. (C). IAPD1 target engagement validation in A549 cells via cellular thermal shift assay. (D). IAPD1 and IA107 are not cell cytotoxic in the tested A549, MDA-MB-468, HCT116, and HT29 cells.

2.1.9 Conclusion

IRE1α is a crucial sensor for mediating the endoplasmic reticulum (ER) stress. Located in the ER lumen, IRE1α possesses dual kinase and ribonuclease functions. When ER stress occurs, the chaperone Bip will dissociate from IRE1α's luminal domain and trigger the cytosolic kinase and RNase domains dimerization and autophosphorylation[196], activate IRE1α to induce X-box binding protein 1 (*XBP1*) mRNA splicing and mediate downstream unfolded protein response signaling pathways. IRE1α dysregulation has been connected to various human diseases, highlighting the potential of small molecules targeting IRE1α for related disease therapy.

In this study, a new IRE1α inhibiting chemotype with an indole scaffold was identified through chemical library screening. Chemical modification effort was started from the hit compound IA01, which exhibited an IC_{50} value of 300 nM against both dephosphorylated and phosphorylated IRE1α. Elaborated SAR studies were performed to obtain a series of more potent compounds. The most potent inhibitor compound IA107 showed potent activity and excellent selectivity, with IC_{50} values of 16 nM and 9 nM against dephosphorylated and phosphorylated IRE1α, respectively. IA107 binds to the kinase ATP-binding pocket of IRE1α with a kinase inhibition IC_{50} value of 768 nM. The affinity of IA107 to IRE1α was measured by ITC assay and MST assay. A K_D of 0.94 μM was obtained through ITC measurement, which is consistent with the result from the MST assay (K_D =1.36 μM). The crystal structure of p-IRE1α in complex with IA107 revealed the inhibitory mechanism of IA107, which binds to the kinase domain and allosterically inhibits the RNase activity. Unlike other reported kinase-inhibiting RNase attenuators (KIRA), IA107 binding did not inhibit the dimerization and oligomerization of p-IRE1α. On the contrary, IA107 binds to the kinase domain with a unique conformation that pushes the α-C helix out without disrupting the Lys–Glu bridge. The binding of IA107 did not disturb the kinase domain dimer interactions but separated the RNase domain dimer interface, therefore displacing the RNase catalytic pocket of IRE1α, and lead to the inhibition of enzymatic activity. The cellular evaluation demonstrated that IA107 inhibited ER stress-induced *XBP1* mRNA splicing in A549 cells. The CETSA experiments validated the binding interaction of IA107 to the wild-type IRE1α protein *in cellulo*. However, a decreased activity of inhibiting the *XBP1* splicing was observed which might be due to the poor cell permeability caused by the carboxyl group of IA107. An ester-containing prodrug IAPD1 was designed and evaluated, with an increased activity of ~50-fold in A549 cells. IAPD1 potently inhibited *XBP1* mRNA splicing in all tested cell lines, and the downstream XBP1s protein expression induced by ER stress was inhibited by the treatment of IAPD1 as well. CETSA experiment showed that IAPD1 dose-dependently stabilized IRE1α protein in cells which confirmed the target engagement of IRE1α by IAPD1. IAPD1 presented no cytotoxicity against a panel of cancer cell lines, which suggested it can be used for studying other non-oncological diseases, such as pain and metabolic diseases.

In summary, a new chemotype of IRE1α inhibitor, IA107, with the indole scaffold, was discovered. IA107 binds to the kinase domain of IRE1α with potent selectivity over a wide range of human kinases and exhibits excellent potency against IRE1α RNase activity. This compound can be further used as a powerful chemical tool to study IRE1α function, as well as a novel chemical entity for potential therapeutic applications.

2.1.10 Discussion and Perspectives

The IRE1α inhibiting small molecules harbor great potential for related disease therapy, while one inhibitor is in clinical trial for cancer therapy. Novel IRE1α inhibitors with diverse structures and biological activities could provide alternative options for the treatment of diseases related to different pathways of IRE1α downstream.

Indole, as a privileged heterocyclic scaffold in drug discovery, has been applied to target various diseases such as inflammation (indomethacin), cancer (sunitinib), neurological disorders (sumatriptan), and viral infection (umifenovir) in the drug market. The unique biological characteristics of indole make it a favorable moiety to be included in many bioactive compounds that target various biological targets[197].

In this study, a novel class of IRE1α inhibitors bearing an indole core scaffold that are structurally distinct from previously reported inhibitors were discovered and optimized. Through the identification of hit compound and systematic SAR studies, 64 indole analogues with structural modifications performed at different positions were obtained. The most potent compound IA107 showed nanomolar IC_{50} potency and great selectivity against the tested human kinases. The biophysical measurements showed IA107 has a single-digit binding affinity K_D against IRE1α, and a ~10-fold higher affinity towards p-IRE1α. IA107 may prefer to bind the active dimeric protein states, and p-IRE1α forms a lot more dimers compared to dephosphorylated IRE1α[126]. Hence, the affinity of IA107 against p-IRE1α is stronger than the affinity of IA107 against IRE1α. This also contributed to the discrepancy observed between the enzymatic inhibition IC_{50} and binding affinity K_D against IRE1α. It was reported that only a small portion of IRE1α forms the RNase active dimers[188]. IA107 preferably binds to the active dimers, leading to inhibition of the RNase activity of IRE1α.

Biochemical evaluations, including a kinetic evaluation, indicated that IA107 binds to the kinase domain of IRE1α, thereby allosterically inhibiting the RNase activity. The co-crystal structure of IRE1α in complex with IA107 confirmed this allosteric inhibition mechanism. Binding of IA107 to the kinase domain of IRE1α induced conformational changes that displaced the RNase catalytic residue, leading to the inhibition of IRE1α RNase activity.

Most of the reported IRE1α kinase domain binding RNase inhibitors inhibit the RNase activity by separating the IRE1α dimer, and then prohibit the RNase active site formation[130, 136, 198]. However, IA107 does not inhibit IRE1α dimerization. Both the co-crystal structure and the crosslinking experiment showed that p-IRE1α dimerization was not affected upon IA107 binding. The IA107-bound p-IRE1α structure presented a more separated RNase domain with displaced RNase catalytic residues. Although the RNase domain is more separated, the dimeric interaction remains. It is speculated that the dimeric interaction might be attributed to the kinase domain interaction. Upon IA107 binding, the kinase domain dimer interface was not impacted much as slight residue shifts were observed. The kinase domain interface may contribute more to the dimer formation compared to the RNase domain interface, since previous studies demonstrated the phosphorylation of the activation loop in the kinase domain greatly promotes the dimerization of IREα[25, 126, 188, 190]. Though the separation of the RNase dimer interface disrupted the interaction between the two protomers and displaced the key catalytic residues, some new interactions were formed with the displaced residues, which maintained the overall dimeric form of p-IRE1α. The property of IA107 that does not disrupt the dimer formation may pave the way for selectively inhibiting one IRE1α downstream pathway over other related pathways. IA107 was assumed not to block the "RIDDLE" pathway of which requires the oligomerization of IRE1α[25], since *in vitro* cleavage assay showed IA107 does not inhibit the cleavage of miR-17. However, more cellular evaluations against this pathway are required to confirm the hypothesis.

Cellular evaluations indicated that IA inhibitors interfered with IRE1α pathways. An ester-containing prodrug was used to improve the cellular uptake to boost the cellular effects. In this study, only the ester-based prodrug was evaluated. Other prodrugs with additional chemical modalities may offer new perspectives to improve cellular activity and selectivity[199]. Notably, the XBP1-related downstreams of IRE1α were evaluated, further evaluations on other IRE1α-related pathways would provide a full landscape of the impact of IRE1α inhibition in cells.

Apart from direct inhibition, new modulation modalities provide novel therapeutic options for disease-related targets, among which the proximity-inducing chimeras are emerging as a promising strategy. The indole-based inhibitors can be used as IRE1α ligands to design bifunctional molecules. Assisted by the complex co-crystal structure, the exit vectors and linkerology can be rationally proposed for such chimeric compounds. One of the options is to design PROTACs to degrade IRE1α to potently block IRE1α-related pathways. By linking the IRE1α ligand with an E3 ligase ligand through a variety of linkers, a series of selective degraders targeting IRE1α can be designed and synthesized. Such IRE1-targeting PROTACs have been reported using the IRE1α RNase domain covalent inhibitor and CRBN ligand[200]. However, the potency and efficacy still need to be improved to degrade the target protein more efficiently. Notably, the IRE1α PROTACs using kinase domain binders or reversible binders are yet to be discovered. Since IRE1α is a ribonuclease, the IRE1α ligand can be used to design ribonuclease targeting chimeras (RIBOTAC) to degrade disease-related RNAs. As the majority of the human genome is not translated to protein[201], targeting RNA directly could provide more options for drug targets. Furthermore, targeting RNA offers a new approach to undruggable protein targets, of which druggable pockets might be difficult to find. To date, most of the previously reported RIBOTACs utilize RNase L-binding ligands[202-204], The limited chemotypes of RNase binders constrained the design of RIBOTACs. Since the various types of IRE1α binders have been reported and validated, IRE1α could be an alternative ribonuclease for IRE1α-mediated RNA degradation, with a dedicated range of RNA substrates[25]. It is foreseeable that IRE1α binders with weak RNase inhibition activity or RNase activating activity could be used to design such chimeric compounds for RNA degradation.

2.2 Aminothiazolone inhibitors disrupt protein–RNA interaction of METTL16 and inhibit m⁶A RNA modification

Parts of the methods described in this section were published in Liu, Y.$^{\#}$; Goebel, G. L.$^{\#}$; Kanis, L.; Hastürk, O.; Kemker, C.; Wu, P., Aminothiazolone Inhibitors Disrupt the Protein–RNA Interaction of METTL16 and Modulate the m6A RNA Modification. JACS Au, 2024, 4, 4, 1436–1449.*

2.2.1 METTL16 protein purification and screening assay establishment

To establish the screening assay for METTL16, a recombinant human METTL16 protein was expressed and purified. The protein contains the methyltransferase domain (MTD) of METTL16, with the sequence ranging from methionine M1 to aspartic acid D291 (Figure 34A-34C). To establish the screening assay, a FAM-labelled MAT2A-hp1 was used. Once METTL16 binds to the FAM-labelled RNA to form a large complex, the complex will rotate more slowly and lead to a higher FP signal compared to the unbound RNA probe. When the inhibitor bound to METTL16 disrupts the protein-RNA interaction, the FP signal will decrease (Figure 34D, 34E). To determine the assay condition, FAM-labelled RNA concentration titration and METTL16 MTD protein concentration titration were performed (Figure 34F, 34G). FAM-labelled RNA concentration titration was performed with a fixed concentration of 1000 nM METTL16 MTD protein (Figure 34F). The result showed that the increased concentration of FAM-MAT2A-hp1 decreased the FP signal. Based on the result, a final concentration of 2 nM FAM-MAT2A-hp1 was chosen to achieve an optimal signal. The METTL16 MTD protein concentration titration was performed with a fixed 2 nM FAM-MAT2A-hp1. The result showed that the final concentration of 80 nM METTL16 MTD protein exhibited an 85% saturation of 2 nM FAM-MAT2A-hp1 with a good signal-to-background ratio. The FP measurements were performed under different incubation times of METTL16 MTD protein and the FAM-MAT2A-hp1 RNA (Figure 34H). Since the incubation time between 5 min and 90 min did not impact the FP signal significantly, the 5 min incubation time was used in the screening assay. The FP assay was performed using unlabeled MAT2A-hp1 as an inhibiting control (Figure 34I). The result indicated that the unlabeled MAT2A-hp1 dose-dependently disrupted the FP signal, with an IC_{50} value of 60.4 nM, which is consistent with the reported affinity of MAT2A-hp1 toward METTL16 MTD protein (K_D = 110 nM)[171]. A small set of experiments was performed to evaluate the Z'-factor. A Z'-factor of 0.91 was obtained, proving that the established FP assay is suitable for screening (Figure 34J).

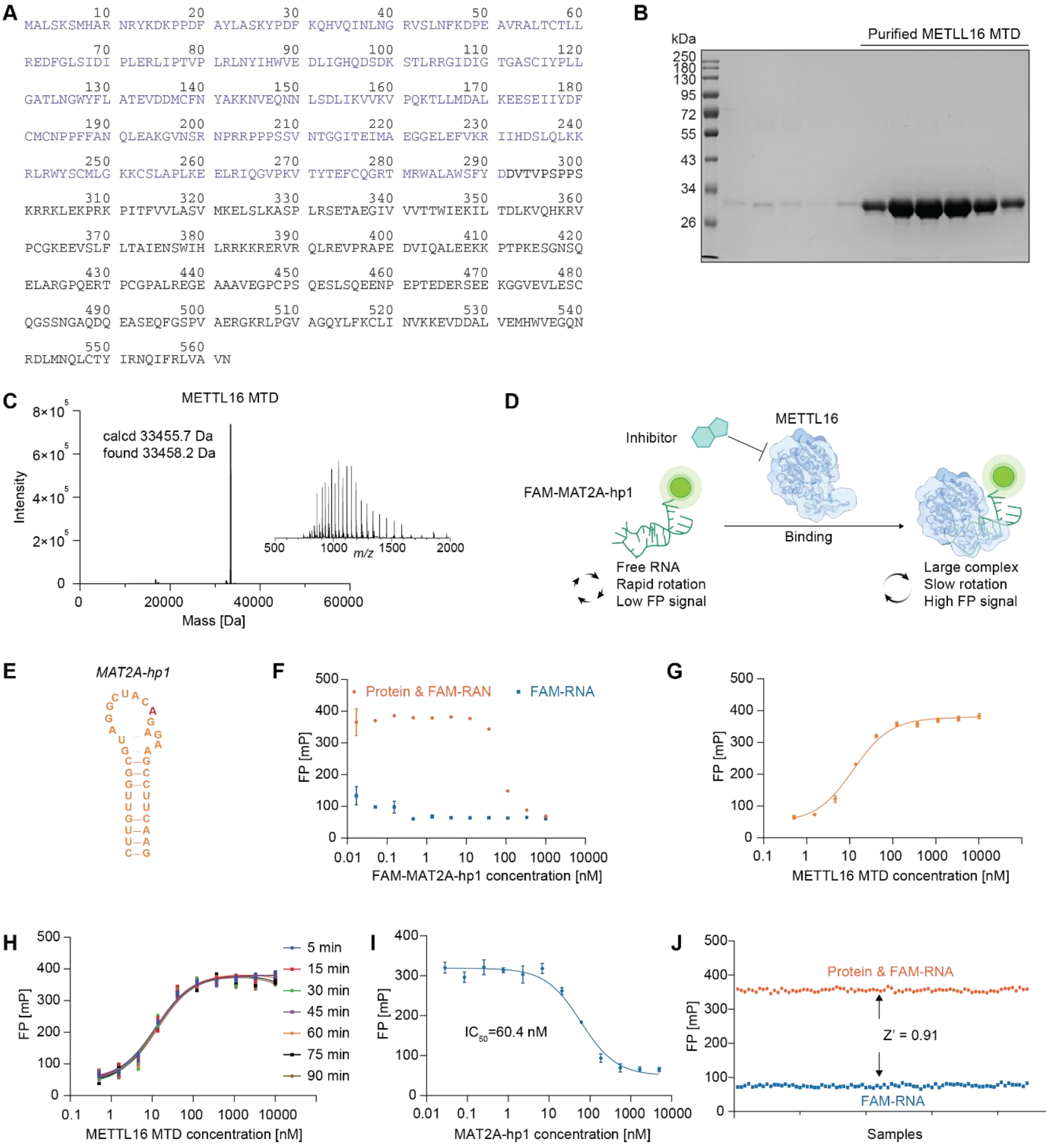

Figure 34. METTL16 protein purification and screening assay establishment. (A). The sequence of METTL16 protein, the MTD protein purified in this study is shown in purple. (B). SDS-PAGE result of purified METTL16 MTD protein. (C). LC-MS analysis of purified METTL16 MTD protein. Calculated mass: 33455.7 Da, found: 33458.2 Da. (D). Schematic illustration of the FP assay. The binding of FAM-labeled RNA to METTL16 formed a large complex and led to a high FP signal. When a small-molecule inhibitor disrupted the METTL16-RNA interaction, the FP signal decreased. (E). The sequence and secondary structure of the *MAT2A-hp1* RNA used in the FP assay. (F). FP signals of FAM-MAT2A-hp1 RNA concentration titration with a fixed concentration of 1000 nM METTL16. (G). FP signals of METTL16 MTD protein titration with a fixed concentration of 2 nM FAM-MAT2A-hp1. (H). FP signals of METTL16 MTD protein titration with a fixed concentration of 2 nM FAM-MAT2A-hp1 under different incubation times ranging between 5 min and 90 min. (I). FP experiment with unlabeled MAT2A-hp1 RNA, which showed an IC_{50} value of 60.4 nM. (J). A small set of experiments gave the FP screening assay a Z-factor of 0.91.

2.2.2 METTL16 inhibitory hit identification

To identify small-molecule METTL16 inhibitors, an in-house chemical library obtained from COMAS which contains 25344 small molecules, was screened using the aforementioned FP assay (Figure 35A). Compound **1**, featuring an aminothiazolone scaffold was identified as a METTL16 inhibitor (Figure 35B), with an IC_{50} of 16.3 μM tested by FP assay using the final concentrations of 50 nM METTL16 MTD protein and 5 nM FAM-MAT2A-hp1 (Figure 35C). To validate the activity of compound **1**, an orthogonal electrophoretic mobility shift assay (EMSA) was performed using the final concentrations of 50 nM METTL16 MTD protein and 5 nM FAM-MAT2A-hp1. (Figure 35D). The EMSA result showed that compound **1** inhibited METTL16-RNA complex formation in a dose-dependent manner, confirming the activity of compound **1**.

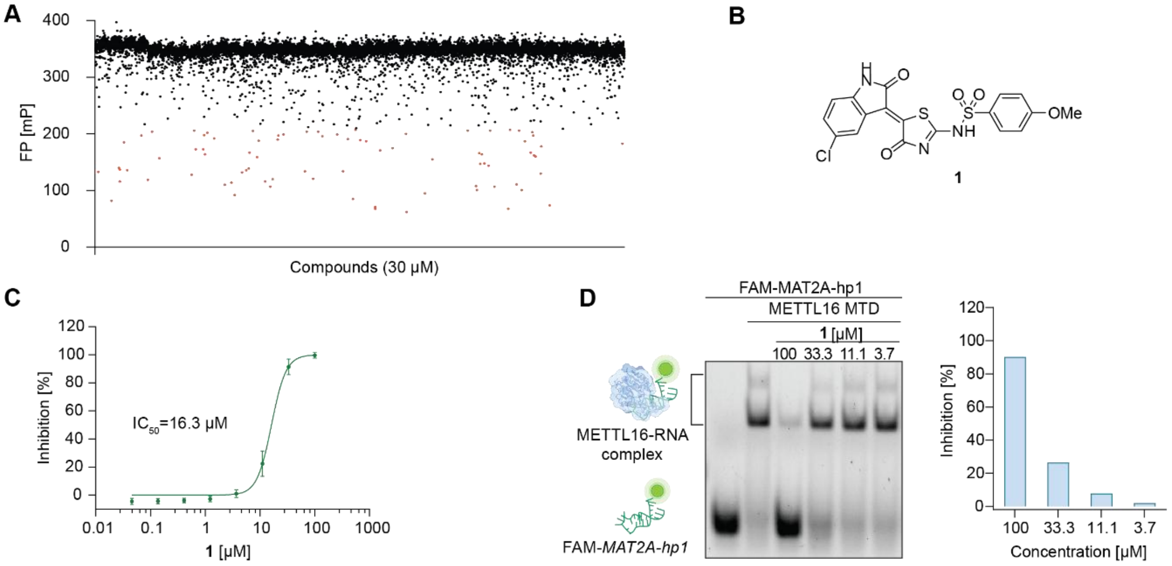

Figure 35. Identification of METTL16 inhibitory hit compound 1. (A). Compound library screening using FP assay. (B). The structure of the aminothiazolone hit compound **1**. (C). **1** dose-dependently disrupted METTL16-MAT2A-hp1 interaction in FP-based assay. (D). Orthogonal assay EMSA showed that **1** inhibited METTL16-RNA interaction in a dose-dependent manner.

2.2.3 Structural optimization yields more potent compounds

Structural optimization based on hit compound **1** was carried out to improve the inhibition potency. Modifications on the oxindole (R^1) moiety, sulfonamide (R^2) moiety as well as on the core thiazolone scaffold were performed (Figure 36). The modifications on R^1 group resulted in several compounds with single-digit micromole IC_{50} values (Figure 36A), including compounds **4**, **5**, and **9** with IC_{50} values of 8.2 μM, 6.8 μM, and 6.8 μM respectively (Figure S1). Modification on the R^2 group obtained compounds **27**, **28**, and **31** with IC_{50} values of 2.7

μM, 9.8 μM, and 9.9 μM, respectively, with improved potencies (Figure 36B, S1). However, when exchanging the thiazolone core scaffold with an oxazolone core (Figure 36C), the inhibitory activity was completely abolished, the corresponding compound **38** showed an IC_{50} higher 100 μM.

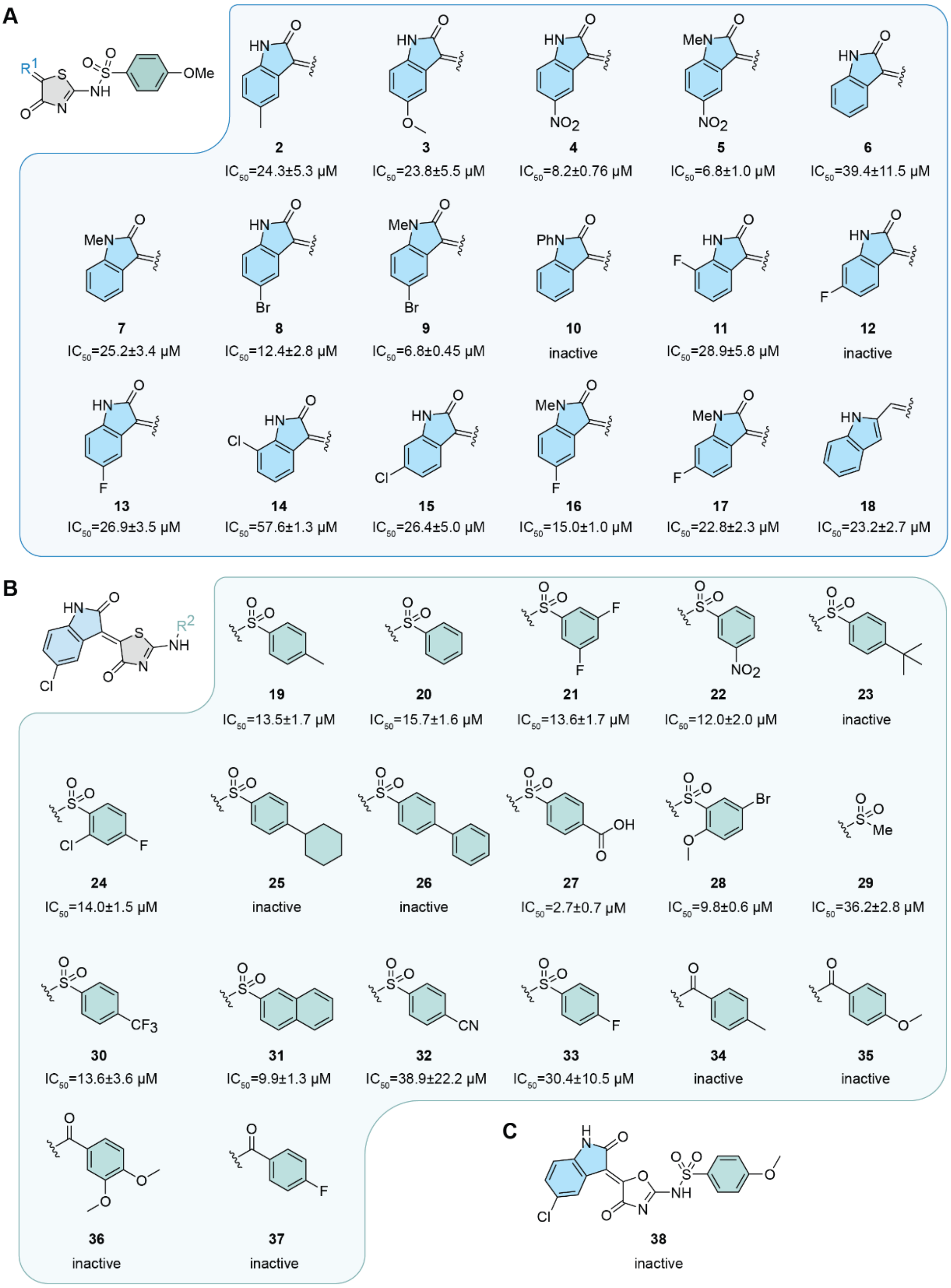

Figure 36. Structural modifications based on compound 1 yield more potent compounds. (A). Structural modifications on the R^1 oxindole groups and the activities measured by FP assay. (B). Structural modifications on

the R^2 sulfonamide moieties and the activities measured by FP assay. (C). The structure of inactive aminooxazolone analogue **38**.

To investigate the impact of the sulfonamide moiety, the aminothiazolone analogues **39**−**44** without the sulfonamide moiety were synthesized and evaluated (Figure 37A). Most compounds without the sulfonamide moiety lost the activity, except compound **42** which showed an IC_{50} of 26.9 µM (Figure 37B). **42** dose-dependently disrupted METTL16-RNA interaction in EMSA assay as well (Figure 37C). This result indicated that the sulfonamide moiety is favored in METTL16 inhibition.

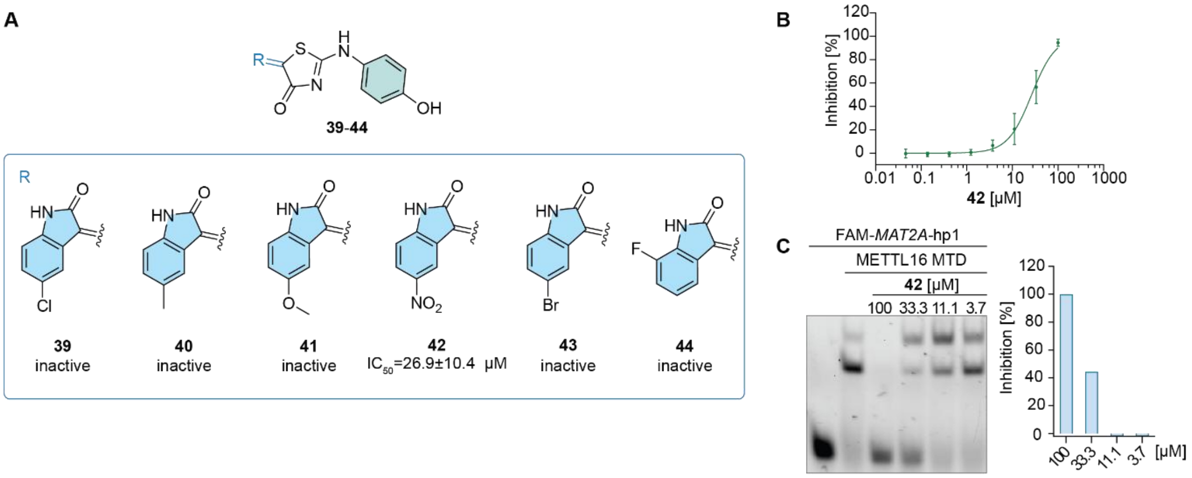

Figure 37. Sulfonamide moiety is important for inhibitory activity. (A). Structure of the aminothiazolone analogues **39**−**44** without a sulfonamide moiety. (B). FP assay result for compound **42**. C. EMSA result and the EMSA gel quantification of compound **42**.

Compound **27** is the most potent compound obtained from the first round of structural modification, with an IC_{50} value of 2.7 µM (Figure 38A, 38B). Meanwhile, compounds **5** and **9** also showed better potency, both possessing an IC_{50} value of 6.8 µM. Further modifications were performed by combining the structural features of these potent aminothiazole compounds **27**, **5**, and **9** to yield the aminothiazolone analogues **45-47** (Figure 38C). Compounds **45**, **46**, and **47** showed improved potency compared to compound **27**, with IC_{50} values of 1.6 µM, 2.0 µM, and 2.1 µM, respectively (Figure 38C, 38E). The impact of the carboxylic acid moiety was evaluated by synthesizing the methyl ester containing analogue **48**, and the analogue **49** bearing the carboxyl group in *meta*-position (Figure 38D, 38E). The activity of the ester-containing analogue **48** decreased 20-fold compared to compound **45**, but the activity of the *meta*-position carboxylic acid analogue **49** was retained, with an IC_{50} value of 3 µM.

Overall, SAR studies based on the aminothiazolone hit compound **1** resulted in a series of compounds with single-digit micromolar inhibitory potency against METTL16, among which compound **45** showed the best potency with an IC_{50} value of 1.7 µM.

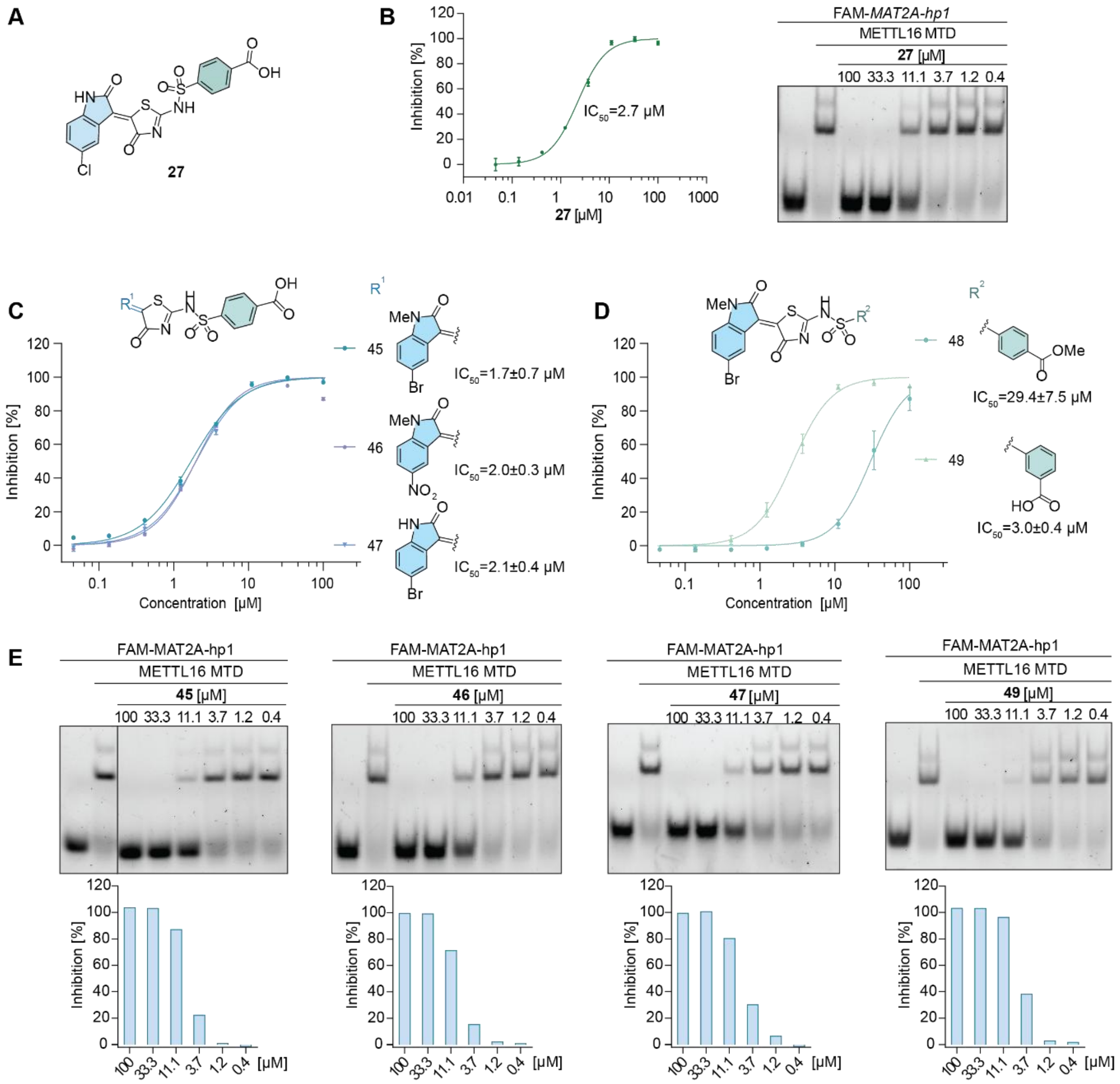

Figure 38. Further structural modifications. (A). Structure of compound **27**. (B). The activity of compound **27**. Measured by FP assay and EMSA assay. (C). Combination of the best-performed aminothiazolones resulted in compounds **45**-**47**. (D). Methyl ester containing analogue **48** and the *meta*-position carboxylic acid analogue **49**. (E). EMSA result and the EMSA gel quantification of compounds **45**, **46**, **47**, and **49**.

2.2.4 Aminothiazolones activity evaluations and binding mechanism studies

To evaluate the binding interaction of aminothiazolones to METTL16, the differential scanning fluorimetry (DSF) assay was performed. Compound **Ia,** which has no inhibitory activity against METTL16 was chosen as a negative reference compound for the assay (Figure 39A, S2). The four most active compounds **27**, **45**, **46**, and **47** were measured in DSF assay, the result indicated that compounds **27**, **45**, **46**, and **47** dose-dependently stabilized the thermal stability of METTL16 MTD (Figure 39B) with positive thermal shifts (ΔT_m). In contrast, the negative compound **Ia** did not show any detectable change in the thermal stability of METTL16 MTD protein (Figure 39B, 39C). The binding affinity of aminothiazolone compounds **45** and **47** were measured through switchSENSE biosensor, using a his-capture kit to immobilize his-tagged METTL16 MTD protein to the chip (Figure 39D). The biosensor results showed that compound **45** and compound **47** have affinity K_D values of 1.35 μM and 1.76 μM against METTL16, respectively, consistent with the inhibitory IC_{50} values measured by FP assay. The DSF assay and biosensor assay indicated that the aminothiazolone compounds disrupted METTL16-RNA interaction via METTL16 binding.

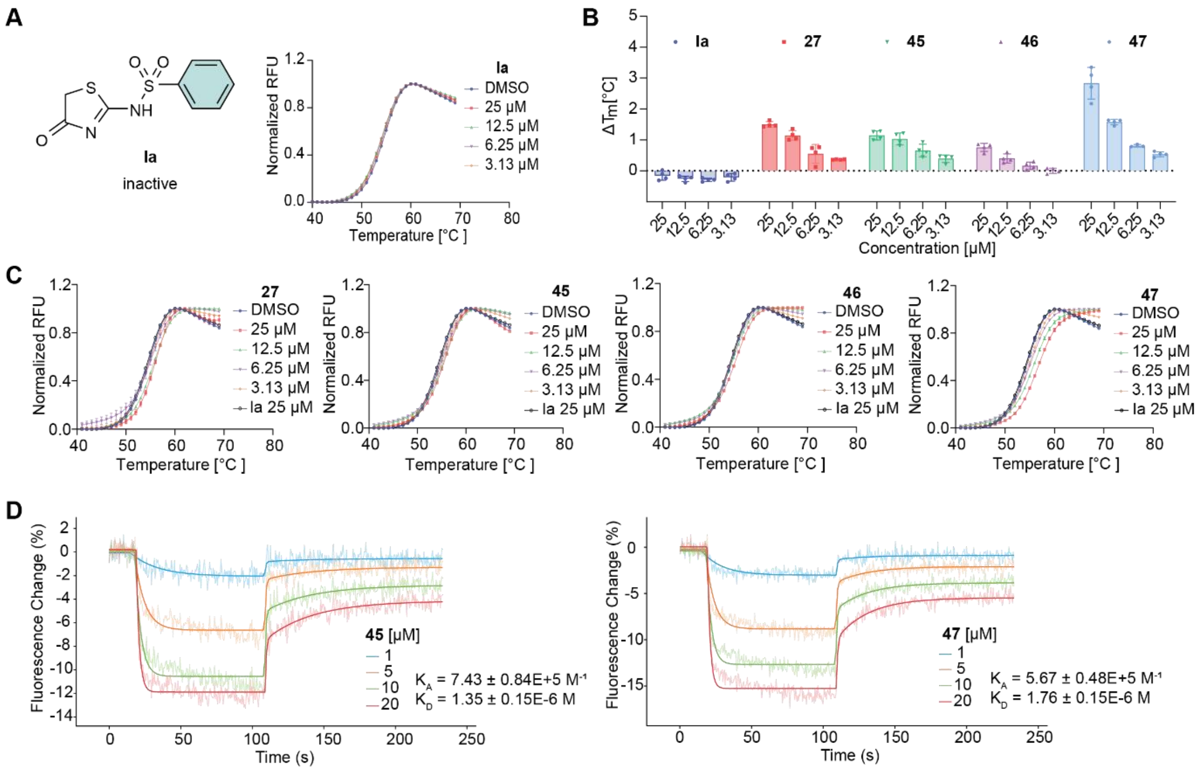

Figure 39. Binding interaction of the aminothiazolone compounds against METTL16. (A). Negative compound **Ia** structure and melting curve of METTL16 MTD under **Ia** treatment form the DSF assay. (B). ΔT_m value of METTL16 MTD treated with different inhibitors. (C). Melting curve of METTL16 MTD under the treatment of compounds **27**, **45**, **46**, and **47**. (D). The binding affinities of compounds **45** and **47** toward. METTL16 measured by biosensor assay.

An irreversible inhibition counter-screen was performed to examine the inhibition mode[205] (Figure 40A). The counter-screen was performed by incubating a final concentration of 250 nM METTL16 MTD with a final concentration of 20 μM compounds for 30 min at room temperature. The FP signals of the samples were measured with a final concentration of 5 nM FAM-labeled MAT2A-hp1 RNA. The other set of samples was diluted 10-fold, and the FP signal was measured with 5 nM FAM-labeled MAT2A-hp1 RNA. The results showed that the dilution significantly changed the inhibition potency of all tested aminothiazolones and the inhibition percentage dropped, implying the inhibition of the aminothiazolones compounds against METTL16 is reversible.

Furthermore, the LC-MS analysis revealed that the aminothiazolone compounds do not covalently bind METTL16 after incubating for 150 min. For covalent binding, the formation of covalent adducts could be observed from the LC-MS data. However, after incubating METTL16 MTD protein with compounds **45** and **47** for 150 min at room temperature, no covalent adducts were observed in comparison with the DMSO control (Figure 40B, 40C, 40D). A small mass shift of ~50 Da was observed in both the DMSO control and compound-treated samples, which was probably formed by the solvent used in the LC-MS system.

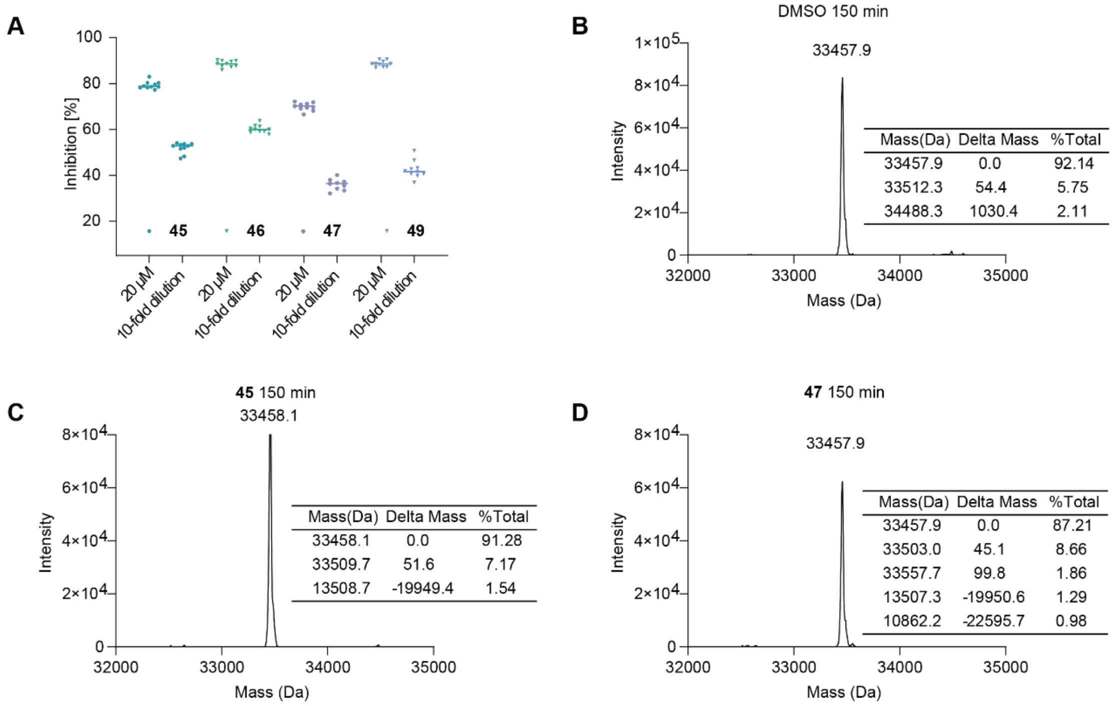

Mass(Da)	Delta Mass	%Total
33457.9	0.0	92.14
33512.3	54.4	5.75
34488.3	1030.4	2.11

Mass(Da)	Delta Mass	%Total
33458.1	0.0	91.28
33509.7	51.6	7.17
13508.7	-19949.4	1.54

Mass(Da)	Delta Mass	%Total
33457.9	0.0	87.21
33503.0	45.1	8.66
33557.7	99.8	1.86
13507.3	-19950.6	1.29
10862.2	-22595.7	0.98

Figure 40. Aminothiazolones reversibly and non-covalently inhibit METTL16. (A). The irreversible counter-screen of compounds **45**, **46**, **47**, and **49**. (B). Deconvoluted mass spectrum of 30 µM METTL16 (1-291) incubated with 1% (v/v) DMSO for 150 min. (C). (D). Deconvoluted mass spectrum of 30 µM METTL16 (1-291) incubated with 100 µM **45** and **47** for 150 min (right). Expected Mass for METTL16 (1-291), 33455.7 Da.

The aminothiazolones disrupted METTL16-RNA interaction in FP and EMSA assay. It is assumed that the aminothiazolone inhibitors bind to the RNA binding pocket of METTL16 and competed off the RNA substrate. However, the SAM pocket and RNA-binding pocket of METTL16 are connected. Compounds that bind to the SAM pocket extend to the RNA pocket would compete both RNA and SAM and show such an effect. To investigate the binding pocket of the aminothiazolones, FP assay was performed under different concentrations of SAM (Figure 41A). The assays were performed by pre-incubating METTL16 protein with different concentrations of SAM to occupy the SAM pocket. If the aminothiazolones compete with SAM, the activity of the aminothiazolones will decrease under the high concentrations of SAM. The result showed that, under different concentrations of SAM, the inhibitory activities of compounds **45**, **46**, and **47** exhibited minimal changes. The IC_{50} values of these compounds remained in the presence of 10 µM, 100 µM, and even 300 µM SAM. It is suggested that the aminothiazolones bind to the RNA-binding pocket of METTL16.

The inhibitory effect of the aminothiazolones on METTL16 methyltransferase activity was evaluated using the MTase Glo assay kit (Promega). The assay principle is based on the formation of the *S*-adenosyl homocysteine (SAH) product, which is converted to ADP and triggers a luciferase reaction (Figure 41B). The MTase Glo assay showed that compounds **27**, **45**, **46,** and **47** dose-dependently inhibited the methyltransferase activity of METTL16 MTD towards the RNA substrate MAT2A-hp1 (Figure 41C).

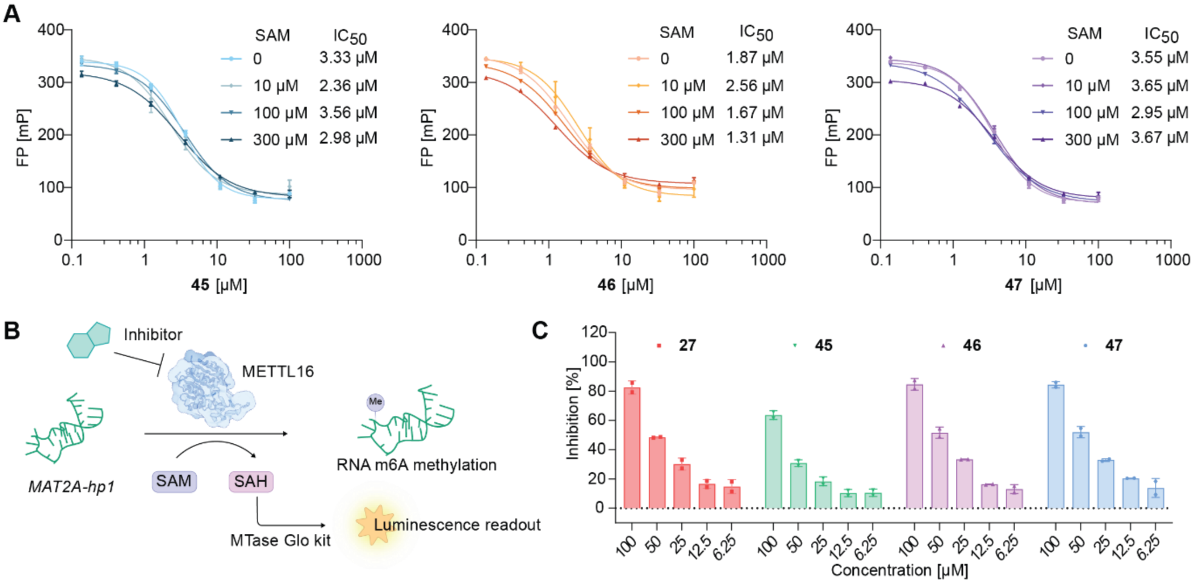

Figure 41. Aminothiazolones showed a SAM-independent inhibition against METTL16 and inhibited the methyltransferase activity of METTL16. (A). FP assay under different concentrations of SAM. (B). Illustration of MTase Glo assay. (C). Compounds **27**, **45**, **46**, and **47** inhibit he methyltransferase activity of METTL16 in a dose-dependent manner.

2.2.5 METTL16 as an RNA-binding protein without m6A methylation activity

Like *MAT2A* RNA, *U6* small nuclear RNA (snRNA) with a conserved UACA(m^{6}A)GAGAA motif can be methylated by METTL16 (Figure 42A). A *U6* snRNA tail stem deletion (U6 snRNAΔ) was reported to be methylated by the METTL16 MTD as efficiently as *MAT2A*[171] (Figure 42B). A Cy5-labelled U6 snRNAΔ was used to evaluate the binding affinity towards METTL16 MTD (Figure 42B), the affinity was measured by RNA concentration titration with a fixed concentration of 50 nM METTL16 MTD protein using FP assay. The FP result showed that the affinity of METTL16 MTD towards U6 snRNAΔ is similar to the affinity towards MAT2A-hp1, with K_D values of 32.14 nM and 29.42 nM, respectively (Figure 42B, 42C). Orthogonal EMSA experiments were performed to further confirm the affinities. The affinity K_D values of METTL16 MTD towards U6 snRNAΔ and MAT2A-hp1 were 6.6 nM and 4.7 nM, respectively, which were also similar to each other (Figure 42D, 42E).

METTL16 as an RNA-binding protein, has been reported to bind diverse RNA substrates[206]. Whether it binds to the GGACU-containing RNA substrate (Figure 42F) favored by the methyltransferase METTL3/14 complex remains unknown. To answer this question, the binding between METTL16 MTD and GGACU-containing RNA motif was evaluated. An unlabeled GGACU-containing RNA substrate was used to compete with FAM-labeled MAT2A-hp1RNA in the FP assay (Figure 42G). The result showed that GGACU RNA dose-dependently disrupted the interaction between METTL16 MTD protein and the FAM-labelled MAT2A-hp1, with an IC_{50} value of 813.8 nM, while the unlabeled MAT2A-hp1 had an IC_{50} value of 47.2 nM. The data indicated that GGACU RNA binds to METTL16 MTD protein but with a weaker affinity compared to MAT2A-hp1 RNA. The binding interaction of GGACU RNA with METTL16 MTD protein was further confirmed through an EMSA assay using a FAM-labelled GGACU RNA (Figure 42H), in which a K_D value of 63.7 nM was measured. To investigate whether the binding of GGACU RNA to METTL16 MTD induces the RNA methylation, an *in vitro* methylation assay was performed using MTase Glo assay kit (Figure 42I). The assay results showed that, unlike MAT2A-hp1 which displayed an increased luminescence signal upon methylation, the methylation signal of GGACU motif-containing RNA by METTL16 MTD was barely visible. The result suggests that METTL16 may only bind to GGACU-containing RNA as an RNA-binding protein without additional methylation activity. In addition to GGACU-containing RNA, the binding interactions of METTL16 with two precursor microRNA were evaluated by using the unlabeled precursor microRNA hairpins to compete with FAM-labelled MAT2A-hp1 RNA in the FP assay. The pre-miR-17-hp, pre-miR-17-hp mutant with two bulges being base paired (pre-miR-17-hp bp), and pre-miR-21-hp were tested (Figure 42J). All three RNAs dose-dependently disrupted the binding of METTL16 MTD protein with the FAM-labelled MAT2A-hp1 RNA, with IC_{50} values of 71.5 nM, 149.4 nM, and 187 nM, respectively. The binding of METTL16 to miRNAs and GGACU-containing RNA implies that METTL16 as an RNA-binding protein may have a diverse range of substrates.

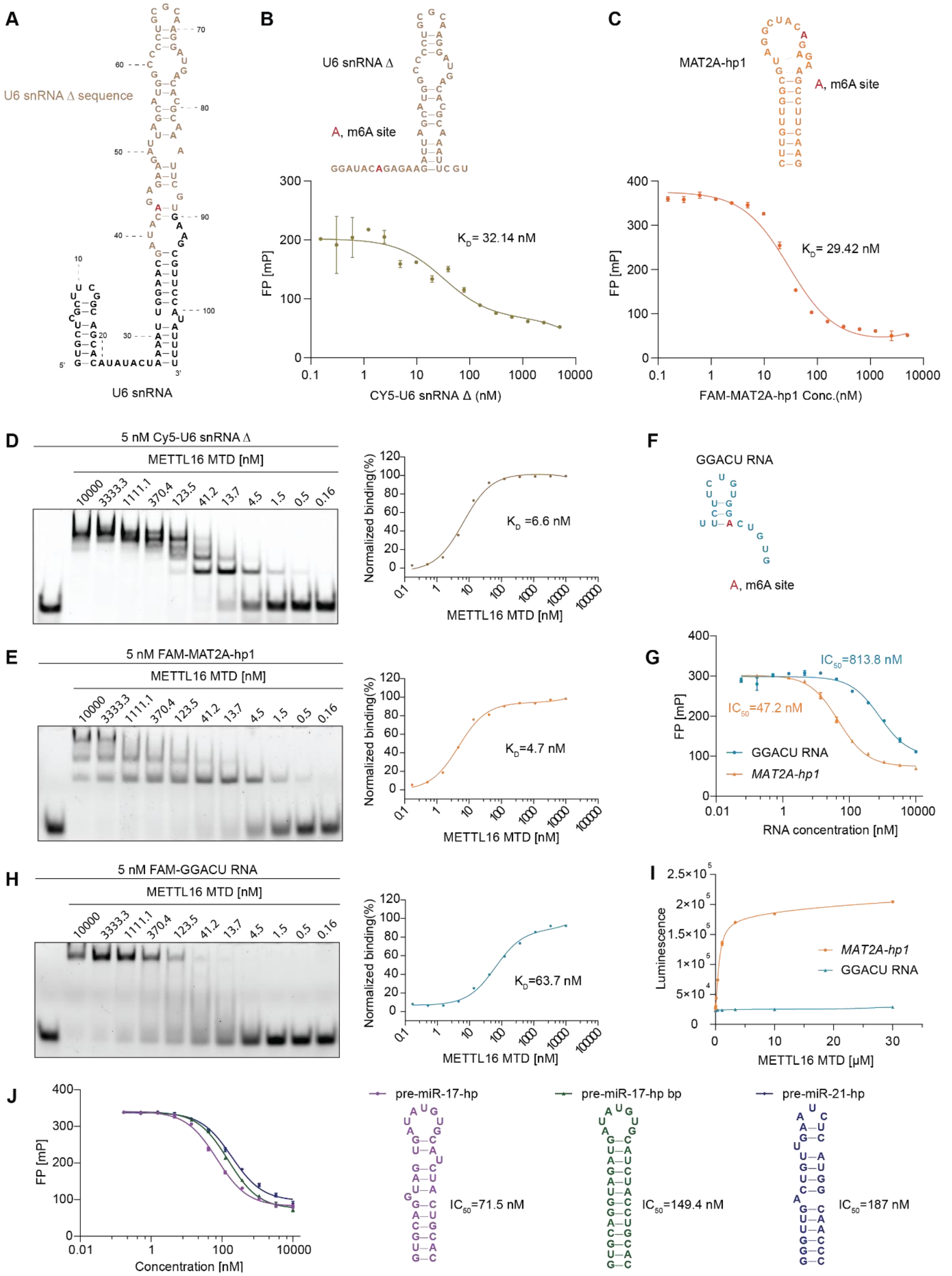

Figure 42. METTL16 as an RNA-binding protein binds to various RNAs. (A). Sequence and structure of U6 snRNA. (B). U6 snRNAΔ sequence and structure, and binding affinity towards METTL16 MTD measured by FP assay. (C). MAT2A-hp1 sequence and structure, and binding affinity measured by FP assay. (D). U6 snRNAΔ binding affinity measured by EMSA. (E). MAT2A-hp1 binding affinity measured by EMSA. (F). Sequence and structure of GGACU RNA. (G). Unlabeled GGACU-RNA and MAT2A-hp1 RNA disrupted the interaction

between METTL16 and the FAM-labelled MAT2A-hp1 RNA in the FP assay. (H). GGACU-RNA binding affinity measured by EMSA. (I). *In vitro* methylation assay using MAT2A-hp1 and GGACU-RNA substrates. (J). Precursor micro-RNA hairpins disrupted METTL16-MAT2A-hp1 interaction in the FP assay. Except the MAT2A-hp1 structure[153], other RNA structures were predicted using the RNA structure web service[207].

2.2.6 Aminothiazolones disrupt the reactions between METTL16 and diverse RNAs

The inhibitory activity of aminothiazolones against METTL16 with other RNA substrates were evaluated as METTL16 binds to various RNA substrates. The impact on METTL16-U6 snRNAΔ interaction was evaluated through an FP-based assay and validated through an orthogonal EMSA assay. A final concentration of 5 nM Cy5-labeled U6 snRNAΔ and a final concentration of 50 nM METTL16 MTD protein were used for both assays. The FP assay showed that aminothiazolones **27**, **45**, **46**, **47** and **49** dose-dependently disrupted the interaction between METTL16 MTD and U6 snRNAΔ, with IC_{50} values of 6.6 µM, 2.5 µM, 2.8 µM, 6.4 µM and 5.3 µM, respectively (Figure 43A). The potency against METTL16 with U6 snRNAΔ is relatively similar to the potency against METTL16 with MAT2A-hp1. EMSA results showed that aminothiazolones **27**, **45**, **46**, **47** and **49** interrupted the interaction between METTL16 and U6 snRNAΔ in a dose-dependent manner (Figure 43B, 43C), further confirming the activities. To evaluate the inhibitory effect against METTL16-GGACU RNA interaction, an EMSA experiment was performed, using a final concentration of 5 nM FAM-labelled GGACU RNA with a final concentration of 600 nM METTL16 MTD protein. Compounds **27**, **45**, **46**, **47** and **49** disrupted METTL16-GGACU RNA interaction dose-dependently in EMSA (Figure 43D). The results indicated that the aminothiazolone inhibitors can disrupt METTL16-RNA interactions with diverse RNA substrates, including MAT2A-hp1, U6 snRNA, and GGACU RNA.

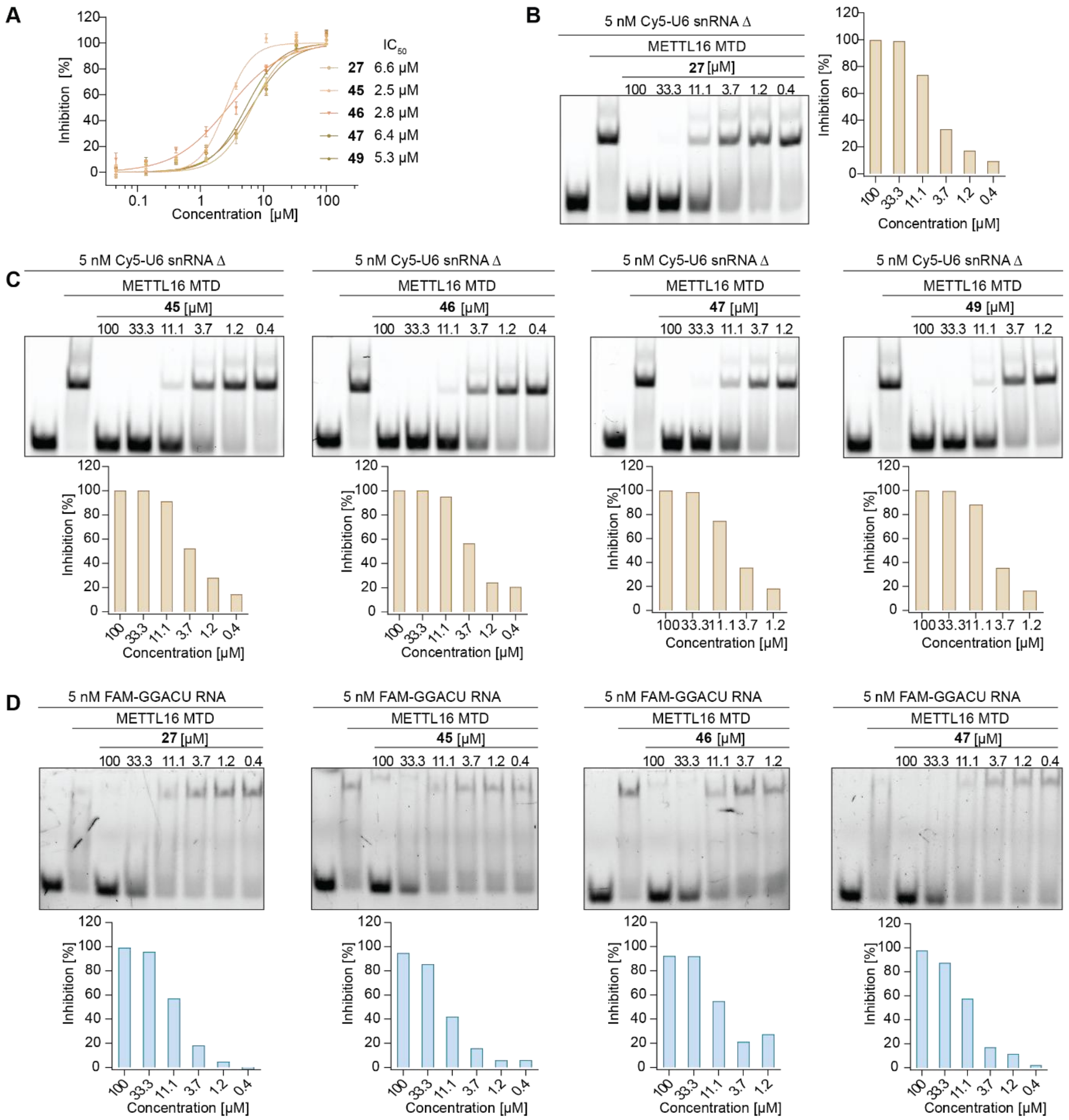

Figure 43. Aminothiazolones disrupt METTL16 interacting with U6 snRNAΔ and GGACU-containing RNA. (A). Compounds **27**, **45**, **46**, **47** and **49** dose-dependently disrupt METTL16 MTD-U6 snRNAΔ interaction in FP assay. (B). Compound **27** disrupts METTL16 MTD-U6 snRNAΔ interaction in EMSA. (C). Compounds **45**, **46**, **47** and **49** disrupt METTL16 MTD-U6 snRNAΔ interaction in EMSA. (D). Compounds **27**, **45**, **46**, and **47** inhibit METTL16 interacting with GGACU RNA in EMSA.

2.2.7 Cellular effects of METTL16 inhibitors

To evaluate the anticancer activity of the aminothiazolones, cell viability assay using CCK-8 was performed against the chronic myeloid leukemia-derived HAP1 cell line, the triple-negative breast cancer MDA-MB-231 cell line, the lung cancer A549 cell line, and the colorectal carcinoma HCT116 cell line (Figure 44A). The results indicated that the tested aminothiazolone compounds **27**, **45**, **46**, and **47** have minimal to partial effect on all four cell lines at the defined concentrations. For the HAP1 cell line, the A549 cell line and the HCT116 cell line, the inhibitory effects are very minimal even at the highest concentration of 50 µM. For the MDA-MB-231 cell line, compound **27** showed a mild effect on the cell viability, with a cell viability of 55% at the highest test concentration of 50 µM, which means 45% inhibitory effect. Compound **46** also presented an inhibition of 32% at 50 µM against MDA-MB-231 cells. Collectively, all compounds have inhibition lower than 30% against the tested cell lines. The anticancer activity against MDA-MB-231 was evaluated through a colony formation assay (Figure 44B). The results indicated that compounds **27** and **47** have mild anti-proliferation activity, however compounds 45 and 46 are less efficient compared to compound **27** and **47**, overall, the aminothiazolone compounds are not potent on the anticancer activity.

To investigate the downstream effects of the inhibitor, the *MAT2A* mRNA splicing and the m^{6}A level of the total RNA were evaluated in both MDA-MB-231 and A549 cell lines (Figure 44C, 44D). Surprisingly, treatment with 50 µM of **45** increased the splicing level of *MAT2A* mRNA as well as the m^{6}A in both cell lines. The increases may be explained by the dynamic regulation network between METTL16, *MAT2A* splicing and SAM levels[43, 153]. Compound **45** may promote METTL16 autoinhibition and further disrupts SAM binding, inhibit the methylation of *MAT2A* by METTL16 and promote *MAT2A* splicing[153]. As a result, the spliced *MAT2A* mRNA is translated into MAT2A protein and promotes SAM biosynthesis, and SAM as a methyl donor is further involved in various RNA methylation processes mediated by other methyltransferases such as the METTL3/METTL14 complex, which might be the reason for the upregulation of total RNA m^{6}A level. Further mechanism studies are required to unravel the underlying dynamic regulatory network of METTL16 and the mechanisms of the aminothiazolone inhibitors.

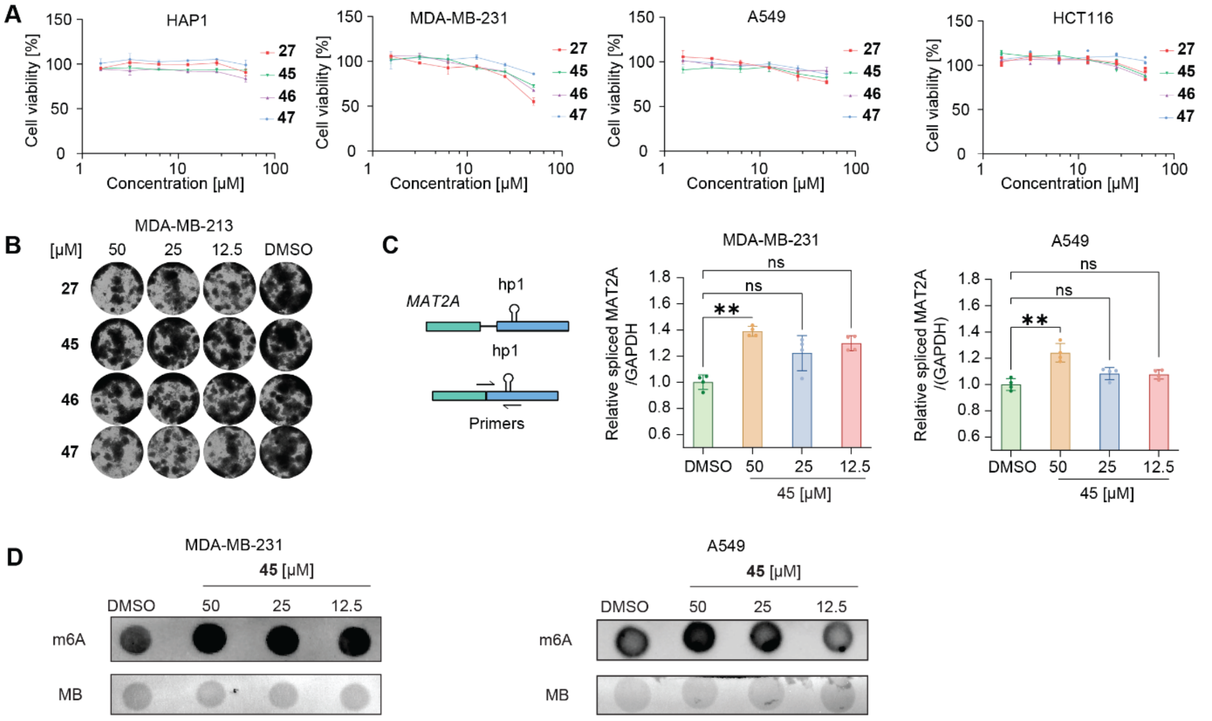

Figure 44. Cellular effect of the aminothiazolone inhibitors. (A). Anti-viability activity of aminothiazolones against HAP1, MDA-MB-231, A549, and HCT116 cell lines. (B). Colony formation assay to evaluate the anti-proliferation effect of the aminothiazolone compounds. (C). *MAT2A* splicing levels in MDA-MB-231 and A549 cell lines under the treatment of compound **45**, measured by RT-qPCR. (D). The m^{6}A levels of total RNA in MDA-MB-231 and A549 cell lines under the treatment of compound **45**, measured by dot blot. For evaluation of *MAT2A* splicing and total m^{6}A level, compound **45** potassium salt was used.

2.2.8 Conclusion

The m^{6}A modification is the most abundant RNA modification in eukaryotic mRNA and is crucial for regulating RNA bioprocessing and related pathways. In addition to the METTL3/14 complex which catalyzes RNA m^{6}A modification, METTL16 is another important methyltransferase that plays a key role in RNA modification. METTL16 catalyzes the methylation of *MAT2A* mRNA and further regulates cellular SAM homeostasis. SAM as a methyl donor compound, is involved in various methylation processes like RNA methylations, DNA methylations, and protein methylations. So far, no potent METTL16-targeting molecules have been reported and validated. An efficient FP-based screening assay was established for identifying METTL16 inhibitors. Hit compound **1,** which disrupts METTL16-*MAT2A* RNA interaction with an IC$_{50}$ value of 16.3 μM, was identified from the in-house compound library. After validating the hit compound through an orthogonal EMSA assay, a structural modification campaign based on the aminothiazolone scaffold of the hit compound **1** was performed. In total, 49 aminothiazolone METTL16 inhibitors were synthesized and evaluated. Compounds such as

45 and **47** showed single-digit micromole inhibitory IC_{50} values disrupting METTL16-RNA interaction via METTL16 binding. The biosensor assay showed that compounds **45** and **47** bind to METTL16 MTD with affinity K_D values of 1.35 μM and 1.76 μM, respectively, aligned with the inhibitory IC_{50} values obtained through biochemical assay. Cellular evaluations demonstrated that the aminothiazolones have modest anti-cancer activities. The treatment of compound **45** promoted *MAT2A* mRNA splicing and increased the overall m^6A RNA levels, which indicated compound **45** modulates the downstream of METTL16. However, the mechanism behind *MAT2A* mRNA splicing, total m^6A RNA levels, and METTL16 inhibition remains unknown, More investigations are required to uncover the underlying process. In conclusion, the first-in-class METTL16 inhibitors featuring an aminothiazolone scaffold were discovered and evaluated. The most potent compounds show single-digit inhibitory IC_{50} values and bind METLL16 with single-digit K_D affinities. Such molecules compensated for the current inaccessibility of the METTL16 inhibitor, which can be used as a promising starting point for the development of chemical probes and therapeutic reagents.

2.2.9 Discussion and Perspectives

Small molecules targeting m^6A RNA methyltransferase are emerging as promising therapeutic reagents. METTL3 is the most advanced studied target among the m^6A-binding and modifying proteins, with METTL3 inhibitors of varied structures and activities have been reported. One compound SCT-15 finished the phase 1 clinical trials for malignancies (NCT05584111). Targeting other m^6A writers, such as METTL5, METTL16, and ZCCHC4, are comparatively much less studied. In comparison, no small molecules targeting METTL16 have been reported and validated. As methyltransferase METTL16 catalyzes U6 small nuclear RNA (snRNA) and *MAT2A* mRNA m^6A methylation, it also functions in the cytoplasmic to regulate other pathways. Many biological functions of METTL16 remain unknown which is partially due to the lack of highly potent small-molecule modulators targeting METTL16. This study provided an efficient discovery platform for the identification of modulators targeting METTL16. This platform enabled the successful identification and characterization of the first-in-class METTL16 targeting small molecules. Following extensive SAR studies based on the aminothiazolone scaffold yielded structural analogues with improved potency (up to single-digit micromolar IC_{50} inhibitory potency). Although the activity of the aminothiazolones is still modest and the anticancer effect of the aminothiazolones is relatively mild, this platform provided a novel chemical entity for further optimization.

To enrich the studies of the aminothiazolones as METTL16 inhibitors, the selectivity of the aminothiazolones should be performed to exclude the off-target effects, especially against other methyltransferases and RNA binding proteins that share the functional and structural similarity with METTL16. Human m^6A methyltransferases share a common Rossmann fold structure and utilize SAM as the methyl donor to catalyze the methylation activity. It is challenging to develop selective inhibitors targeting METTL16 over other paralogs especially when the inhibitor binds to the SAM binding pocket of the methyltransferase. Targeting the RNA binding pocket of METTL16 may be a promising strategy, as the RNA binding pocket is more different from other methyltransferases. The aminothiazolones are supposed to bind to the RNA binding pocket of METTL16, making it possible to target METTL16 selectively over other m^6A writers. Further investigation into the selectivity is required to fully address the selectivity of the aminothiazolones.

The aminothiazolone showed modest antiproliferation activity, which on the one hand, has limited the possibility to develop anticancer reagents. On the other hand, it could be used as a probe to investigate related pathways in cells without cytotoxicity. METLL16, *MAT2A* RNA splicing, and SAM levels are dynamically regulated though the treatment of compound **45**, leading to mildly increased *MAT2A* mRNA splicing level and the total m^6A mRNA level. The exact underlying mechanism remains unknown, which guarantees further investigations. The limited cellular activity of the aminothiazolone indicates potential challenges such as poor cell membrane permeability, which justify the need for structural optimizations to improve cellular activities.

Additionally, further investigation into the biological functions of METTL16 as an RNA-binding protein that binds to various RNA substrates without imposing methylation activity is required to explore the unknown function of METTL16 and its regulatory network, to imply further applications of METTL16 targeting small molecules.

In summary, the discovery of aminothiazolones as the first-in-class METTL16 inhibitors proved a solid foundation for subsequent mechanistic studies on improving the activity, addressing the selectivity, and understanding the underlying cellular effect of the aminothiazolones. As the full landscape of the biological functions of METTL16 remains unknown, investigations into METTL16 pathways to understand its function are crucial for target identification and developing therapeutics for related diseases, such as various cancers including hepatocellular carcinoma and lung cancers[179, 180].

2.3 Outlooks

In summary, the Thesis describes the discovery of small-molecule inhibitors that target two RNA-binding and -modifying proteins, the ribonuclease IRE1α and the m^6A methyltransferase METTL16. RNAs are emerging promising drug targets with many RNA-focused therapeutic strategies have been advanced in the past decade, such as antisense oligonucleotides (ASOs), RNA aptamers, and small interfering RNAs (siRNAs) [208-210]. While targeting RNA with small molecules is challenging due to the flexible nature of RNAs, targeting RNA-binding and -modifying proteins could provide new and alternative RNA regulatory strategies. IRE1α and METTL16 both serve as RNA-modifying proteins and play critical roles in RNA regulation and metabolism. IRE1α acts as an ER stress sensor, regulates *XBP1* mRNA splicing and selected RNA substrates degradation, METTL16 as an m^6A writer, catalyzes the dynamic RNA m^6A methylation, IRE1α and METTL16 impact related RNA splicing, stability, and translation. Small-molecule inhibitors targeting IRE1α and METTL16 can modulate related RNA metabolisms, emerging as a new approach to small-molecule-based RNA-modulation therapies.

Apart from the RNA modulation roles played by IRE1α and METTL16, the two proteins themselves are promising targets for the treatment of associated diseases. The dysregulation of IRE1α has been associated with cancers[118, 211-213], metabolic and neurodegenerative disorders[103, 214, 215], pain[216], and many other human diseases. ORIN1001(MKC8866) which covalently binds to the IRE1α RNase domain, inhibiting IRE1α RNase activity finished the phase 1 clinical trial for advanced solid tumor therapy (NCT03950570). Emerging compounds with novel scaffolds and different modes of action could offer alternative solutions for therapeutic purposes. The indole inhibitor identified in this thesis presents a new scaffold that inhibits IRE1α activity by binding to its kinase domain. For METTL16, besides its methyltransferase activity, it is reported to promote RNA transcription by interacting with eukaryotic initiation factors (eIFs), for example, eIF3a/b and eIF4E2[180, 181]. METTL16 has been identified as one of the most important genes in the human methyltransferase family in terms of human cancer survivability[180], and has emerged as a potential target for cancer therapy. Despite these reported functions, many cellular functions of METTL16 remain unknown. No small-molecule METTL16 inhibitors have previously been identified and validated. Our studies have identified the first-in-class METTL16 small-molecule inhibitor and performed an extensive SAR study, filling the gap in the lack of METTL16 modulators.

Future efforts to improve selectivity and activity of the inhibitors will promote the ultimate development of therapeutic candidates targeting IRE1α and METTL16. One possible approach to improve the selectivity and activity is to employ the identified molecules as building components for the design of proximity-inducing bifunctional molecules to degrade IRE1α or METTL16. Other proximity-induced compounds that induce RNA degradation and RNA modification are also feasible and impactable approaches by linking the ribonuclease or methyltransferase ligands to RNA binders. Such new chemical modalities could represent a new approach in modulating the structure and function of RNAs, as well as the related cellular pathways.

3. Methods

3.1 Materials

3.1.1 Reagents and chemicals

Table 1, reagents and chemicals used in this thesis.

Name	**Supplier**	**Product number**
10x Buffer PE140	Dynamic Biosensors	BU-PE-140-10
Amersham ECL prime western blotting detection kit	Cytiva	RPN2232
BCA protein assay kit	Thermo Fisher Scientific	23227
Benzonase	Sigma-Aldrich	E1014
CCK-8 solution	Vazyme	A311
chloramphenicol	Carl Roth	3886.3
Color Prestained Protein Standard	New England Biolabs	P7719s
disuccinimidyl suberate	Thermo Fisher Scientific	A39267
DMEM medium	Gibco	61965026
DPBS	Gibco	14190169
FBS	Gibco	10500064
Glycerol	Gerbu Biotechnik	2006
Glycin	Carl Roth	3790.2
HEPES	Gerbu Biotechnik	1009
High-Capacity cDNA Reverse Transcription Kit	Thermo Fisher Scientific	4368814
His-capture kit	Dynamic Biosensors	HK-NTA-1
his-HRV-3C protease	PCF dortmund	\
his-TEV protease	PCF dortmund	\
IMEM medium	Gibco	12440046
imidazole	Sigma-Aldrich	56749
Insect GeneJuice® Transfection Reagent	Sigma-Aldrich	71259-3
IPTG	Carl Roth	CN08.3
kanamycin	Carl Roth	T832.2

lambda protein phosphatase	New England BioLabs	P0753S
MTase GloTM kit	Promega	V7601
NuPAGE LDS Sample Buffer (4×)	Thermo Fisher Scientific	NP0007
PageRuler Prestained Protein Ladder	Thermo Fisher Scientific	26616
penicillin-streptomycin solution	Gibco	15140122
Phusion® High-Fidelity PCR Kit	New Egeland Biolabs	E0553S
PMSF	VWR international	M145-25G
PowerUp™ SYBR™ Green Master Mix	Thermo Fisher Scientific	A25742
protease inhibitor cocktail	Sigma-Aldrich	P8340
protease inhibitor cocktail tablet	Sigma-Aldrich	S8830
Protein Labeling Kit RED-NHS 2nd Generation	NanoTemper	MO-L011
QIAprepn miniprep	Qiagen	27106
RIPA buffer	Sigma-Aldrich	R0278
RNeasy mini kit	Qiagen	74106
SDS	Carl Roth	CN30.2
Sf-900™ III medium	Gibco	12658027
Skim milk	Carl Roth	T145.2
SYPRO Orange	Sigma-Aldrich	S5692
TCEP	TCI	T1656
Tris	Carl Roth	4855.2
Triton X-100	Sigma-Aldrich	1001054580
Trypsin-EDTA solution	Sigma-Aldrich	T4049
tunicamycin	MP Biomedi	215002805
Tween-20	SERVA Electrophoresis GmbH	39796.01
UltraPure TBE Buffer 10×	Thermo Fisher Scientific	15581044
Urea	PanReac AppliChem	1198549

3.1.2 Cell lines

Table 2, cell lines used in this thesis.

Cell line	Organism	Tissue	Disease	Supplier
Sf9	Spodoptera frugiperda	Ovary	NA	PCF Dortmund
HT-29	human	Colon	Adenocarcinoma; Colorectal	ATCC
HCT 116	human	Large intestine; Colon	Carcinoma; Colorectal	DSMZ
A549	human	Lung	Carcinoma	ATCC
MDA-MB-468	human	Breast; Mammary gland	Adenocarcinoma	ATCC
MDA-MB-231	human	Breast; Mammary gland	Adenocarcinoma	DSMZ
HAP1	human	Leukemia	Leukemia	Horizon

3.1.3 Oligos

Table 3, oligos used in this thesis.

Oligos	Sequence (5’- 3’)	Experiment	Supplier
FAM-XBP1-BHQ	5′FAM-CAUGUCCGCAGCGCAUG-3′BHQ1	FRET, cleavage assay	IDT
IRE1α_G547_Fwd	CTGTATTTTCAGGGCGGATCCGGCAGCAGCCCCTCCC	subclone	IDT
IRE1α_L977_Rev	TCCTCTAGTACTTCTCGACAAGCTTTTAGAGGGCGTCTGGAGTCACTG	subclone	IDT
hActin Fwd	GCGAGAAGATGACCCAGATC	RT-qPCR	IDT
hActin Rev	CCAGTGGTACGGCCAGAGG	RT-qPCR	IDT
hXBP1s-Fwd	GAGTCCGCAGCAGGTG	RT-qPCR	IDT
hXBP1s-Rev	CAATACCGCCAGAATCCA	RT-qPCR	IDT
hIRE1α-Fwd	GTGAGCGACAGAATAGAAAAGG	RT-qPCR	IDT
hIRE1α-Rev	GGAAGCGAGATGTGAAGTAGC	RT-qPCR	IDT
METTL16_M1_Fwd	AAGTTCTGTTTCAGGGCCCGATGGCTCTGAGTAAATCAATGCATGCAAG	subclone	IDT
METTL16_D291_Rev	ATGGTCTAGAAAGCTTTAATCATAAAAACTCCAAGCTAAGGCCCATCTC	subclone	IDT
FAM-*MAT2A*-hp1	FAM-CUUGUUGGCGUAGGCUACAGAGAAGCCUUCAAG	FP, EMSA	IDT

MAT2A-hp1	CUUGUUGGCGUAGGCUACAGAGAAGCCUUCAAG	MTase Glo	IDT
Cy5-U6 snRNAΔ	Cy5-GGAUACAGAGAAGAUUAGCAUGGCCCCUGCGCAAGGAUGACACGCAAAUUCGU	FP, EMSA	IDT
FAM- GGACU-RNA	FAM-UUCUUCUGUGGACUGUG	FP, EMSA	IDT
GGACU-RNA	UUCUUCUGUGGACUGUG	MTase Glo	IDT
Pre-miR-17-hp	GUGCAGGUAGUGAUAUGUGCAUCUACUGCAC	FP	IDT
Pre-miR-17-hp bp	GUGCAGGUAGAUGAUAUGUGCAUCUACCUGCAC	FP	IDT
Pre-miR-21-hp	GGGUUGACUGUUGAAUCUCAUGGCAACCC	FP	IDT
*GAPDH*_Fwd	GAAGGTGAAGGTCGGAGTC	RT-qPCR	IDT
*GAPDH*_Rev	GAAGATGGTGATGGGATTTC	RT-qPCR	IDT
*MAT2As*_Fwd	GAATTTCGATCTCCGCCCTG	RT-qPCR	IDT
*MAT2As*_Rev	AGCCTACGCCAACAAGTCTG	RT-qPCR	IDT

3.1.4 Antibodies

Table 4, antibodies used in this thesis.

Antibody	**Dilution**	**Supplier**	**Product number**
antibody IRE1α	1:1000	Cell Signaling Technology	#3294s
GAPDH	1:6000	Proteintech	10494-1-AP
HRP-conjugated Goat Anti-Rabbit	1:6000	Proteintech	SA00001-2
anti-m^{6}A antibody	1µg/mL	Synaptic systems	202003

3.2 Methods for the discovery of IRE1α inhibitors

Parts of the methods described in this section will be published in Liu, Y.[#]*; Avathan Veettil, A. K.* [#]*; Gasper, R.; Jiang, M.; Wagner, L.; Hastürk, O.; Wu, P. *, Harnessing Indole Scaffolds to Identify Small-molecule IRE1α Inhibitors Modulating XBP1 mRNA Splicing. Accepted in principle*

3.2.1 IRE1α protein expression and purification

Insect cell culture

Sf9 cells were obtained from the Protein Chemistry Facility (MPI Dortmund). Sf9 cells were cultured in Sf-900™ III medium at 27°C, 120 rpm shaking.

Bacmid generation and isolation

Human IRE1α kinase and RNase domain (residues 547-977) was subcloned into pLIB plasmid by Protein Chemistry Facility (PCF) Dortmund, with an *N*-terminal His tag and TEV cleavage site, and further expressed using Bac-to-Bac expression system. Briefly, IREα encoded pLIB plasmid was transformed into *E.coli* DH10EmBacY competent cells by heat shock and plated onto X-Gal/IPTG LB agar plate with 50µg/ml kanamycin, 7µg/ml gentamicin, 10 µg/ml tetracycline, 100 µg/ml X-gal, and 40 µg/ml IPTG. The positive white colonies were validated by colony PCR and then cultured in 5 mL 2YT medium overnight to isolate the bacmid. The bacmid was isolated using a Qiagen miniprep kit following the manufacturer’s protocol until the “neutralization” step. After adding 350 µL neutralization buffer (buffer N3), the solution was immediately mixed by inverting and then centrifuged at 13000 rpm for 10 min. The supernatant was transferred into a new tube and 700 µL of isopropanol was added and mixed. Then the sample was incubated on ice for 10 min and centrifuged at 13000 rpm at 4°C for 10 min to remove the supernatant. The DNA pellet was further washed three times with 70% ethanol, then air-dried and dissolved in buffer EB. The bacmid concentration was measured by Nanodrop and used for Sf9 cell transfection.

Bacmid transfection and baculovirus generation

1 mL mid-log-phase Sf9 cells were seeded into a 6-well plate using Sf-900™ III medium with a density of 1×10^6 cells per well. The plate was incubated for 30 min at room temperature for cells to attach. The bacmid DNA (2µg, 4 µg, 10 µg) and 10 µL transfection reagent (Insect GeneJuice® Transfection Reagent) were diluted separately into 100 µL medium. The bacmid solution was then added dropwise into the transfection solution and gently mixed. After

incubating for 15 min at room temperature, 800 µL of medium was added to the solution. After the cells adhered, the medium from the 6-well plate was discarded and the transfection mixtures were slowly added to each well. One well of Sf9 cells without transfection was used as the negative control. The transfected plate was incubated at 27°C for 96 h in the dark, and the YFP (yellow fluorescent protein) fluorescence appeared for positive transfections. The supernatant of the positive transfection from the 6-well plate was filtered with a 0.45 µM filter and collected as the P1 virus for further amplification. For storage, 5% FBS was added to the virus, and the virus was stored at 4°C in the dark.

Baculovirus amplification

10 mL 1×10^6 cell/mL mid-log-phase Sf9 cells were seeded into a 100 mm cell culture dish with Sf-900™ III medium, then incubated for 30 min at room temperature, allowing cells to attach. 1 mL of the different P1 virus was added to each dish, and one dish without adding the virus was used as the negative control. Then the dishes were incubated at 27°C for 72 h in the dark. P2 virus was harvested by filtering the supernatant from the positive dish with a 0.45 µM filter, and then supplemented with 5% FBS for further storage. For P3 virus amplification, 100 mL 2×10^6 cell/mL Sf9 cells were seeded in a conical flask, to which 1 mL P2 virus was added. The cells were then incubated at 27°C, shaking at 120 rpm for 96 h in the dark. The P3 virus was harvested by centrifuging the culture at 4000 rpm for 10 min. The supernatant was then filtered using a 0.45 µM filter. 5% FBS was added to the virus, which was then stored at 4°C. P2-virus titering was performed by a YFP viral titer assay.

Protein expression and purification

For protein expression, 1L 2×10^6 Sf9 cells were seeded into a conical flask, 10 mL of P3 virus was added to the flask, and the cells were cultured at 27°C, 120 rpm for 72 h. The protein purification procedure was performed according to a published method[126] and adapted in-house. The Sf9 cells cultured with P3 virus were harvested by centrifugation at 4000 rpm for 15 min, cell pellets were collected and resuspended in lysis buffer containing 50 mM HEPES pH 7.5, 300 mM NaCl, 10% glycerol, 1 mM $MgCl_2$, 1 mM TCEP, and 5 mM imidazole. Benzonase (1:1000, Sigma, E1014), 1 mM PMSF, and protease inhibitor cocktail tablet (1 tablet per 25 mL, Sigma, S8830) were added to the cell suspension, then the cell suspension was lysed by sonication at 60% amplitude, 10 s on, 10 s off for a total of 10 min, on ice. The cell lysate was centrifuged at 20000 rpm for 45 min, then filtered and loaded onto a nickel affinity column (GE Healthcare, Ni Sepharose™ 6 Fast Flow). The loaded nickel column was washed with 50 mL lysis buffer, followed by 30 mL lysis buffer containing 30 mM imidazole. His-tagged IRE1α protein was eluted with lysis buffer containing 300 mM imidazole. His-TEV protease was added to the protein sample at a 1:50 m:m concentration and incubated at 4°C overnight to remove the His-tag. The protein was further diluted 1:6 to a NaCl concentration of 50 mM using dilution buffer containing 50 mM HEPES pH 7.5, 1 mM TCEP, 5% glycerol before loading onto an anion exchange column (Cytiva, HiTrap Q HP). The Q HP column was pre-equilibrated with QA buffer (50 mM HEPES, pH 7.5, 50 mM NaCl, 1 mM TCEP, 5% glycerol) before sample loading. The unphosphorylated and phosphorylated proteins were separated by eluting the protein with a very long gradient with 0-60% buffer QB (50 mM HEPES, pH 7.5, 500 mM NaCl, 1 mM TCEP, 5% glycerol) over a length of 400 mL. Fractions from different peaks were collected separately and measured by LC-MS. The fully phosphorylated fraction was further purified by size exclusion chromatography (Cytiva, HiLoad 16/600 Superdex 200 pg,) with SEC buffer (25 mM HEPES pH 7.5, 250 mM NaCl, 1 mM TCEP, 10% glycerol). The remaining protein fractions from the Q HP anion exchange column were dephosphorylated by incubation with lambda protein phosphatase (New England BioLabs, P0753S) at 4°C overnight. Dephosphorylation was confirmed by LC-MS, and the dephosphorylated protein was further purified by size exclusion chromatography with the SEC buffer described above. The purity of the purified phosphorylated (p-IRE1α) and dephosphorylated (IRE1α) protein was determined by SDS-PAGE gel and LC-MS. Protein concentrations were measured using NanoDrop. Proteins were aliquoted, snap-frozen in liquid nitrogen, and then stored at -80°C for future use.

Protein mass spectrometry analysis

Purified IRE1α protein was diluted in PBS buffer, and around 1µg protein was injected for LC-MS measurement using an Agilent 1260 II Infinity system with an electrospray ion source in positive mode. The sample was run through a desalting cartridge (AdvanceBio Desalting-RP, 2.1 mm, 12.5mm, Agilent) with a gradient of 5-80% HPLC-grade acetonitrile (with 0.1% TFA) in HPLC-grade water (with 0.1% TFA) with a 0.4 mL/min flow rate, 6 min runtime. The spectra data were deconvoluted using the ProMass software (Novatia).

3.2.2 Assay establishment and compound library screen

FRET-based IRE1α RNase assay

The FRET assay was performed following the published procedure[126] and optimized in-house. The FRET assay was performed in a black 384-well plate with a total reaction volume of 20 µL in reaction buffer containing 20mM HEPES, pH 7.5, 50 mM potassium acetate, 1 mM magnesium acetate, 1 mM DTT, 0.05% v/v TritonX-100. The purified recombinant unphosphorylated IRE1α (IRE1α) and phosphorylated IRE1α (p-IRE1α) protein and the 5' FAM, 3' BHQ-1 dual-labeled XBP1 RNA hairpin substrate (5′FAM-CAUGUCCGCAGCGCAUG-3′BHQ1) were used for this assay. The final concentrations of the protein and RNA substrate were identified by titrations. Final concentrations of 40 nM IRE1α protein and 100 nM FAM-XBP1-BHQ RNA substrate were used for measuring the unphosphorylated IRE1α. And final concentrations of 4 nM p-IRE1α protein and 200 nM FAM-XBP1-BHQ RNA were used for unphosphorylated IRE1α. Compounds and IRE1α protein were incubated in the wells for 30 min at room temperature. After adding the FAM-XBP1-BHQ RNA substrate, the fluorescence kinetics were immediately measured. The measurement was conducted over one hour, with 2.5 min per measurement cycle, at room temperature using a TECAN Spark plate reader. Fluorescence top-reading mode was used, with an excitation wavelength of 485 nm, an emission wavelength of 535 nm, and 10 nm bandwidths. After measurement, the linear part of the reaction curve was fitted with a simple linear regression to obtain the slope to represent the reaction rate. The inhibition % was calculated using the following equation: inhibition% = 100 × (slope of the DMSO control - slope of the sample)/ (slope of the DMSO control - slope of the blank control), DMSO control: DMSO with protein and RNA substrate; Blank control: DMSO with RNA substrate, without protein. The IC_{50} values were calculated using a dose-response model in GraphPad Prism 9.

Compound screen

Compound library screening was performed using the FRET-based activity assay described above with the final concentrations of 5 μM compound, 40 nM IRE1α, and 100 nM dual-labeled RNA substrate in a 384-well black plate (4514, Corning). A compound library containing 11393 compounds was provided and dispensed into 384-well plates using an ECHO dispenser by COMAS (Compound Management and Screening Center, MPI Dortmund). For controls, a final 0.05% v/v DMSO was dispensed into the wells. Protein solution was added to the 384-well plates by Multidrop dispenser and incubated for 30 min at room temperature. After incubation, the dual-labeled RNA substrate was dispensed into each well, and the fluorescence was kinetically measured. Screening information in detail is listed in Table 5.

Table 5, Compound library screening information for IRE1α

Category	**Parameter**	**Description**
Assay	Type of assay	Fluorescence resonance energy transfer (FRET), *in vitro*
	Target	IRE1α
	Primary measurement	Real-time fluorescence intensity, excitation 485, emission 535
	Assay protocol and reagents	Protocol and reagents are posted in the Method section.
Library	Library size	11393 compounds at 10 mM in DMSO
	Library composition	Small molecules and pseudo-natural products
	Quality control	LC-MS and Tube Auditor™ inspection of the sample collection
	Source	Compound Management and Screening Center Dortmund
Screen	Format	384-well plate
	Concentration tested	5 µM, 0.05% DMSO
	Plate controls	Control: DMSO control; Blank control: only substrate
	Dispensing system	ECHO dispenser (Beckmann), Multidrop dispenser (Thermo)
	Detection instrument	TECAN spark
	Normalization	inhibition% = 100 × (average slope of DMSO control - slope of sample)/ (average slope of DMSO control - average slope of blank control)
Post-HTS	Hit criteria	inhibition% ≥ 50%
	Hit rate	48/11393, 0.42%
	Retesting of initial activities	Hits retested in dose-response mode using screening assay
	Compound purity and structure	Resynthesized hit compound and validate
	Structure confirmation	NMR, HRMS
	Additional assay(s)	Gel-based cleavage assay; DSF assay; ITC

3.2.3 Methods for IRE1α inhibitor characterizations and mechanism studies

Gel-based RNA-cleavage assay

Compound and a final concentration of 10 nM purified p-IRE1α were incubated for 30 min at room temperature, a final concentration of 50 nM FAM-XBP1-BHQ RNA was added to the reaction and the reaction solution was further incubated for 45 min at room temperature. The reaction solution was mixed with 2 µL 6×TBE blue loading dye (45 % H_2O, 40 % glycerol, 15 % 10×TBE, 0.1% bromophenol blue) and 5 µL of the sample was loaded to pre-run 15% urea-PAGE. The gel was run in pre-warmed (~60°C) 1×TBE buffer at 220 V for 30 min in the dark. After electrophoresis, the fluorescence of the gel was detected and imaged using a ChemiDoc MP imaging system (Bio-Rad).

Differential scanning fluorimetry (DSF) assay for IRE1α

The DSF assay was performed in a white 96-well PCR plate with a total reaction volume of 20 µL in PBS buffer supplemented with 2 mM DTT, including compounds (final 1% DMSO), a final concentration of 1 µM IRE1α or p-IRE1α protein and 5×SYPRO Orange fluorescent dye (5000× in DMSO, Sigma S5692). The melting curve was measured over a temperature range from 25°C to 95°C with 1°C increments every 30 seconds, using a Bio-Rad CFX96 Real-Time PCR detection system with the FRET scan mode. The melting temperature (T_m) was obtained by fitting the melting curve to Boltzmann sigmoidal in GraphPad Prism and the thermal shift (ΔT_m) was calculated by using the equation: $\Delta T_m = T_{m(\mathrm{compound})} - T_{m(\mathrm{DMSO})}$.

Isothermal titration calorimetry (ITC) assay

A MicroCal PEAQ-ITC system (Malvern) was used for performing the ITC experiments. ITC experiments were performed at 25°C in ITC buffer containing 25 mM HEPES pH 7.5, 250 mM NaCl, 1 mM TCEP, and 5% glycerol, with a final of 1% v/v DMSO. The dephosphorylated IRE1α protein was freshly prepared for the ITC experiment in ITC buffer. For the ITC binding experiments, 60 µL 200 µM of compound was prepared and loaded into the syringe, and 300 µL 10 µM of IRE1α protein was prepared and loaded into the sample cell. For the competitive ITC experiments, the IRE1α protein at a final concentration of 10 µM was incubated with the indicated compound for 20 min at 24°C (final 1% DMSO) before loading into the sample cell. All samples used for ITC experiments were degassed and warmed to 24°C before loading. The instrument settings for the measurements were: reference power 10 µcal/s, feedback high, stir speed 750 rpm, initial delays 60s, injection spacing 150 s, injection duration 4 s. The experiments were performed with a single 0.4 µL injection followed by 18 (or 15) times of 2 µL injections. Data were analyzed using MicroCal PEAQ-ITC analysis software.

Microscale thermophoresis (MST)

Dephosphorylated IRE1α protein was labeled and purified using a Protein Labeling Kit RED-NHS 2nd Generation (NanoTemper, MO-L011) following the manufacturer's protocol. Buffer containing 50 mM HEPES, pH 7.5, 200 mM NaCl, 2% glycerol, 0.5 mM TCEP, 0.05% tween-

20 was used as labelling buffer. Briefly, 10 μL of the 300 μM dye solution (prepared in the labeling buffer) was added into 90 μL of 10 μM IRE1α protein (in labeling buffer) and mixed carefully by pipetting, then incubated for 30 min at room temperature in the dark. The ladled protein was purified with a pre-equilibrated B column, and the A280 and A650 of the purified protein were measured using NanoDrop, and then the concentration and labeling degree were calculated. A Monolith Nt.115 instrument (NanoTemper) was used for measuring microscale thermophoresis, and the binding affinity experiments were performed according to the instrument's instructions. Compound IA107 was serially diluted 2-fold in labeling buffer with a final concentration of 2.5 % DMSO, then the compound solutions were incubated with a final concentration of 20 nM labeled IRE1α protein for 20 min at room temperature. After incubation, the samples were transferred to capillaries and loaded into the machine. MST measurements were carried out using the Nano-RED excitation color, with 60% excitation power. Data were analyzed using the manufacturer's software, and results from three individual measurements were merged for analysis.

Michaelis-Menten kinetic studies

Michaelis-Menten kinetic studies were performed using the FRET assay described above, with different concentrations of *XBP1* RNA substrates. Briefly, the compound was incubated with a final concentration of 40 nM dephosphorylated IRE1α for 30 min in a black 384-well plate at room temperature. Then different concentrations of dual-labeled *XBP1* RNA substrates were added into each well. The fluorescence was immediately read using a TECAN Spark plate reader with the kinetic measurement as described above.

LanthaScreen^{TM} Eu kinase binding assay

LanthaScreen^{TM} Eu kinase binding assays were performed by SelectScreen Kinase Profiling Services (Thermo Fisher Scientific). The test compounds are tested in a final 1% DMSO in a low-volume, white 384-well plate (Greiner #784207). Alexa Fluor conjugated kinase "tracer", tagged kinase protein, and Eu-labeled anti-tag antibody were used for the assay. When the "tracer" binds to the kinase, it will form the tracer-kinase complex, resulting in a high FRET signal with the Eu-labeled anti-tag antibody, while the displacement of the tracer by a kinase inhibitor will lead to a decreased FRET signal. For IRE1α (ERN1) kinase binding assay, 5 nM of ERN1, 2 nM of Eu-anti-GST, and 100 nM tracer 236 (with K_D = 160 nM) was used. For IRE1β (ERN2) kinase binding assay, 5 nM of ERN2, 2 nM of Eu-anti-GST, and 100 nM tracer 236 (with K_D = 108 nM) were used. For both proteins, kinase buffer A containing 50 mM HEPES pH 7.5, 0.01% BRIJ-35, 10 mM $MgCl_2$, and 1 mM EGTA was used.

Co-crystallization of IA107-pIRE1α

15 mg/mL p-IRE1α protein in buffer containing 25 mM HEPES pH 7.5, 150 mM NaCl, and 1 mM TCEP was incubated with IA107 at a final concentration of 1 mM (1% DMSO) at 4°C overnight. The protein-ligand solution was centrifuged at 13000 rpm for 30 min at 4°C before crystallization. Co-crystallization was carried out using hanging drop sitting with a 24-well plate. 1 μL of reservoir buffer (0.05 M bicine pH 9.0, 36% v/v PEG300, and 0.12 M NaCl) was mixed with 1.5 μL of the protein-ligand solution on siliconized glass cover slides and then sealed the slide to the plate. Thin plate-shaped crystals grew over 3-4 days at 20°C. Crystals were fished from the drop using cryoloops, flash-frozen, and stored in liquid nitrogen. X-ray diffraction data were collected at the ID30A-3 beamline at the European Synchrotron Radiation Facility (ESRF). The dataset was collected from a single crystal, and the processing and scaling were carried out using XDS and XSCALE[217]. The structures were solved by molecular replacement using PHASER[218] within the Phenix software suite[219]. The topology file for ligand IA107 was generated using AceDRG[220] within the CCP4 suite[221], based on its SMILES string. The structure was manually refined using COOT[222] and refined using Phenix.refine[223] program. Part of chain D (K851 to M948) was eliminated from the structure due to the poor electron density data. X-ray crystallography data collection and refinement statistics were provided in Table S1.

DSS-crosslinking assay

Phosphorylated IRE1α (p-IRE1α) and test compounds were incubated for 30 min at room temperature, with a total reaction volume of 20 μL. The final concentrations of p-IRE1α and compound are 2 μM and 100 μM, respectively. The reaction buffer contains 20 mM HEPES, pH 7.5, 50 mM potassium acetate, 1 mM magnesium acetate, 1 mM DTT, and 0.05% v/v TritonX-100. After incubation, disuccinimidyl suberate (DSS, Thermo Fisher Scientific, A39267) was added at a final concentration of 250 μM and then incubated at room temperature for 1h to induce the crosslinking. The reaction was quenched by adding a final concentration of 50 mM Tris (pH 7.5). Crosslinking samples were then analyzed using a mass photometry instrument (Refeyn Ltd), and PBS buffer was used for the measurements. Samples were diluted in PBS to a protein concentration of 100 nM before measurement. 18 μL PBS buffer was added to the center of the gasket on the coverslips to focus, followed by adding and mixing of 2 μL of the diluted sample, before measuring the samples. Data analysis was performed using Discover MP software. The analysis was calibrated with a calibration sample, which was a BSA protein and TG protein mixture at a final concentration of 50 nM of each protein in PBS. For each sample, the results of 3 individual measurements were merged. For the SDS-PAGE-based crosslinking assay, the indicated concentrations of protein were incubated with 100 μM final concentration of compound for 30 min at room temperature, in the reaction buffer mentioned above. Then, a final concentration of 250 μM DSS was added into each sample and incubated for 1h. After crosslinking the reaction was quenched by adding a final concentration of 50 mM Tris (pH 7.5) and incubated for 15 min at room temperature. The samples were mixed with 4× protein loading buffer (Invitrogen, 2463559), and 10μL of samples were loaded and analyzed by SDS-PAGE gel.

Kinase profiling

Kinase profiling was performed by the SelectScreen Kinase Profiling Services (Thermo Fisher Scientific). The Z′-LYTE, Adapta and LanthaScreen Eu Kinase Binding Assay were used for measuring different kinases. The kinase targets, measuring assays, and used ATP concentrations are listed in Table S2. The kinome phylogenetic tree was created using the KinMap web portal.

3.2.4 Cellular experiments

Mammalian cell culture

HT-29, A549, and MDA-MB-468 cell lines were purchased from ATCC (American Type Culture Collection). HCT 116 cell line was purchased from DSMZ (German Collection of Microorganisms and Cell Cultures). The cells were cultured in high-glucose DMEM medium (Gibco, 61965026) supplemented with 10% FBS (Gibco, 10500064) and 1% penicillin-streptomycin solution (Gibco, 15140122). All cell lines were cultured at 37°C under a humidified 5% CO_2 atmosphere. Cells were examined and subcultured regularly.

Cell Counting Kit-8 cell viability assay

Cell viability assay was performed using CCK-8 solution (Vazyme, A311) according to the manufacturer’s instructions. Cells were harvested and seeded into 96-well plates at a density of 2000-4000 cells per well with a 100 μL volume. The plates were incubated in the incubator overnight. After cell attachment, 100 μL of test compound solutions (prepared in cell culture medium, with a final 0.5% DMSO) were added to each well at the desired final concentration, and the plate was incubated for 72 h. After compound treatment for 72 h, 20 μL CCK-8 solution was added into each well and incubated at 37°C for another 2-4 h. Absorbance was measured at a wavelength of 450 nm using a TECAN plate reader. Cell viability was calculated using the following equation: Cell viability (%) =100×(Absorbance of compound treated cell -Absorbance of the Blank control)/(Absorbance of the DMSO -Absorbance of compound treated cells -Absorbance of the Blank control); Blank control: medium and CCK-8 solution, no cells.

RT-qPCR measurement of the *XBP1* mRNA splicing

A549 cells were seeded in 6-well plates with a density of 5×10^5 cells per well and incubated overnight to allow cells to attach. The cells were treated with compound or DMSO for 2 h before a final concentration of 0.5 μg/ mL tunicamycin (Tm, MP Biomedi, 0215002805) was added into each well to induce the ER stress, except the DMSO control. After incubating for 2 h, the total RNA of the cells was purified using a RNeasy mini kit (Qiagen, 74106). Then 500 ng of total RNA was reverse transcribed using the High-Capacity cDNA Reverse Transcription Kit (Thermo Fisher Scientific, 4368814). The obtained cDNA was diluted 1: 5 using RNase-free water, and 1 μL of cDNA was used for each qPCR reaction. The qPCR was performed in a 10 μL total reaction volume using PowerUp™ SYBR™ Green Master Mix (Thermo Fisher Scientific, A25742) with a Bio-Rad CFX96 Real-Time PCR Detection System. The standard cycling program (primer $T_m \geq 60°C$) of the SYBR green master mix was used for qPCR measurement. Data was normalized and analyzed using the $2^{-\Delta\Delta Ct}$ method. The primers used are listed in Table 3. The inhibition % was calculated by using the equation: inhibition%=100× (normalized Tm control - normalized of the sample)/ (normalized Tm control - normalized DMSO control). Tm control: Cells treated with tunicamycin; DMSO control: Cells treated with DMSO only. The *p* values were calculated using a one-tailed independent Student's t-test.

Western blot analysis of XBP1s protein.

A549 cells and MDA-MB-231 cells were seeded into 6-well plates at a density of 8×10^5 cells per well and cultured overnight. After attaching to the plates, cells were treated with different concentrations of IAPD1, KIRA8, or G1749 with a final 0.1% DMSO for 2 hours, followed by the addition of 1 μg/mL tunicamycin (MP Biomedi, 0215002805) to induce ER stress for 4 hours. After compound treatment, the cells were washed with pre-cooled DPBS (Gibco, 14190169) three times and then lysed using RIPA buffer (Sigma, R0278) supplemented with phosphatase inhibitor (Roche, 4906845001) and 1x protease inhibitor cocktail (Sigma, P8340) on ice. The cell lysates were collected and centrifuged at 15,000 g for 10 minutes, and then the supernatants were collected. The protein concentrations of the lysates were measured using a BCA protein assay kit (Thermo Scientific, 23227), and all lysates were diluted to the same protein concentration. The lysates were mixed with 4× protein loading buffer (Invitrogen, 2463559), and a total protein of 40 μg of each sample was loaded onto a 4-15% MP stain-free gel (Bio-Rad, 4568085). The samples were separated by electrophoresis using Tris-glycine-SDS buffer as running buffer. After electrophoresis, the protein transfers were carried out on a Trans-Blot Turbo Transfer System with a 0.45 µm PVDF membrane. After protein transfer to the membrane, the membranes were blocked in 5% skim milk (in PBST) for 1 h at room temperature and then incubated with primary antibodies of IRE1α, XBP1s, or GAPDH at 4°C with shaking overnight. Subsequently, the membranes were incubated with a secondary goat anti-rabbit antibody for 1 hour at room temperature. After being washed with PBST, the membranes were incubated with the substrate solution from the ECL prime Western blotting detection kit, and then the chemiluminescence was detected and imaged with a ChemiDoc MP imaging system. The antibodies used were: IRE1α (Cell Signaling Technology, #3294s, 1:1000), XBP1s (Cell Signaling Technology, #12782s, 1:1000), GAPDH (Proteintech, 10494-1-AP, 1:6000) and Goat Anti-Rabbit (Proteintech, SA00001-2, 1:6000).

Cellular thermal shift assay (CETSA)

The CETSA assay for IA107 was performed using A549 cell lysate. The A549 cells were harvested at 80% confluency and lysed by incubating with RIPA buffer (Sigma, R0278) supplemented with 1 mM PMSF and 1× protease inhibitor cocktail (Sigma, P8340) on ice for 30 min, and collected by cell scraper. Cell lysate was centrifuged at 13000 rpm 4°C for 30 min to collect the supernatant. The lysate was aliquoted to 550 µL per tube and then incubated with DMSO or different concentrations of IA107 (final 0.1% DMSO) at room temperature for 30 min. Then the lysate was further aliquoted to 50 µL per tube and heated at the desired temperature in a PCR cycler for 3 min (25°C for 1 min; X°C for 3 min; 16°C, hold). After heating, samples were centrifuged at 13000 rpm, 4°C for 30 min. The supernatants were carefully transferred and mixed with protein loading buffer (Invitrogen, 2463559), then analyzed by western blot using 4-20% MP stain-free gel (Bio-Rad, 4568095) and the abovementioned western blot method.

The CETSA assay for IAPD1 was performed using A549 cells. The cells were harvested and seeded into 100 mm standard cell culture dishes at 80% confluency and cultured overnight. After attachment, the cells were treated with different concentrations of APD1 or DMSO (final 0.1% DMSO) and incubated for 4 h. Then cells were gently washed with pre-cooled DPBS (Gibco,14190169) and lysed using RIPA buffer (Sigma, R0278) supplement with 1 mM PMSF and 1× protease inhibitor cocktail (Sigma, P8340) on ice for 30 min. Cell lysates were collected by scraping and transferred into 1.5 mL tubes, then centrifuged at 13000 rpm 4°C for 30 min. The protein concentrations of the supernatants were quantified using a BCA protein assay kit

(Thermo Fisher Scientific, 23227), and all samples were diluted to the same concentration. The cell lysate from each sample was aliquoted into 11 PCR tubes, with 45 μL of lysate per tube. Cell lysate aliquots were further heated at the indicated temperatures using a PCR cycler (25°C for 1 min; X°C for 3 min; 16°C, hold). After heating, samples were centrifuged at 13000 rpm for 30 min at 4°C, and the supernatants were collected, mixed with 4× protein loading buffer (Invitrogen, 2463559), heated at 95°C for 10 min, and then separated by 4-20% MP stain-free gel. Then analyzed by western blot using the aforementioned methods.

3.3 Methods for the discovery of METTL16 inhibitors

*Parts of the methods described in this section were published in Liu, Y.#; Goebel, G. L.#; Kanis, L.; Hastürk, O.; Kemker, C.; Wu, P. *, Aminothiazolone Inhibitors Disrupt the Protein–RNA Interaction of METTL16 and Modulate the m6A RNA Modification. JACS Au, 2024, 4, 4, 1436–1449.*

3.3.1 METTL16 protein expression and purification

METTL16 plasmid construction

The plasmid encoding the full-length human METTL16 sequence is a gift from Prof. Jessica A. Brown's lab (University of Notre Dame). The METTL16 MTD (1-291) sequence was amplified using Phusion high-fidelity DNA polymerase (New England Biolabs) and then subcloned to a pOPINB plasmid with an N-terminal His tag followed by an HRV 3C cleavage site. The primers used are listed in Table 3.

METTL16 protein expression and purification

Plasmid encoded METTL16 MTD was transformed into *E.coli* Rosetta (DE3) competent cells, and the protein was expressed and purified as previously described with modifications in-house[169]. Briefly, the *E.coli* was cultured in LB medium supplemented with 50 µg/mL kanamycin and 34 µg/mL chloramphenicol at 37°C, under 170 rpm shaking. After OD600 reached 0.8, the cultures were chilled to 18°C, and a final concentration of 0.5 mM IPTG was added to the culture. Then the cells were incubated at 18°C 170 rpm for 16-20 h to induce expression. Afterwards, the cells were harvested by centrifugation at 5000g, 18°C for 15 min, and the cell pellet was resuspended with lysis buffer containing 50 mM HEPES, pH 7.5, 500 mM NaCl, 5% v/v glycerol, 0.5 mM TCEP, 5 mM imidazole. Before lysing by sonication on ice, the cell lysate was supplemented with a final concentration of 1 mM PMSF. The cell lysate was centrifuged at 25000g, 4°C for 30 min, and the supernatant was collected. The supernatant was filtered and loaded to a nickel-affinity column (Ni Sepharose™ 6 Fast Flow, GE Healthcare), and the column was washed by 50 mL lysis buffer, 50 mL lysis buffer supplemented with 20 mM imidazole, 30 mL lysis buffer supplemented with 30 mM imidazole subsequently, and finally protein was eluted using 15 mL lysis buffer supplemented with 300 mM imidazole. The protein elution was treated with His-HRV-3C protease with a ratio of 1:30 w/w, and dialysis in dialysis buffer (50 mM HEPES, pH 7.5, 250 mM NaCl, 5% v/v glycerol, 0.5 mM TCEP) overnight to cleave the His tag and decrease the imidazole concentration to be lower than 20 mM. Then the protein sample was loaded onto a nickel-affinity column again to remove the cleaved His6-tag and His-HRV-3C protease. The flow-through from the nickel affinity column was collected and concentrated using an Amicon ultra-centrifugal filter unit (Millipore). The protein was further purified by a SEC75 column (Cytiva, HiLoad 16/600 Superdex 75 pg,) using SEC buffer containing 20 mM pH 7.5, 200 mM NaCl, 0.5 mM TCEP,2% v/v glycerol. Protein purity and mass are confirmed by SDS-PAGE and LC-MS. The purified protein was concentrated to 10 mg/mL, aliquoted, snap frozen in liquid nitrogen, and stored at -80˚C for future experiments. His-tagged METTL16 (1-291) was purified using the same protocol. After elution from the first nickel-affinity column, the sample was concentrated and loaded onto the SEC75 column directly without further protease cleavage and the reverse nickel column purification.

3.3.2 METTL16 screening assay and library screen

METTL16 Fluorescence polarization (FP) screening assay

The compound library screening was performed against a chemical library provided by COMAS (Compound Management and Screening Center, MPI Dortmund), which contains 25344 compounds. The compound screening method is a FP assay using the final concentrations of 30 µM compound, 80 nM METTL16 protein and 2 nM FAM-MAT2A-hp1 RNA in 384-well black plates (4514, Corning) with a total reaction volume of 18 µL in the FP buffer contains 20 mM HEPES, pH 7.5, 50 mM NaCl, 0.05% v/v Tween 20, 0.05 mg/mL BGG. Compounds and the same volume of DMSO as the control groups were transferred to the plates using an Echo acoustic dispenser, followed by the dispensation of protein solution to the plates using a Multidrop dispenser. And incubated with compounds at room temperature for 30 min. FAM-RNA substrate solution was then dispensed into each well and the fluorescence polarization was measured by a TECAN Spark plate reader under the excitation wavelength of 485 nm and the emission wavelength of 535 nm. Hits from the primary screen were tested in serial dilutions to identify the IC_{50} value, and the potential lead compounds were further validated through the orthogonal electrophoretic mobility shift assay (EMSA). Z-factor calculated with the equation: $Z' = 1 - (3\sigma_{c+} + 3\sigma_{c-}) / (|\mu_{c+} - \mu_{c-}|) = 0.91$; σ_{c+} and σ_{c-} are standard deviations of the signals for protein binding with the FAM-RNA probe and the unbound FAM-RNA probe alone, respectively; μ_{c+} and μ_{c-} are means of bound (protein with FAM-RNA probe) and unbound (FAM-RNA probe only) signals, respectively. The information on the compound library screening is listed in Table 6 below.

Table 6, Compound library screening information for METT16

Category	Parameter	Description
Assay	Type of assay	Fluorescence polarization (FP) assay, *in vitro*
	Target	METTL16 (MTD)
	Primary measurement	Fluorescence polarization, excitation 485, emission 535
	Assay protocol and reagents	Protocol and reagents are posted in the Method section
Library	Library size	25344 compounds in DMSO
	Library composition	Small molecules and pseudo-natural products
	Quality control	LC-MS and Tube Auditor™ inspection of the sample collection
	Source	Compound Management and Screening Center Dortmund
Screen	Format	384-well plate
	Concentration tested	30 μM, 0.3% ~ 1.5% DMSO
	Plate controls	Control: DMSO control; Blank control: only substrate
	Dispensing system	ECHO dispenser (Beckmann), Multidrop dispenser (Thermo)
	Detection instrument	TECAN spark
	Normalization	inhibition% = 100 × (FP of DMSO control - FP of sample)/ (FP of DMSO control - FP of blank control)
Post-HTS	Hit criteria	inhibition% ≥ 48%
	Hit rate	140/25344, 0.55%
	Retesting of initial activities	Hits retested in dose-response mode using the screening assay
	Compound purity and structure	Resynthesized hit compounds and validated
	Structure confirmation	NMR, HRMS
	Additional assay(s)	EMSA; DSF assay; *In vitro* methylation assay;

3.3.3 Methods for METTL16 inhibitor characterizations and mechanism studies

METTL16 FP assay for compound test

The METTL16 FP assay for compound test is similar to the FP assay for compound library screening, the assay was performed in a total reaction volume of 20 μL with the final concentrations of protein and RNA at 50 nM and 5 nM, respectively. The test compound was diluted using FP buffer and incubated with METTL16 MTD protein for 30 mins at room temperature, then the FAM-MAT2A-hp1 RNA probe was added into each reaction and the fluorescence polarization was measured with a TECAN Spark plate reader, under the excitation wavelength of 485 nm and the emission wavelength of 535 nm with a bandwidth of 20 nm. DMSO was used as the control group with the final v/v of 1%. The inhibition % of the test compound was calculated with the equation: inhibition % =100% (FP value of control – FP value of compound) / (FP value of control - FP value of blank); control: DMSO with protein and FAM-RNA; blank: DMSO with FAM-RNA; compound: compound with protein and FAM-RNA. The IC_{50} value was calculated using GraphPad Prism 9. FP assay using U6 snRNAΔ followed the aforementioned protocol, the final concentration of METTL16 MTD protein and U6 snRNA are 50 nM and 5 nM, respectively. The polarization was measured under the excitation wavelength of 630 nm and the emission wavelength of 680 nm with a bandwidth of 20 nm.

Electrophoretic mobility shift assay (EMSA)

Test compound (or DMSO as control with a final v/v of 1%) was diluted in the FP buffer (20 mM HEPES, pH 7.5, 50 mM NaCl, 0.05% v/v Tween 20, 0.05 mg/mL BGG) and incubated with METTL16 MTD protein for 30 min at room temperature, then the FAM-MAT2A-hp1 was added into each reaction and incubated for 10 min, with the final concentrations of protein and RNA are 50 nM and 5 nM respectively. The samples were mixed with 6×TBE blue loading dye (45 % H2O, 40 % glycerol, 15 % 10x TBE buffer, 0.1% bromophenol blue) and loaded to a 6.6% native PAGE gel. The samples from FP measurement can be analyzed by mixing with the loading dye and loaded to the native PAGE gel directly. The electrophoresis was run at 120 V for 40 min at 4°C in the dark with 0.5×TBE buffer. After electrophoresis, the gel was imaged using Chemi Doc MP (Bio-Rad) through the fluorescein channel. The EMSA for testing compounds with FAM labeled GGAUC-motif containing RNA and METTL16 MTD interaction was performed using a similar method described above, while the final of METTL16 MTD protein and FAM-labeled-GGACU RNA are 600 nM and 5 nM respectively. The EMSA with Cy5 labeled U6 snRNAΔ as substates followed the similar protocol as described above, with the final concentrations of METTL16 MTD protein and U6 snRNA are 50 nM and 5 nM, respectively, the reaction samples were mixed with 6×TBE orange loading dye (45% H2O, 40% glycerol, 15% 10x TBE buffer, 0.1% Orange G) and separated by electrophoresis, and the image of the gel was taken through the Cy5 channel. EMSA for measuring protein-RNA binding was performed with a similar protocol.

METTL16 Differential scanning fluorimetry (DSF) assay

The DSF assay for METTL16 MTD was performed using a similar protocol as the DSF assay for IRE1α described in section 3.2.3. The assay was performed using the final concentration of 1 µM METTL16 MTD protein, 5×SYPRO Orange fluorescent dye (Sigma S5692), and 0.35% v/v DMSO in a total reaction volume of 20 µl with PBS buffer supplemented with 2mM DTT. The melt curve of the protein was measured using the FRET scan mode of a Bio-Rad CFX96 Real-Time PCR Detection System. The temperature range is 25°C to 95°C with an increment of 1°C per 30 seconds. The midpoint of the transition (T_m) and the thermal shift (ΔT_m) were calculated using the same method described in section 3.2.3

SwitchSENSE biosensor assay

The biosensor binding assay was performed using a heliX adapter chip on the heliX biosensors instrument. His-tagged METTL16 MTD protein was captured and immobilized on the surface using the His-capture kit (Dynamic Biosensors, HK-NTA-1). The surface was regenerated using the imidazole solution provided in the capture kit each time after measurement. The experiments were run using PE140 buffer (10 mM Na_2HPO_4/NaH_2PO_4, pH 7.4, 140 mM NaCl, 0.05% Tween-20, 50 µM EDTA), and a final v/v of 0.2% DMSO was used. The measurement was carried out with an association flow rate of 200 µL/min, association time of 90 s; dissociation flow rate of 200 µL/min, and dissociation time of 120 s. Data were analyzed using heliOS software with the "kinetics-mono & biphasic-free amplitudes fitting" mode.

Irreversible inhibition counter-screen

The Irreversible counter screen was performed by incubating a final concentration of 250 nM (5×) METTL16 MTD protein with a final concentration of 20 µM compounds (~5× IC_{50}) for 30 min at room temperature. After incubation, the FP signal of the 5× sample and the samples the 10-fold diluted samples (diluted the 5× sample 10-fold) were measured with a final concentration of 5 nM FAM-labeled MAT2A-hp1 RNA, respectively.

In vitro methylation assay

METTL16 MTD methyltransferase activity was measured using an MTase Glo^{TM} Methyltransferase Assay kit, which measures the luminescence readout transforming from the methylation reaction product S-adenosyl homocysteine (SAH). The methylation assay was performed in a white 384-well plate (Corning #3824) following the manufacturer's instruction. The total methylation reaction volume is 8 µL with the final concentrations of 1 µM METTL16

MTD, 1 μM MAT2A-hp1, and 10 μM SAM. 1% v/v of DMSO was used as the control. The test compound was diluted and incubated with METTL16 MTD protein in a 384-well plate for 30 min at room temperature in reaction buffer containing 20 mM Tris, pH 8.0, 50 mM NaCl, 1 mM EDTA, 3 mM $MgCl_2$, 0.1 mg/ml BSA, 1 mM DTT. 2× substrate solution containing MAT2A-hp1 and SAM was freshly prepared in reaction buffer and added to each well, then incubated for 1 h at room temperature. After the methyltransferase reaction, 5× MTase-Glo Reagent was added and incubated for 30 min. Then the MTase-Glo Detection Solution was added into each well, after another 30 min incubation, the luminescence of the reaction was measured using a TECAN Spark plate reader. To examine the methyltransferase activity under different SAM concentrations, the concentration of SAM in 2× substrate solution was adjusted accordingly. The inhibition% was calculated using the equation: inhibition% =100% (luminescence of control - luminescence of sample)/ (luminescence of control - luminescence of blank), control: DMSO with protein and RNA; Blank: DMSO with RNA; sample: tested compound with protein and RNA.

3.3.4 Cellular experiments

Cell culture

A549 was purchased from ATCC (American Type Culture Collection). HCT 116 and MDA-MB-231 were purchased from DSMZ (German Collection of Microorganisms and Cell Cultures), HAP1 cell line was purchased from Horizon. A549, HCT 116, and MDA-MB-231 cell lines were cultured in high glucose DMEM medium (Gibco, 61965026) supplemented with 10% FBS (Gibco, 10500064) and 1% penicillin-streptomycin (Gibco, 15140122). HAP1 cell line was cultured in IMEM medium (Gibco, 12440046) supplemented with 10% FBS (Gibco, 10500064) and 1% penicillin-streptomycin (Gibco, 15140122). All cells were cultured in a cell culture incubator at 37°C with 5% CO_2 atmosphere.

Anti-proliferation assay

The anti-proliferation assay was performed using CCK-8 (cell counting kit-8) solution (Vazyme, A311). HCT116 and HAP1 cells were collected and seeded in 96-well plates with a density of 2000 cells per well and cultured overnight. Test compounds were diluted in the cell culture medium and were added into each well (0.5% DMSO was used as controls). After 72 h treatment, CCK-8 solution was added to the wells and incubated at 37°C for 2 hours. The absorbance at 450 nM was measured using a TECAN Spark plate reader. Cell viability % was calculated using the equation: Cell viability% =100% (absorbance of compound treatment - absorbance of only medium)/ (absorbance of DMSO control - absorbance of only medium).

Colony formation assay

MDA-MB-231 cells were collected and seeded into 24-well plates with a density of 1000 cells per well. After culture overnight, the medium was changed to compound solutions or DMSO (0.5% v/v) solutions, which were diluted in the cell culture medium. The medium exchange and treatment were performed every three days. After 7 days, the cell culture medium was discarded and the cells were gently washed with PBS, and then the cells were fixed by incubating with 4% paraformaldehyde solution at room temperature for 15 min. After fixing, the paraformaldehyde solution was removed, and the cells were washed with PBS to remove the remaining paraformaldehyde. The cells were further stained with 0.1% (w/v) crystal violet. After staining for 15 min, the crystal violet solution was removed, and the cells were washed with water to remove the extra dye. The plates were air-dried and then photographed.

MAT2A mRNA splicing evaluation using RT-qPCR

MDA-MB-231 cells and A549 cells were collected and seeded into 6-well plates at a confluency of 70% confluency and cultured overnight to allow cells to attach. Compound **45** potassium salt was used for the compound treatment. After 24 h of treatment, discard the cell culture medium and wash the cells with DPBS three times to remove the remaining medium. The total RNA of the cells was purified using a RNeasy Mini Kit (Qiagen, 74106) following the instruction. The concentrations of the RNA samples were measured with Nanodrop and 500 ng of total RNA was used for reverse transcription. The reverse transcription was carried out with a High-Capacity cDNA Reverse Transcription Kit (Thermo Fisher, 4368814) following the manufacturer's protocol. The real-time qPCR was performed using PowerUp™ SYBR™ Green Master Mix (Thermo Fisher Scientific, A25742) with a 10 µL reaction volume. The cycling was performed on a BioRad CFX96 Real-Time PCR Detection System with the standard cycling mode (primer Tm ≥60°C) (50°C 2 min; 95°C 2 min; 95°C 15s, 60°C 1 min, 40 cycles) plus a melt curve analysis. The primers used for the reaction are listed in Table 3. The RT-qPCR data was normalized and analyzed using the $2^{-\Delta\Delta Ct}$ method. The p value was calculated using GraphPad Prism software with the one-way ANOVA analysis.

Dot blot

The dot blot experiments were performed with the same RNA samples for the RT-qPCR evaluation mentioned above. The RNA samples were diluted to the same concentration using

RNase-free water, heated at 95˚C for 3 min, and then immediately chilled on ice to disrupt the secondary structures. Each RNA sample was dropped onto a positively charged nylon membrane (Invitrogen, AM10102) with a total amount of 1 µg, and crosslinked under the UV light 2 times and 5 min each time, using a UVP crosslinker instrument (analytik jena) equipped with a 254 nM bulb. After cross-linking, the membrane was washed with TBST (1xTBS with 0.1% Tween-20) for 10 min and blocked with 5% w/v skimmed milk solution (in TBST) for 1 h at room temperature. 1µg/mL anti-m^6A antibody (Synaptic systems, 202003) diluted in skimmed milk solution was applied and incubated with the membrane overnight at 4˚C under gentle shaking. After washing the membrane with TBST three times and each time for 10 min, the membrane was incubated with a secondary HRP-conjugated Goat Anti-Rabbit antibody (Proteintech, SA00001-2) 1 h at a 37˚C shaker. The membrane was washed using TBST to remove the extra secondary antibody and imaged with the Amersham ECL Prime Western Blotting Detection Reagent on a Chemi Doc MP (Bio-Rad) through the chemiluminescence channel. After imaging, the membrane was washed with TBST three times each time for 10 min to remove the detection reagent and then stained with methylene blue solution (0.2% methylene blue in 0.2M sodium acetate and 0.2M acetic acid) as the loading control. After staining, the membrane was washed with TBST to remove extra dye and then imaged through the colorimetric channel of the Chemi Doc machine.

4. Supplementary

4.1 Plasmid Maps

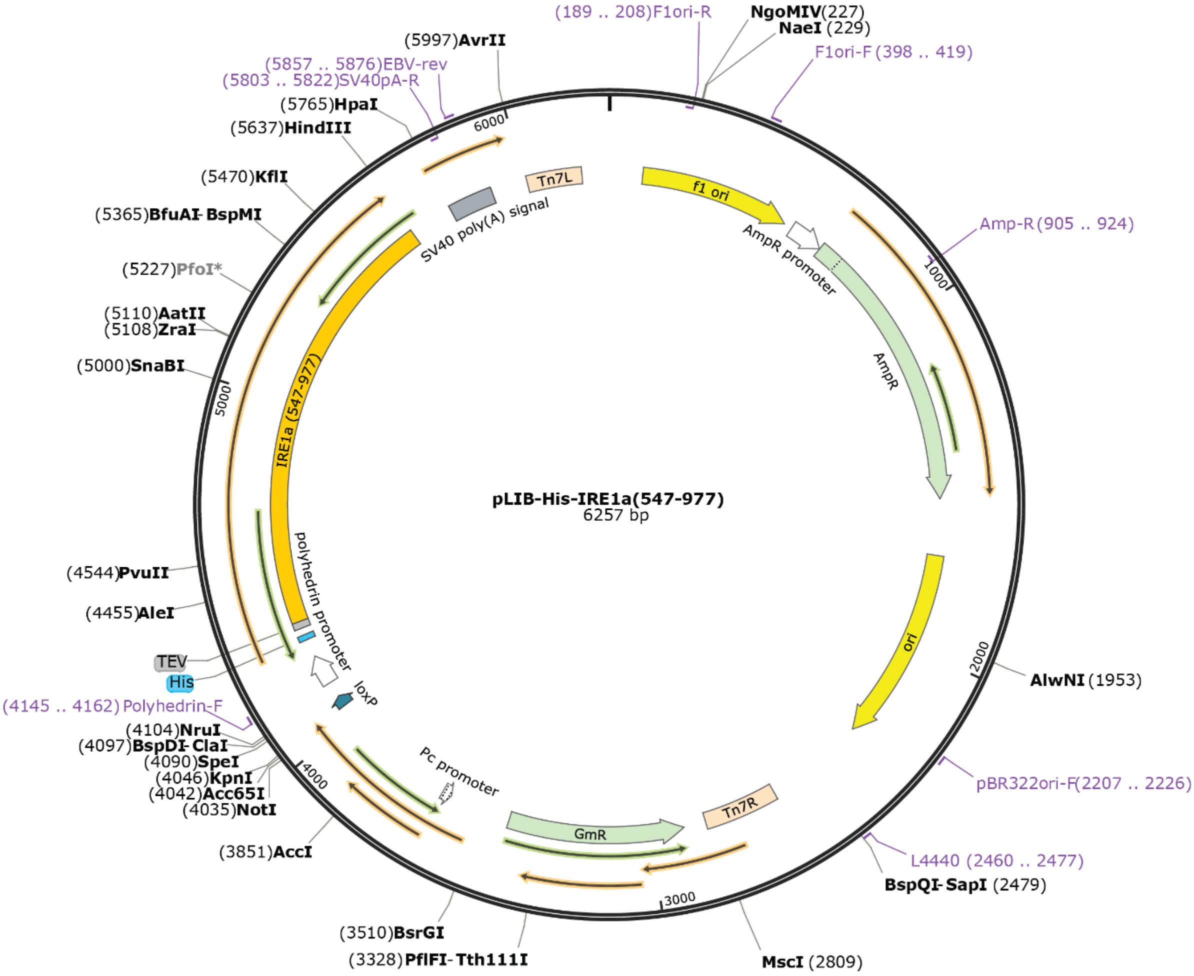

Plasmid pLIB-His-IRE1α (547-977). pLIB plasmid encodes the IRE1α KR domain for IRE1α protein purification.

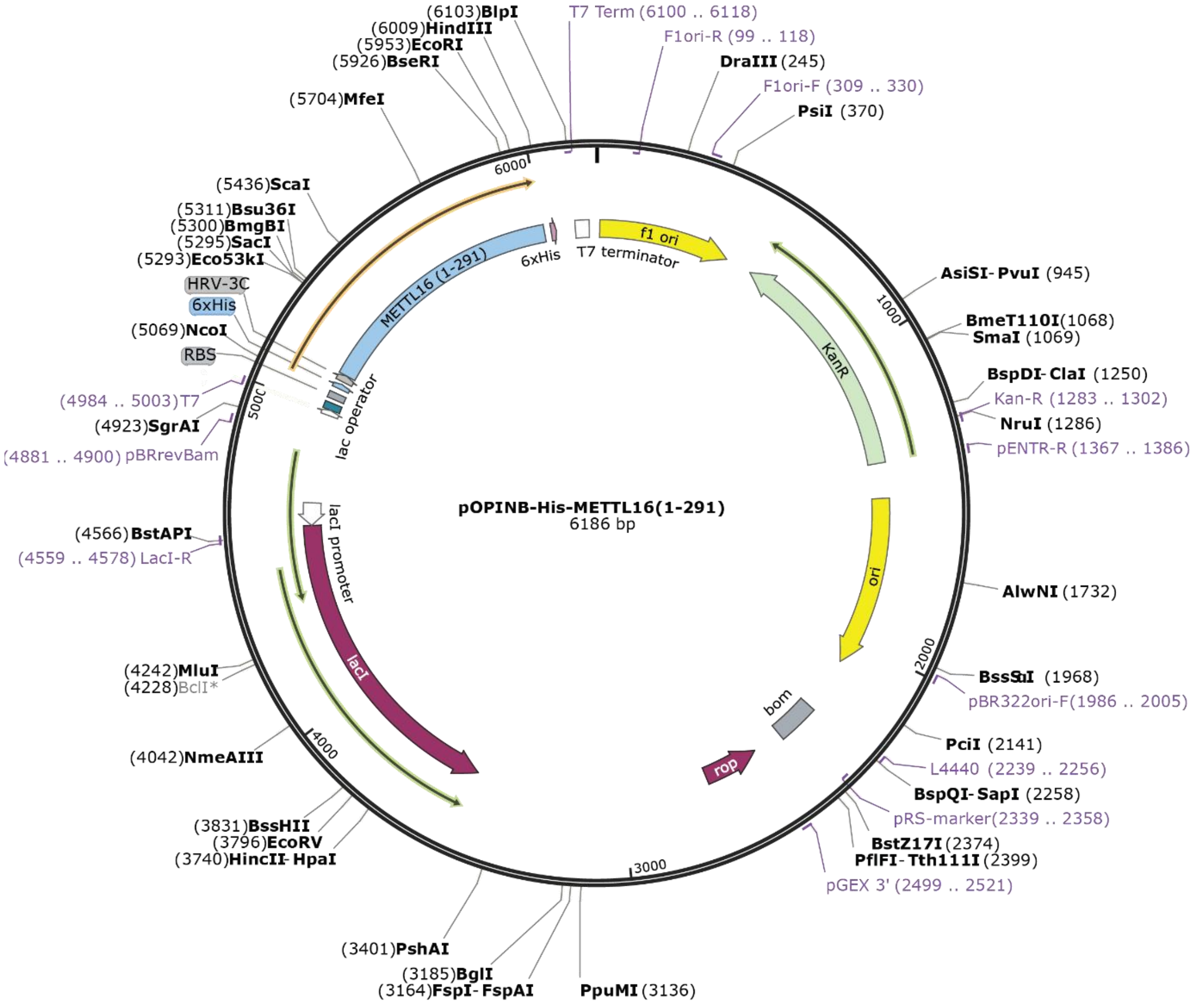

Plasmid pOPINB-His-METTL16 (1-291). pOPINB plasmid encodes the METTL16 MTD domain for METTL16 MTD protein purification.

4.2 Supplementary Figures

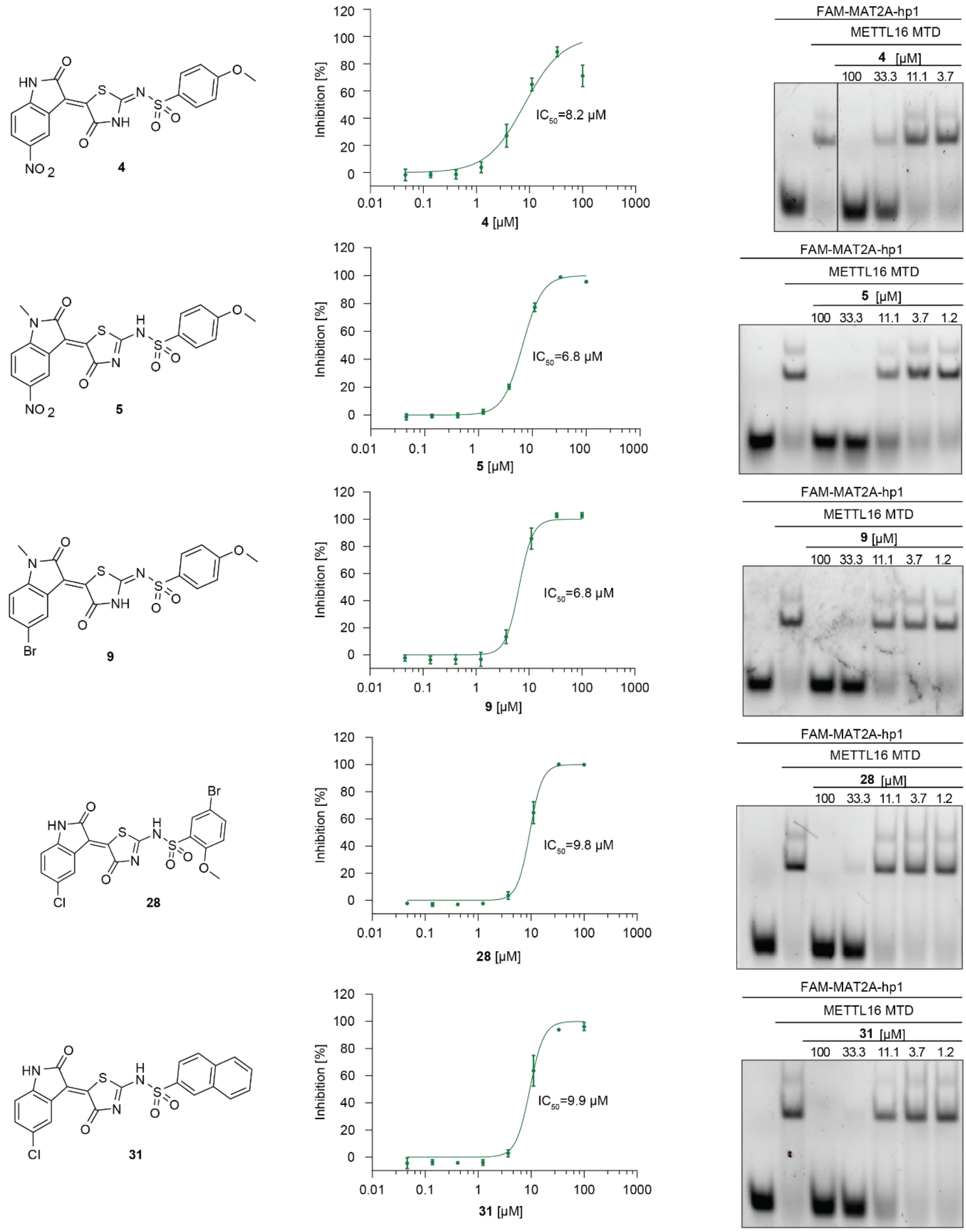

Figure. S1. **Structure and activities of compounds with single-digit micromolar IC$_{50}$ values.**

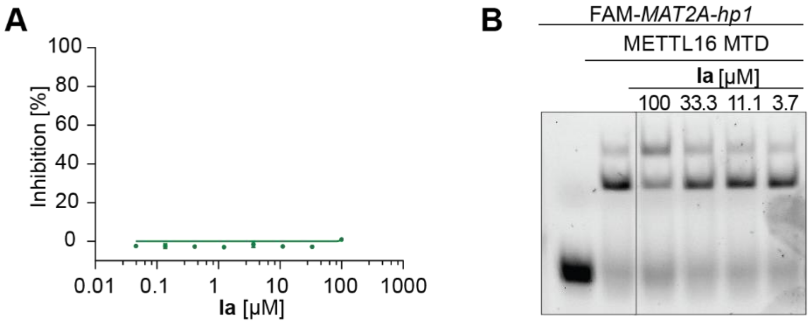

Figure. S2. **Ia is inactive against METTL16. (**A). activity of compound **Ia** measured by FP assay. (B). activity of compound **Ia** measured by EMSA.

4.3 Supplementary Tables

Table S1, X-ray crystallography data collection and refinement statistics for phosphorylated IRE1a in complex with IA107

	p-IRE1α /IA107
PDB ID	9GOW
Data collection	
Wavelength (Å)	0.9677
Resolution (Å)	45.06-3.0 (3.107-3.0)
Space group	P1
Cell dimension	
a, *b*, *c* (Å)	67.18, 77.5, 141.06
α, β, γ (°)	74.607, 78.089, 65.634
R_{merge}	0.2049 (2.029)
R_{meas}	0.2388 (2.355)
$I/\sigma(I)$	6.14 (0.79)
$CC_{1/2}$	0.989 (0.301)
Completeness (%)	91.89 (92.1)
Redundancy	3.8 (3.9)
Wilson *B* (Å^2)	78.24
Refinement	
Resolution (Å)	3.0
Number of reflections	45705
R_{work} / R_{free}	0.2312 / 0.2806
Number of atoms	
Protein	12263
Ligand	156
B factors (Å^2)	85.58
Protein (Å^2)	85.58
Ligand (Å^2)	85.59
R.m.s. d	
Bond lengths (Å)	0.003
Bond angles (°)	0.57
Ramachandran (favored/allowed/outlier) (%)	94/6/0
Copies/ a.s.u.	4

The dataset was collected from a single crystal. Statistics for the highest-resolution shell are shown in parentheses. r.m.s.d., root mean square deviation; a.s.u., asymmetric unit.

Table S2, Kinase profiling data of IA107 at 5 μM.

Kinase	**Technology**	**ATP(μM)**	**%Inhibition average**	**Dup Difference**
ABL1	ZLYTE	Km app	3	1
ACVR1B (ALK4)	ZLYTE	Km app	-5	6
AKT1 (PKB alpha)	ZLYTE	Km app	0	0
AMPK A1/B1/G1	ZLYTE	Km app	9	2
AURKA (Aurora A)	ZLYTE	Km app	5	1
BTK	ZLYTE	Km app	8	2
CAMK1D (CaMKI delta)	ZLYTE	Km app	8	0
CDK1/cyclin B	ZLYTE	Km app	4	1
CHEK1 (CHK1)	ZLYTE	Km app	10	12
CLK2	ZLYTE	Km app	7	1
CSNK1G2 (CK1 gamma 2)	ZLYTE	Km app	6	1
CSNK2A1 (CK2 alpha 1)	ZLYTE	Km app	6	2
DAPK3 (ZIPK)	ZLYTE	Km app	1	2
DNA-PK	ZLYTE	Km app	-2	0
DYRK1A	ZLYTE	Km app	4	1
DYRK3	ZLYTE	Km app	2	0
EEF2K	ZLYTE	Km app	5	2
EGFR (ErbB1)	ZLYTE	Km app	5	7
EPHA2	ZLYTE	Km app	4	2
EPHB4	ZLYTE	Km app	3	3
ERBB2 (HER2)	ZLYTE	Km app	-3	1
FGFR1	ZLYTE	Km app	4	0
FLT3	ZLYTE	Km app	6	2
FRAP1 (mTOR)	ZLYTE	Km app	5	0
GSK3B (GSK3 beta)	ZLYTE	Km app	21	1
HIPK4	ZLYTE	Km app	6	5

IGF1R	ZLYTE	Km app	3	3
IKBKB (IKK beta)	ZLYTE	Km app	4	1
IKBKE (IKK epsilon)	ZLYTE	Km app	2	3
INSR	ZLYTE	Km app	5	0
JAK3	ZLYTE	Km app	0	3
KDR (VEGFR2)	ZLYTE	Km app	1	1
KIT	ZLYTE	Km app	0	0
LCK	ZLYTE	Km app	8	3
MAP2K1 (MEK1)	ZLYTE	100	3	1
MAP2K6 (MKK6)	ZLYTE	100	2	4
MAPK1 (ERK2)	ZLYTE	Km app	2	1
MAPK14 (p38 alpha)	ZLYTE	100	6	1
MAPK8 (JNK1)	ZLYTE	100	-8	1
MAPKAPK2	ZLYTE	Km app	5	1
MARK2	ZLYTE	Km app	8	3
MET (cMet)	ZLYTE	Km app	3	2
NEK1	ZLYTE	Km app	17	7
NTRK2 (TRKB)	ZLYTE	Km app	5	1
PAK4	ZLYTE	Km app	-3	4
PDGFRB (PDGFR beta)	ZLYTE	Km app	0	2
PHKG2	ZLYTE	Km app	26	11
PIM1	ZLYTE	Km app	39	1
PLK1	ZLYTE	Km app	3	0
PRKACA (PKA)	ZLYTE	Km app	9	5
PRKCB1 (PKC beta I)	ZLYTE	Km app	7	1
PRKD1 (PKC mu)	ZLYTE	Km app	0	2
PTK2 (FAK)	ZLYTE	Km app	4	0
RET	ZLYTE	Km app	9	3

ROCK1	ZLYTE	Km app	1	2
RPS6KA3 (RSK2)	ZLYTE	Km app	1	0
RPS6KB1 (p70S6K)	ZLYTE	Km app	3	1
SGKL (SGK3)	ZLYTE	Km app	1	1
SRC	ZLYTE	Km app	4	4
STK4 (MST1)	ZLYTE	Km app	0	5
SYK	ZLYTE	Km app	3	1
TAOK2 (TAO1)	ZLYTE	Km app	-4	9
TEK (Tie2)	ZLYTE	Km app	6	7
GSG2 (Haspin)	Adapta	Km app	4	11
ACVR1 (ALK2)	LanthaScreen Binding		2	3
BMPR1B (ALK6)	LanthaScreen Binding		12	1
BMPR2	LanthaScreen Binding		-4	4
BRSK2	LanthaScreen Binding		1	3
CAMKK2 (CaMKK beta)	LanthaScreen Binding		4	8
CASK	LanthaScreen Binding		-14	23
CDC7/DBF4	LanthaScreen Binding		8	9
CDK8/cyclin C	LanthaScreen Binding		35	11
DDR2	LanthaScreen Binding		-1	2
ERN1 (IRE1α)	LanthaScreen Binding		91	7
ERN2 (IRE1β)	LanthaScreen Binding		70	6
ICK	LanthaScreen Binding		-2	4
LIMK1	LanthaScreen Binding		-16	8
MAP3K11 (MLK3)	LanthaScreen Binding		-3	0
MAP3K14 (NIK)	LanthaScreen Binding		0	0
MAP4K1 (HPK1)	LanthaScreen Binding		-2	10
MAPK15 (ERK7)	LanthaScreen Binding		17	5
MYO3B (MYO3 beta)	LanthaScreen Binding		-2	2

RIPK2	LanthaScreen Binding	0	2
STK32B (YANK2)	LanthaScreen Binding	2	13
STK33	LanthaScreen Binding	-4	6
STK38 (NDR)	LanthaScreen Binding	6	3
TGFBR1 (ALK5)	LanthaScreen Binding	54	6
TLK1	LanthaScreen Binding	-12	0
TNIK	LanthaScreen Binding	8	4
TTK	LanthaScreen Binding	6	1
ULK2	LanthaScreen Binding	-3	7

Inhibition% higher than 50% were marked in red color.

5. List of Abbreviations

Abbreviation	**Explanation**
AD	Alzheimer’s disease
ALKBH5	AlkB homolog 5
AML	acute myelogenous leukemia
ASO	antisense oligonucleotides
ATF6	activating transcription factor 6
ATP	adenosine triphosphate
bZIP60	basic leucine zipper 60
CCR4	carbon catabolite repression 4
CETSA	cellular thermal shift assay
CHD	coronary heart disease
CHOP	C/EBP homologous protein
CPSF	polyadenylation specificity factor
CRBN	cereblon
CRC	colorectal cancer
DSF	differential scanning fluorimetry
DSS	disuccinimidyl suberate
eIF	eukaryotic translation initiation factor
EMSA	electrophoretic mobility shift assay
ER	endoplasmic reticulum
FP	fluorescence polarization
FTO	obesity-associated protein
GADD34	growth arrest and DNA damage–inducible 34
HAA	hydroxy aryl aldehyde
HAC1	homologous to ATF/CREB 1
HD	Huntington's disease
HIF1α	hypoxia-inducing factor 1α
HTS	high-throughput screening
IRE1	inositol-requiring enzyme 1α
ITC	isothermal titration calorimetry
JNK	c-Jun N-terminal kinase
KEN	kinase extension nuclease
LC-MS	liquid chromatography–mass spectrometry
LD	luminal domain
lncRNA	long noncoding RNA
m^5C	5-methylcytidine
m^6A	N^6-methyladenosine
m^7G	7-methylguanosine
MALAT1	metastasis-associated lung adenocarcinoma transcript 1

MAT2A	methionine adenosyltransferase 2A
METTL14	methyltransferase-like protein 14
METTL16	methyltransferase-like proteins 16
METTL3	methyltransferase-like protein 3
miRNA	micro RNA
MST	microscale thermophoresis
MTD	methyltransferase domain
mtHTT	mutant huntingtin protein
NAFLD	nonalcoholic fatty liver disease
NOT	negative on TATA
NTP	nucleoside triphosphate
PABPC	cytoplasmic poly(A)-binding protein
PABPN	nuclear poly(A)-binding protein
PAN2	poly(A)-specific Nuclease 2
PAN3	poly(A)-specific Nuclease 3
PAP	poly(A) polymerase
PD	Parkinson’s disease
PDK4	pyruvate dehydrogenase kinase 4
PERK	double-stranded RNA-activated protein kinase (PKR)-like ER kinase
pre-mRNA	precursor mRNA
RBM15	RNA-binding motif protein 15
RIDD	IRE1-dependent decay
rRNA	ribosomal RNA
S1P	site-1 protease
S2P	site-2 protease
SAH	S-adenosylhomocysteine
SAM	S-adenosylmethionine
SAR	structure-activity relationship
siRNA	small interfering RNA
snRNA	small nuclear RNA
snRNPs	small nuclear ribonucleoproteins
SOGA1	suppressor of glucose autophagy associated 1
TNBC	triple-negative breast cancer
TRMT112	METTL5–tRNA methyltransferase 112 complex
tRNA	transfer RNA
UPR	unfolded protein response
UTR	untranslated region
VCR	vertebrate conserved regions
VHL	Von Hippel–Lindau tumor suppressor
VIRMA	Vir-like m^6A methyltransferase associated
WTAP	Wilms’ tumor 1-associated protein

XBP1	X-box binding protein 1
XRN1	5'-3' exoribonuclease 1
ZC3H13	zinc finger CCCH domain-containing protein 13
Ψ	Pseudouridine

6. References

1. Crick, F., Central dogma of molecular biology. *Nature* **1970,** *227* (5258), 561-3.

2. Crick, F. H., On protein synthesis. *Symp Soc Exp Biol* **1958,** *12*, 138-63.

3. Revyakin, A.; Zhang, Z. J.; Coleman, R. A.; Li, Y.; Inouye, C.; Lucas, J. K.; Park, S. R.; Chu, S.; Tjian, R., Transcription initiation by human RNA polymerase II visualized at single-molecule resolution. *Gene Dev* **2012,** *26* (15), 1691-1702.

4. Nudler, E., RNA Polymerase Active Center: The Molecular Engine of Transcription. *Annu Rev Biochem* **2009,** *78*, 335-361.

5. Han, Z.; Moore, G. A.; Mitter, R.; Martinez, D. L.; Wan, L.; Svejstrup, A. B. D.; Rueda, D. S.; Svejstrup, J. Q., DNA-directed termination of RNA polymerase II transcription. *Mol Cell* **2023,** *83* (18), 3253.

6. Consortium, E. P., An integrated encyclopedia of DNA elements in the human genome. *Nature* **2012,** *489* (7414), 57-74.

7. Cross, S. T.; Michalski, D.; Miller, M. R.; Wilusz, J., RNA regulatory processes in RNA virus biology. *Wiley Interdiscip Rev RNA* **2019,** *10* (5), e1536.

8. Boccaletto, P.; Stefaniak, F.; Ray, A.; Cappannini, A.; Mukherjee, S.; Purta, E.; Kurkowska, M.; Shirvanizadeh, N.; Destefanis, E.; Groza, P.; Avsar, G.; Romitelli, A.; Pir, P.; Dassi, E.; Conticello, S. G.; Aguilo, F.; Bujnicki, J. M., MODOMICS: a database of RNA modification pathways. 2021 update. *Nucleic Acids Res* **2022,** *50* (D1), D231-D235.

9. Sharma, B.; Prall, W.; Bhatia, G.; Gregory, B. D., The Diversity and Functions of Plant RNA Modifications: What We Know and Where We Go from Here. *Annu Rev Plant Biol* **2023,** *74*, 53-85.

10. Schaefer, M.; Kapoor, U.; Jantsch, M. F., Understanding RNA modifications: the promises and technological bottlenecks of the 'epitranscriptome'. *Open Biol* **2017,** *7* (5).

11. Monde, R. A.; Schuster, G.; Stern, D. B., Processing and degradation of chloroplast mRNA. *Biochimie* **2000,** *82* (6-7), 573-82.

12. Matera, A. G.; Terns, R. M.; Terns, M. P., Non-coding RNAs: lessons from the small nuclear and small nucleolar RNAs. *Nat Rev Mol Cell Biol* **2007,** *8* (3), 209-20.

13. Bird, J. G.; Zhang, Y.; Tian, Y.; Panova, N.; Barvik, I.; Greene, L.; Liu, M.; Buckley, B.; Krasny, L.; Lee, J. K.; Kaplan, C. D.; Ebright, R. H.; Nickels, B. E., The mechanism of RNA 5' capping with NAD+, NADH and desphospho-CoA. *Nature* **2016,** *535* (7612), 444-7.

14. Mancini, F.; Cahova, H., The Mysterious World of Non-Canonical Caps - What We Know and Why We Need New Sequencing Techniques. *Chembiochem* **2025,** *26* (3), e202400604.

15. Wahl, M. C.; Will, C. L.; Luhrmann, R., The spliceosome: design principles of a dynamic RNP machine. *Cell* **2009,** *136* (4), 701-18.

16. Sharp, P. A., The discovery of split genes and RNA splicing. *Trends Biochem Sci* **2005,** *30* (6), 279-81.

17. Wilkinson, M. E.; Charenton, C.; Nagai, K., RNA Splicing by the Spliceosome. *Annu Rev Biochem* **2020,** *89*, 359-388.

18. Zhan, X.; Lu, Y.; Zhang, X.; Yan, C.; Shi, Y., Mechanism of exon ligation by human spliceosome. *Mol Cell* **2022,** *82* (15), 2769-2778 e4.

19. Shi, Y., The Spliceosome: A Protein-Directed Metalloribozyme. *J Mol Biol* **2017,** *429* (17), 2640-2653.

20. Cech, T. R., Self-splicing RNA: implications for evolution. *Int Rev Cytol* **1985,** *93*, 3-22.

21. Schmidt, C. A.; Matera, A. G., tRNA introns: Presence, processing, and purpose. *Wiley Interdiscip Rev RNA* **2020,** *11* (3), e1583.

22. Yoshida, H.; Matsui, T.; Yamamoto, A.; Okada, T.; Mori, K., XBP1 mRNA is induced by ATF6 and spliced by IRE1 in response to ER stress to produce a highly active transcription factor. *Cell* **2001,** *107* (7), 881-891.

23. Mori, K.; Ogawa, N.; Kawahara, T.; Yanagi, H.; Yura, T., MRNA splicing-mediated C-terminal replacement of transcription factor Hac1p is required for efficient activation of the unfolded protein response. *P Natl Acad Sci USA* **2000,** *97* (9), 4660-4665.

24. Nagashima, Y.; Mishiba, K.; Suzuki, E.; Shimada, Y.; Iwata, Y.; Koizumi, N., Arabidopsis IRE1 catalyses unconventional splicing of mRNA to produce the active transcription factor. *Sci Rep-Uk* **2011,** *1*.

25. Le Thomas, A.; Ferri, E.; Marsters, S.; Harnoss, J. M.; Lawrence, D. A.; Zuazo-Gaztelu, I.; Modrusan, Z.; Chan, S.; Solon, M.; Chalouni, C.; Li, W.; Koeppen, H.; Rudolph, J.; Wang, W.; Wu, T. D.; Walter, P.; Ashkenazi, A., Decoding non-canonical mRNA decay by the endoplasmic-reticulum stress sensor IRE1alpha. *Nat Commun* **2021,** *12* (1), 7310.

26. Li, W. H.; Okreglak, V.; Peschek, J.; Kimmig, P.; Zubradt, M.; Weissman, J. S.; Walter, P., Engineering ER-stress dependent non-conventional mRNA splicing. *Elife* **2018,** *7*.

27. Lu, Y.; Liang, F. X.; Wang, X., A synthetic biology approach identifies the mammalian UPR RNA ligase RtcB. *Mol Cell* **2014,** *55* (5), 758-70.

28. Jurkin, J.; Henkel, T.; Nielsen, A. F.; Minnich, M.; Popow, J.; Kaufmann, T.; Heindl, K.; Hoffmann, T.; Busslinger, M.; Martinez, J., The mammalian tRNA ligase complex mediates splicing of XBP1 mRNA and controls antibody secretion in plasma cells. *EMBO J* **2014,** *33* (24), 2922-36.

29. Travers, K. J.; Patil, C. K.; Wodicka, L.; Lockhart, D. J.; Weissman, J. S.; Walter, P., Functional and genomic analyses reveal an essential coordination between the unfolded protein response and ER-associated degradation. *Cell* **2000,** *101* (3), 249-58.

30. Acosta-Alvear, D.; Zhou, Y.; Blais, A.; Tsikitis, M.; Lents, N. H.; Arias, C.; Lennon, C. J.; Kluger, Y.; Dynlacht, B. D., XBP1 controls diverse cell type- and condition-specific transcriptional regulatory networks. *Mol Cell* **2007,** *27* (1), 53-66.

31. Calfon, M.; Zeng, H.; Urano, F.; Till, J. H.; Hubbard, S. R.; Harding, H. P.; Clark, S. G.; Ron, D., IRE1 couples endoplasmic reticulum load to secretory capacity by processing the XBP-1 mRNA. *Nature* **2002,** *415* (6867), 92-6.

32. Ratni, H.; Ebeling, M.; Baird, J.; Bendels, S.; Bylund, J.; Chen, K. S.; Denk, N.; Feng, Z.; Green, L.; Guerard, M.; Jablonski, P.; Jacobsen, B.; Khwaja, O.; Kletzl, H.; Ko, C. P.; Kustermann, S.; Marquet, A.; Metzger, F.; Mueller, B.; Naryshkin, N. A.; Paushkin, S. V.; Pinard, E.; Poirier, A.; Reutlinger, M.; Weetall, M.; Zeller, A.; Zhao, X.; Mueller, L., Discovery of Risdiplam, a Selective Survival of Motor Neuron-2 (SMN2) Gene Splicing Modifier for the Treatment of Spinal Muscular Atrophy (SMA). *J Med Chem* **2018,** *61* (15), 6501-6517.

33. Neil, E. E.; Bisaccia, E. K., Nusinersen: A Novel Antisense Oligonucleotide for the Treatment of Spinal Muscular Atrophy. *J Pediatr Pharmacol Ther* **2019,** *24* (3), 194-203.

34. Seiler, M.; Yoshimi, A.; Darman, R.; Chan, B.; Keaney, G.; Thomas, M.; Agrawal, A. A.; Caleb, B.; Csibi, A.; Sean, E.; Fekkes, P.; Karr, C.; Klimek, V.; Lai, G.; Lee, L.; Kumar, P.; Lee, S. C.; Liu, X.; Mackenzie, C.; Meeske, C.; Mizui, Y.; Padron, E.; Park, E.; Pazolli, E.; Peng, S.; Prajapati, S.; Taylor, J.; Teng, T.; Wang, J.; Warmuth, M.; Yao, H.; Yu, L.; Zhu, P.; Abdel-Wahab, O.; Smith, P. G.; Buonamici, S., H3B-8800, an orally available small-molecule splicing modulator, induces lethality in spliceosome-mutant cancers. *Nat Med* **2018,** *24* (4), 497-504.

35. Folco, E. G.; Coil, K. E.; Reed, R., The anti-tumor drug E7107 reveals an essential role for SF3b in remodeling U2 snRNP to expose the branch point-binding region. *Genes Dev* **2011,** *25* (5), 440-4.

36. Sun, H.; Li, K.; Liu, C.; Yi, C., Regulation and functions of non-m(6)A mRNA modifications. *Nat Rev Mol Cell Biol* **2023,** *24* (10), 714-731.

37. Chu, J. M.; Ye, T. T.; Ma, C. J.; Lan, M. D.; Liu, T.; Yuan, B. F.; Feng, Y. Q., Existence of Internal N7-Methylguanosine Modification in mRNA Determined by Differential Enzyme Treatment Coupled with Mass Spectrometry Analysis. *ACS Chem Biol* **2018,** *13* (12), 3243-3250.

38. Zhang, L. S.; Liu, C.; Ma, H.; Dai, Q.; Sun, H. L.; Luo, G.; Zhang, Z.; Zhang, L.; Hu, L.; Dong, X.; He, C., Transcriptome-wide Mapping of Internal N(7)-Methylguanosine Methylome in Mammalian mRNA. *Mol Cell* **2019,** *74* (6), 1304-1316 e8.

39. Guy, M. P.; Phizicky, E. M., Two-subunit enzymes involved in eukaryotic post-transcriptional tRNA modification. *RNA Biol* **2014,** *11* (12), 1608-18.

40. Sloan, K. E.; Warda, A. S.; Sharma, S.; Entian, K. D.; Lafontaine, D. L. J.; Bohnsack, M. T., Tuning the ribosome: The influence of rRNA modification on eukaryotic ribosome biogenesis and function. *RNA Biol* **2017,** *14* (9), 1138-1152.

41. Yang, Y.; Wang, L.; Han, X.; Yang, W. L.; Zhang, M.; Ma, H. L.; Sun, B. F.; Li, A.; Xia, J.; Chen, J.; Heng, J.; Wu, B.; Chen, Y. S.; Xu, J. W.; Yang, X.; Yao, H.; Sun, J.; Lyu, C.; Wang, H. L.; Huang, Y.; Sun, Y. P.; Zhao, Y. L.; Meng, A.; Ma, J.; Liu, F.; Yang, Y. G., RNA 5-Methylcytosine Facilitates the Maternal-to-Zygotic Transition by Preventing Maternal mRNA Decay. *Mol Cell* **2019,** *75* (6), 1188-1202 e11.

42. Dai, Q.; Zhang, L. S.; Sun, H. L.; Pajdzik, K.; Yang, L.; Ye, C.; Ju, C. W.; Liu, S.; Wang, Y.; Zheng, Z.; Zhang, L.; Harada, B. T.; Dou, X.; Irkliyenko, I.; Feng, X.; Zhang, W.; Pan, T.; He, C., Quantitative sequencing using BID-seq uncovers abundant pseudouridines in mammalian mRNA at base resolution. *Nat Biotechnol* **2023,** *41* (3), 344-354.

43. Pendleton, K. E.; Chen, B.; Liu, K.; Hunter, O. V.; Xie, Y.; Tu, B. P.; Conrad, N. K., The U6 snRNA m(6)A Methyltransferase METTL16 Regulates SAM Synthetase Intron Retention. *Cell* **2017,** *169* (5), 824-835 e14.

44. Jia, G.; Fu, Y.; Zhao, X.; Dai, Q.; Zheng, G.; Yang, Y.; Yi, C.; Lindahl, T.; Pan, T.; Yang, Y. G.; He, C., N6-methyladenosine in nuclear RNA is a major substrate of the obesity-associated FTO. *Nat Chem Biol* **2011,** *7* (12), 885-7.

45. Liu, J.; Yue, Y.; Han, D.; Wang, X.; Fu, Y.; Zhang, L.; Jia, G.; Yu, M.; Lu, Z.; Deng, X.; Dai, Q.; Chen, W.; He, C., A METTL3-METTL14 complex mediates mammalian nuclear RNA N6-adenosine methylation. *Nat Chem Biol* **2014,** *10* (2), 93-5.

46. Zheng, G.; Dahl, J. A.; Niu, Y.; Fedorcsak, P.; Huang, C. M.; Li, C. J.; Vagbo, C. B.; Shi, Y.; Wang, W. L.; Song, S. H.; Lu, Z.; Bosmans, R. P.; Dai, Q.; Hao, Y. J.; Yang, X.; Zhao, W. M.; Tong, W. M.; Wang, X. J.; Bogdan, F.; Furu, K.; Fu, Y.; Jia, G.; Zhao, X.; Liu, J.; Krokan, H. E.; Klungland, A.; Yang, Y. G.; He, C., ALKBH5 is a mammalian RNA demethylase that impacts RNA metabolism and mouse fertility. *Mol Cell* **2013,** *49* (1), 18-29.

47. Wang, X.; Lu, Z.; Gomez, A.; Hon, G. C.; Yue, Y.; Han, D.; Fu, Y.; Parisien, M.; Dai, Q.; Jia, G.; Ren, B.; Pan, T.; He, C., N6-methyladenosine-dependent regulation of messenger RNA stability. *Nature* **2014,** *505* (7481), 117-20.

48. Wang, X.; Zhao, B. S.; Roundtree, I. A.; Lu, Z.; Han, D.; Ma, H.; Weng, X.; Chen, K.; Shi, H.; He, C., N(6)-methyladenosine Modulates Messenger RNA Translation Efficiency. *Cell* **2015,** *161* (6), 1388-99.

49. Du, H.; Zhao, Y.; He, J.; Zhang, Y.; Xi, H.; Liu, M.; Ma, J.; Wu, L., YTHDF2 destabilizes m(6)A-containing RNA through direct recruitment of the CCR4-NOT deadenylase complex. *Nat Commun* **2016,** *7*, 12626.

50. Frye, M.; Harada, B. T.; Behm, M.; He, C., RNA modifications modulate gene expression during development. *Science* **2018,** *361* (6409), 1346-1349.

51. Boo, S. H.; Kim, Y. K., The emerging role of RNA modifications in the regulation of mRNA stability. *Exp Mol Med* **2020,** *52* (3), 400-408.

52. Madugalle, S. U.; Meyer, K.; Wang, D. O.; Bredy, T. W., RNA N(6)-Methyladenosine and the Regulation of RNA Localization and Function in the Brain. *Trends Neurosci* **2020,** *43* (12), 1011-1023.

53. Karikó, K.; Muramatsu, H.; Welsh, F. A.; Ludwig, J.; Kato, H.; Akira, S.; Weissman, D., Incorporation of Pseudouridine Into mRNA Yields Superior Nonimmunogenic Vector With Increased Translational Capacity and Biological Stability. *Mol Ther* **2008,** *16* (11), 1833-1840.

54. Nance, K. D.; Meier, J. L., Modifications in an Emergency: The Role of N1-Methylpseudouridine in COVID-19 Vaccines. *Acs Central Sci* **2021,** *7* (5), 748-756.

55. Stockert, J. A.; Weil, R.; Yadav, K. K.; Kyprianou, N.; Tewari, A. K., Pseudouridine as a novel biomarker in prostate cancer. *Urol Oncol-Semin Ori* **2021,** *39* (1), 63-71.

56. Amuro, Y.; Nakaoka, H.; Shimomura, S.; Fujikura, M.; Yamamoto, T.; Tamura, S.; Hada, T.; Higashino, K., Serum Pseudouridine as a Biochemical Marker in Patients with Hepatocellular-Carcinoma. *Clin Chim Acta* **1988,** *178* (2), 151-158.

57. Yankova, E.; Blackaby, W.; Albertella, M.; Rak, J.; De Braekeleer, E.; Tsagkogeorga, G.; Pilka, E. S.; Aspris, D.; Leggate, D.; Hendrick, A. G.; Webster, N. A.; Andrews, B.; Fosbeary, R.; Guest, P.; Irigoyen, N.; Eleftheriou, M.; Gozdecka, M.; Dias, J. M. L.; Bannister, A. J.; Vick, B.; Jeremias, I.; Vassiliou, G. S.; Rausch, O.; Tzelepis, K.; Kouzarides, T., Small-molecule inhibition of METTL3 as a strategy against myeloid leukaemia. *Nature* **2021,** *593* (7860), 597.

58. Iles, M. M.; Law, M. H.; Stacey, S. N.; Han, J.; Fang, S.; Pfeiffer, R.; Harland, M.; Macgregor, S.; Taylor, J. C.; Aben, K. K.; Akslen, L. A.; Avril, M. F.; Azizi, E.; Bakker, B.; Benediktsdottir, K. R.; Bergman, W.; Scarra, G. B.; Brown, K. M.; Calista, D.; Chaudru, V.; Fargnoli, M. C.; Cust, A. E.; Demenais, F.; de Waal, A. C.; Debniak, T.; Elder, D. E.; Friedman, E.; Galan, P.; Ghiorzo, P.; Gillanders, E. M.; Goldstein, A. M.; Gruis, N. A.; Hansson, J.; Helsing, P.; Hocevar, M.; Hoiom, V.; Hopper, J. L.; Ingvar, C.; Janssen, M.; Jenkins, M. A.; Kanetsky, P. A.; Kiemeney, L. A.; Lang, J.; Lathrop, G. M.; Leachman, S.; Lee, J. E.; Lubinski, J.; Mackie, R. M.; Mann, G. J.; Martin, N. G.; Mayordomo, J. I.; Molven, A.; Mulder, S.; Nagore, E.; Novakovic, S.; Okamoto, I.; Olafsson, J. H.; Olsson, H.; Pehamberger, H.; Peris, K.; Grasa, M. P.; Planelles, D.; Puig, S.; Puig-Butille, J. A.; Randerson-Moor, J.; Requena, C.; Rivoltini, L.; Rodolfo, M.; Santinami, M.; Sigurgeirsson, B.; Snowden, H.; Song, F.; Sulem, P.; Thorisdottir, K.; Tuominen, R.; Van Belle, P.; van der Stoep, N.; van Rossum, M. M.; Wei, Q.; Wendt, J.; Zelenika, D.; Zhang, M.; Landi, M. T.; Thorleifsson, G.; Bishop, D. T.; Amos, C. I.; Hayward, N. K.; Stefansson, K.; Bishop, J. A.; Barrett, J. H.; Geno, M. E. L. C.; Q, M.; Investigators, A., A variant in FTO shows association with melanoma risk not due to BMI. *Nat Genet* **2013,** *45* (4), 428-32, 432e1.

59. Shi, L.; Yang, X. M.; Tang, D. D.; Liu, G.; Yuan, P.; Yang, Y.; Chang, L. S.; Zhang, L. R.; Song, D. K., Expression and significance of m1A transmethylase, hTrm6p/hTrm61p and its related gene hTrm6/hTrm61 in bladder urothelial carcinoma. *Am J Cancer Res* **2015,** *5* (7), 2169-79.

60. Passmore, L. A.; Coller, J., Roles of mRNA poly(A) tails in regulation of eukaryotic gene expression. *Nat Rev Mol Cell Biol* **2022,** *23* (2), 93-106.

61. Edmonds, M.; Vaughan, M. H., Jr.; Nakazato, H., Polyadenylic acid sequences in the heterogeneous nuclear RNA and rapidly-labeled polyribosomal RNA of HeLa cells: possible evidence for a precursor relationship. *Proc Natl Acad Sci U S A* **1971,** *68* (6), 1336-40.

62. Slater, D. W.; Slater, I.; Gillespie, D., Post-fertilization synthesis of polyadenylic acid in sea urchin embryos. *Nature* **1972,** *240* (5380), 333-7.

63. Slomovic, S.; Laufer, D.; Geiger, D.; Schuster, G., Polyadenylation of ribosomal RNA in human cells. *Nucleic Acids Res* **2006,** *34* (10), 2966-75.

64. Wigington, C. P.; Williams, K. R.; Meers, M. P.; Bassell, G. J.; Corbett, A. H., Poly(A) RNA-binding proteins and polyadenosine RNA: new members and novel functions. *Wiley Interdiscip Rev RNA* **2014,** *5* (5), 601-22.

65. Kumar, G. R.; Glaunsinger, B. A., Nuclear import of cytoplasmic poly(A) binding protein restricts gene expression via hyperadenylation and nuclear retention of mRNA. *Mol Cell Biol* **2010,** *30* (21), 4996-5008.

66. Jacobson, A.; Favreau, M., Possible involvement of poly(A) in protein synthesis. *Nucleic Acids Res* **1983,** *11* (18), 6353-68.

67. Brewer, G.; Ross, J., Poly(A) shortening and degradation of the 3' A+U-rich sequences of human c-myc mRNA in a cell-free system. *Mol Cell Biol* **1988,** *8* (4), 1697-708.

68. Eisen, T. J.; Eichhorn, S. W.; Subtelny, A. O.; Lin, K. S.; McGeary, S. E.; Gupta, S.; Bartel, D. P., The Dynamics of Cytoplasmic mRNA Metabolism. *Mol Cell* **2020,** *77* (4), 786-799 e10.

69. Garneau, N. L.; Wilusz, J.; Wilusz, C. J., The highways and byways of mRNA decay. *Nat Rev Mol Cell Biol* **2007,** *8* (2), 113-26.

70. Beelman, C. A.; Parker, R., Degradation of mRNA in eukaryotes. *Cell* **1995,** *81* (2), 179-83.

71. Liu, H.; Kiledjian, M., Decapping the message: a beginning or an end. *Biochem Soc Trans* **2006,** *34* (Pt 1), 35-8.

72. Mitchell, P.; Petfalski, E.; Shevchenko, A.; Mann, M.; Tollervey, D., The exosome: a conserved eukaryotic RNA processing complex containing multiple 3'-->5' exoribonucleases. *Cell* **1997,** *91* (4), 457-66.

73. Chen, C. Y.; Shyu, A. B., Mechanisms of deadenylation-dependent decay. *Wiley Interdiscip Rev RNA* **2011,** *2* (2), 167-83.

74. Fenger-Gron, M.; Fillman, C.; Norrild, B.; Lykke-Andersen, J., Multiple processing body factors and the ARE binding protein TTP activate mRNA decapping. *Mol Cell* **2005,** *20* (6), 905-15.

75. Ajiro, M.; Katagiri, T.; Ueda, K.; Nakagawa, H.; Fukukawa, C.; Lin, M. L.; Park, J. H.; Nishidate, T.; Daigo, Y.; Nakamura, Y., Involvement of RQCD1 overexpression, a novel cancer-testis antigen, in the Akt pathway in breast cancer cells. *Int J Oncol* **2009,** *35* (4), 673-81.

76. Pal, S.; Gordijenko, I.; Schmeing, S.; Biswas, S.; Akbulut, Y.; Gasper, R.; 't Hart, P., Stapled Peptides as Inhibitors of mRNA Deadenylation. *Angew Chem Int Edit* **2025,** *64* (1).

77. Tong, Y. Q.; Lee, Y.; Liu, X. H.; Childs-Disney, J. L.; Suresh, B. M.; Benhamou, R. I.; Yang, C. Y.; Li, W. M.; Costales, M. G.; Haniff, H. S.; Sievers, S.; Abegg, D.; Wegner, T.; Paulisch, T. O.; Lekah, E.; Grefe, M.; Crynen, G.; Van Meter, M.; Wang, T. H.; Gibaut, Q. M. R.; Cleveland, J. L.; Adibekian, A.; Glorius, F.; Waldmann, H.; Disney, M. D., Programming inactive RNA-binding small molecules into bioactive degraders. *Nature* **2023,** *618* (7963), 169.

78. Meyer, S. M.; Tanaka, T.; Zanon, P. R. A.; Baisden, J. T.; Abegg, D.; Yang, X.; Akahori, Y.; Alshakarchi, Z.; Cameron, M. D.; Adibekian, A.; Disney, M. D., DNA-Encoded Library Screening To Inform Design of a Ribonuclease Targeting Chimera (RiboTAC). *J Am Chem Soc* **2022,** *144* (46), 21096-21102.

79. Almanza, A.; Carlesso, A.; Chintha, C.; Creedican, S.; Doultsinos, D.; Leuzzi, B.; Luís, A.; McCarthy, N.; Montibeller, L.; More, S.; Papaioannou, A.; Püschel, F.; Sassano, M. L.; Skoko, J.; Agostinis, P.; de Belleroche, J.; Eriksson, L. A.; Fulda, S.; Gorman, A. M.; Healy, S.; Kozlov, A.; Muñoz-Pinedo, C.; Rehm, M.; Chevet, E.; Samali, A., Endoplasmic reticulum stress signalling - from basic mechanisms to clinical applications. *Febs J* **2019,** *286* (2), 241-278.

80. Wang, M.; Kaufman, R. J., The impact of the endoplasmic reticulum protein-folding environment on cancer development. *Nat Rev Cancer* **2014,** *14* (9), 581-597.

81. Tabas, I.; Ron, D., Integrating the mechanisms of apoptosis induced by endoplasmic reticulum stress. *Nature Cell Biology* **2011,** *13* (3), 184-190.

82. Ron, D.; Walter, P., Signal integration in the endoplasmic reticulum unfolded protein response. *Nat Rev Mol Cell Biol* **2007,** *8* (7), 519-29.

83. Kopp, M. C.; Larburu, N.; Durairaj, V.; Adams, C. J.; Ali, M. M. U., UPR proteins IRE1 and PERK switch BiP from chaperone to ER stress sensor. *Nat Struct Mol Biol* **2019,** *26* (11), 1053-1062.

84. Zhou, J.; Liu, C. Y.; Back, S. H.; Clark, R. L.; Peisach, D.; Xu, Z.; Kaufman, R. J., The crystal structure of human IRE1 luminal domain reveals a conserved dimerization interface required for activation of the unfolded protein response. *Proc Natl Acad Sci U S A* **2006,** *103* (39), 14343-8.

85. Moore, K.; Hollien, J., Ire1-mediated decay in mammalian cells relies on mRNA sequence, structure, and translational status. *Mol Biol Cell* **2015,** *26* (16), 2873-84.

86. Hollien, J.; Lin, J. H.; Li, H.; Stevens, N.; Walter, P.; Weissman, J. S., Regulated Ire1-dependent decay of messenger RNAs in mammalian cells. *J Cell Biol* **2009,** *186* (3), 323-31.

87. Hollien, J.; Weissman, J. S., Decay of endoplasmic reticulum-localized mRNAs during the unfolded protein response. *Science* **2006,** *313* (5783), 104-7.

88. Nishitoh, H.; Matsuzawa, A.; Tobiume, K.; Saegusa, K.; Takeda, K.; Inoue, K.; Hori, S.; Kakizuka, A.; Ichijo, H., ASK1 is essential for endoplasmic reticulum stress-induced neuronal cell death triggered by expanded polyglutamine repeats. *Genes Dev* **2002,** *16* (11), 1345-55.

89. Huang, M.; Xu, A.; Wu, X.; Zhang, Y.; Guo, Y.; Guo, F.; Pan, Z.; Kong, L., Japanese encephalitis virus induces apoptosis by the IRE1/JNK pathway of ER stress response in BHK-21 cells. *Arch Virol* **2016,** *161* (3), 699-703.

90. Haze, K.; Yoshida, H.; Yanagi, H.; Yura, T.; Mori, K., Mammalian transcription factor ATF6 is synthesized as a transmembrane protein and activated by proteolysis in response to endoplasmic reticulum stress. *Mol Biol Cell* **1999,** *10* (11), 3787-99.

91. Ye, J.; Rawson, R. B.; Komuro, R.; Chen, X.; Dave, U. P.; Prywes, R.; Brown, M. S.; Goldstein, J. L., ER stress induces cleavage of membrane-bound ATF6 by the same proteases that process SREBPs. *Mol Cell* **2000,** *6* (6), 1355-64.

92. Wu, J.; Rutkowski, D. T.; Dubois, M.; Swathirajan, J.; Saunders, T.; Wang, J.; Song, B.; Yau, G. D.; Kaufman, R. J., ATF6alpha optimizes long-term endoplasmic reticulum function to protect cells from chronic stress. *Dev Cell* **2007,** *13* (3), 351-64.

93. Vattem, K. M.; Wek, R. C., Reinitiation involving upstream ORFs regulates ATF4 mRNA translation in mammalian cells. *Proc Natl Acad Sci U S A* **2004,** *101* (31), 11269-74.

94. Han, J.; Back, S. H.; Hur, J.; Lin, Y. H.; Gildersleeve, R.; Shan, J.; Yuan, C. L.; Krokowski, D.; Wang, S.; Hatzoglou, M.; Kilberg, M. S.; Sartor, M. A.; Kaufman, R. J., ER-stress-induced transcriptional regulation increases protein synthesis leading to cell death. *Nat Cell Biol* **2013,** *15* (5), 481-90.

95. Hetz, C.; Zhang, K.; Kaufman, R. J., Mechanisms, regulation and functions of the unfolded protein response. *Nat Rev Mol Cell Biol* **2020,** *21* (8), 421-438.

96. Marciniak, S. J.; Yun, C. Y.; Oyadomari, S.; Novoa, I.; Zhang, Y.; Jungreis, R.; Nagata, K.; Harding, H. P.; Ron, D., CHOP induces death by promoting protein synthesis and oxidation in the stressed endoplasmic reticulum. *Genes Dev* **2004,** *18* (24), 3066-77.

97. Tsaytler, P.; Harding, H. P.; Ron, D.; Bertolotti, A., Selective inhibition of a regulatory subunit of protein phosphatase 1 restores proteostasis. *Science* **2011,** *332* (6025), 91-4.

98. Oakes, S. A.; Papa, F. R., The role of endoplasmic reticulum stress in human pathology. *Annu Rev Pathol* **2015,** *10*, 173-94.

99. Logue, S. E.; McGrath, E. P.; Cleary, P.; Greene, S.; Mnich, K.; Almanza, A.; Chevet, E.; Dwyer, R. M.; Oommen, A.; Legembre, P.; Godey, F.; Madden, E. C.; Leuzzi, B.; Obacz, J.; Zeng, Q.; Patterson, J. B.; Jager, R.; Gorman, A. M.; Samali, A., Inhibition of IRE1 RNase activity modulates the tumor cell secretome and enhances response to chemotherapy. *Nat Commun* **2018,** *9* (1), 3267.

100. Chen, X.; Iliopoulos, D.; Zhang, Q.; Tang, Q.; Greenblatt, M. B.; Hatziapostolou, M.; Lim, E.; Tam, W. L.; Ni, M.; Chen, Y.; Mai, J.; Shen, H.; Hu, D. Z.; Adoro, S.; Hu, B.; Song, M.; Tan, C.; Landis, M. D.; Ferrari, M.; Shin, S. J.; Brown, M.; Chang, J. C.; Liu, X. S.; Glimcher, L. H., XBP1 promotes triple-negative breast cancer by controlling the HIF1alpha pathway. *Nature* **2014,** *508* (7494), 103-107.

101. Song, M.; Sandoval, T. A.; Chae, C. S.; Chopra, S.; Tan, C.; Rutkowski, M. R.; Raundhal, M.; Chaurio, R. A.; Payne, K. K.; Konrad, C.; Bettigole, S. E.; Shin, H. R.; Crowley, M. J. P.; Cerliani, J. P.; Kossenkov, A. V.; Motorykin, I.; Zhang, S.; Manfredi, G.; Zamarin, D.; Holcomb, K.; Rodriguez, P. C.; Rabinovich, G. A.; Conejo-Garcia, J. R.; Glimcher, L. H.; Cubillos-Ruiz, J. R., IRE1alpha-XBP1 controls T cell function in ovarian cancer by regulating mitochondrial activity. *Nature* **2018,** *562* (7727), 423-428.

102. Chen, L.; Bi, M.; Zhang, Z.; Du, X.; Chen, X.; Jiao, Q.; Jiang, H., The functions of IRE1alpha in neurodegenerative diseases: Beyond ER stress. *Ageing Res Rev* **2022,** *82*, 101774.

103. Sha, H.; He, Y.; Yang, L.; Qi, L., Stressed out about obesity: IRE1alpha-XBP1 in metabolic disorders. *Trends Endocrinol Metab* **2011,** *22* (9), 374-81.

104. Shan, B.; Wang, X.; Wu, Y.; Xu, C.; Xia, Z.; Dai, J.; Shao, M.; Zhao, F.; He, S.; Yang, L.; Zhang, M.; Nan, F.; Li, J.; Liu, J.; Liu, J.; Jia, W.; Qiu, Y.; Song, B.; Han, J. J.; Rui, L.; Duan, S. Z.; Liu, Y., The metabolic ER stress sensor IRE1alpha suppresses alternative activation of macrophages and impairs energy expenditure in obesity. *Nat Immunol* **2017,** *18* (5), 519-529.

105. Keestra-Gounder, A. M.; Byndloss, M. X.; Seyffert, N.; Young, B. M.; Chavez-Arroyo, A.; Tsai, A. Y.; Cevallos, S. A.; Winter, M. G.; Pham, O. H.; Tiffany, C. R.; de Jong, M. F.; Kerrinnes, T.; Ravindran, R.; Luciw, P. A.; McSorley, S. J.; Baumler, A. J.; Tsolis, R. M., NOD1 and NOD2 signalling links ER stress with inflammation. *Nature* **2016,** *532* (7599), 394-7.

106. Chen, X.; Cubillos-Ruiz, J. R., Endoplasmic reticulum stress signals in the tumour and its microenvironment. *Nat Rev Cancer* **2021,** *21* (2), 71-88.

107. Wu, M.; Zhang, L.; Pi, L.; Liu, L.; Wang, S.; Wu, Y.; Pan, H.; Liu, M.; Yi, Z., IRE1alpha inhibitor enhances paclitaxel sensitivity of triple-negative breast cancer cells. *Cell Oncol (Dordr)* **2024,** *47* (5), 1797-1809.

108. Tang, C. H.; Ranatunga, S.; Kriss, C. L.; Cubitt, C. L.; Tao, J.; Pinilla-Ibarz, J. A.; Del Valle, J. R.; Hu, C. C., Inhibition of ER stress-associated IRE-1/XBP-1 pathway reduces leukemic cell survival. *J Clin Invest* **2014,** *124* (6), 2585-98.

109. Carrasco, D. R.; Sukhdeo, K.; Protopopova, M.; Sinha, R.; Enos, M.; Carrasco, D. E.; Zheng, M.; Mani, M.; Henderson, J.; Pinkus, G. S.; Munshi, N.; Horner, J.; Ivanova, E. V.; Protopopov, A.; Anderson, K. C.; Tonon, G.; DePinho, R. A., The differentiation and stress response factor XBP-1 drives multiple myeloma pathogenesis. *Cancer Cell* **2007,** *11* (4), 349-60.

110. Sheng, X.; Arnoldussen, Y. J.; Storm, M.; Tesikova, M.; Nenseth, H. Z.; Zhao, S.; Fazli, L.; Rennie, P.; Risberg, B.; Waehre, H.; Danielsen, H.; Mills, I. G.; Jin, Y.; Hotamisligil, G.; Saatcioglu, F., Divergent androgen regulation of unfolded protein response pathways drives prostate cancer. *EMBO Mol Med* **2015,** *7* (6), 788-801.

111. Le Reste, P. J.; Pineau, R.; Voutetakis, K.; Samal, J.; Jegou, G.; Lhomond, S.; Gorman, A. M.; Samali, A.; Patterson, J. B.; Zeng, Q.; Pandit, A.; Aubry, M.; Soriano, N.; Etcheverry, A.; Chatziioannou, A.; Mosser, J.; Avril, T.; Chevet, E., Local intracerebral inhibition of IRE1 by MKC8866 sensitizes glioblastoma to irradiation/chemotherapy in vivo. *Cancer Lett* **2020,** *494*, 73-83.

112. Pavlovic, N.; Calitz, C.; Thanapirom, K.; Mazza, G.; Rombouts, K.; Gerwins, P.; Heindryckx, F., Inhibiting IRE1alpha-endonuclease activity decreases tumor burden in a mouse model for hepatocellular carcinoma. *Elife* **2020,** *9*.

113. Lucas, D.; Sarkar, T.; Niemeyer, C. Y.; Harnoss, J. C.; Schneider, M.; Strowitzki, M. J.; Harnoss, J. M., IRE1 is a promising therapeutic target in pancreatic cancer. *Am J Physiol Cell Physiol* **2025,** *328* (3), C806-C824.

114. Lazaro, D. F.; Bellucci, A.; Brundin, P.; Outeiro, T. F., Editorial: Protein Misfolding and Spreading Pathology in Neurodegenerative Diseases. *Front Mol Neurosci* **2019,** *12*, 312.

115. Duran-Aniotz, C.; Cornejo, V. H.; Espinoza, S.; Ardiles, A. O.; Medinas, D. B.; Salazar, C.; Foley, A.; Gajardo, I.; Thielen, P.; Iwawaki, T.; Scheper, W.; Soto, C.; Palacios, A. G.; Hoozemans, J. J. M.; Hetz, C., IRE1 signaling exacerbates Alzheimer's disease pathogenesis. *Acta Neuropathol* **2017,** *134* (3), 489-506.

116. Yan, C.; Liu, J.; Gao, J.; Sun, Y.; Zhang, L.; Song, H.; Xue, L.; Zhan, L.; Gao, G.; Ke, Z.; Liu, Y.; Liu, J., IRE1 promotes neurodegeneration through autophagy-dependent neuron death in the Drosophila model of Parkinson's disease. *Cell Death Dis* **2019,** *10* (11), 800.

117. Lee, H.; Noh, J. Y.; Oh, Y.; Kim, Y.; Chang, J. W.; Chung, C. W.; Lee, S. T.; Kim, M.; Ryu, H.; Jung, Y. K., IRE1 plays an essential role in ER stress-mediated aggregation of mutant huntingtin via the inhibition of autophagy flux. *Hum Mol Genet* **2012,** *21* (1), 101-14.

118. Raymundo, D. P.; Doultsinos, D.; Guillory, X.; Carlesso, A.; Eriksson, L. A.; Chevet, E., Pharmacological Targeting of IRE1 in Cancer. *Trends Cancer* **2020,** *6* (12), 1018-1030.

119. Gabrail, N. Y.; Hamilton, E. P.; Elias, A. D.; Rimawi, M. F.; Li, C.; Corvez, M. M.; Li, W.; Feng, Y.; Wei, J.; Greene, S.; Patterson, J.; Zeng, Q. P.; Hui, A. M., A phase 1/2 trial of ORIN1001, a first-in-class IRE1 inhibitor, in patients with advanced solid tumors. *J Clin Oncol* **2021,** *39* (15).

120. Martino, M. B.; Jones, L.; Brighton, B.; Ehre, C.; Abdulah, L.; Davis, C. W.; Ron, D.; O'Neal, W. K.; Ribeiro, C. M. P., The ER stress transducer IRE1β is required for airway epithelial mucin production. *Mucosal Immunol* **2013,** *6* (3), 639-654.

121. Tsuru, A.; Fujimoto, N.; Takahashi, S.; Saito, M.; Nakamura, D.; Iwano, M.; Iwawaki, T.; Kadokura, H.; Ron, D.; Kohno, K., Negative feedback by IRE1β optimizes mucin production in goblet cells. *P Natl Acad Sci USA* **2013,** *110* (8), 2864-2869.

122. Iwawaki, T.; Hosoda, A.; Okuda, T.; Kamigori, Y.; Nomura-Furuwatari, C.; Kimata, Y.; Tsuru, A.; Kohno, K., Translational control by the ER transmembrane kinase/ribonuclease IRE1 under ER stress. *Nature Cell Biology* **2001,** *3* (2), 158-164.

123. Cloots, E.; Simpson, M. S.; De Nolf, C.; Lencer, W. I.; Janssens, S.; Grey, M. J., Evolution and function of the epithelial cell-specific ER stress sensor IRE1β. *Mucosal Immunol* **2021,** *14* (6), 1235-1246.

124. Amin-Wetzel, N.; Neidhardt, L.; Yan, Y.; Mayer, M. P.; Ron, D., Unstructured regions in IRE1alpha specify BiP-mediated destabilisation of the luminal domain dimer and repression of the UPR. *Elife* **2019,** *8*.

125. Ali, M. M. U.; Bagratuni, T.; Davenport, E. L.; Nowak, P. R.; Silva-Santisteban, M. C.; Hardcastle, A.; McAndrews, C.; Rowlands, M. G.; Morgan, G. J.; Aherne, W.; Collins, I.; Davies, F. E.; Pearl, L. H., Structure of the Ire1 autophosphorylation complex and implications for the unfolded protein response. *Embo Journal* **2011,** *30* (5), 894-905.

126. Ferri, E.; Le Thomas, A.; Wallweber, H. A.; Day, E. S.; Walters, B. T.; Kaufman, S. E.; Braun, M. G.; Clark, K. R.; Beresini, M. H.; Mortara, K.; Chen, Y. A.; Canter, B.; Phung, W.; Liu, P. S.; Lammens, A.; Ashkenazi, A.; Rudolph, J.; Wang, W., Activation of the IRE1 RNase through remodeling of the kinase front pocket by ATP-competitive ligands. *Nat Commun* **2020,** *11* (1), 6387.

127. Ali, M. M.; Bagratuni, T.; Davenport, E. L.; Nowak, P. R.; Silva-Santisteban, M. C.; Hardcastle, A.; McAndrews, C.; Rowlands, M. G.; Morgan, G. J.; Aherne, W.; Collins, I.; Davies, F. E.; Pearl, L. H., Structure of the Ire1 autophosphorylation complex and implications for the unfolded protein response. *EMBO J* **2011,** *30* (5), 894-905.

128. Ron, D.; Hubbard, S. R., How IRe1 reacts to ER stress. *Cell* **2008,** *132* (1), 24-26.

129. Lee, K. P. K.; Dey, M.; Neculai, D.; Cao, C.; Dever, T. E.; Sicheri, F., Structure of the dual enzyme ire1 reveals the basis for catalysis and regulation in nonconventional RNA splicing. *Cell* **2008,** *132* (1), 89-100.

130. Langlais, T.; Pelizzari-Raymundo, D.; Mahdizadeh, S. J.; Gouault, N.; Carreaux, F.; Chevet, E.; Eriksson, L. A.; Guillory, X., Structural and molecular bases to IRE1 activity modulation. *Biochem J* **2021,** *478* (15), 2953-2975.

131. Korennykh, A. V.; Egea, P. F.; Korostelev, A. A.; Finer-Moore, J.; Zhang, C.; Shokat, K. M.; Stroud, R. M.; Walter, P., The unfolded protein response signals through high-order assembly of Ire1. *Nature* **2009,** *457* (7230), 687-93.

132. Korennykh, A. V.; Korostelev, A. A.; Egea, P. F.; Finer-Moore, J.; Stroud, R. M.; Zhang, C.; Shokat, K. M.; Walter, P., Structural and functional basis for RNA cleavage by Ire1. *BMC Biol* **2011,** *9*, 47.

133. Mendez, A. S.; Alfaro, J.; Morales-Soto, M. A.; Dar, A. C.; McCullagh, E.; Gotthardt, K.; Li, H.; Acosta-Alvear, D.; Sidrauski, C.; Korennykh, A. V.; Bernales, S.; Shokat, K. M.; Walter, P., Endoplasmic reticulum stress-independent activation of unfolded protein response kinases by a small molecule ATP-mimic. *Elife* **2015,** *4*.

134. Newbatt, Y.; Hardcastle, A.; McAndrew, P. C.; Strover, J. A.; Mirza, A.; Morgan, G. J.; Burke, R.; Davies, F. E.; Collins, I.; van Montfort, R. L., Identification of autophosphorylation inhibitors of the inositol-requiring enzyme 1 alpha (IRE1alpha) by high-throughput screening using a DELFIA assay. *J Biomol Screen* **2013,** *18* (3), 298-308.

135. Joshi, A.; Newbatt, Y.; McAndrew, P. C.; Stubbs, M.; Burke, R.; Richards, M. W.; Bhatia, C.; Caldwell, J. J.; McHardy, T.; Collins, I.; Bayliss, R., Molecular mechanisms of human IRE1 activation through dimerization and ligand binding. *Oncotarget* **2015,** *6* (15), 13019-13035.

136. Feldman, H. C.; Tong, M.; Wang, L.; Meza-Acevedo, R.; Gobillot, T. A.; Lebedev, I.; Gliedt, M. J.; Hari, S. B.; Mitra, A. K.; Backes, B. J.; Papa, F. R.; Seeliger, M. A.; Maly, D. J., Structural and Functional Analysis of the Allosteric Inhibition of IRE1α with ATP-Competitive Ligands. *ACS Chemical Biology* **2016,** *11* (8), 2195-2205.

137. Grandjean, J. M. D.; Madhavan, A.; Cech, L.; Seguinot, B. O.; Paxman, R. J.; Smith, E.; Scampavia, L.; Powers, E. T.; Cooley, C. B.; Plate, L.; Spicer, T. P.; Kelly, J. W.; Wiseman, R. L., Pharmacologic IRE1/XBP1s activation confers targeted ER proteostasis reprogramming. *Nat Chem Biol* **2020,** *16* (10), 1052.

138. Sun, J.; Lee, K.; Kutseikin, S.; Guerrero, A.; Rius, B.; Madhavan, A.; Buasakdi, C.; Cheong, K. N.; Chatterjee, P.; Rosen, D. A.; Yoon, L.; Ardejani, M. S.; Mendoza, A.; Rosarda, J. D.; Saez, E.; Kelly, J. W.; Wiseman, R. L., Identification of a Selective Pharmacologic IRE1/XBP1s Activator with Enhanced Tissue Exposure. *Acs Chemical Biology* **2025,** *20* (5), 993-1003.

139. Wang, L. K.; Perera, B. G. K.; Hari, S. B.; Bhhatarai, B.; Backes, B. J.; Seeliger, M. A.; Schürer, S. C.; Oakes, S. A.; Papa, F. R.; Maly, D. J., Divergent allosteric control of the IRE1α endoribonuclease using kinase inhibitors. *Nat Chem Biol* **2012,** *8* (12), 982-989.

140. Thamsen, M.; Ghosh, R.; Auyeung, V. C.; Brumwell, A.; Chapman, H. A.; Backes, B. J.; Perara, G.; Maly, D. J.; Sheppard, D.; Papa, F. R., Small molecule inhibition of IRE1α kinase/RNase has anti-fibrotic effects in the lung. *Plos One* **2019,** *14* (1).

141. Harrington, P. E.; Biswas, K.; Malwitz, D.; Tasker, A. S.; Mohr, C.; Andrews, K. L.; Dellamaggiore, K.; Kendall, R.; Beckmann, H.; Jaeckel, P.; Materna-Reichelt, S.; Allen, J. R.; Lipford, J. R., Unfolded Protein Response in Cancer: IRE1alpha Inhibition by Selective Kinase Ligands Does Not Impair Tumor Cell Viability. *ACS Med Chem Lett* **2015,** *6* (1), 68-72.

142. Concha, N. O.; Smallwood, A.; Bonnette, W.; Totoritis, R.; Zhang, G.; Federowicz, K.; Yang, J.; Qi, H.; Chen, S.; Campobasso, N.; Choudhry, A. E.; Shuster, L. E.; Evans, K. A.; Ralph, J.; Sweitzer, S.; Heerding, D. A.; Buser, C. A.; Su, D. S.; DeYoung, M. P., Long-Range Inhibitor-Induced Conformational Regulation of Human IRE1alpha Endoribonuclease Activity. *Mol Pharmacol* **2015,** *88* (6), 1011-23.

143. Colombano, G.; Caldwell, J. J.; Matthews, T. P.; Bhatia, C.; Joshi, A.; McHardy, T.; Mok, N. Y.; Newbatt, Y.; Pickard, L.; Strover, J.; Hedayat, S.; Walton, M. I.; Myers, S. M.; Jones, A. M.; Saville, H.; McAndrew, C.; Burke, R.; Eccles, S. A.; Davies, F. E.; Bayliss, R.; Collins, I., Binding to an Unusual Inactive Kinase Conformation by Highly Selective Inhibitors of Inositol-Requiring Enzyme 1alpha Kinase-Endoribonuclease. *J Med Chem* **2019,** *62* (5), 2447-2465.

144. Cross, B. C.; Bond, P. J.; Sadowski, P. G.; Jha, B. K.; Zak, J.; Goodman, J. M.; Silverman, R. H.; Neubert, T. A.; Baxendale, I. R.; Ron, D.; Harding, H. P., The molecular basis for selective inhibition of unconventional mRNA splicing by an IRE1-binding small molecule. *Proc Natl Acad Sci U S A* **2012,** *109* (15), E869-78.

145. Volkmann, K.; Lucas, J. L.; Vuga, D.; Wang, X.; Brumm, D.; Stiles, C.; Kriebel, D.; Der-Sarkissian, A.; Krishnan, K.; Schweitzer, C.; Liu, Z.; Malyankar, U. M.; Chiovitti, D.; Canny, M.; Durocher, D.; Sicheri, F.; Patterson, J. B., Potent and selective inhibitors of the inositol-requiring enzyme 1 endoribonuclease. *J Biol Chem* **2011,** *286* (14), 12743-55.

146. Sanches, M.; Duffy, N. M.; Talukdar, M.; Thevakumaran, N.; Chiovitti, D.; Canny, M. D.; Lee, K.; Kurinov, I.; Uehling, D.; Al-awar, R.; Poda, G.; Prakesch, M.; Wilson, B.; Tam, V.; Schweitzer, C.; Toro, A.; Lucas, J. L.; Vuga, D.; Lehmann, L.; Durocher, D.; Zeng, Q.; Patterson, J. B.; Sicheri, F., Structure and mechanism of action of the hydroxy-aryl-aldehyde class of IRE1 endoribonuclease inhibitors. *Nat Commun* **2014,** *5*, 4202.

147. Ri, M.; Tashiro, E.; Oikawa, D.; Shinjo, S.; Tokuda, M.; Yokouchi, Y.; Narita, T.; Masaki, A.; Ito, A.; Ding, J.; Kusumoto, S.; Ishida, T.; Komatsu, H.; Shiotsu, Y.; Ueda, R.; Iwawaki, T.; Imoto, M.; Iida, S., Identification of Toyocamycin, an agent cytotoxic for multiple myeloma cells, as a potent inhibitor of ER stress-induced XBP1 mRNA splicing. *Blood Cancer J* **2012,** *2* (7), e79.

148. Jiang, D.; Lynch, C.; Medeiros, B. C.; Liedtke, M.; Bam, R.; Tam, A. B.; Yang, Z.; Alagappan, M.; Abidi, P.; Le, Q. T.; Giaccia, A. J.; Denko, N. C.; Niwa, M.; Koong, A. C., Identification of Doxorubicin as an Inhibitor of the IRE1alpha-XBP1 Axis of the Unfolded Protein Response. *Sci Rep* **2016,** *6*, 33353.

149. Sepich-Poore, C.; Zheng, Z.; Schmitt, E.; Wen, K.; Zhang, Z. S.; Cui, X. L.; Dai, Q.; Zhu, A. C.; Zhang, L.; Sanchez Castillo, A.; Tan, H.; Peng, J.; Zhuang, X.; He, C.; Nachtergaele, S., The METTL5-TRMT112 N(6)-methyladenosine methyltransferase complex regulates mRNA translation via 18S rRNA methylation. *J Biol Chem* **2022,** *298* (3), 101590.

150. Ma, H.; Wang, X.; Cai, J.; Dai, Q.; Natchiar, S. K.; Lv, R.; Chen, K.; Lu, Z.; Chen, H.; Shi, Y. G.; Lan, F.; Fan, J.; Klaholz, B. P.; Pan, T.; Shi, Y.; He, C., N(6-)Methyladenosine methyltransferase ZCCHC4 mediates ribosomal RNA methylation. *Nat Chem Biol* **2019,** *15* (1), 88-94.

151. Schwartz, S.; Mumbach, M. R.; Jovanovic, M.; Wang, T.; Maciag, K.; Bushkin, G. G.; Mertins, P.; Ter-Ovanesyan, D.; Habib, N.; Cacchiarelli, D.; Sanjana, N. E.; Freinkman, E.; Pacold, M. E.; Satija, R.; Mikkelsen, T. S.; Hacohen, N.; Zhang, F.; Carr, S. A.; Lander, E. S.; Regev, A., Perturbation of m6A Writers Reveals Two Distinct Classes of mRNA Methylation at Internal and 5′ Sites. *Cell Rep* **2014,** *8* (1), 284-296.

152. Su, S.; Li, S.; Deng, T.; Gao, M.; Yin, Y.; Wu, B.; Peng, C.; Liu, J.; Ma, J.; Zhang, K., Cryo-EM structures of human m(6)A writer complexes. *Cell Res* **2022,** *32* (11), 982-994.

153. Doxtader, K. A.; Wang, P.; Scarborough, A. M.; Seo, D.; Conrad, N. K.; Nam, Y., Structural Basis for Regulation of METTL16, an S-Adenosylmethionine Homeostasis Factor. *Molecular Cell* **2018,** *71* (6), 1001.

154. Satterwhite, E. R.; Mansfield, K. D., RNA methyltransferase METTL16: Targets and function. *Wiley Interdiscip Rev RNA* **2022,** *13* (2), e1681.

155. Lan, Q.; Liu, P. Y.; Bell, J. L.; Wang, J. Y.; Huttelmaier, S.; Zhang, X. D.; Zhang, L.; Liu, T., The Emerging Roles of RNA m(6)A Methylation and Demethylation as Critical Regulators of Tumorigenesis, Drug Sensitivity, and Resistance. *Cancer Res* **2021,** *81* (13), 3431-3440.

156. You, Y. Z.; Fu, Y. D.; Huang, M. J.; Shen, D. D.; Zhao, B.; Liu, H. M.; Zheng, Y. C.; Huang, L. H., Recent Advances of m6A Demethylases Inhibitors and Their Biological Functions in Human Diseases. *Int J Mol Sci* **2022,** *23* (10).

157. Li, G. W.; Chen, W.; Liu, D.; Tang, S. B., Recent advances in medicinal chemistry strategies for the development of METTL3 inhibitors. *European Journal of Medicinal Chemistry* **2025,** *290*.

158. Dolbois, A.; Bedi, R. K.; Bochenkova, E.; Müller, A.; Moroz-Omori, E. V.; Huang, D. Z.; Caflisch, A., 1,4,9-Triazaspiro[5.5]undecan-2-one Derivatives as Potent and Selective METTL3 Inhibitors. *Journal of Medicinal Chemistry* **2021,** *64* (17), 12738-12760.

159. Dutheuil, G.; Oukoloff, K.; Korac, J.; Lenoir, F.; El Bousmaqui, M.; Probst, N.; Lapin, A.; Nakhabina, G.; Sorlet, C.; Parmentier, N.; Karila, D.; Ghavtadze, N.; Casault, P.; Claridge, S.; Sapmaz, S.; Slater, M. J.; Fraser, G. L., Discovery, Optimization, and Preclinical Pharmacology of EP652, a METTL3 Inhibitor with Efficacy in Liquid and Solid Tumor Models. *Journal of Medicinal Chemistry* **2025,** *68* (3), 2981-3003.

160. Hwang, K.; Bae, J.; Jhe, Y. L.; Kim, J.; Cheong, J. H.; Choi, H. S.; Sim, T., Targeted degradation of METTL3 against acute myeloid leukemia and gastric cancer. *Eur J Med Chem* **2024,** *279*, 116843.

161. Errani, F.; Invernizzi, A.; Herok, M.; Bochenkova, E.; Stamm, F.; Corbeski, I.; Romanucci, V.; Di Fabio, G.; Zalesak, F.; Caflisch, A., Proteolysis Targeting Chimera Degraders of the METTL3-14 m(6)A-RNA Methyltransferase. *JACS Au* **2024,** *4* (2), 713-729.

162. Du, W.; Huang, Y.; Chen, X.; Deng, Y.; Sun, Y.; Yang, H.; Shi, Q.; Wu, F.; Liu, G.; Huang, H.; Ding, J.; Huang, X.; Xu, S., Discovery of a PROTAC degrader for METTL3-METTL14 complex. *Cell Chem Biol* **2024,** *31* (1), 177-183 e17.

163. Gao, S.; Li, X.; Zhang, M.; Zhang, N.; Wang, R.; Chang, J., Structural characteristics of small-molecule inhibitors targeting FTO demethylase. *Future Med Chem* **2021,** *13* (17), 1475-1489.

164. Micaelli, M.; Vedove, A. D.; Cerofolini, L.; Vigna, J.; Sighel, D.; Zaccara, S.; Bonomo, I.; Poulentzas, G.; Rosatti, E. F.; Cazzanelli, G.; Alunno, L.; Belli, R.; Peroni, D.; Dassi, E.; Murakami, S.; Jaffrey, S. R.; Fragai, M.; Mancini, I.; Lolli, G.; Quattrone, A.; Provenzani, A., Small-Molecule Ebselen Binds to YTHDF Proteins Interfering with the Recognition of N6-Methyladenosine-Modified RNAs. *Acs Pharmacol Transl* **2022,** *5* (10), 872-891.

165. Zálesák, F.; Nai, F.; Herok, M.; Bochenkova, E.; Bedi, R. K.; Li, Y. Z.; Errani, F.; Caflisch, A., Structure-Based Design of a Potent and Selective YTHDC1 Ligand. *Journal of Medicinal Chemistry* **2024,** *67* (11), 9516-9535.

166. Fang, Z.; Mu, B.; Liu, Y.; Guo, N.; Xiong, L.; Guo, Y.; Xia, A.; Zhang, R.; Zhang, H.; Yao, R.; Fan, Y.; Li, L.; Yang, S.; Xiang, R., Discovery of a potent, selective and cell active inhibitor of m(6)A demethylase ALKBH5. *Eur J Med Chem* **2022,** *238*, 114446.

167. Mitra, A.; Manna, S.; Kundu, R.; Hazra, D.; Roychowdhury, A., Brute Force Virtual Drug Screening with Molecular Dynamics Simulation and MM/PBSA to Find Potent Inhibitors of METTL16. *Ieee Acm T Comput Bi* **2023,** *20* (3), 2356-2361.

168. Mendel, M.; Chen, K. M.; Homolka, D.; Gos, P.; Pandey, R. R.; McCarthy, A. A.; Pillai, R. S., Methylation of Structured RNA by the m(6)A Writer METTL16 Is Essential for Mouse Embryonic Development. *Mol Cell* **2018,** *71* (6), 986-1000 e11.

169. Ruszkowska, A.; Ruszkowski, M.; Dauter, Z.; Brown, J. A., Structural insights into the RNA methyltransferase domain of METTL16. *Scientific Reports* **2018,** *8*.

170. Oerum, S.; Meynier, V.; Catala, M.; Tisne, C., A comprehensive review of m6A/m6Am RNA methyltransferase structures. *Nucleic Acids Res* **2021,** *49* (13), 7239-7255.

171. Aoyama, T.; Yamashita, S.; Tomita, K., Mechanistic insights into m(6)A modification of U6 snRNA by human METTL16. *Nucleic Acids Research* **2020,** *48* (9), 5157-5168.

172. Murray, B.; Antonyuk, S. V.; Marina, A.; Van Liempd, S. M.; Lu, S. C.; Mato, J. M.; Hasnain, S. S.; Rojas, A. L., Structure and function study of the complex that synthesizes S-adenosylmethionine. *IUCrJ* **2014,** *1* (Pt 4), 240-9.

173. Shima, H.; Matsumoto, M.; Ishigami, Y.; Ebina, M.; Muto, A.; Sato, Y.; Kumagai, S.; Ochiai, K.; Suzuki, T.; Igarashi, K., S-Adenosylmethionine Synthesis Is Regulated by Selective N(6)-Adenosine Methylation and mRNA Degradation Involving METTL16 and YTHDC1. *Cell Rep* **2017,** *21* (12), 3354-3363.

174. Mroczek, S.; Dziembowski, A., U6 RNA biogenesis and disease association. *Wiley Interdiscip Rev RNA* **2013,** *4* (5), 581-92.

175. Brown, J. A.; Kinzig, C. G.; DeGregorio, S. J.; Steitz, J. A., Methyltransferase-like protein 16 binds the 3'-terminal triple helix of MALAT1 long noncoding RNA. *Proc Natl Acad Sci U S A* **2016,** *113* (49), 14013-14018.

176. Breger, K.; Brown, J. A., Elucidating the Kinetic Mechanism of Human METTL16. *Biochemistry* **2023,** *62* (2), 494-506.

177. Warda, A. S.; Kretschmer, J.; Hackert, P.; Lenz, C.; Urlaub, H.; Hobartner, C.; Sloan, K. E.; Bohnsack, M. T., Human METTL16 is a N(6)-methyladenosine (m(6)A) methyltransferase that targets pre-mRNAs and various non-coding RNAs. *EMBO Rep* **2017,** *18* (11), 2004-2014.

178. Nance, D. J.; Satterwhite, E. R.; Bhaskar, B.; Misra, S.; Carraway, K. R.; Mansfield, K. D., Characterization of METTL16 as a cytoplasmic RNA binding protein. *Plos One* **2020,** *15* (1), e0227647.

179. Barone, S.; Cerchia, C.; Summa, V.; Brindisi, M., Methyl-Transferase-Like Protein 16 (METTL16): The Intriguing Journey of a Key Epitranscriptomic Player Becoming an Emerging Biological Target. *J Med Chem* **2024,** *67* (17), 14786-14806.

180. Su, R.; Dong, L.; Li, Y.; Gao, M.; He, P. C.; Liu, W.; Wei, J.; Zhao, Z.; Gao, L.; Han, L.; Deng, X.; Li, C.; Prince, E.; Tan, B.; Qing, Y.; Qin, X.; Shen, C.; Xue, M.; Zhou, K.; Chen, Z.; Xue, J.; Li, W.; Qin, H.; Wu, X.; Sun, M.; Nam, Y.; Chen, C. W.; Huang, W.; Horne, D.; Rosen, S. T.; He, C.; Chen, J., METTL16 exerts an m(6)A-independent function to facilitate translation and tumorigenesis. *Nat Cell Biol* **2022,** *24* (2), 205-216.

181. Wang, F.; Zhang, J.; Lin, X.; Yang, L.; Zhou, Q.; Mi, X.; Li, Q.; Wang, S.; Li, D.; Liu, X. M.; Zhou, J., METTL16 promotes translation and lung tumorigenesis by sequestering cytoplasmic eIF4E2. *Cell Rep* **2023,** *42* (3), 112150.

182. Dai, Y. Z.; Liu, Y. D.; Li, J.; Chen, M. T.; Huang, M.; Wang, F.; Yang, Q. S.; Yuan, J. H.; Sun, S. H., METTL16 promotes hepatocellular carcinoma progression through downregulating RAB11B-AS1 in an m(6)A-dependent manner. *Cell Mol Biol Lett* **2022,** *27* (1), 41.

183. Wei, W.; Zhang, Z. Y.; Shi, B.; Cai, Y.; Zhang, H. S.; Sun, C. L.; Fei, Y. F.; Zhong, W.; Zhang, S.; Wang, C.; He, B.; Jiang, G. M.; Wang, H., METTL16 promotes glycolytic metabolism reprogramming and colorectal cancer progression. *J Exp Clin Cancer Res* **2023,** *42* (1), 151.

184. Tang, J.; Zhao, X.; Wei, W.; Liu, W.; Fan, H.; Liu, X. P.; Li, Y.; Wang, L.; Guo, J., METTL16-mediated translation of CIDEA promotes non-alcoholic fatty liver disease progression via m6A-dependent manner. *PeerJ* **2022,** *10*, e14379.

185. Peng, Q.; Zhang, H.; Li, Z., Methyltransferase-like 16 drives diabetic nephropathy progression via epigenetic suppression of V-set pre-B cell surrogate light chain 3. *Life Sci* **2025,** *374*, 123694.

186. Ruan, R.; Zhang, Y., METTL16 Contributes to Coronary Heart Disease by Inducing TET2 m6A Modification. *J Inflamm Res* **2025,** *18*, 6821-6830.

187. Prischi, F.; Nowak, P. R.; Carrara, M.; Ali, M. M., Phosphoregulation of Ire1 RNase splicing activity. *Nat Commun* **2014,** *5*, 3554.

188. Lee, K. P.; Dey, M.; Neculai, D.; Cao, C.; Dever, T. E.; Sicheri, F., Structure of the dual enzyme Ire1 reveals the basis for catalysis and regulation in nonconventional RNA splicing. *Cell* **2008,** *132* (1), 89-100.

189. Harnoss, J. M.; Le Thomas, A.; Shemorry, A.; Marsters, S. A.; Lawrence, D. A.; Lu, M.; Chen, Y. C. A.; Qing, J.; Totpal, K.; Kan, D.; Segal, E.; Merchant, M.; Reichelt, M.; Wallweber, H. A.; Wang, W. R.; Clark, K.; Kaufman, S.; Beresini, M. H.; Laing, S. T.; Sandoval, W.; Lorenzo, M.; Wu, J. S.; Lyh, J.; De Bruyn, T.; Heidersbach, A.; Haley, B.; Gogineni, A.; Weimer, R. M.; Lee, D.; Braun, M. G.; Rudolph, J.; VanWyngarden, M. J.; Sherbenou, D. W.; Gomez-Bougie, P.; Amiot, M.; Acosta-Alvear, D.; Walter, P.; Ashkenazi, A., Disruption of IRE1 alpha through its kinase domain attenuates multiple myeloma. *P Natl Acad Sci USA* **2019,** *116* (33), 16420-16429.

190. Korennykh, A. V.; Egea, P. F.; Korostelev, A. A.; Finer-Moore, J.; Zhang, C.; Shokat, K. M.; Stroud, R. M.; Walter, P., The unfolded protein response signals through high-order assembly of Ire1. *Nature* **2009,** *457* (7230), 687-U2.

191. Zhou, J. H.; Liu, C. Y.; Back, S. H.; Clark, R. L.; Peisach, D.; Xu, Z. H.; Kaufman, R. J., The crystal structure of human IRE1 luminal domain reveals a conserved dimerization interface required for activation of the unfolded protein response. *P Natl Acad Sci USA* **2006,** *103* (39), 14343-14348.

192. Wang, L.; Perera, B. G.; Hari, S. B.; Bhhatarai, B.; Backes, B. J.; Seeliger, M. A.; Schurer, S. C.; Oakes, S. A.; Papa, F. R.; Maly, D. J., Divergent allosteric control of the IRE1alpha endoribonuclease using kinase inhibitors. *Nat Chem Biol* **2012,** *8* (12), 982-9.

193. Upton, J. P.; Wang, L.; Han, D.; Wang, E. S.; Huskey, N. E.; Lim, L.; Truitt, M.; McManus, M. T.; Ruggero, D.; Goga, A.; Papa, F. R.; Oakes, S. A., IRE1alpha cleaves select microRNAs during ER stress to derepress translation of proapoptotic Caspase-2. *Science* **2012,** *338* (6108), 818-22.

194. Volkamer, A.; Eid, S.; Turk, S.; Jaeger, S.; Rippmann, F.; Fulle, S., Pocketome of human kinases: prioritizing the ATP binding sites of (yet) untapped protein kinases for drug discovery. *J Chem Inf Model* **2015,** *55* (3), 538-49.

195. Menichetti, R.; Kanekal, K. H.; Bereau, T., Drug-Membrane Permeability across Chemical Space. *Acs Central Sci* **2019,** *5* (2), 290-298.

196. Bertolotti, A.; Zhang, Y.; Hendershot, L. M.; Harding, H. P.; Ron, D., Dynamic interaction of BiP and ER stress transducers in the unfolded-protein response. *Nat Cell Biol* **2000,** *2* (6), 326-32.

197. Sravanthi, T. V.; Manju, S. L., Indoles - A promising scaffold for drug development. *Eur J Pharm Sci* **2016,** *91*, 1-10.

198. Ghosh, R.; Wang, L.; Wang, E. S.; Perera, B. G.; Igbaria, A.; Morita, S.; Prado, K.; Thamsen, M.; Caswell, D.; Macias, H.; Weiberth, K. F.; Gliedt, M. J.; Alavi, M. V.; Hari, S. B.; Mitra, A. K.; Bhhatarai, B.; Schurer, S. C.; Snapp, E. L.; Gould, D. B.; German, M. S.; Backes, B. J.; Maly, D. J.; Oakes, S. A.; Papa, F. R., Allosteric inhibition of the IRE1alpha RNase preserves cell viability and function during endoplasmic reticulum stress. *Cell* **2014,** *158* (3), 534-48.

199. Fralish, Z.; Chen, A.; Khan, S.; Zhou, P.; Reker, D., The landscape of small-molecule prodrugs. *Nat Rev Drug Discov* **2024,** *23* (5), 365-380.

200. Zerfas, B. L.; Liu, Y.; Che, J.; Donovan, K. A.; Hatcher, J. M.; Huerta, F.; Metivier, R. J.; Nowak, R. P.; Ragosta, L.; Tsang, T.; Fischer, E. S.; Jones, L. H., Structure-guided design of a truncated heterobivalent chemical probe degrader of IRE1alpha. *RSC Med Chem* **2025**.

201. Clamp, M.; Fry, B.; Kamal, M.; Xie, X.; Cuff, J.; Lin, M. F.; Kellis, M.; Lindblad-Toh, K.; Lander, E. S., Distinguishing protein-coding and noncoding genes in the human genome. *Proc Natl Acad Sci U S A* **2007,** *104* (49), 19428-33.

202. Tong, Y.; Zhang, P.; Yang, X.; Liu, X.; Zhang, J.; Grudniewska, M.; Jung, I.; Abegg, D.; Liu, J.; Childs-Disney, J. L.; Gibaut, Q. M. R.; Haniff, H. S.; Adibekian, A.; Mouradian, M. M.; Disney, M. D., Decreasing the intrinsically disordered protein alpha-synuclein levels by targeting its structured mRNA with a ribonuclease-targeting chimera. *Proc Natl Acad Sci U S A* **2024,** *121* (2), e2306682120.

203. Dai, J.; Jiang, X.; da Silva-Junior, E. F.; Du, S.; Liu, X.; Zhan, P., Recent advances in the molecular design and applications of viral RNA-targeting antiviral modalities. *Drug Discov Today* **2024,** *29* (8), 104074.

204. Su, X. X.; Ma, W. X.; Feng, D.; Cheng, B. Y.; Wang, Q.; Guo, Z. F.; Zhou, D. M.; Tang, X. J., Efficient Inhibition of SARS-CoV-2 Using Chimeric Antisense Oligonucleotides through RNase L Activation**. *Angew Chem Int Edit* **2021,** *60* (40), 21662-21667.

205. Aldrich, C.; Bertozzi, C.; Georg, G. I.; Kiessling, L.; Lindsley, C.; Liotta, D.; Merz, K. M., Jr.; Schepartz, A.; Wang, S., The Ecstasy and Agony of Assay Interference Compounds. *ACS Cent Sci* **2017,** *3* (3), 143-147.

206. Warda, A. S.; Kretschmer, J.; Hackert, P.; Lenz, C.; Urlaub, H.; Hobartner, C.; Sloan, K. E.; Bohnsack, M. T., Human METTL16 is a N-6-methyladenosine (m(6)A) methyltransferase that targets pre-mRNAs and various non-coding RNAs. *Embo Rep* **2017,** *18* (11), 2004-2014.

207. Andronescu, M.; Aguirre-Hernandez, R.; Condon, A.; Hoos, H. H., RNAsoft: A suite of RNA secondary structure prediction and design software tools. *Nucleic Acids Res* **2003,** *31* (13), 3416-22.

208. Zhu, Y.; Zhu, L.; Wang, X.; Jin, H., RNA-based therapeutics: an overview and prospectus. *Cell Death Dis* **2022,** *13* (7), 644.

209. Chery, J., RNA therapeutics: RNAi and antisense mechanisms and clinical applications. *Postdoc J* **2016,** *4* (7), 35-50.

210. Keefe, A. D.; Pai, S.; Ellington, A., Aptamers as therapeutics. *Nature Reviews Drug Discovery* **2010,** *9* (7), 537-550.

211. Sheng, X.; Nenseth, H. Z.; Qu, S.; Kuzu, O. F.; Frahnow, T.; Simon, L.; Greene, S.; Zeng, Q.; Fazli, L.; Rennie, P. S.; Mills, I. G.; Danielsen, H.; Theis, F.; Patterson, J. B.; Jin, Y.; Saatcioglu, F., IRE1alpha-XBP1s pathway promotes prostate cancer by activating c-MYC signaling. *Nat Commun* **2019,** *10* (1), 323.

212. Zhao, N.; Cao, J.; Xu, L. Y.; Tang, Q. Z.; Dobrolecki, L. E.; Lv, X. D.; Talukdar, M.; Lu, Y.; Wang, X. R.; Hu, D. Z.; Shi, Q.; Xiang, Y.; Wang, Y. F.; Liu, X.; Bu, W.; Jiang, Y.; Li, M. Z.; Gong, Y. Y.; Sun, Z.; Ying, H. Q.; Yuan, B.; Lin, X.; Feng, X. H.; Hartig, S. M.; Li, F.; Shen, H. F.; Chen, Y. W.; Han, L.; Zeng, Q. P.; Patterson, J. B.; Kaipparettu, B. A.; Putluri, N.; Sicheri, F.; Rosen, J. M.; Lewis, M. T.; Chen, X., Pharmacological targeting of MYC-regulated IRE1/XBP1 pathway suppresses MYC-driven breast cancer. *J Clin Invest* **2018,** *128* (4), 1283-1299.

213. Le Reste, P. J.; Pineau, R.; Voutetakis, K.; Samal, J.; Jegou, G.; Lhomond, S.; Gorman, A. M.; Samali, A.; Patterson, J. B.; Zeng, Q. P.; Pandit, A.; Aubry, M.; Soriano, N.; Etcheverry, A.; Chatziioannou, A.; Mosser, J.; Avril, T.; Chevet, E., Local intracerebral inhibition of IRE1 by MKC8866 sensitizes glioblastoma to irradiation/chemotherapy in vivo. *Cancer Lett* **2020,** *494*, 73-83.

214. Madhavan, A.; Kok, B. P.; Rius, B.; Grandjean, J. M. D.; Alabi, A.; Albert, V.; Sukiasyan, A.; Powers, E. T.; Galmozzi, A.; Saez, E.; Wiseman, R. L., Pharmacologic IRE1/XBP1s activation promotes systemic adaptive remodeling in obesity. *Nature Communications* **2022,** *13* (1).

215. Hetz, C.; Saxena, S., ER stress and the unfolded protein response in neurodegeneration. *Nat Rev Neurol* **2017,** *13* (8), 477-491.

216. Chopra, S.; Giovanelli, P.; Alvarado-Vazquez, P. A.; Alonso, S.; Song, M.; Sandoval, T. A.; Chae, C. S.; Tan, C.; Fonseca, M. M.; Gutierrez, S.; Jimenez, L.; Subbaramaiah, K.; Iwawaki, T.; Kingsley, P. J.; Marnett, L. J.; Kossenkov, A. V.; Crespo, M. S.; Dannenberg, A. J.; Glimcher, L. H.;

Romero-Sandoval, E. A.; Cubillos-Ruiz, J. R., IRE1 alpha-XBP1 signaling in leukocytes controls prostaglandin biosynthesis and pain. *Science* **2019,** *365* (6450), 248.

217. Kabsch, W., Xds. *Acta Crystallogr D Biol Crystallogr* **2010,** *66* (Pt 2), 125-32.

218. McCoy, A. J.; Grosse-Kunstleve, R. W.; Adams, P. D.; Winn, M. D.; Storoni, L. C.; Read, R. J., Phaser crystallographic software. *J Appl Crystallogr* **2007,** *40* (Pt 4), 658-674.

219. Liebschner, D.; Afonine, P. V.; Baker, M. L.; Bunkoczi, G.; Chen, V. B.; Croll, T. I.; Hintze, B.; Hung, L. W.; Jain, S.; McCoy, A. J.; Moriarty, N. W.; Oeffner, R. D.; Poon, B. K.; Prisant, M. G.; Read, R. J.; Richardson, J. S.; Richardson, D. C.; Sammito, M. D.; Sobolev, O. V.; Stockwell, D. H.; Terwilliger, T. C.; Urzhumtsev, A. G.; Videau, L. L.; Williams, C. J.; Adams, P. D., Macromolecular structure determination using X-rays, neutrons and electrons: recent developments in Phenix. *Acta Crystallogr D Struct Biol* **2019,** *75* (Pt 10), 861-877.

220. Long, F.; Nicholls, R. A.; Emsley, P.; Graaeulis, S.; Merkys, A.; Vaitkus, A.; Murshudov, G. N., AceDRG: a stereochemical description generator for ligands. *Acta Crystallogr D Struct Biol* **2017,** *73* (Pt 2), 112-122.

221. Agirre, J.; Atanasova, M.; Bagdonas, H.; Ballard, C. B.; Basle, A.; Beilsten-Edmands, J.; Borges, R. J.; Brown, D. G.; Burgos-Marmol, J. J.; Berrisford, J. M.; Bond, P. S.; Caballero, I.; Catapano, L.; Chojnowski, G.; Cook, A. G.; Cowtan, K. D.; Croll, T. I.; Debreczeni, J. E.; Devenish, N. E.; Dodson, E. J.; Drevon, T. R.; Emsley, P.; Evans, G.; Evans, P. R.; Fando, M.; Foadi, J.; Fuentes-Montero, L.; Garman, E. F.; Gerstel, M.; Gildea, R. J.; Hatti, K.; Hekkelman, M. L.; Heuser, P.; Hoh, S. W.; Hough, M. A.; Jenkins, H. T.; Jimenez, E.; Joosten, R. P.; Keegan, R. M.; Keep, N.; Krissinel, E. B.; Kolenko, P.; Kovalevskiy, O.; Lamzin, V. S.; Lawson, D. M.; Lebedev, A. A.; Leslie, A. G. W.; Lohkamp, B.; Long, F.; Maly, M.; McCoy, A. J.; McNicholas, S. J.; Medina, A.; Millan, C.; Murray, J. W.; Murshudov, G. N.; Nicholls, R. A.; Noble, M. E. M.; Oeffner, R.; Pannu, N. S.; Parkhurst, J. M.; Pearce, N.; Pereira, J.; Perrakis, A.; Powell, H. R.; Read, R. J.; Rigden, D. J.; Rochira, W.; Sammito, M.; Sanchez Rodriguez, F.; Sheldrick, G. M.; Shelley, K. L.; Simkovic, F.; Simpkin, A. J.; Skubak, P.; Sobolev, E.; Steiner, R. A.; Stevenson, K.; Tews, I.; Thomas, J. M. H.; Thorn, A.; Valls, J. T.; Uski, V.; Uson, I.; Vagin, A.; Velankar, S.; Vollmar, M.; Walden, H.; Waterman, D.; Wilson, K. S.; Winn, M. D.; Winter, G.; Wojdyr, M.; Yamashita, K., The CCP4 suite: integrative software for macromolecular crystallography. *Acta Crystallogr D Struct Biol* **2023,** *79* (Pt 6), 449-461.

222. Emsley, P.; Lohkamp, B.; Scott, W. G.; Cowtan, K., Features and development of Coot. *Acta Crystallogr D Biol Crystallogr* **2010,** *66* (Pt 4), 486-501.

223. Afonine, P. V.; Grosse-Kunstleve, R. W.; Echols, N.; Headd, J. J.; Moriarty, N. W.; Mustyakimov, M.; Terwilliger, T. C.; Urzhumtsev, A.; Zwart, P. H.; Adams, P. D., Towards automated crystallographic structure refinement with phenix.refine. *Acta Crystallogr D Biol Crystallogr* **2012,** *68* (Pt 4), 352-67.

Affidavit

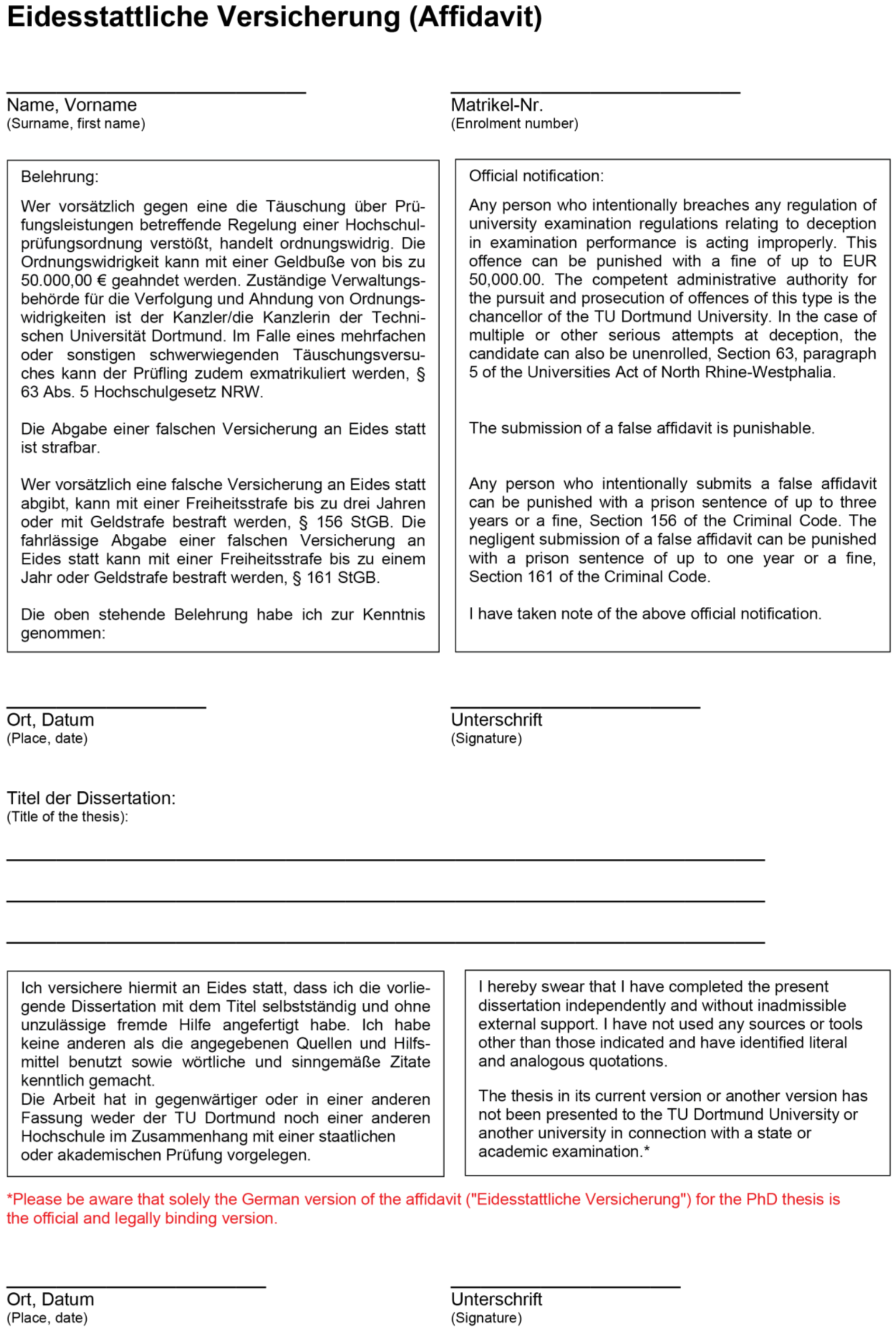

Eidesstattliche Versicherung (Affidavit)

Name, Vorname
(Surname, first name)

Matrikel-Nr.
(Enrolment number)

Belehrung:

Wer vorsätzlich gegen eine die Täuschung über Prüfungsleistungen betreffende Regelung einer Hochschulprüfungsordnung verstößt, handelt ordnungswidrig. Die Ordnungswidrigkeit kann mit einer Geldbuße von bis zu 50.000,00 € geahndet werden. Zuständige Verwaltungsbehörde für die Verfolgung und Ahndung von Ordnungswidrigkeiten ist der Kanzler/die Kanzlerin der Technischen Universität Dortmund. Im Falle eines mehrfachen oder sonstigen schwerwiegenden Täuschungsversuches kann der Prüfling zudem exmatrikuliert werden, § 63 Abs. 5 Hochschulgesetz NRW.

Die Abgabe einer falschen Versicherung an Eides statt ist strafbar.

Wer vorsätzlich eine falsche Versicherung an Eides statt abgibt, kann mit einer Freiheitsstrafe bis zu drei Jahren oder mit Geldstrafe bestraft werden, § 156 StGB. Die fahrlässige Abgabe einer falschen Versicherung an Eides statt kann mit einer Freiheitsstrafe bis zu einem Jahr oder Geldstrafe bestraft werden, § 161 StGB.

Die oben stehende Belehrung habe ich zur Kenntnis genommen:

Official notification:

Any person who intentionally breaches any regulation of university examination regulations relating to deception in examination performance is acting improperly. This offence can be punished with a fine of up to EUR 50,000.00. The competent administrative authority for the pursuit and prosecution of offences of this type is the chancellor of the TU Dortmund University. In the case of multiple or other serious attempts at deception, the candidate can also be unenrolled, Section 63, paragraph 5 of the Universities Act of North Rhine-Westphalia.

The submission of a false affidavit is punishable.

Any person who intentionally submits a false affidavit can be punished with a prison sentence of up to three years or a fine, Section 156 of the Criminal Code. The negligent submission of a false affidavit can be punished with a prison sentence of up to one year or a fine, Section 161 of the Criminal Code.

I have taken note of the above official notification.

Ort, Datum
(Place, date)

Unterschrift
(Signature)

Titel der Dissertation:
(Title of the thesis):

Ich versichere hiermit an Eides statt, dass ich die vorliegende Dissertation mit dem Titel selbstständig und ohne unzulässige fremde Hilfe angefertigt habe. Ich habe keine anderen als die angegebenen Quellen und Hilfsmittel benutzt sowie wörtliche und sinngemäße Zitate kenntlich gemacht.
Die Arbeit hat in gegenwärtiger oder in einer anderen Fassung weder der TU Dortmund noch einer anderen Hochschule im Zusammenhang mit einer staatlichen oder akademischen Prüfung vorgelegen.

I hereby swear that I have completed the present dissertation independently and without inadmissible external support. I have not used any sources or tools other than those indicated and have identified literal and analogous quotations.

The thesis in its current version or another version has not been presented to the TU Dortmund University or another university in connection with a state or academic examination.*

*Please be aware that solely the German version of the affidavit ("Eidesstattliche Versicherung") for the PhD thesis is the official and legally binding version.

Ort, Datum
(Place, date)

Unterschrift
(Signature)